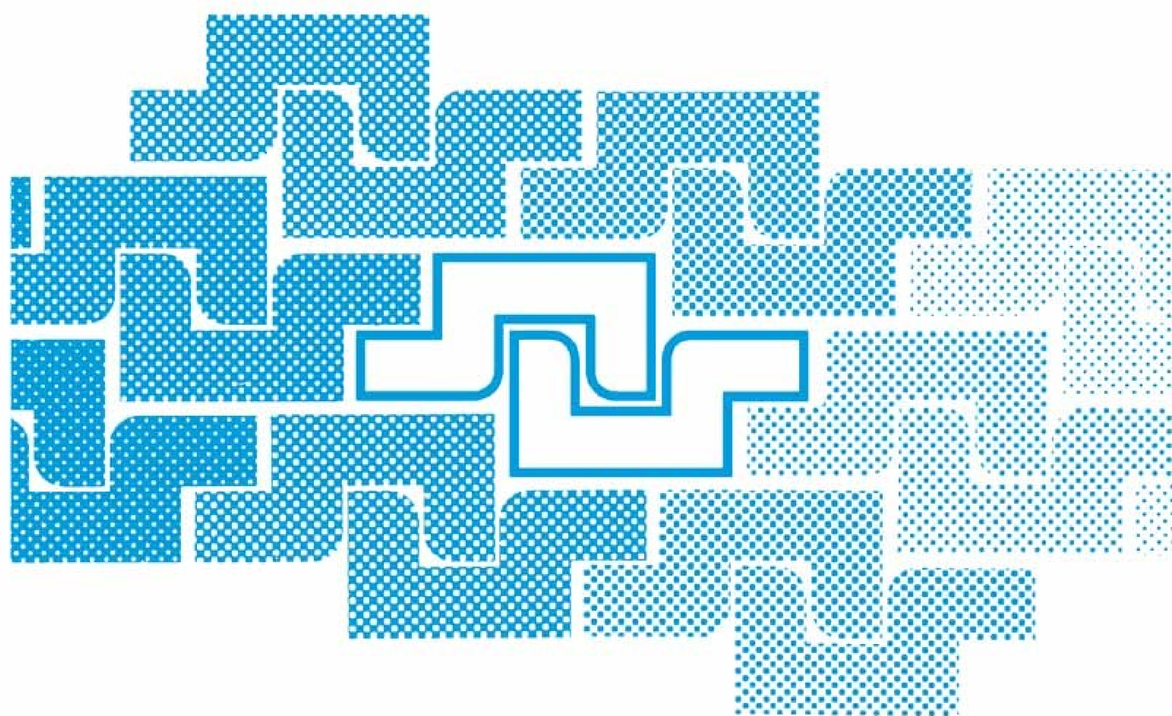

Zinc Oxide - A Material for Micro- and Optoelectronic Applications

Edited by

Norbert H. Nickel and Evgenii Terukov

NATO Science Series

II. Mathematics, Physics and Chemistry – Vol. 194

Zinc Oxide – A Material for Micro- and Optoelectronic Applications

NATO Science Series

A Series presenting the results of scientific meetings supported under the NATO Science Programme.

The Series is published by IOS Press, Amsterdam, and Springer (formerly Kluwer Academic Publishers) in conjunction with the NATO Public Diplomacy Division.

Sub-Series

I. Life and Behavioural Sciences	IOS Press
II. Mathematics, Physics and Chemistry	Springer (formerly Kluwer Academic Publishers)
III. Computer and Systems Science	IOS Press
IV. Earth and Environmental Sciences	Springer (formerly Kluwer Academic Publishers)

The NATO Science Series continues the series of books published formerly as the NATO ASI Series.

The NATO Science Programme offers support for collaboration in civil science between scientists of countries of the Euro-Atlantic Partnership Council. The types of scientific meeting generally supported are “Advanced Study Institutes” and “Advanced Research Workshops”, and the NATO Science Series collects together the results of these meetings. The meetings are co-organized by scientists from NATO countries and scientists from NATO’s Partner countries — countries of the CIS and Central and Eastern Europe.

Advanced Study Institutes are high-level tutorial courses offering in-depth study of latest advances in a field.
Advanced Research Workshops are expert meetings aimed at critical assessment of a field, and identification of directions for future action.

As a consequence of the restructuring of the NATO Science Programme in 1999, the NATO Science Series was re-organized to the four sub-series noted above. Please consult the following web sites for information on previous volumes published in the Series.

http://www.nato.int/science
http://www.springeronline.com
http://www.iospress.nl

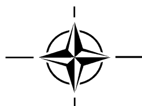

Series II: Mathematics, Physics and Chemistry – Vol. 194

Zinc Oxide – A Material for Micro- and Optoelectronic Applications

edited by

Norbert H. Nickel

Hahn-Meitner-Institut Berlin,
Germany

and

Evgenii Terukov

A.F. Ioffe Physico-Technical Institute,
St. Petersburg, Russia

Published in cooperation with NATO Public Diplomacy Division

Proceedings of the NATO Advanced Research Workshop on
Zinc Oxide as a Material for Micro- and Optoelectronic Applications
St. Petersburg, Russia
23–25 June 2004

A C.I.P. Catalogue record for this book is available from the Library of Congress.

ISBN-10 1-4020-3474-1 (PB)
ISBN-13 978-1-4020-3474-9 (PB)
ISBN-10 1-4020-3473-3 (HB)
ISBN-10 1-4020-3475-X (e-book)
ISBN-13 978-1-4020-3473-2 (HB)
ISBN-13 978-1-4020-3475-6 (e-book)

Published by Springer,
P.O. Box 17, 3300 AA Dordrecht, The Netherlands.

www.springeronline.com

Printed on acid-free paper

All Rights Reserved
© 2005 Springer
No part of this work may be reproduced, stored in a retrieval system, or transmitted in any form or by any means, electronic, mechanical, photocopying, microfilming, recording or otherwise, without written permission from the Publisher, with the exception of any material supplied specifically for the purpose of being entered and executed on a computer system, for exclusive use by the purchaser of the work.

Printed in the Netherlands.

Contents

Contributing Authors ix

Preface xv

PART I: ZnO Bulk and Layer Growth 1

The Scope of Zinc Oxide Bulk Growth 3
ROBERT TRIBOULET, VICENTE MUNOZ-SANJOSE, RAMON TENA-ZAERA, MARI CARMEN MARTINEZ-TOMAS, AND SAÏD HASSANI

Growth Mechanism of ZnO Layers 15
A. KH. ABDUEV, A. SH. ASVAROV, A. K. AKHMEDOV, I. K. KAMILOV, AND S. N. SULYANOV

Kinetics of High-Temperature Defect Formation in ZnO in the Stream of Oxygen Radicals 25
M. B. KOTLYAREVSKY, I. V. ROGOZIN, AND A. V. MARAKHOVSKY

PART II: Electrical, Optical, and Structural Properties 35

Electrical Properties of ZnO 37
DAVID C. LOOK, BRUCE B. CLAFLIN, GENE CANTWELL, SEONG-JU PARK, AND GARY M. RENLUND

Electrical Properties of ZnO Thin Films and Single Crystals 47
M. GRUNDMANN, H. VON WENCKSTERN, R. PICKENHAIN, S. WEINHOLD, B. CHENGNUI, AND O. BREITENSTEIN

Structure, Morphology, and Photoluminescence of ZnO Films 59
V. A. KARPINA, V. D. KHRANOVSKYY, V. I. LAZORENKO, G. V. LASHKAREV, I. V. BLONSKY, AND V. A. BATURIN

Optics and Spectroscopy of Point Defects in ZnO 69
VLADIMIR NIKITENKO

Whispering Gallery Modes in Hexagonal Zinc Oxide Micro- and Nanocrystals 83
THOMAS NOBIS, EVGENI M. KAIDASHEV, ANDREAS RAHM, MICHAEL LORENZ, AND MARIUS GRUNDMANN

Properties of Dislocations in Epitaxial ZnO Layers Analyzed by Transmission Electron Microscopy 99
E. MÜLLER, D. LIVINOV, D. GERTHSEN, C. KIRCHNER, A. WAAG, N. OLEYNIK, A. DADGAR, AND A. KROST

PART III: Role of Hydrogen 113

Muon Spin Rotation Measurements on Zinc Oxide 115
E. A. DAVIS

Hydrogen Donors in Zinc Oxide 125
M. D. MCCLUSKEY AND S. J. JOKELA

Hydrogen-Related Defects in Zno Studied by IR Absorption Spectroscopy 133
E.V. LAVROV, F. BÖRRNERT, AND J. WEBER

Influence of the Hydrogen Concentration on H Bonding in Zinc Oxide 145
N. H. NICKEL

PART IV: Fundamental Properties 157

Valence Band Ordering and Magneto-Optical Properties of Free and Bound Excitons in ZnO 159
A.V. RODINA, M. STRASSBURG, M. DWORZAK, U. HABOECK, A. HOFFMANN, H. R. ALVES, A. ZEUNER, D. M. HOFMANN, AND B. K. MEYER

Fundamental Optical Spectra and Electronic Structure of Zno Crystals 171
V. VAL. SOBOLEV AND V. V. SOBOLEV

Photo-Induced Localized Lattice Vibrations in ZnO Doped with 3d Transition Metal Impurities 183
ALEXEY KISLOV

PART V: Device Applications 195

ZnO Window Layers for Solar Cells 197
WALTHER FUHS

ZnO/AlGaN Ultraviolet Light Emitting Diodes 211
E. V. KALININA, A. E. CHERENKOV, G. A. ONUSHKIN, YA. I. ALIVOV, D. C. LOOK, B. M. ATAEV, A. K. OMAEV, AND C. M. CHUKICHEV

ZnO Transparent Thin-Film Transistor Device Physics 217
J. F. WAGER

Zinc Oxide Thin-Film Transistors 225
E. FORTUNATO, P. BARQUINHA, A. PIMENTEL, A. GONÇALVES, A. MARQUES, L. PEREIRA, AND R. MARTINS

Index 239

Contributing Authors

A. Kh. Abduev
Russian Academy of Sciences, Makhachkala, Russia

A. K. Akhmedov
Russian Academy of Sciences, Makhachkala, Russia

Ya. I. Alivov
Institute of Microel. Technology, Chernogolovka, Russia

H. R. Alves
Justus-Liebig-Universität Giessen, Giessen, Germany

A. Sh.Asvarov
Russian Academy of Sciences, Makhachkala, Russia

B. M. Ataev
Daghestan Scientific Centre of RAS, Makhachkala, Russia

P. Barquinha
New University of Lisbon, Caparica, Portugal

V. A. Baturin
National Academy of Sciences of Ukraine, Kyiv, Ukraine

I. V. Blonsky
National Academy of Sciences of Ukraine, Kyiv, Ukraine

F. Börrnert
Technical University Dresden, Dresden, Germany

O. Breitenstein
Max-Planck-Institut für Mikrostrukturphysik, Halle / Saale, Germany

Gene Cantwell
ZN Technology, Brea, California, USA

B. Chengnui
Universität Leipzig, Leipzig, Germany

A. E. Cherenkov
A. F. Ioffe Physico-Technical Institute, St. Petersburg, Russia

C. M. Chukichev
Moscow State University, Moscow, Russia

Bruce B. Claflin
Wright State University, Dayton, Ohio, USA

A. Dadgar
Otto von Guericke Universität, Magdeburg, Germany

E. A. Davis
University of Cambridge, Cambridge, United Kingdom

M. Dworzak
Technical University of Berlin, Berlin, Germany

E. Fortunato
New University of Lisbon, Caparica, Portugal

Walther Fuhs
Hahn-Meitner-Institut Berlin, Berlin, Germany

D. Gerthsen
Universität Karlsruhe (TH), Karlsruhe, Germany

A. Gonçalves
New University of Lisbon, Caparica, Portugal

Marius Grundmann
Universität Leipzig, Leipzig, Germany

U. Haboeck
Technical University of Berlin, Berlin, Germany

Saïd Hassani
CNRS, Meudon, France

A. Hoffmann
Technical University of Berlin, Berlin, Germany

D. M. Hofmann
Justus-Liebig-Universität Giessen, Giessen, Germany

S. J. Jokela
Washington State University, Pullman, Washington, USA

Evgeni M. Kaidashev
Universität Leipzig, Leipzig, Germany

E. V. Kalinina
A. F. Ioffe Physico-Technical Institute, St. Petersburg, Russia

I. K. Kamilov
Russian Academy of Sciences, Makhachkala, Russia

V. A. Karpina
National Academy of Sciences of Ukraine, Kyiv, Ukraine

V. D. Khranovskyy
National Academy of Sciences of Ukraine, Kyiv, Ukraine

C. Kirchner
Universität Ulm, Ulm, Germany

Alexey Kislov
Ural State Technical University, Ekaterinburg, Russia

M. B. Kotlyarevsky
Academy of Management and Information Techn., Berdyansk, Ukraine

A. Krost
Otto von Guericke Universität, Magdeburg, Germany

G. V. Lashkarev
National Academy of Sciences of Ukraine, Kyiv, Ukraine

E. V. Lavrov
Technical University Dresden, Dresden, Germany

V. I. Lazorenko
National Academy of Sciences of Ukraine, Kyiv, Ukraine

D. Livinov
Universität Karlsruhe (TH), Karlsruhe, Germany

David C. Look
Wright State University, Dayton, Ohio, USA

Michael Lorenz
Universität Leipzig, Leipzig, Germany

A. V. Marakhovsky
Berdyansk Teachers Training University, Berdyansk, Ukraine

A. Marques
New University of Lisbon, Caparica, Portugal

R. Martins
New University of Lisbon, Caparica, Portugal

Mari Carmen Martinez-Tomas
Universitat de València, Burjassot, Spain

M. D. McCluskey
Washington State University, Pullman, Washington, USA

B. K. Meyer
Justus-Liebig-Universität Giessen, Giessen, Germany

E. Müller
Universität Karlsruhe (TH), Karlsruhe, Germany

Vicente Munoz-Sanjosé
Universitat de València, Burjassot, Spain

Norbert H. Nickel
Hahn-Meitner-Institut Berlin, Berlin, Germany

Vladimir Nikitenko
Moscow State Transport University, Moscow, Russia

Thomas Nobis
Universität Leipzig, Leipzig, Germany

N. Oleynik
Otto von Guericke Universität, Magdeburg, Germany

A. K. Omaev
Daghestan Scientific Centre of RAS, Makhachkala, Russia

G. A. Onushkin
A. F. Ioffe Physico-Technical Institute, St. Petersburg, Russia

Seong-Ju Park
K-JIST, Kwangju, Korea

L. Pereira
New University of Lisbon, Caparica, Portugal

R. Pickenhain
Universität Leipzig, Leipzig, Germany

A. Pimentel
New University of Lisbon, Caparica, Portugal

Andreas Rahm
Universität Leipzig, Leipzig, Germany

Gary M. Renlund
ON International, Salt Lake City, Utah, USA

A.V. Rodina
A. F. Ioffe Physico-Technical Institute, St. Petersburg, Russia

I. V. Rogozin
Berdyansk Teachers Training University, Berdyansk, Ukraine

M. Strassburg
Technical University of Berlin, Berlin, Germany

Ramon Tena-Zaera
Universitat de València, Burjassot, Spain

Robert Triboulet
CNRS, Meudon, France

V. Val. Sobolev
Udmurt State University, Izhevsk, Russia

V. V. Sobolev
Udmurt State University, Izhevsk, Russia

S. N. Sulyanov
Russian Academy of Sciences, Moscow, Russia

A. Waag
Universität Braunschweig, Braunschweig, Germany

J. F. Wager
Oregon State University, Corvallis, Oregon, USA

H. von Wenckstern
Universität Leipzig, Leipzig, Germany

J. Weber
Technical University Dresden, Dresden, Germany

S. Weinhold
Universität Leipzig, Leipzig, Germany

A. Zeuner
Justus-Liebig-Universität Giessen, Giessen, Germany

Preface

Recently, a significant effort has been devoted to the investigation of ZnO as a suitable semiconductor for UV light-emitting diodes, lasers, and detectors and hetero-substrates for GaN. Research is driven not only by the technological requirements of state-of-the-art applications but also by the lack of a fundamental understanding of growth processes, the role of intrinsic defects and dopants, and the properties of hydrogen. The NATO Advanced Research Workshop on "*Zinc oxide as a material for micro- and optoelectronic applications",* held from June 23 to June 25 2004 in St. Petersburg, Russia, was organized accordingly and started with the growth of ZnO. A variety of growth methods for bulk and layer growth were discussed. These techniques comprised growth methods such as closed space vapor transport (CSVT), metal-organic chemical vapor deposition, reactive ion sputtering, and pulsed laser deposition. From a structural point of view using these growth techniques ZnO can be fabricated ranging from single crystalline bulk material to polycrystalline ZnO and nanowhiskers. A major aspect of the ZnO growth is doping. *n*-type doping is relatively easy to accomplish with elements such al Al or Ga. At room temperature single crystal ZnO exhibits a resistivity of about 0.3 Ω-cm, an electron mobility of 225 cm^2/Vs, and a carrier concentration of $\approx 10^{17}$ cm^{-3}. In *n*-type ZnO two shallow donors are observable with activation energies of 30 – 40 meV and 60 – 70 meV. It has been established that the shallower donor is interstitial hydrogen while it is believed that the deeper donor is a group IV element such as Al. On the other hand, reliable *p*-type doping is very difficult to achieve. Usually group I and group V elements are used as acceptors. So far the most common acceptor has been nitrogen because it should readily substitute for O and not distort the lattice significantly. A major problem is

the fact that most growth techniques either use hydrogen as a transport gas or H containing precursor gases such as NH_3. Therefore, in order to achieve *p*-type conductivity ZnO has to be subjected to a post-growth thermal treatment at temperatures above 650 °C. The purpose is two-fold: (i) interstitial hydrogen donors are eliminated and (ii) H passivated nitrogen acceptors are activated. The properties of H in ZnO expand well beyond the formation of donors and the neutralization of impurities and deep defects. The presence of "hidden H" has been suggested, which might be molecular H_2 that can be activated to form IR active O-H centers. Moreover, in sputtered ZnO the total H concentration can be as high as 10^{21} cm^{-3}. In addition, with increasing H concentration the average H binding energy increases; H becomes more strongly bound. Besides N, phosphorous and arsenic have been successfully used to fabricate *p*-type ZnO. Since the fabrication of *p*-type ZnO becomes more and more reliable the fabrication of *p-n* homojunction LEDs is not far off.

Recently, a new and rapidly developing area emerged, namely the field of transparent electronics based on ZnO transparent thin-film transistors. These devices exhibit an on-off ratio of 6 orders of magnitude, a channel mobility of 1 – 3 cm^2/Vs and can be fabricated at room temperature. Hence, already in the near future invisible large area electronics based on ZnO will revolutionize the electronics market. Although first small steps towards ZnO based optoelectronic applications are currently being made there is still a vast lack of fundamental knowledge regarding doping mechanisms, influence of impurities, formation of point and line defects, and their interactions with hydrogen. Some controversies and questions that arose during the workshop are based upon the fact that a materials basis for state-of-the-arte ZnO has not been established yet. Depending on the fabrication process the materials qualities such as impurities, their concentration, H content, number of point defects and grain boundaries can vary significantly.

This book reviews the latest experimental and theoretical studies in the field of ZnO. The chapters reflect the topics that were discussed during the NATO advanced research workshop, which brought together researchers from NATO countries, Russia, Ukraine, and Kazakhstan to encourage cross fertilization and wider dissemination of the advances in this important research field.

We would like to thank NATO for funding the Advanced Research Workshop. Above all, we would like to thank all participants for their interest in this workshop and active work in the vibrant field of ZnO.

Norbert H. Nickel

Evgenii Terukov

PART I: ZnO BULK AND LAYER GROWTH

Chapter 1

THE SCOPE OF ZINC OXIDE BULK GROWTH

Robert Triboulet[1], Vicente Munoz-Sanjosé[2], Ramon Tena-Zaera[2], Mari Carmen Martinez-Tomas[2] and Saïd Hassani[1]

[1]CNRS, Laboratoire de Physique des Solides et de Cristallogenèse, 1 Place Aristide Briand, F-92195 Meudon Cedex, France ; [2]Dept. Física Aplicada i Electromagnetisme, Universitat de València, C/ Dr. Moliner 50, 46100 Burjassot, Spain

Abstract: The techniques classically used for the growth of bulk ZnO crystals, melt-growth, vapour growth, solution-growth and hydrothermal growth, are reviewed. In the case of vapor growth, numerical simulations suggest that such species as H_2 + H_2O, CH_4, Zn, C or Fe could act as sublimation activators. The electrical and structural properties of crystals obtained by these various techniques are compared.

Key words: ZnO synthesis, melt-growth, vapor-growth, solution-growth, hydrothermal-growth, electrical and structural properties

1. INTRODUCTION

ZnO can be considered as an 'old' semiconductor which has been compelling research attention for a long time because of its applications in many scientific and industrials areas such as piezoelectric transducers, optical waveguides, acoustooptic media, conductive gas sensors, transparent conductive electrodes, varistors.[1] It has now received increasing attention and recognized as a promising candidate for applications related to its optoelectronic possibilities in the UV range. Its piezoelectric properties could also allow developing SAW filters to be integrated in future analog circuits for portable electronic for which there is a strong need. Furthermore, ZnO transparent thin-film transistors (TTFTs) are a recent and important development in the emerging field of transparent electronics. These potential applications have boosted research related to the growth of high quality ZnO thin films by a lot of different techniques that need high quality substrates.

N.H. Nickel and E. Terukov (eds.),
Zinc Oxide – A Material for Micro- and Optoelectronic Applications, 3–14.
© 2005 *Springer. Printed in the Netherlands.*

That is why research related to the ZnO bulk growth has received a considerable interest during these last years.

As a result of the small ionic radii of its constituting elements, mainly the oxygen one, and of its subsequently very short and energetic chemical bond, ZnO has a very high melting point of about 1900°C. Furthermore, because of the high electronegativity of its oxygen and zinc and because of its usual off-stoichiometry, ZnO shows an extremely high reactivity with any surrounding material at high temperature. This intrinsic property will be shown to affect strongly its growth, not only its melt-growth but also its vapour-growth.

In this chapter, the various techniques classically used for the growth of bulk ZnO crystals will be reviewed.

2. ZINC OXIDE SYNTHESIS

It is worth noting that ZnO occupies already an enviable place in the industrial market. Tens of thousands tons of ZnO powder are industrially produced each year which are used in the rubber industry as vulcanisation activator (~36 %), in the industry of ceramics as a flux (~26 %), in the chemical industry (desulphuration of gases, fabrication of stearates, phosphates. etc) (~20 %), as trace elements in the animal food (~12 %), in the paints (~3 %; 50 % in 1961!). The last ~3 % are used for different applications, in electronics (ferrites, varistors), ends of matches, pharmaceutic industry (fungicidal properties of ZnO for skin-problems, trace elements ...etc.).

ZnO powder is produced from the combustion of vapors coming from the distillation of metallic zinc according to the so-called French process or dry process. Using vapors coming from fractionated distillation, extra-pure oxide powders are produced, as illustrated from the chemical analysis data of two kinds of powder produced by two different companies:

‘pharmacy B’ grade, produced by Union Minière: Pb<20 ppm, Cd<10ppm, Fe<5 ppm, Cu<1 ppm.

‘colloidal’ grade, produced by Silar SA: Pb<20 ppm, Cd<30 ppm, Fe<5 ppm, Cu<2 ppm, Mn<2 ppm.

The grain size can change according to the variety considered.

3. ZINC OXIDE MELT-GROWTH

In spite of its very high melting-point (~ 1900°C) and very high reactivity with any surrounding material at high temperature, large ZnO bulk are grown from the melt at Cermet, Inc., Atlanta, GA, using a patented pressurized melt growth process.[2,3] The technique uses a high-pressure induction melting apparatus, wherein the ZnO melt is contained in a water-cooled crucible. The whole melting and containment process is carried out in under a controlled oxygen overpressure close to 50 atm preventing the decomposition of the compound into atomic species and establishing a thermodynamic equilibrium between the liquid ZnO and the oxygen pressure, thereby preventing reduction of the lattice. The molten charge is somewhat contained in a ZnO liner, because the cooled material in contact with the cold-wall crucible constitutes a solid thermal barrier. This prevents the molten material from coming into direct contact with the cooled surface and solves the problem of the extreme reactivity of ZnO with any crucible material at high temperature. This allows furthermore to get rid from any contamination from the crucible material. 5.5-inch-diameter, kilogram sized ingots have been reported to be grown.[3] But the drawback of the technique lies in the concave liquid/solid growth interface, as a result of the cold-wall crucible, which makes it difficult to get a large grain size.

4. ZINC OXIDE VAPOR GROWTH

Because of the high melting-point of ZnO, there have been many attempts of growth of ZnO single crystals in the vapor phase.

Small crystals have been obtained by chemical vapour transport (CVT) in closed tubes using such chemical transport agents as Zn, $ZnCl_2$, ammonium halides (NH_4X), HCl, Cl_2, NH_3, NH_4Cl, $HgCl_2$, H_2, Br_2, at source temperatures ranging from 800 to 1150°C and ΔT from 20 to 200°C.[4-8]

Crystals of small size have been grown as well in open tube systems, either by oxidation of ZnI_2,[9] ZnS, ZnSe,[10] $ZnBr_2$[11] and Zn[12-14] or by hydrolysis of ZnF_2,[15] $ZnCl_2$,[16,17] ZnI_2.[18] The oxidation or hydrolysis character of the reaction can depend on the temperature range used for a same source. The temperature of the growth region ranges generally from 900 to 1350°C.

This field of research on the vapor-growth of ZnO has been reactivated from ~ 1998 by the need of ZnO substrates for growing epitaxial structures in view of photonic applications.

Large diameter (2-inch diameter) boules have been reported to be grown at Eagle Picher at 1000-1200 °C by seeded chemical vapor transport (SCVT) in a nearly closed horizontal tube using H_2 as a carrier gas and a small

amount of water to maintain the proper stoichiometry:[19] The crystals are seeded at full diameter; the source/substrate distance is of about 3 inches; the stoichiometry is controlled from the presence of a residual water pressure; the growth rates are of about 40 μm per hour. 2-inch diameter crystals of about 1-cm-thickness are produced after 150-175 h; the etch pit (dislocation) density is of about 10^4 cm^{-2}; the X-ray double diffraction rocking curve FWHM is of about 40 arcsec, with some scattering indicating the presence of residual strains. GDMS analysis reveals the purest material ever done by Eagle Picher. The crystals are of *n*-type with $n \sim 8\times10^{16}$ cm^{-3} and μ ~150-350 cm^2/Vs @ RT. The homoepitaxial growth of ZnO on such substrates has been achieved on <0001> Zn faces chemo-mechanically polished. The future goal is the growth of larger diameter substrates, up to 3 inch.

Centimeter-size single crystals with rocking curve FWHM ~ 28 arcsec have been obtained using C or CH_4 as a transporting chemical agent.[20, 21]

ZnO, ZnO:Mn and $Zn_{1-x}Mn_xO$ (x<0.05) crystals were grown by CVT as well using hydrogen or nitrogen or chlorine and a little of water and carbon as a transporting agent.[22]

We had observed that a weak sublimation only occurred in a classical Piper and Polich configuration when using ampoules sealed under vacuum or filled with pure dry hydrogen with the material charge at 1000-1030°C and the top of the ampoule at 950°C. When such gases and gas mixtures as H_2+H_2O or Ar are introduced in the ampoules, fast transport to the cold point was observed, demonstrating the activator role of theses gases and gas mixtures.[23]

Given the fact that the free enthalpy of the reactions: $ZnO + H_2 \leftrightarrow Zn + H_2O$ and $ZnO + H_2O \leftrightarrow Zn + H_2 + O_2$ are positive and that such reactions cannot consequently occur towards the right-hand side, we have tried to investigate the actual mechanisms of the “CVT” transport with hydrogen and other species both from close-spaced vapor transport (CSVT) experiments and from a numerical modeling.

4.1 CSVT experiments

CSVT allows short experiments and easy determination of the growth rate. In this technique, a source and a substrate are placed at very short distance (~ 1mm). The experiments were achieved under a hydrogen flow of 1 l/min at two source temperatures, 550 and 600°C. In Fig. 1 is pictured the instantaneous growth rate as a function of the inverse substrate temperature for these two source temperatures. The solid and dashed lines correspond to a fit using a theoretical model.[23, 24]

From this fit, the enthalpy of formation has been calculated and found abnormally small, with a value of 0.42 eV, more than three times lower than

the one found for ZnSe. Furthermore, the variation of the instantaneous growth rate as a function of time has been found to be non-linear, as shown in Figure 2.

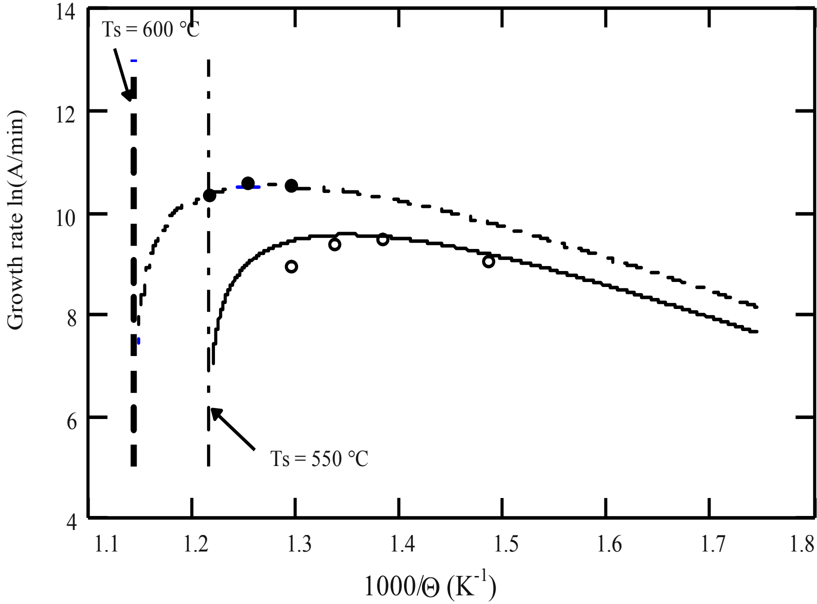

Figure 1. ZnO instantaneous growth rate as the function of the inverse source temperature for two source temperatures, 550°C and 600°C.

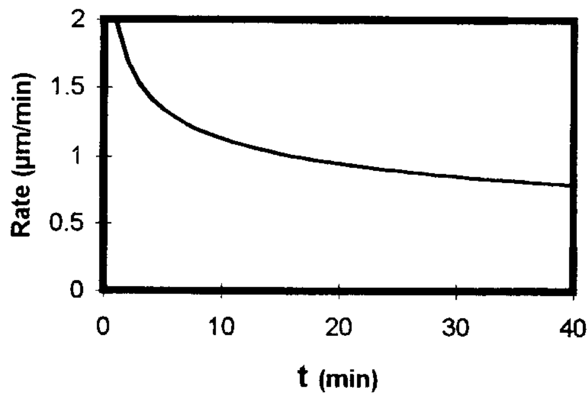

Figure 2. Instantaneous growth rate as a function of time.

From this variation of the growth rate with time and from the small ΔH value, compared to the ZnSe one, we suggested that the vapor growth of ZnO with hydrogen occurred according to a complex chemically assisted sublimation mechanism involving a competition between two different mechanisms, one associated with ZnO, the other with Zn.

4.2 Numerical simulation

In addition to this "chemically assisted" sublimation suggested with such gaseous mixtures like H_2 + H_2O, acting as "sublimation activators", several experimental observations have led us to undertake a numerical simulation of the transport.[25] While no sublimation has been found to occur in closed ampoules under vacuum conditions, high vapor transport rates are observed not only with gases like H_2 + H_2O or CH_4 but also if some particular additional species like Zn, C or Fe are introduced in the ampoule.

A simple experimental set-up consisting in a horizontal ampoule of diameter D and length L with the source material at one end and the growing crystal at the other one has been taken into account for the simulation.[25] The source and crystal temperatures are T_S and T_C respectively and the ampoule wall being subjected to a given temperature profile. We consider a PVT process in which, after ZnO decomposition, the O_2 (g) and Zn (g) are treated as two species transported in a residual gas considered as inert. These species combine at the crystallization interface giving ZnO. The involved mechanism of decomposition and crystallization being unclear, we focus only on transport phenomena. Following previous numerical studies of the mass transport process on II-VI materials,[26] surface reactions are taken into account via the partial pressures of compounds at interfaces by using the equilibrium constant and experimental data, if known, for the stoichiometric coefficient. The governing equations for the vapor transport are the conservation equations for momentum, heat and mass transfer. For the numerical resolution of the conservation equations, the computational code FLUENT has been used. The simulation has shown that if equilibrium partial pressures at interfaces are considered, the growth can only occur for a reduced interval of residual gas pressure (~10^{-3} atm). Fig. 3 shows that mass fluxes through both interfaces are only similar for a narrow subinterval of total pressures around 10^{-3} atm. Partial pressures of species, mainly Zn, higher than those corresponding to the congruent sublimation ("equilibrium pressures") are required to obtain an effective mass transport in a wide interval of total pressures. The generation of such pressures higher than the equilibrium ones becomes a limiting step in the transport of ZnO by vapor transport. This behaviour suggests the presence of an "activated" mechanism

in the ZnO decomposition, as proposed in the CSVT approach. Some kind of "autocatalytic" process is induced from the reaction of ZnO with such species as H_2 + H_2O, H_2O, Zn, C, CO, CH_4 or Fe resulting in the generation of an excess of Zn.

Searching for a mechanism that could justify these high pressures, we have suggested that:

A plausible mechanism could be the autocatalytic role of Zn that, by means of a surface reaction, would reduce the activation energy of the ZnO decomposition and would generate partial pressures higher than those at equilibrium.

The role of some additional species as Zn, Fe, Cu, C and H_2, in the ZnO growth by vapor transport, can be interpreted in this framework. These species would produce a Zn excess, either directly or from an O_2 consumption.

This "autocatalytic" mechanism paves the way to new processes to promote the growth of ZnO by vapor transport using the generation of an additional Zn vapor pressure and limiting the off-stoichiometric effects by controlling it.

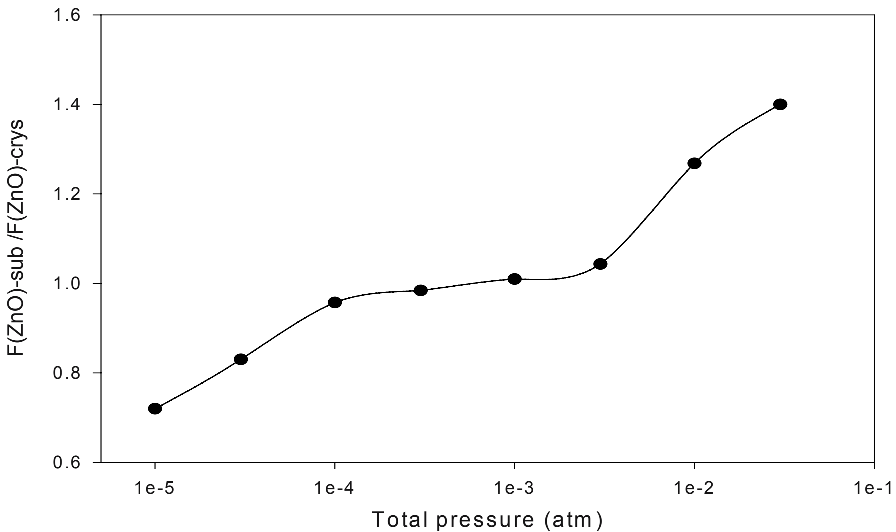

Figure 3. Calculated ratio between ZnO mass fluxes at both interfaces as a function of total pressure under equilibrium conditions.

5. ZINC OXIDE SOLUTION GROWTH

Such solvents as PbF_2[27] and V_2O_5/P_2O_5 mixtures[28] have been used for the flux growth of ZnO crystals. Using PbF_2 as the solvent in sealed Pt crucibles, ZnO crystals have been grown by THM.[29] $PbCl_2$ has been found to be a very good solvent of ZnO as well, but showing also great reactivity with any surrounding material but platinum.[30] The same authors have found the Zn-In alloys to be good solvents of ZnO without reactivity with silica. NaCl has been found recently to be an excellent solvent of ZnO allowing solution-growth in silica at temperatures of about 900°C.[31] Figure 4 pictures a ZnO crystal grown using NaCl as a solvent.

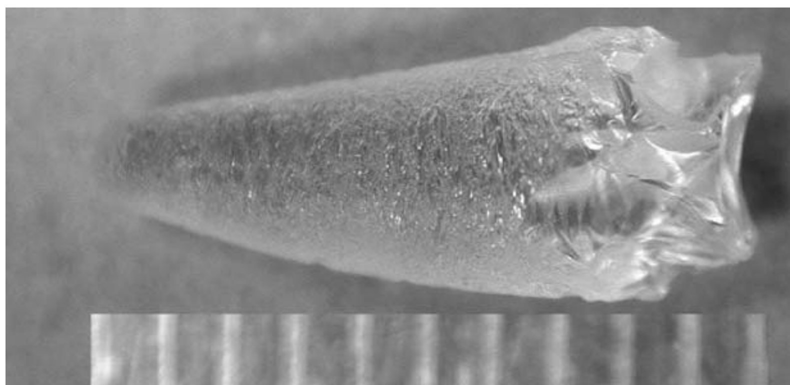

Figure 4. ZnO crystal grown using NaCl as a solvent.

6. ZINC OXIDE HYDROTHERMAL GROWTH

Hydrothermal-growth is usually defined as the use of an aqueous solvent at elevated temperature and pressure to dissolve a solute which would be insoluble under ordinary conditions. The advantages of the hydrothermal technique are a low growth temperature, a ΔT close to 0 at liquid/solid interface, an 'easily scalable' technique, the reduction of most of the impurities from source. The disadvantages are the presence of intermediate products, the lithium or sodium or potassium incorporation when such solvents as LiOH, NaOH or KOH are used, the slow growth rates (~10 mils per day), the inert liner needed, the occasional incorporation of OH and H_2O.

The first experiments on ZnO crystal growth by the hydrothermal method began in the early sixties, both in Bell Telephone Laboratories and in the Institute of Crystallography of the USSR Academy of Sciences. The

hydrothermal method has been shown suitable for the growth of large ZnO crystals from $(OH)^-$ solutions at temperatures <500°C under high pressure (15 to 150 MPa) with a temperature difference ΔT ~ 3 - 80K and a growth rate in the range 0.05-0.3 mm/day.[32-37] More recently, high quality ZnO crystals, as demonstrated by X-ray rocking curves in the 40 arcsec range and sharp PL peaks, have been grown hydrothermally at 355 °C with a ΔT of 10°C from NaOH/KOH solutions as the solvent, pressures of 18,000 to 22,000 psi (maximum pressure 1500 atm).[38] The crystals present a dislocation density < 500 cm^{-2}, a X-ray double diffraction FWHM ~130 arcsec and carrier mobilities ~175 cm^2/Vs @ RT. The O and Zn surfaces of (0001) planes have been found to behave differently. GaN layers deposited at 750 °C on such substrates show DDX FWHM of 735 arcsec. Using a KOH/LiOH solvent, ZnO bulk single crystals about 10 mm in dimension have been grown at temperatures less than 400 °C at pressures ranging from 830 to 1110 Mpa.[39]

Hydrothermal growth of ZnO remains very active in the Institute of Crystallography of the Russian Academy of Sciences.[40] Typical growth conditions are[40]: temperature of the dissolution zone 270-350°C, temperature difference between the growth and the dissolution zones, ΔT ~ 20-80°C, pressure 15-140 MPa, solvent KOH + LiOH, silver liner of capacity 500 cm^3 put in autoclaves of capacity 1000 cm^3. The growth rate is shown to depend on the crystal orientation on the basis of the polar character of the crystal structure along the c-axis and the presence of negatively charged species in hydrothermal solutions.[40] Typical crystals have a cross section equal to about 3 cm and a height along the hexagonal axis equal to 1-1.5 cm.[41] They contain concentrations 10^{-2}-10^{-4} wt. % of Li and also concentrations 10^{-3}-10^{-4} wt. % of Cu, Mg, Si, Fe, Mn and Ag.

Very spectacular results in the hydrothermal growth of ZnO have been recently reported by Oshshima *et al.*[42] from Fukuda's laboratory in Sendaï. 2-in ZnO single crystals (size up to 50×50×15 mm3) have been grown using KOH/LiOH @ T= 300-400°C and P = 80-100 MPa. Rocking-curve FWHM of 8 arc.sec for (002) reflections and 25 arc.sec for the (101) reflections are reported (to be compared with 42 and 370 arc.sec respectively for a CVT-grown one). But incorporation of Li and K originated from LiOH and KOH was observed at concentrations of 0.5-12 ppm for Li and 0.04-0.2 ppm for K. In addition, incorporation of Fe and Al was also observed. Note that the complex equipment used includes a 3 m length and 200 mm inner diameter Pt liner preventing impurity incorporation from the autoclave inner surface.

7. CHARACTERIZATION OF THE CRYSTALS

Some electrical and structural properties of crystals grown by various techniques, melt-growth, hydrothermal growth, SCVT and CVT are summarized in the following table.

Table 1. Electrical and structural characteristics of the crystals.

technique	growth conditions	size	FWHM (arcsec)	*n* (cm^{-3})	*μ* cm^2/Vs	Ref.
Melt-growth	CERMET's Process	1 inch	125	5×10^{17}	130	2
“”	“”	5.5 inch	40-100	8.4×10^{16}	150	3
Hydrothermal growth	335-400°C, ΔT=10°C KOH/NaOH or /LiOH Pmax ~ 800-1500 MPa		~ 100		175	33-35
“”	KOH/LiOH Pmax ~ 80-100 MPa Growth rate ~ 8 µm/h	2-in	8			38
SCVT	Source 1000-1200°C dist. source-substrate 3 inch res. atm. H_2+H_2O; seeds Growth rate: 40 µm/h	Ø 40 mm	40	8×10^{16}		13
CVT	C as an “activator”	cm-size	28			20

Whatever the method used, the electrical and structural properties of the crystals are very close except the record structural quality recently reported for hydrothermally grown crystals by Ohshima *et al*.[38] Note the low growth rates of the vapor grown crystals and more again of the hydrothermally grown ones which could be a handicap in view of industrial production.

8. CONCLUSIONS

In spite of the numerous efforts dedicated to the ZnO bulk growth for several years, high quality large and cheap ZnO substrates are not yet available. The best crystals obtained so far as far as the crystallographic quality is concerned have been grown by the hydrothermal method, whose possibilities are limited by an extremely weak growth rate and the unavoidable incorporation of impurities coming from the solvent, in addition to complex equipment. The better knowledge and understanding of the mechanisms of vapor transport can let expect significant progresses in this field in a near future.

REFERENCES

1. R. Triboulet, *Proceedings SPIE* **4412,** 1 (2000).
2. G. Agarwal, J. E. Nause, and D. N. Hill, *Mat. Res. Soc. Symp. Proc.* **512**, 41 (1998).
3. D. C. Reynolds, C. W. Litton, D. C. Look, J. E. Hoeschler, B. Claflin, T. C. Collins, J. Nause, and B. Nemeth, *J. Appl. Phys*. **95**, 4802 (2004).
4. M. Shiloh and J. Gutman, *J. Crystal Growth* **11**, 105 (1971).
5. W. Piekarczyk, S. Gazda, and T. Niemyski, *J. Crystal Growth* **12**, 272 (1972).
6. K. Matsumoto, K. Konemura, and G. Shimaoka, *J. Crystal Growth* **71**, 99 (1985).
7. K. Matsumoto and G. Shimaoka, *J. Crystal Growth* **86**, 410 (1988).
8. K. Matsumoto and K. Noda, *J. Crystal Growth* **102**, 137 (1990).
9. M. Hirose and I. Kubo, *Jpn. J. Appl. Phys*. **8**, 402 (1969).
10. Y. S. Park and D. C. Reynolds, *J. Appl. Phys.* **38**, 756 (1967).
11. M. Hirose, Y. Furuya, and I. Kubo, *Jpn. J. Appl. Phys.* **9**, 726 (1970).
12. E. Scharowsky, *Z. Phys.* **135**, 318 (1953).
13. K. F. Nielsen, *J. Crystal Growth* **3/4**, 141 (1968).
14. K. J. Fischer, *J. Crystal Growth* **34,** 139 (1976).
15. I. Kubo, *J. Phys. Soc. Jap.* **16**, 2358 (1961).
16. T. Takahasi, A. Ebina, and A. Kamigawa, *Jpn. J. Appl. Phys.* **5,** 560 (1966).
17. E. A. Weaver, *J. Crystal Growth* **1**, 320 (1967).
18. M. Hirose and Y. Furuya, *Jpn. J. Appl. Phys.* **9**, 423 (1970).
19. D. C. Look, D. C. Reynolds, J. R. Sizelove, R. L. Jones, C. W. Litton, G. Cantwell, and W. C. Harsch, *Solid State Comm.* **105**, 399 (1998).
20. J.-M. Ntep, S. Said Hassani, A. Lusson, A. Tromson-Carli, D. Ballutaud, G. Didier, and R. Triboulet, *J. Crystal Growth,* **207**, 30 (1999).
21. S. Hassani, A. Tromson-Carli, A. Lusson, G. Didier, and R. Triboulet, *Phys. Stat. Sol.* **229**, 835 (2002).
22. A. Mycielski, A. Szadkowski, L. Kowalczyk, B. Witkowska, W. Kaliszek, B. Chwalisz, A. Wysmolek, R. Stepniewski, J. M. Baranowski, M. Potemski, A. Witowski, R. Jakiela, A. Barsz, P. Aleshkevych, M. Jouanne, W. Szuszkiewicz, A. Suchocki, E. Lusakowska, E. Kaminska, and W. Dobrowsolski, Proc. 11th International Conference on II-VI Compounds, to be published.
23. J.-M. Ntep, M. Barbé, G. Cohen-Solal, F. Bailly, A. Lusson, and R. Triboulet, *J. Crystal Growth* **184/185**, 1026 (1998).
24. R. Triboulet, J.-M. N'tep, M. Barbé, P. Lemasson, I. Mora-Sero, and V. Munoz, *J. Crystal Growth* **198/199**, 968 (1999).
25. R.Tena-Zaera, M. C. Martínez-Tomás, S. Hassani, R. Triboulet, and V. Muñoz-Sanjosé, *J. Crystal Growth*, to be published.
26. N. Ramachandran, C. Su, and S. L. Lehoczky, *J. Crystal Growth* **208**, 269 (2000).
27. K. F. Nielsen and E. F. Dearborn, *J. Phys. Chem.* **64**, 1762, (1960).
28. B. M. Wanklyn, *J. Crystal Growth* **7**, 107 (1970).
29. G. A. Wolf and H. E. LaBelle Jr., *J. Am. Ceram. Soc*., **48,** 441 (1965).
30. J.-M. Ntep, PhD thesis, Paris 2000.
31. S. Hassani, G. Didier, P. Galtier, and R. Triboulet, to be published.
32. R. A. Laudise and A. Ballman, *J. Phys. Chem.* **64**, 688 (1960).
33. E. D Kolb and R. A. Laudise, *J. Am. Ceram. Soc.***49**, 302 (1966).
34. R. A. Laudise, E. D. Kolb, and A.J. Caporaso, *J. Am. Ceram. Soc.* **47**, 9 (1964).
35. E. F. Venger, A. V. Melnichuk, L. Yu. Melnichuk, and Yu. A. Pasechnik, *phys. stat. sol.* (b) **188**, 823 (1995).

36. I. P. Kuzmina and V. F. Antonova, *M. Nauka* **4**, 151 (1964).
37. I. P. Kuzmina, *Kristallografiya* **13**, 920 (1968).
38. M. Suscavage, M. Harris, D. Bliss, P. Yip, S.-Q. Wang, D. Schwall, L. Bouthillette, J. Bailey, M. Callahan, D. C. Look, D. C. Reynolds, R. L. Jones, and C. W. Litton, *Mat. Res. Soc. Symp. Proc.* **537,** 1999 to be published.
39. T. Sekiguchi, S. Miyashita, K. Obara, T. Shishido, and N. Sakagami, *J. Crystal Growth* **214/215**, 72 (2000).
40. L. N. Demianets and D. V. Kostomarov, *Ann. Chim. Sci*. **26**, 193 (2001).
41. V. A. Nikitenko, *J. Appl. Spectr*. **57**, 783 (1994).
42. E. Ohshima, H. Ogino, I. Niikura, K. Maeda, M. Sato, M. Ito, and T. Fukuda, *J. Crystal Growth* **260**, 166 (2004).

Chapter 2

GROWTH MECHANISM OF ZnO LAYERS

A. Kh. Abduev[1], A. Sh.Asvarov[1], A. K. Akhmedov[1], I. K. Kamilov[1] and S. N. Sulyanov[2]
[1]Institute of physics, DSC of RAS, 367003, Yaragscogo str., 94 Makhachkala, Russia; *[2]Institute of Crystalografy of RAS, 119333, Leninski pr-t 59, Moscow, Russia*

Abstract: The formation processes of clusters in gas phase in the Zn - O_2 system were studied. It was shown that $Zn_{12}O$ clusters are formed in a surplus of zinc vapor. We studied dc-magnetron sputtering of ZnO layers by co-sputtering with ZnO:Ga ceramic and Zn metal targets method. We observe that at surplus of zinc vapor in the reagent stream leads to synthesis of homogeneous layers without columnar structure. We propose that growth of ZnO layers at surplus of zinc vapor is governed by the vapor-liquid-solid mechanism.

Key words: Cluster, whisker, columnar structure, vapor-liquid-solid mechanism

1. INTRODUCTION

Development of new technologies of synthesis of ZnO layers is stimulated by potential applications in opto- and nanoelectronics. In the past decade, blue-UV generation has been obtained in ZnO thin films[1] and ZnO whiskers[2] at room temperature; p-type ZnO thin films,[3] thin-film diode structures[4]. Also transparent transistors[5] were synthesized. The interest in ZnO layers is also motivated by the search of alternatives to expensive transparent electrodes on the basis of In_2O_3-SnO_2 system.[6] Unique surface properties of zinc oxide materials stimulate research toward development of gas-sensing devices.[7] Thin layers of ZnO have been grown by various techniques, including chemical vapor deposition (CVD),[8,9] pulsed laser deposition (PLD), molecular beam epitaxy (MBE),[10,11] dc- and rf- magnetron sputtering.[12-16] From a commercial viewpoint, the method of dc-magnetron sputtering is the most attractive method for the synthesis of ZnO layers on

N.H. Nickel and E. Terukov (eds.),
Zinc Oxide – A Material for Micro- and Optoelectronic Applications, 15–24.
© 2005 *Springer. Printed in the Netherlands.*

large-area substrates. Meanwhile there are several essential drawbacks in this method including:

- the formation of columnar structures into ZnO layers, which results in decrease of carrier mobility and dispersion of light on grain boundaries;
- the presence of irradiated defects caused by the method itself;
- the poor structural perfection of ZnO layers due to far from equilibrium growth conditions of ZnO layers.

In the present work, the influence of reagents stream composition on the structure of ZnO layers has been investigated for dc-magnetron sputtering. Particular attention has been dedicated to the study of processes of reagent interactions in the gas phase. And, for a deeper understanding of this process, the process of formation of clusters in the gas phase of the simple Zn-O_2 system was investigated.

2. EXPERIMENT

To examine the processes of cluster formation in the gas phase a Knudsen Cell has been used. A mixture of ZnO and graphite powders was positioned inside the effusion cell. The carbothermal reaction between ZnO and graphite was used to create zinc vapor. The effusion cell was heated up to a temperature above 1000°C.

The co-sputtering method, when ZnO:Al (2 at.%) ceramic target and Zn metal target were sputtered simultaneously in atmosphere of pure Ar (99.99%), was used for the formation of the ZnO-Zn flow. The targets were discs 3 mm in thickness and 30 mm in diameter. The discharge current for the ZnO:Ga target was maintained at 60 mA. Sputtering of the Zn target was carried out at a discharge current in the range of 25-90 mA. The ZnO layers were deposited on amorphous SiO_2 thermally grown on Si substrate. The thickness of amorphous SiO_2 was 100 nm.

The chamber pressure was down to 5×10^{-4} Pa using a diffusion pump before introducing the Ar sputtering gas. During deposition the pressure of Ar was maintained at ≈1 Pa.

X-ray diffraction measurements were carried out using KARD-6 diffractometer with a 2D-area detector based on the multi-wire planar proportional chamber (Cu K_α-radiation, graphite monochromator, 0.1mm width incident beam slit).

LEO-1450 scanning electron microscope (SEM) was used to characterize the surface and the cross-section of the samples.

Hall voltage was measured by a four-point probe method for the samples shaped like a cross, using dc current and dc magnetic field.

3. RESULTS

3.1 Cluster formation in the gas phase

We took interest in the study of formation of nanoparticles in a gas phase and their influence on the formation of columnar structures of ZnO layers.

It is known,[17,18] that non-equilibrium conditions of scattering and cooling of the plasma leads to interactions of plasma components and the formation of clusters and nanoparticles.

Our previous studies[19,20] have shown that the interaction of equal fractions of zinc vapor and oxygen in a gas phase result in the step-by-step formation of clusters, fractal clusters and nanoparticles according to the Witten-Sander mechanism. Also it has been shown, that formation of whiskers at surplus of Zn vapour in gas phase proceeds with the vapour-liquid-solid (VLS) mechanism in the absence of a liquid-forming impurity agent. We believe that the liquid-forming agent was a ZnO_{1-x} surface phase with relatively low melting-point. ZnO_{1-x} was formed due to high pressure of Zn vapor near the growing surface.

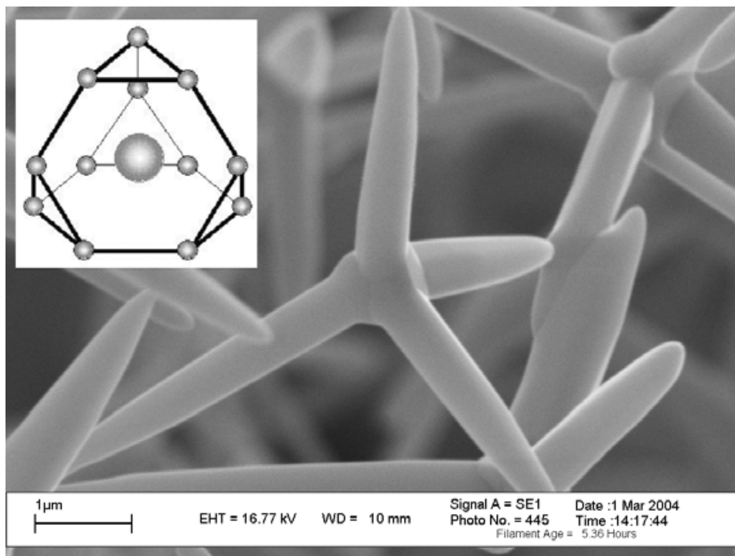

Figure 1. ZnO tetrahedral aggregate. The inset shows the model of $Zn_{12}O$ nucleus-cluster

In order to model the processes of cluster formation in a gas phase at a surplus of zinc vapour we carried out the effusion of zinc vapour in the oxygen atmosphere. There is the nucleation and the growth of the symmetric

tetrahedral aggregates in a gas phase (Fig. 1).

The characteristic feature of these tetrahedral aggregates was the simultaneous growth of four (0001)-oriented ZnO whiskers from one nucleus. Apparently the nucleus of such tetrahedral aggregates cannot be a close-packed crystallite. We speculate that the nucleus of such aggregate has tetragonal structure that leads to the further growth of the four hexagonal crystallites (whiskers).

Hence, we suggest the following model of $Zn_{12}O$ nucleus-clusters. The nucleus-cluster has the shape of the truncated tetrahedron with 12 atoms of zinc and one atom of oxygen in the center (inset of Fig. 1). Such nucleus-cluster is a loosely coupled system formed by an atom of oxygen and 12 equidistant atoms of zinc. Scattering in zinc vapor at increased partial pressure of oxygen, facilitates the nucleation and growth of (0001)ZnO whiskers on four facets of the $Zn_{12}O$ cluster occurs.

3.2 Magnetron co-sputtering of ZnO and Zn target

The columnar structure with dominant basic orientation is typical feature of the ZnO layers synthesized by methods of magnetron sputtering in conditions far from equilibrium. According to Knuyt et al.[21] the formation of columnar structures is bound to the tendency of a system to diminish its free energy. Earlier it has been shown, that ZnO columns can be formed from nano-sized grains.[22] Thus there is an angle of several degrees of disorder of these grains. However our results reveals that columns may grow in isolation and thus do not interact at the initial stage of deposition. We believe that it is possible to explain formation of columnar structure by the presence of clusters in a flow of reagents at high chamber pressures.

At first we have investigated the structure of ZnO layers grown by dc-magnetron sputtering of ZnO:Ga ceramic target, as a function of the distance between the target and the substrate.

ZnO layers were deposited on the substrate at room temperature. Target-to-substrate distances were 30, 60 and 100 mm. SEM micrographs of cross-sections of ZnO layers that have been deposited at these target-to-substrate distances are given in figure 2. The increase of the distance leads to a decrease of column width. This distance dependence may be explained by the cluster separation based on height and sizes of the clusters that reached the growing surface. In other words, we believe that the size of clusters diminishes due to smaller free length and gravity as target-to-substrate distance increases. The formation of the columnar structure can be explained by the presence of nano-sized clusters in a flow of reagents, and that the formation of layers can be described by a model close to Witten-Sanders one.

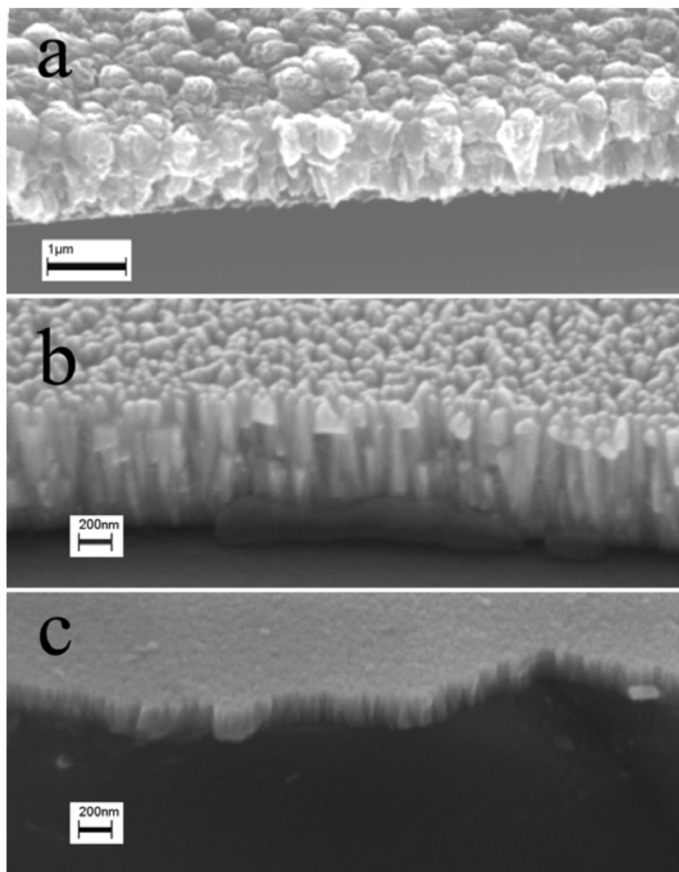

Figure 2. SEM micrograph of cross-sections of ZnO layers prepared with various target-to-substrate distances: a - 30 mm; b - 60 mm; c - 100 mm.

In order to eliminate columnar structures it is necessary to increase the migration ability of atoms and molecules on the surface and also to remove the involvement of clusters in the process of growth. To prevent the participation of clusters and nanoparticles during growth and in order to create the conditions for highly perfect ZnO layers synthesis, we explored the possibility of ZnO layers growth according to VLS-model.

The co-sputtering of ZnO:2at%Ga ceramic target and Zn metal target in Ar atmosphere had resulted in the surplus of zinc in a flow of reagents and thus created favorable conditions for the growth of ZnO layers according to VLS-model. SEM micrographs of a surfaces and cross-section of ZnO layers which have been deposited at various temperatures are given in figure 3.

At substrate temperatures of about 300°C the ZnO layers have the advanced surface and typical columnar structure. The increase of the

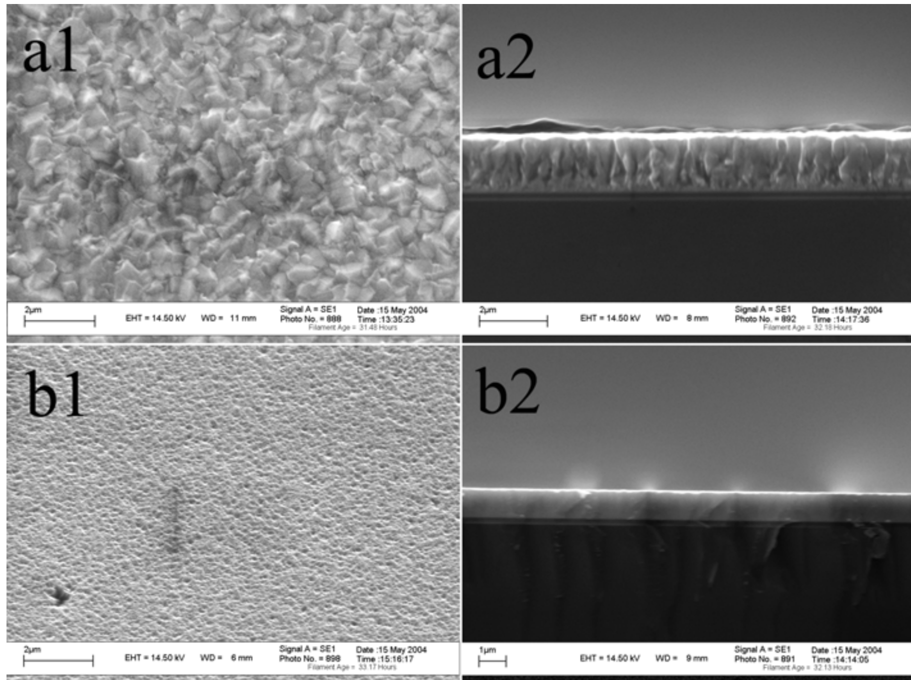

Figure 3. SEM micrographs of surfaces (a1, b1) and cross-sections (a2, b2) of ZnO layers deposited by dc-magnetron co-sputtering (a - T_{sub}=300^{0}C; b - T_{sub}=500^{0}C).

substrate temperature to 500$_0$C gives in the essential reduction of the surface relief of ZnO layer and the disappearance of columnar structures.

These ZnO layers and also the control ZnO layer deposited without co-sputtering (by dc-magnetron sputtering only of ZnO:Ga target) were characterized by the X-ray diffraction method. Si-single crystal substrate 111-reflection was used as a reference for the instrumental resolution function determination. For every exposure, the 0002-reflection from the layer was integrated in the same small rectangular area of detector. The method described in reference [23] was used. Results are plotted in fig. 4. Figure 4 shows that the FWHM values of X-ray rocking are 1.8^0 and 1.2^0 for ZnO layers deposited by co-sputtering on a substrate heated at 300^{0}C (curve 3) and 500^{0}C (curve 4), respectively, whereas the FWHM value of X-ray rocking for control ZnO layer (curve 1) is much wider. From these data it is possible to draw the conclusion, that the presence of zinc surplus in a flow of reagents near the growing surface results in the considerable improvement of the perfection of ZnO layers.

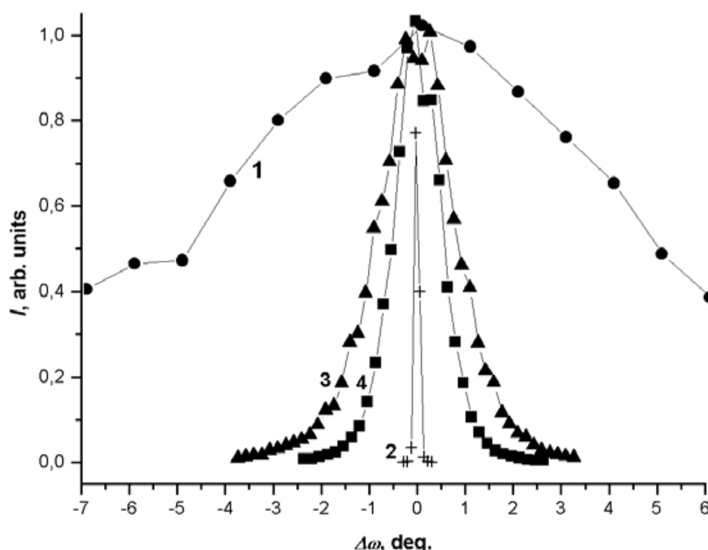

Figure 4. XRD date of: curve 1 - without co-sputtering (only sputtering of ZnO:Ga target); curve 2 - instrumental resolution function; curve 3 - co-sputtering ($T_{substrate}$=300^0C); curve 4 - co-sputtering ($T_{substrate}$=500^0C)

The resistivity of these ZnO layers decreased with increasing substrate temperature, caused mainly by an increase in Hall mobility. So, the values of Hall mobility were 18.65 $cm^2/V{\cdot}s$ and 33.78 $cm^2/V{\cdot}s$ for ZnO layers deposited by dc-magnetron co-sputtering on a substrate heated at 300^0C and 500^0C respectively, whereas the value of Hall mobility for the control ZnO layer (without co-sputtering) was 8.31 $cm^2/V{\cdot}s$. Herewith, carrier concentrations for all three samples were similar and approximately 3×10^{20} cm^{-3}.

Also the structure of ZnO layers as a function of the ratio of discharge currents for ZnO:Ga and Zn targets has been investigated. Synthesis of layers was carried out at various discharge currents for Zn target (25, 50 and 90 mA) and constant discharge current for ZnO:Ga target. The temperature of substrates was 500^0C. SEM micrographs of ZnO layers obtained under these conditions are shown in figure 5. We observe that upon an increase of zinc component in the flow of reagents there is a transition from a typical columnar structure (fig. 5a) to homogeneous layers (fig. 5d). It is clearly seen (fig. 5b), that at low discharge current of the Zn target the columnar structure of layer is still present. But the data of the XRD-measurements show, that the structural perfection of ZnO layers, deposited under maximum discharge current for Zn metal target, was improved. The value of Hall

mobility at maximum discharge current of Zn target also decreased. This trend has not been explained clearly. The films, prepared at the substrate temperature above 500^{0}C and current of Zn target 50 mA, shown best structural and electrical properties.

The involvement of clusters during growth is excluded by the increasing of vapor pressure of Zn mass and the creation of low-melting ZnO_{1-x} phase at the growing surface.

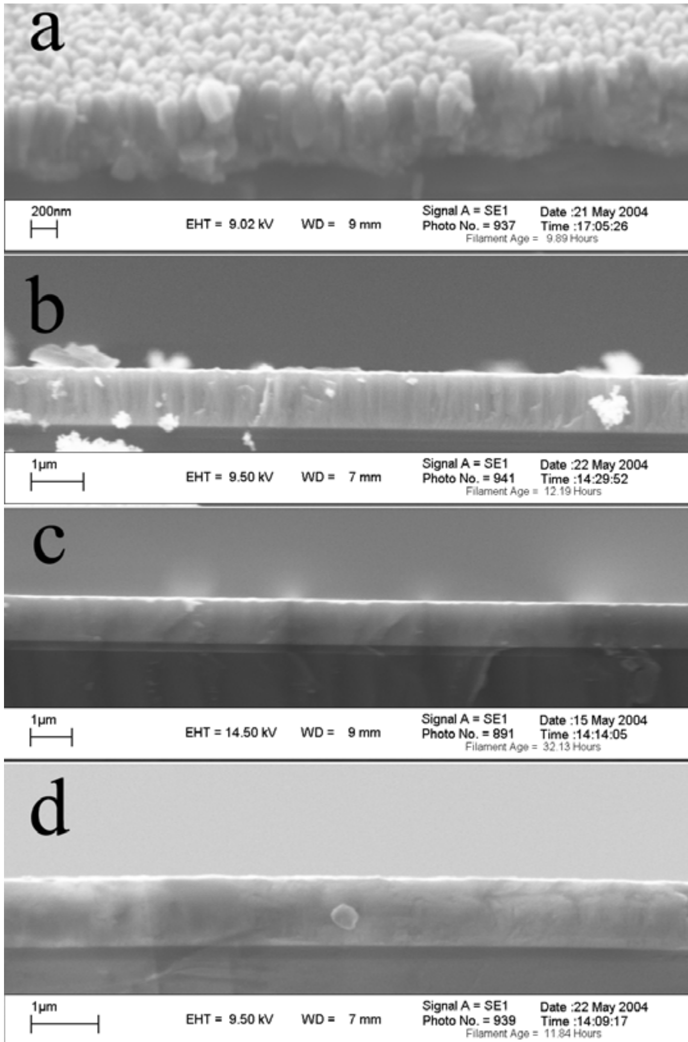

Figure 5. SEM micrographs of the cross-section of ZnO layers, deposited at various discharge currents for the Zn target: a - 0 mA; b - 25 mA; c - 50 mA; d - 90 mA.

4. CONCLUSION

Our experimental results and their subsequent analysis lead us to the following conclusions:

1. At relatively high chamber pressure (P ≈ 1 Pa) the partial aggregation of reagents is observed in the plasma of magnetron discharge.
2. When zinc vapors are spurted through the gas mixture containing oxygen, the formation of tetrahedral aggregates consisting of four whiskers originated at the nucleus tends to occur in the gas phase. According to our model, the growth of these aggregates occurs under non-equilibrium conditions as a result of the formation of $Zn_{12}O$ nucleus-clusters which subsequently grow into the tetrahedral aggregates at the adiabatic expansion of zinc vapors and $Zn_{12}O$ clusters in the gas mixture containing oxygen.
3. The mechanism of growth of columnar structure ZnO layers assumes the presence of nanosized clusters in the reagent flow and that the formation of ZnO layers can be described by a model close to the one of Witten-Sanders. Increase of target-to-substrate distance leads to the decrease of the number of aggregates in the flow near the substrate and to the improvement of the structural perfection of ZnO layers.
4. Ata a substrate temperature above 500 ^{O}C and at surplus of zinc in the flow of reagents near the growing surface there is a synthesis of structurally perfect ZnO layers. The growth mechanism of ZnO layers at surplus of zinc vapor is governed by vapor-liquid-solid mechanism. It is shown, that in the absence of liquid-forming impurity agent (Au) the growth mechanism of ZnO layers and ZnO whiskers is governed by the vapor-liquid-solid mechanism. ZnO_{1-x} surface phase with relatively low melting-point is formed due to high pressure of Zn vapor near the growing surface.

ACKNOWLEDGMENTS

This research was supported by Analytical Centre of DSC RAN.

REFERENCES

1. Sunglae Cho, Yunki Kim, Yi Sun, George K.L., *Appl. Phys. Lett.* **75**, 2761 (1999).
2. M. H. Hiang, S. Mao, H. Feick et al, *Science* **292**, 1897 (2001).
3. K. Minegishi, Y. Koiwai, Y. Kikuchi et al. , *Jpn. J. Appl. Phys.* **36**, L1454 (1997).
4. Y. R. Ryu, W. J. Kim, H. W. White. , *J. of Cryst. Growth*, **219**, 419 (2000).

5. P. F. Carsia, R. S. McLean, M. H. Reilly et al. , *Appl. Phys. Lett.* **82**, 1117 (2003).
6. T. Minami, *MRS BULLETIN* AUGUST, 38-44 (2000).
7. S. Roy, S. Basu, *Bull. Mater. Sci.* **25**, 513 (2002).
8. C. R. Gorla, N. W. Emanetoglu, S. Liang et al., *J. Appl. Phys.* **85**, 2595 (1999).
9. B. S. Li, Y. C. Liu, Z. Z. Zhi et al., *J. Vac. Sci. Technol. A* **20**, 1779 (2002).
10. H. Z. Wu, K. M. He, D. J. Qiu, and D. M. Huang, *J. of Crystal Growth* **217**, 131 (2000).
11. T. Ohgaki, N. Ohashi, H. Kakemoto et al., *J. Appl. Phys.* **93**, 1961 (2003).
12. M. Chen, Z. L. Pei, C. Sun et al., *J. Crystal Growth* **220**, 254 (2000).
13. K. Tominaga, T. Murayama, I. Mori et al., *Thin Solid Films* **386**, 267 (2001).
14. Y. Igasaki, T. Naito, K. Murakami et al., *Appl. Surf. Science* **169-170**, 512 (2001).
15. F-J. Haug, Zs. Geller, H. Zogg et al, *J. Vac. Sci. Technol. A* **19**, 171 (2001).
16. T. Minami, T. Miyata, T. Yamamoto et al., *J. Vac. Sci. Technol. A* **18**, 1584 (2000).
17. B. M. Smirnov, *Phys. Usp.* **37**, 621 (1994).
18. V. N. Tsytovich, *Phys. Usp.*, **40**, 53 (1997).
19. A. Kh. Abduev, A. K. Achmedov, V. G. Baryshnikov et al., *Technical Physics Letters* **26**, 332 (2000).
20. A. Kh. Abduev, A. Sh. Asvarov, A. K. Achmedov et al., *Technical Physics Letters*, **28**, 952 (2002).
21. G. Knuyt, C. D. Quaeyhaegens, J. Haen et al., *Thin Solid Films* **258**, 159 (1995).
22. I. Sieber, N. Wanderka, I. Urban et al., *Thin Solid Films* **330**, 108 (1998).
23. S. N. Sulyanov, A. N. Popov, and D. M. Kheiker, *J.Appl.Cryst.* **27**, 934, (1994)

Chapter 3

KINETICS OF HIGH-TEMPERATURE DEFECT FORMATION IN ZnO IN THE STREAM OF OXYGEN RADICALS

M. B. Kotlyarevsky[1], I. V. Rogozin[2], and A. V. Marakhovsky[2]
[1]Academy of Management and Information Technologies "ARIM", 3, Uritskogo Str., Berdyansk, Ukraine, 17118; [2]Berdyansk Teachers Training University, 4, Shmidt Str., Berdyansk, Ukraine, 71100

Abstract: The kinetic analysis of defect formation made it possible to develop a new method for obtaining single crystal layers by means of heat treating the II-VI compound single crystal substrates in the atomic chalcogen flux. With this method, an inversion of the conductivity in ZnO from n- to p-type has been accomplished. This technology made it also possible to obtain heterostructures.

Key words: Kinetic analysis, oxygen radicals, heterostructures, n-type ZnO, p-type ZnO

1. INTRODUCTION

In this work methods of high-energy chemistry are widely employed in the synthesis of II-VI compounds with controlled properties.[1] In this approach, a gaseous reactant is activated to produce excited neutral radicals (atoms) using an external source (photolysis, gas discharge, and others) and is then delivered to the reaction zone. One of the chief advantages of the high-energy chemical methods is that the synthesis temperature can be reduced substantially.

We have shown that this approach has also considerable potential for use in the technology of II-VI semiconductors containing nonmetals (O, S, Se, and Te) that exist only in the vapor phase at typical synthesis temperatures. A drawback common to the wide-gap ($E_g \geq 2.5$ eV) semiconductors in question (ZnS, ZnO, ZnSe) is the high and, hence, difficult to control

N.H. Nickel and E. Terukov (eds.),
Zinc Oxide – A Material for Micro- and Optoelectronic Applications, 25–34.
© 2005 *Springer. Printed in the Netherlands.*

concentration of native defects, which are generated at a high rate during high-temperature synthesis. This, in turn, leads to native-defect monopolar (n-type) conduction, limiting the application of these compounds in semiconductor optoelectronics.

Consider the interaction of II-VI crystals (ZnS, ZnSe, ZnO) with chalcogen VI (S, Se, O) vapor. High-temperature annealing of a II-VI crystal in chalcogen vapor under equilibrium conditions does not produce a chalcogen excess (e.g.: due to native acceptors such as chalcogen interstitials B_i or Zn vacancies V_{Zn}) because the formation of an acceptor center must be accompanied by the formation of a compensating donor, V_B or Zn_i, for the system to remain in thermodynamic equilibrium. Thermodynamic analysis of the high-temperature native-defect equilibrium in ZnS, ZnSe and ZnO were analyzed.[2-4] The calculations unambiguously show that there is a broad range of chalcogen vapor pressures (e.g.: up to $p \approx 100$–1000 GPa for ZnS and ZnSe) in which the dominant defect species in these compounds are V'_A and V'_B, so that the native defect conduction is fully compensated.

The thermodynamic and kinetic aspects of hole conduction self-compensation were analyzed in detail.[5–7] It was concluded that the main reason for the monopolar conduction in the compounds under consideration is that the chalcogen is present in the vapor phase in molecular form. It was also shown that the compensation of acceptor centers in II-VI compounds can be suppressed by reducing the synthesis or doping temperature to below a critical temperature, if the process is run in saturated chalcogen vapor.

Figure 1 shows the calculated defect densities in ZnS as functions of the zinc and sulfur partial pressures at 1000 K. As it is visible from the figure, there is a rather broad range of chalcogen vapor pressures (10^{-1} to 10^6 Pa) in which the conductivity is very low and varies insignificantly. The accounts show, that area of pressure p_{B_2} , at which the degree of self-compensation begins to decrease, is in the range of unattainable chalcogen vapor pressure. These conclusions relate to ZnO as well.

Thermodynamic analysis suggests approaches to achieving native-defect and impurity-related hole conduction in II-VI compounds. These are primarily non-equilibrium, high-energy chemical methods, such as ion implantation of the B component or acceptor impurity, annealing under a layer of a substance that dissolves markedly different amounts of the A and B components, and annealing in an atomic-chalcogen atmosphere.[6–7] This last method will be considered further.

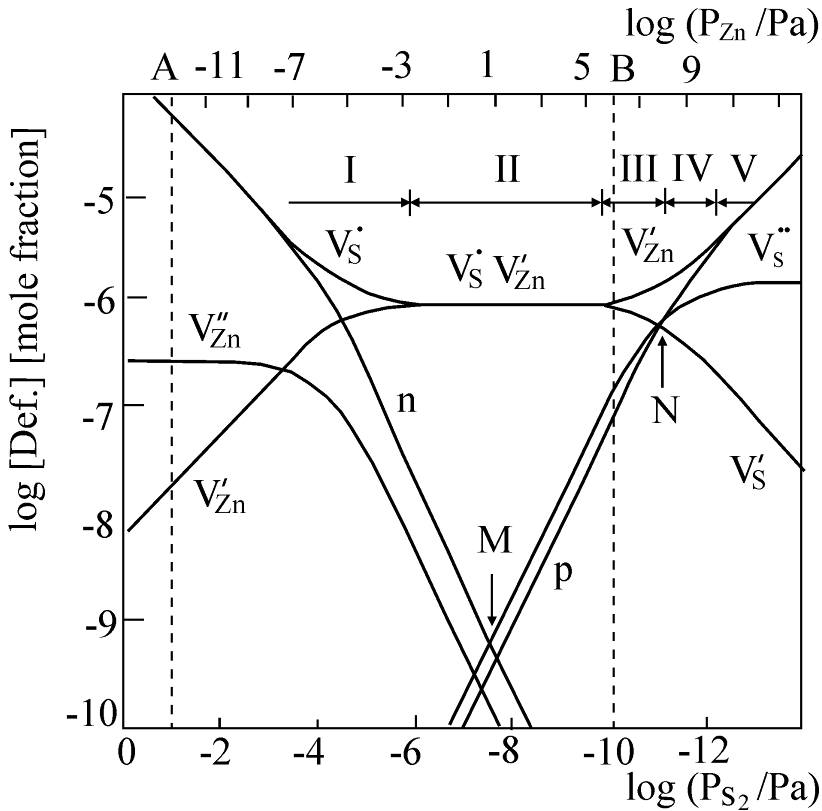

Figure 1. Native-defect equilibrium in ZnS at 1000 K; points *A* and *B* correspond to saturated Zn and S_2 vapors, respectively. Other designations are explained in text.

2. KINETIC ANALYSIS

This method consists of increasing the atomic chalcogen flux J_B to the above equilibrium value for a given pressure and temperature via dissociation of chalcogen molecules in response to external influences. As shown,[10] the fraction of dissociated oxygen molecules in an RF discharge attains 15%. At $p_{O_2} \approx 1$ Pa, the dissociation of 1% of the oxygen molecules produces atomic oxygen pressure $p_O \sim 10^{-2}$ Pa. The same activated oxygen pressure can be achieved via thermal dissociation of molecular oxygen at 1000 K and a pressure $p_{O_2} = p_O^2 / K_D = 10^2\,\text{GPa}$ where K_D is the equilibrium constant of the reaction $O_2 = 2O + D$ (*D* is the dissociation energy of molecular oxygen). Thus, RF activation during heat treatment in the vapor phase produces an atomic oxygen pressure that is essentially unattainable via thermal dissociation under typical heat-treatment conditions.

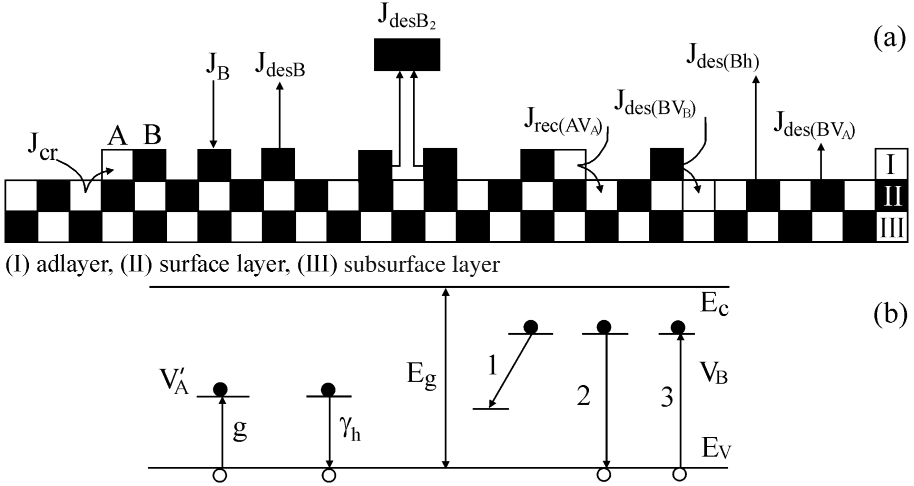

Figure 2. (a) Schematic illustrating the ADC equilibrium on the surface of an AB crystal and (b) the corresponding electronic transitions: (*1*) transition resulting from the interaction of a surface B atom with a V_A vacancy ($J_{des\,(BV_A)}$), (*2*) transition resulting from the interaction of a surface B atom with a hole ($J_{des\,(Bh)}$), (*3*) transition resulting from the recombination of a B adatom with a $V_B^{\bullet}$ vacancy ($J_{rec\,(BV_B^{\bullet})}$).

The non-equilibrium chalcogen concentration during annealing corresponds to a higher effective p_{B_2} accompanied by no condensation, which offers the possibility of achieving the states represented by points *M* and *N* in Fig. 1 (stoichiometric and chalcogen-enriched compositions). Kinetic analysis of the chemistry of native defects proved very useful in the case of crystal-activated chalcogen vapor systems. It is this approach that revealed the possibility of substantially extending the ranges of controlled native-defect conductivities[5] and achieving a type conversion in the compounds under consideration. Analysis of defect formation kinetics allowed us to propose a number of physicochemical approaches to controlling defect formation processes, which are governed by the dynamic adsorption-desorption-crystallization (ADC) equilibrium on the crystal surface (Fig. 2).

Based on the ADC model, we proposed a kinetic model for defect formation in II-VI compounds. A system of rate equations describing the interaction between a II-VI crystal and chalcogen vapor was set up and solved under the assumption that only the atomic component of the vapor phase reacts with the crystal surface. In calculating the ADC equilibrium on

the crystal surface, we took into account the interactions of neutral and charged defects with the vapor phase.

System of rate equation describing processes of defect formation can be written in the form:

$$\frac{dN_B'}{d\tau} = J_B - J_{\text{dec B}} - 2J_{\text{des B}_2} - J_{\text{cr}} + J_{\text{rec (A}V_A)} - J_{\text{rec}\left(BV_B^{\bullet}\right)}, \tag{1}$$

$$\frac{dV_A}{d\tau} = J_{\text{cr}} - J_{\text{rec (A}V_A)} - g[V_A] + \gamma_h p[V_A'] - J_{\text{des (B}V_A)}, \tag{2}$$

$$\frac{dV_A'}{d\tau} = g[V_A] - \gamma_h p[V_A'] + J_{\text{des (B}V_A)}, \tag{3}$$

$$\frac{dV_B^{\cdot}}{d\tau} = J_{\text{des (B}V_A)} + J_{\text{des (Bh)}} - J_{\text{rec}\left(BV_B^{\bullet}\right)}, \tag{4}$$

$$\frac{dp}{d\tau} = g[V_A] - \gamma_h p[V_A'] - J_{\text{des (Bh)}} + J_{\text{rec}\left(BV_B^{\bullet}\right)}, \tag{5}$$

$$p + \left[V_B\right] = \left[V_A'\right]. \tag{6}$$

Figure 3 shows the surface concentrations of defects in ZnO as functions of the atomic-oxygen flux. As seen, raising the temperature at a constant flux J_B increases the degree of compensation, without influencing the hole conductivity. The flux at which the conductivity changes from compensated to uncompensated and the charge neutrality condition changes from $\left[V_{Zn}'\right] = \left[V_0^{\bullet}\right]$ to $\left[V_{Zn}'\right] = p$ (the formation of a metal vacancy is accompanied by the appearance of a free hole in the valence band, rather than by the formation of a compensated chalcogen vacancy) depends on the annealing temperature.

For a given flux, there is a critical temperature above which uncompensated hole conduction cannot be achieved:

$$T_C = \frac{G_{desB} - E_g + E_{a_1} + E_{d_1} + G_A + G_{diffB}}{k\left\{\ln\left(\nu_A d_B^2 N_B \nu_B^{1/2}\right) - \ln\left(J_B^{1/2} \nu_B d_A\right)\right\}} \quad . \tag{7}$$

Figure 4 shows the critical temperature as a function of the atomic-oxygen flux. These data demonstrate that the critical temperature can only be raised substantially by increasing J_B. The calculations show that for ZnO T_c = 800 K at chalcogen fluxes of orders 10^{16}-10^{17} $cm^{-2}s^{-1}$ in really reachable experiments. Thus, it follows from the above thermodynamic and kinetic analyses that one way of controlling the chemistry of native defects in II-VI compounds is by increasing J_B to above the equilibrium value at a given p_{B_2} and temperature via activation of chalcogen molecules.

3. RADICAL-BEAM GETTERING EPITAXY

Based on the kinetic analysis of the ADC equilibrium on a crystal surface exposed to chalcogen radicals (atoms) in the vapor phase, we devised a method for hetero- and homoepitaxial growth of II-VI films. This method was the first to rely on the heat treatment of II-VI compounds in chalcogen vapor consisting of radicals[7] (atoms) generated using an RF discharge or photolysis. The method was called radical-beam gettering epitaxy (RBGE). During annealing in atomic chalcogen vapor (e.g., annealing of ZnO in O radicals), the dominant growth mechanism is quasi-epitaxy: the growth of crystalline layers on a crystalline matrix via sorption of chalcogen atoms from the vapor phase and gettering of metal atoms from the crystal bulk. This process is accompanied by the formation of Zn vacancies, which act as acceptors.

Since Zn vacancies may be in two charge states, either of the two levels corresponding to the singly and doubly charged Zn vacancies ($V_{Zn}^{'}$ and $V_{Zn}^{''}$) may show up in the conductivity of p-type crystals, depending on the degree of compensation of Zn vacancies by O vacancies and the position of the Fermi level.

The PL of oxygen-enriched ZnO was studied[8] using single-crystal ZnO layers grown on substrates vapor-grown ZnO single crystals, both nominally undoped and doped with Li and Na. The doping level was 10^{16} to 10^{17} cm^{-3}, and the conductivity of the samples was 10^{-5} to 10^{-7} S/cm. All of the samples were heat-treated under radical-beam gettering epitaxy conditions. The parent ZnO single crystals substrate was annealed at temperatures from 670 to 970 K in an atmosphere containing oxygen radicals (atoms). The oxygen pressure in the growth chamber was 10^{0}–10^{-3} Pa. Oxygen radicals were generated by an 80-W RF discharge. The resulting ions were separated by a

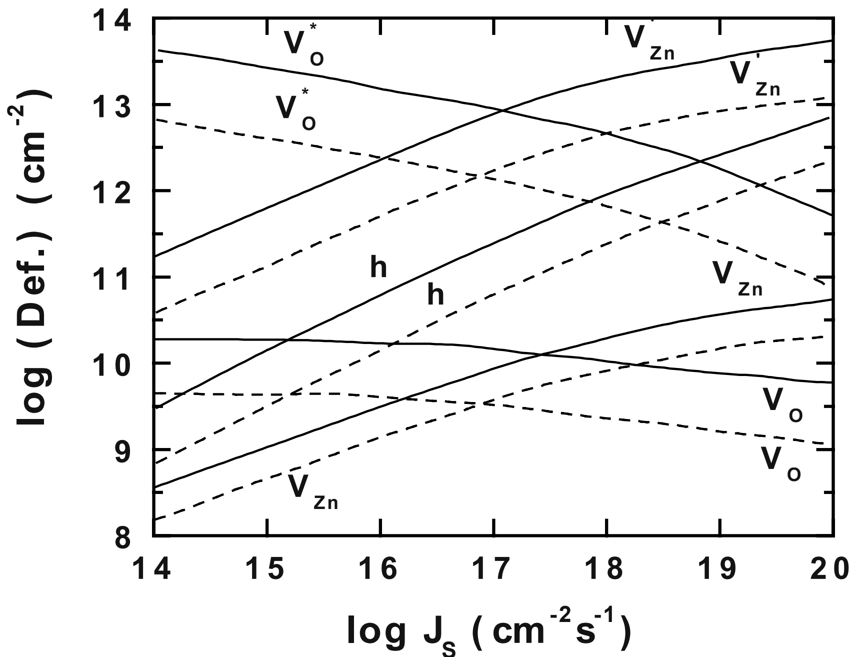

Figure 3. Defect densities in the surface layer of ZnO the flux of oxygen radicals (atoms) at 1200 (solid lines) and 1000 K (broken lines).

magnetic filter. The atomic oxygen flux, $J_O=10^{16}$ to 10^{17} $cm^{-2}s^{-1}$, was determined as described. ZnO layers grown at an oxygen radical flux $J_O \approx 1.5\times10^{17}$ $cm^{-2}s^{-1}$ and annealing temperatures in the range of 670–870 K were *p*-type, as determined by Hall effect measurements. The lowest resistivity *p*-type ZnO layers, with $\rho \approx 6\times10^2$ Ωcm and hole mobility μ_p~23 $cm^2/(Vs)$, were obtained at 710 K. Raising the annealing temperature to 810 K was found to increase ρ to about 3×10^7 Ωcm. The layers produced at $T_{ann} \geq 910$ K were *n*-type, with the resistivity above 10^9 Ωcm. These data indicate that the critical annealing temperature of ZnO is about 910 K, in accordance with theoretical estimates.

In the UV range, the PL spectrum of oxygen-enriched ZnO (*p*-type) shows a strong line at 369.5 nm with a full width at half maximum (FWHM) of 14 meV. In the visible range, we observe a weak band centered at 400 nm. Comparison of the luminescence spectra of *n*- and *p*-type ZnO indicates that the 369.0 and 369.5-nm lines are due to bound excitons. As shown by Butkhuzi *et al.*,[9] the 369.0 and 369.5-nm emissions arise from excitons bound to neutral donors and acceptors, respectively. Increasing the annealing time at 710 K increases the intensity of the 400-nm band. The spectra of samples annealed for 4 h show only the 400-nm band, which spans the entire

excitonic region. By analogy with the 345-nm emission[6] in ZnS, we assume that the 400-nm emission in ZnO is due to the singly positively charged associate $\left(V_{Zn} - V_{O}\right)^{\bullet}$. This assumption is supported by the fact that the concentration of oxygen vacancies in ZnO decreases with increasing oxygen content, and, for electro neutrality to be maintained, some of the oxygen vacancies pass into the doubly charged state ($V_{O}^{\bullet\bullet}$).

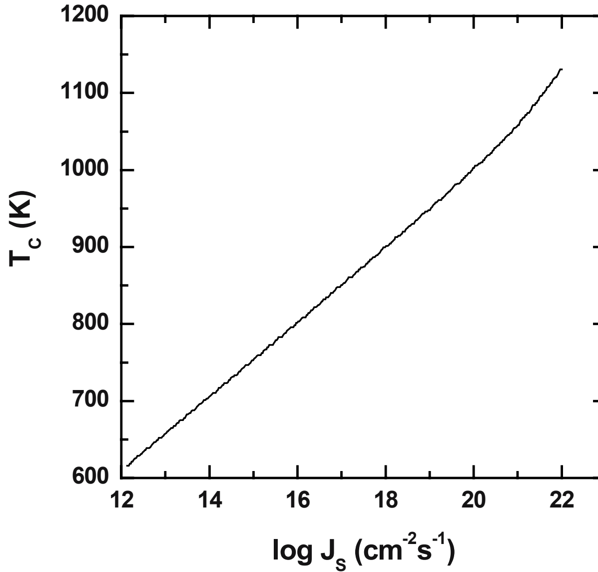

Figure 4. Critical temperature as a function of the atomic oxygen flux.

4. HETEROEPITAXY OF II-VI COMPOUNDS

The kinetics of defect formation in a heterophase system such as a single-crystal compound of one chalcogen, B' (e.g.: selenium), exposed to a flow of radicals of another chalcogen, B" (e.g.: oxygen), are more difficult to analyze. The general trends of defect formation in such systems must, however, be the same as above. The formation of V_A vacancies in an AB' crystal is accompanied by the transition of A atoms to the surface layer, where they combine with B" atoms to form AB' dimers. In the system of rate equations (1-5) one must take into account the formation of molecules containing both chalcogens (e.g.: SeO_2) and desorption of such molecules. This process results in the formation of $V_{B'}$ defects in the crystal, whose composition gradually changes to AB" owing to B" in-diffusion through $V_{B'}$ vacancies.

To a first approximation, the system of rate equations describing processes in such heterophase systems can be written in the form (A = Zn, B' = Se, B'' = O)

$$\frac{dN_O^{'}}{d\tau} = J_O - J_{des\,O} - 2J_{des\,O_2} - J_{des\,(SeO_2)} - J_{cr} - J_{rec\,(OV_{Se})} - J_{rec\,(ZnV_{Zn})} \quad (8)$$

$$\frac{dN_O}{d\tau} = \lambda[V_{Se}]J_O + J_{rec\,(OV_{Se})} - J_{des\,(OV_{Zn})}, \quad (9)$$

$$\frac{dN_{Zn}}{d\tau} = J_{cr} - J_{rec\,(ZnV_{Zn})}, \quad (10)$$

$$\frac{dN_{Se}}{d\tau} = J_{des\,(SeO_2)} - J_{rec\,(OV_{Se})} + J_{des\,(SeV_{Zn})}, \quad (11)$$

The mass-balance constraint has the form $[V_{Se}]+[O]+[Se]=\text{const.}$ [O] + [Se] = const. In these relations we use designations analogous to those in Eqs. (1-5): J_O is the flux of oxygen atoms (radicals) incident on a two-dimensional crystal, $N_O^{'}$ is the surface concentration of oxygen adatoms, N_O is the concentration of oxygen atoms in the surface layer, and [O] is the net oxygen concentration in the adlayer and surface layer.

Diffusion from the surface layer to the crystal bulk plays an important role in heterophase systems. It is the diffusion processes that determine in large part whether or not ZnO layers will grow and whether the ZnO/ZnSe(S,Te) heterojunction will have a sharp interface or the ZnO layer will grow via oxygen diffusion into the crystal bulk and will have a broad boundary. Solving Eqs. (8-11), one can determine, from the relationship between the generation rates of A and B vacancies, the quasi-heteroepitaxy parameters at which particular kinds of heterojunctions, conductivity types, and defect concentrations in ZnO and ZnSe(S, Te) layers can be obtained.

Thus, the proposed method for analyzing the kinetics of defect formation, based on the quasi-epitaxy model, clearly demonstrates the role of the surface in the ADC equilibrium and allows one to assess the effects of temperature and J_B of the equilibration of defect concentrations. Computer simulations of defect formation kinetics in II-VI crystal non-equilibrium chalcogen vapor systems indicate that steady state defect concentrations in the surface layer are reached very rapidly and, accordingly, are not

influenced by the diffusion of defects to the crystal bulk, as was assumed in the model in question.

The approach in question allows one to produce a wide range of device structures for opto- and acoustoelectronics, e.g.: ZnO/ZnSe, ZnS/ZnSe, CdS/CdSe, and ZnO/ZnTe, with variable parameters. For example, ZnO layers grown on ZnSe may be both *n*- and *p*-type.

Using this approach, we prepared light-emitting ZnO/ZnSe structures.[10] A typical 300-K electroluminescence (EL) spectrum (bias voltage of 4–6 eV) of ZnO/ZnSe structures produced by annealing ZnSe at 870 K for 0.5 h in a flow of atomic oxygen is shows strong bands at 467 and 525 nm and a weak band centered around 615 nm. The following features of the EL warrant attention: low injection voltages and the presence of an EL band near the intrinsic edge. The external luminescence efficiency of the structures was determined to be 0.1%.

At forward biases below 2.5 V, the curve shows a linear region. The deviation from the exponential behavior at bias voltages above 2.5 V can be accounted for by the volume resistance of zinc selenide. Therefore, the barrier height at the *p–n* junction is ≈ 2.5 V. It follows from the *I–V* data that the *p–n* junction lies within the zinc selenide layer. Therefore, a *p*-ZnO/*p*-ZnSe/*n*-ZnSe structure was produced. The ZnO serves as an injecting contact to the *p*-ZnSe layer and as an exit "window" for radiation.

REFERENCES

1. A. N. Georgobiani, M. B. Kotlyarevsky, V. N. Mikhalenko, *USSR Inventor's Certificate* no. **684**, 810 (1977).
2. N. K. Morozova and O. M. Morozova, *Izv. Akad. Nauk SSSR, Neorg. Mater.* **17**, 1335 (1981).
3. M. T. Nyges, Cand. Sci. (Phys.–Math.) Dissertation, Tallinn (1974).
4. V. A. Nikitenko, S. A. Stenli, and N. K. Morozova, *Izv. Akad. Nauk SSSR, Neorg. Mater.* **24**, 1830 (1988).
5. V. N. Mikhalenko, B. P. Dement'ev, M. B. Kotlyarevsky, and A. N. Georgobiani, *Izv. Vyssh. Uchebn. Zaved., Fiz.* **8,** 150 (1978).
6. A. N. Georgobiani, M. B. Kotlyarevsky, and V. N. Mikhalenko, *Tr. Fiz. Inst. im. P. N. Lebedeva, Akad. Nauk. SSSR.* **138,** 79 (1983).
7. A. N. Georgobiani, M. B. Kotlyarevsky, and V. N. Mikhalenko, V.N., *Izv. Akad. Nauk SSSR, Neorg. Mater.* **18**, 12 (1982).
8. M. B. Kotlyarevsky, A. N. Georgobiani, I. V. Rogozin, and A. V. Marakhovskii, *Zh. Prikl. Spektrosk.* **70**, 86 (2003).
9. T. V. Butkhuzi, A. V. Bureyev, A. N. Georgobiani, N. P. Kekelidze, and T. G. Khulordava *J. Cryst. Growth* **117**, 366 (1992).
10. A. N. Georgobiani, M. B. Kotlyarevsky, V. V. Kidalov, and I. V. Rogozin, *Neorg. Mater.* **33**, 232 (1997) [*Inorg. Mater.* (Engl. Transl.) **33**, 185].

PART II: ELECTRICAL, OPTICAL, AND STRUCTURAL PROPERTIES

Chapter 4

ELECTRICAL PROPERTIES OF ZnO

David C. Look[1], Bruce B. Claflin[1], Gene Cantwell[2], Seong-Ju Park[3], and Gary M. Renlund[4]

[1]Semiconductor Research Center, Wright State University, Dayton, OH 45435; [2]ZN Technology, 910 Columbia St., Brea, CA 92821; [3]Dept. of Mat. Sci. and Tech., K-JIST, Kwangju, 500-712, Korea; [4]ON International, 418 W. Winchester St., Salt Lake City, UT 84107

Abstract: Temperature-dependent Hall-effect measurements have been used to determine donor and acceptor concentrations and energies in n-type and p-type ZnO. Commonly observed donor energies in n-type material grown from the vapor phase (VP) are 35 and 65 meV, with the 35-meV donor identified as H, and the 65-meV donor, probably Al. Total donor concentrations in VP-grown material are as low as mid-10^{16} cm^{-3}. The only acceptors unambiguously identified so far in this material are the Zn vacancy, at the low-10^{15}-cm^{-3} level, and substitutional N_O, at a higher level but evidently passivated with H. Acceptors that have been successfully used to create p-type ZnO by doping include N, P, and As, and resistivities as low as 0.1 Ω-cm have been obtained. The acceptor energy for N is about 90 meV for [N] ~ 10^{19} cm^{-3}, and can be estimated to be about 130 - 150 meV at low concentrations of N.

Key words: ZnO, Hall-effect, donor, acceptor, n-type, p-type

1. INTRODUCTION

ZnO has long been touted as a potential candidate for UV emitters, but the lack of a good, reproducible p-type technology has hindered its development in the past.[1] Fortunately, in the last few years, much progress has been made in this area and a few p-n homojunctions and heterojunctions have even shown light emission.[2] In spite of this recent success, much better performance will be needed if ZnO is to compete with GaN-based light-emitting diodes (LEDs) in the blue and UV regions. One of the key required elements will be the growth of bulk and epitaxial ZnO with low background

N.H. Nickel and E. Terukov (eds.),
Zinc Oxide – A Material for Micro- and Optoelectronic Applications, 37–46.
© 2005 *Springer. Printed in the Netherlands.*

concentrations of donors, so that p-type material can be produced with only minimum initial compensation. The most important background donors that must be considered are H, the O vacancy V_O, the Zn interstitial Zn_I, and the group III elements, especially Al. Then, a way must be found to limit *self* compensation during the acceptor doping process, so that the added acceptors can efficiently produce free holes. The most suitable acceptor dopants that have been discovered so far are the group V elements, N, P, As, and Sb. To control the donor and acceptor species we must be able to measure their concentrations and energies, and the only known method to accomplish this task is temperature-dependent Hall-effect (TDH) measurements.[3] We will first discuss how such measurements are carried out and analyzed, and then how they are applied to the problem at hand.

2. HALL-EFFECT MEASUREMENTS AND ANALYSIS

Few semiconductor laboratories in existence today are without a Hall-effect system capable of room-temperature operation, at least. The only basic requirements are a current source, a voltmeter, and a small magnet, of typical field strength 0.1 – 1.0 T. If the current is imposed perpendicular to the magnetic field, a voltage will be generated in the mutually perpendicular direction, and this is the classical Hall voltage. The current, magnetic field strength, and Hall voltage are all easily measurable quantities, and their combined values immediately give the Hall coefficient R, where R is related to the carrier concentration, n or p, by n = r/eR. Here e is the electronic charge and r is the so-called Hall factor, which is usually close to unity but also may be calculated by fitting the temperature-dependent Hall mobility data. Indeed, the Hall mobility μ_H is simply defined as $\mu_H = R\sigma$, where σ is the conductivity, measured from the voltage drop parallel to the current. To relate n and μ_H to physical parameters, such as the donor concentration, we must solve the Boltzmann transport equation, which describes the relaxation of carrier momentum via carrier scattering. If the various scattering mechanisms are elastic, then a relaxation time τ can be defined, and the Boltzmann equation can be easily solved to give

$$\mu_H = \frac{e}{m^*}\frac{\langle \tau^2 \rangle}{\langle \tau \rangle} \tag{1}$$

where m* is the effective mass and $<\tau^n>$ is defined by

$$\left\langle \tau^n(E) \right\rangle = \frac{\int_0^\infty \tau^n(E) E^{3/2} \frac{\partial f_0}{\partial E} dE}{\int_0^\infty E^{3/2} \frac{\partial f_0}{\partial E} dE} \rightarrow \frac{\int_0^\infty \tau^n(E) E^{3/2} e^{-E/kT} dE}{\int_0^\infty E^{3/2} e^{-E/kT} dE} \quad (2)$$

Here, E is the carrier energy and the second expression in Eq. 2 is valid for Boltzmann (nondegenerate) statistics. We must note that τ is the total relaxation time, made up of contributions from various phonon and impurity scattering mechanisms. The additive quantity is the relaxation *rate*, τ^{-1}, so that the total relaxation rate is given by

$$\tau^{-1}(E) = \tau_{ac}^{-1}(E) + \tau_{pe}^{-1}(E) + \tau_{po}^{-1}(E) + \tau_{ii}^{-1}(E) + \tau_{dis}^{-1}(E) \quad (3)$$

where *ac* and *po* denote scattering by acoustical-mode and optical-mode lattice vibrations, respectively, *pe*, the piezoelectric potential, *ii*, ionized-impurities, and *dis*, dislocations. As an example

$$\tau_{ac}(E) = \frac{\pi \hbar^4 \rho_d s^2 E^{-1/2}}{2^{1/2} E_1^2 \left(m^*\right)^{3/2} kT} \quad (4)$$

where ρ_d is the density, s is the speed of sound, and E_1 is the deformation potential. The other formulas can be found in Ref. 3, including an expression for τ_{po}, which is only approximate because polar-optical scattering is not really elastic. A more accurate treatment requires a full numerical solution of the Boltzmann equation.[3,4]

Equations 1 – 4 can easily be set up on a PC and used to simulate or fit temperature-dependent mobility data. In an n-type sample, the only undetermined parameter is the acceptor concentration N_A, so usually N_A is varied to give the best fit to the data. (For this fit, the approximate carrier concentration, $n_H = 1/Re$, can be used when n is required in the various scattering formulas.) Then, the Hall factor $r = <\tau^2>/<\tau>^2$ can be calculated at each temperature, and the true carrier concentration determined from the expression n = r/eR. Next, n vs. T is fitted by use of the charge-balance equation

$$n + N_A = \sum_i \frac{N_{Di}}{1 + n/\phi_{Di}} \quad (5)$$

where i denotes a particular donor N_{Di} and

$$\phi_{Di} = \frac{g_{0i}}{g_{1i}} e^{\frac{\alpha_{Di}}{k}} N_C' T^{3/2} e^{-\frac{E_{D0i}}{kT}} \quad (6).$$

For each donor, g_0/g_1 is a degeneracy factor, $N_C' = 2(2\pi m_n^* k)^{3/2}/h^3$ is the effective conduction-band density of states at 1K, h is Planck's constant, E_D is the donor energy, and E_{D0} and α_D are defined by $E_D = E_{D0} - \alpha_D T$. The above equation describes the simplest type of charge balance, in which each of the one or more donors has only one charge-state transition within a few kT of the Fermi energy. An example of such a donor is Ga on a Zn site in ZnO. If there are double or triple donors, or more than one acceptor, proper variations of Eq. 5 can be found in the literature[3].

An example of a mobility fit for bulk ZnO grown by the VP method is presented in Fig. 1. Here, the fitted acceptor concentration is $N_A = 2\times10^{15}$ cm^{-3}.

This value is then used in the charge-balance equation, Eq. 5, to fit the carrier concentration data, as shown in Fig. 2. As seen, two donors are

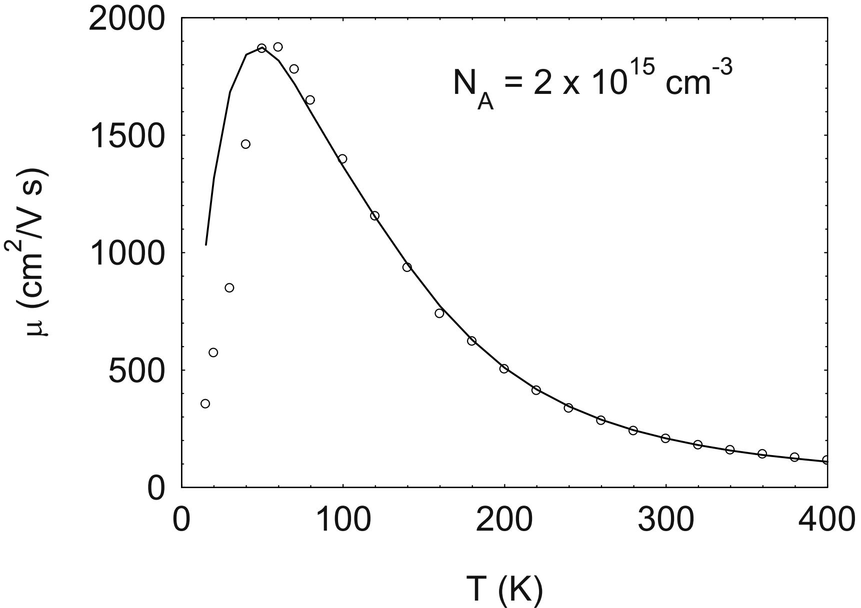

Figure 1. Temperature-dependent mobility of bulk ZnO.

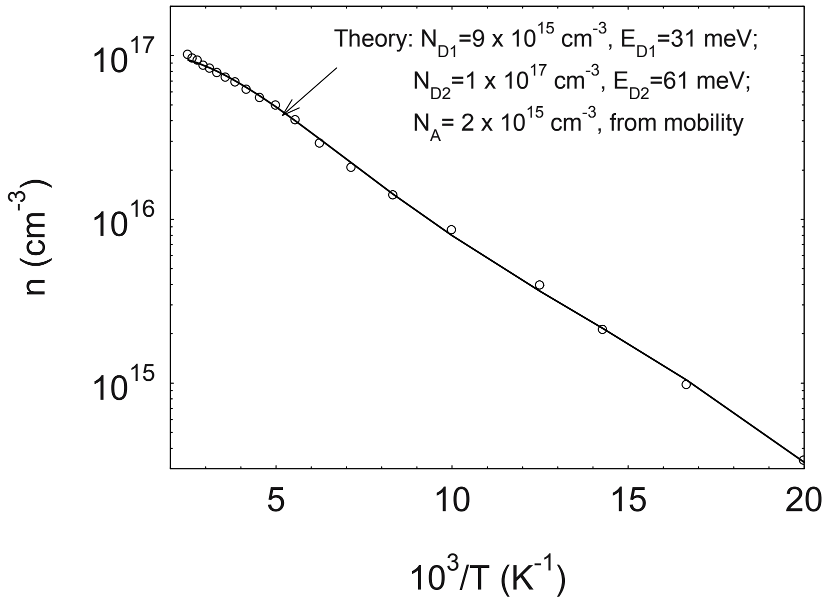

Figure 2. Temperature-dependent carrier concentration of bulk ZnO.

found, of concentrations 9×10^{15} and 1×10^{17} cm^{-3}, and energies 31 and 61 meV, respectively. Their identities will be discussed in more detail below.

3. BACKGROUND DONORS AND ACCEPTORS IN ZnO

We first will discuss the identities of the acceptor and two donors found in the VP-grown ZnO represented by Figs. 1 and 2. The acceptor was found by positron annihilation to be the Zn vacancy V_{Zn}.[5] This is somewhat surprising in light of secondary-ion mass spectroscopic (SIMS) data on similar material which shows that N is present at the 10^{17}-cm^{-3} level.[6] However, we believe that the N is passivated by H that is present during the VP growth process,[7,8] and that a further supply of H is responsible for the shallow 31-meV donor, N_{D1}. This assertion is supported by annealing results, shown in Figs. 3 and 4. The annealing temperature, 715 °C, is high enough to get rid of H, and indeed, the donor of shallow slope in Fig. 4 has disappeared. Furthermore, the acceptor concentration has increased from about 2×10^{15} cm^{-3} to about 1×10^{16} cm^{-3}, as illustrated by the strong decrease in low-temperature mobility shown in Fig. 3. Since H-N complexes have

been tentatively identified by infrared absorption experiments[8], it is likely that they exist in the as-grown material, and that the anneal breaks them apart, thus "activating" the N acceptors. Further evidence for the annihilation of the shallow donor comes from photoluminescence (PL) data, Fig. 5, which shows the disappearance of a donor-bound exciton line at 3.363 eV. Recent evidence has confirmed that this donor is related to H. Two-electron transitions, appearing near 3.33 eV in Fig. 5, lead to a donor transition energy of about 4/3(3.63 – 3.33) ~ 40 meV for H, close enough to the 31 meV measured by Hall effect measurements, especially considering that Hall measurements in various samples give between 30 and 40 meV.

The deeper donor, having an energy of 61 meV in this sample but ranging up to 70 meV in other samples, is probably Al_{Zn}. This identification is based on the fact that Al is a common background impurity in ZnO, and that it should be a simple, hydrogenic donor, i.e., with an energy of about 55 - 65 meV. Its D^0X PL line has been shown, by doping experiments, to have an energy of about 3.360 eV[9], and such a line is clearly visible in Fig. 5.

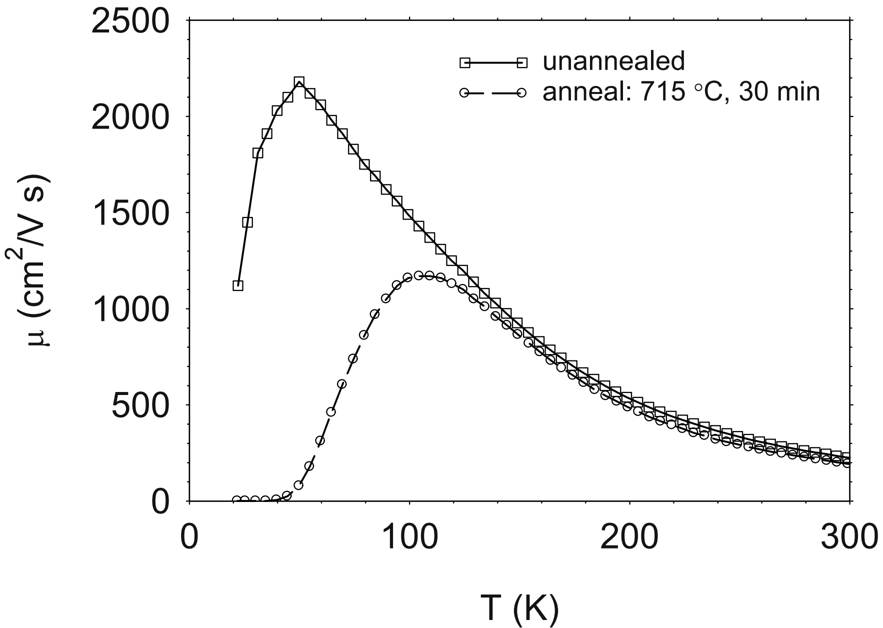

Figure 3. Effects of annealing on mobility of bulk ZnO. The fits (not shown) give acceptor concentrations of $N_A = 1.8\times10^{15}$ cm^{-3} for the unannealed sample, and 1.2×10^{16} cm^{-3} for the annealed sample.

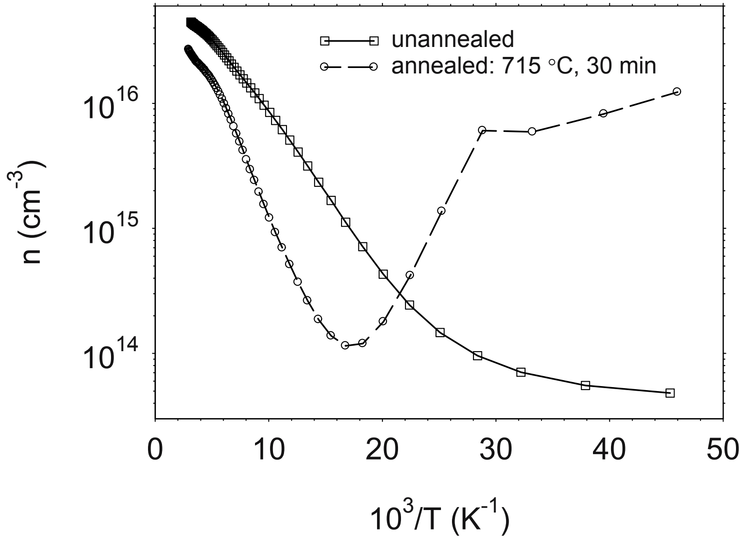

Figure 4. Effect of annealing on carrier concentration of bulk ZnO. The fits (not shown) give donor concentrations of 2.8×10^{16} and 3.7×10^{16} cm^{-3}, and energies of 37 and 66 meV, respectively, for the unannealed sample; and donor concentrations of 2.1×10^{16} and 2.8×10^{16} cm^{-3}, and energies of 44 and 77 meV, respectively, for the annealed sample.

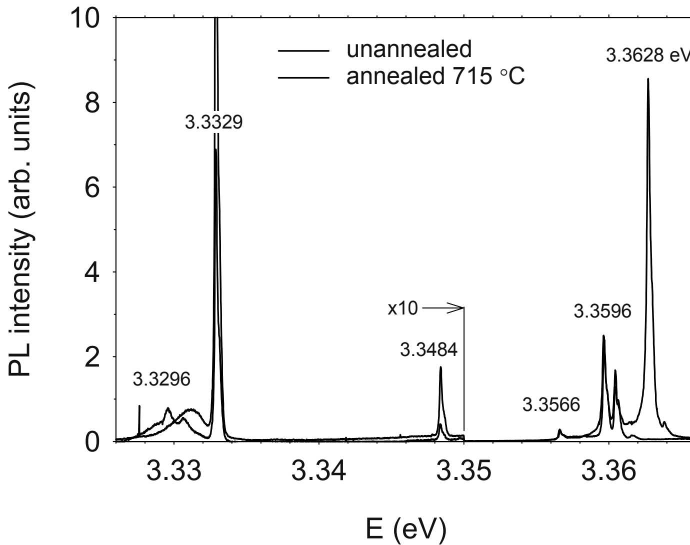

Figure 5. Effect of annealing on 4-K photoluminescence of bulk ZnO.

4. P-TYPE ZnO

The difficulty in producing p-type ZnO has hindered the development of ZnO-based p-n junctions, and thus ZnO UV LEDs and LDs. It wasn't until 1997 that the first p-type ZnO was reported[10], and further reports on this subject were sparse until 2003. (A recent review on this subject has been given in Ref. 2). But now (2004), several groups have obtained p-type ZnO with N doping, and a few, with P, As, and Sb doping. As an example, we show temperatrure-dependent p and μ_p curves for As-doped ZnO in Fig. 6.

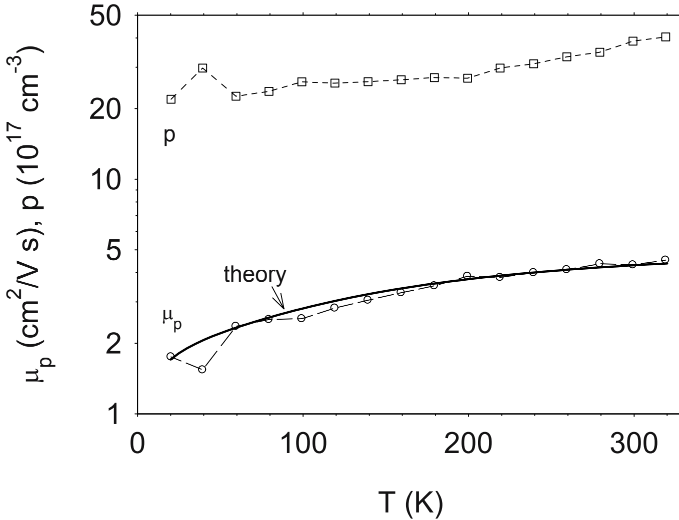

Figure 6. Hole concentration p and mobility μ_p for an As-doped ZnO sample. The solid line is a theoretical fit to the mobility.

Here, the mobility μ_p is fitted (solid line) with a very simple, single-valence-band model, assuming an effective mass of 0.64 m_0. The only fitting parameter is the donor concentration, which turns out to be $N_D = 8\times10^{19}$ cm^{-3}. Although the temperature dependence of the hole concentration p cannot be easily fitted, because it is partially degenerate, we can estimate that $p \approx N_A - N_D \approx 10^{19}$ cm^{-3} at high temperatures, giving $N_A \approx 9\times10^{19}$ cm^{-3}. Indeed, SIMS results show an As concentration of mid-10^{19}, consistent with As being the dominant acceptor in this material. The fact that As can be doped to such a high concentration is quite surprising, because, unlike the N_O case, As is much larger than O, and should not substitute for it readily. Some theoreticians have recently suggested that As does not enter the lattice simply as As_O, but as a much more complex acceptor-type defect, As_{Zn}-

$2V_{Zn}$[11]. Although this defect is consistent with our data, still it must be confirmed by more direct means.

The most studied acceptor dopant up to now, by far, is N, and this element has been shown by electron paramagnetic resonance data to go predominantly onto the O site and have acceptor nature[12,13]. It has an acceptor transition at ~ 90 meV, for [N] ~ 10^{19} cm^{-3}, and this energy can be estimated to be about 130 – 150 meV at infinite dilution[14]. Thus, it is perhaps not surprising that p-type ZnO can be produced with N doping; however, it is still somewhat of a mystery as to why As, P, and Sb also work. In any case, the recent success in creating p-type ZnO bodes well for the future of the ZnO LED industry, although much more research will be necessary before the situation is well understood.

5. SUMMARY

Electrical measurements, mainly temperature-dependent Hall-effect measurements, have been critical in the elucidation of donors and acceptors in ZnO. The main background donors in state-of-the-art VP-grown ZnO have been shown to be H and Al, and the acceptor, V_{Zn}. Other possible donors that must be investigated further are the defects V_O and Zn_I. Although V_{Zn} seems to be the main electrically active acceptor, still N is evidently present at a much higher concentration. If this is true, then N must be passivated, and the likely passivator is H. Indeed, annealing experiments lead to a much higher acceptor concentration, presumable due to the breaking of the H-N bond. Deliberate doping of N can produce [N] ~ 10^{19} cm^{-3} or higher, and p-type ZnO has been produced in this way. Surprisingly, however, even P, As, and Sb have been successfully used for p-doping. Research into these matters is proceeding at a rapid pace, and the next few years should produce a much clearer understanding.

REFERENCES

1. D. C. Look, *Mater. Sci. and Eng. B* **80**, 383 (2001).
2. D .C. Look and B. Claflin, *phys. stat. sol. (b)* **241**, 624 (2004).
3. D. C. Look, *Electrical Characterization of GaAs Materials and Devices* (Wiley, New York, 1989).
4. B. R. Nag, *Electron Transport in Compound Semiconductors* (Springer, Berlin, 1980).
5. F. Tuomisto, K. Saarinen, and D. C. Look, *Phys. Rev. Lett.* **91**, 205502 (2003).
6. D. C. Look, D. C. Reynolds, C. W. Litton, R. L. Jones, D. B. Eason, and G. Cantwell, *Appl. Phys. Lett.* **81**, 1830 (2002).

7. N. Y. Garces, L. Wang, N. C. Giles, L. E. Halliburton, G. Cantwell, and D. B. Eason, *J. Appl. Phys.* **94**, 519 (2003).
8. N. H. Nickel and K. Fleischer, *Phys. Rev. Lett.* **90**, 197402 (2003).
9. H. Shibata, M. Watanabe, M. Sakai, K. Oka, P. Fons, K. Iwata, A. Yamada, K. Matsubara, K. Sakurai, H. Tampo, K. Nakahara, and S. Niki, *phys. stat. sol. (c)* **1**, 872 (2004).
10. K. Minegishi, Y. Koiwai, and Y. Kikuchi, K. Yano, M. Kasuga, and A. Shimizu, *Jpn. J. Appl. Phys.* **36**, L1453 (1997).
11. S. Limpijumnong, S. B. Zhang, S. H. Wei, and C. H. Park, *Phys. Rev. Lett.* **92**, 155504 (2004).
12. W. E. Carlos, E. R. Glaser, and D. C. Look, *Physica B* **308-310,** 976 - 979 (2001).
13. N. Y. Garces, N. C. Giles, L. E. Halliburton, G. Cantwell, D. B. Eason, D. C. Reynolds, and D. C. Look, *Appl. Phys. Lett.* **80**, 1334 - 1336 (2002).
14. D. C. Look, B. Claflin, Ya. I. Alivov, and S. J. Park, *phys. stat. sol. (a)* (in press).

Chapter 5

ELECTRICAL PROPERTIES OF ZnO THIN FILMS AND SINGLE CRYSTALS

M. Grundmann[1], H. von Wenckstern[1], R. Pickenhain[1], S. Weinhold[1], B. Chengnui[1], and O. Breitenstein[2]

[1]Institut für Experimentelle Physik II, Fakultät für Physik und Geowissenschaften, Universität Leipzig, Linnéstr. 5, D-04103 Leipzig, Germany; [2]Max-Planck-Institut für Mikrostrukturphysik, Experimental Department II, Weinberg 2, D- 06120 Halle / Saale

Abstract: We have investigated the electrical properties of ZnO single crystals and thin films. Low resistive ohmic contacts were realized by annealing thermally evaporated Ti-Au contacts at 400°C in vacuum. Hall effect measurements provided information about dominant scattering mechanisms in the single crystals and the epitaxial thin films. Dominant donor levels were found in an energy range from 37 meV to 350 meV below the conduction band for the different samples. Schottky contacts of good quality ($j(-5V)$ = 4 x 10^{-5} A/cm^2, n = 1.3) were produced on thin films after etching with HNO_3. Deep level transient spectroscopy yielded the activation energy of deep traps for single crystals of 300 meV and 540 meV and for the thin films of 300 meV, respectively.

Key words: Hall effect, schottky contacts, DLTS, thermography, PLD

1. INTRODUCTION

The wide band gap semiconductor ZnO has attracted much attention in recent years. This is stimulated by the development of transparent electronics, the growing need of emitters and detectors working in the ultra-violet range of the electromagnetic spectrum, and the progress in the realization of ferromagnetic semiconductors with Curie temperatures close to or above room temperature. ZnO is nowadays applied as transparent front contacts of solar cells competing with the commonly used material indium tin oxide (ITO). The low cost of ZnO as well as the radiation hardness[1] make

N.H. Nickel and E. Terukov (eds.),
Zinc Oxide – A Material for Micro- and Optoelectronic Applications, 47–57.
© 2005 *Springer. Printed in the Netherlands.*

this material favorable compared to ITO. Material properties as the high exciton binding energy of 61 meV[2], the comparatively high optical gain[3], unproblematic wet-chemical etching[4], or the widely tunable band gap by alloying with CdO or MgO[5] give ZnO an extraordinary role compared to other wide band gap semiconductors. The possibility of low-temperature fabrication (300 – 800 K) makes it favorable compared to GaN. The availability of ZnO substrates and the growing quality of ZnO thin films have put forward systematic studies. We will focus in this article on the electrical properties of commercially available ZnO single crystals and heteroepitaxially grown ZnO thin films produced by pulsed laser deposition (PLD).

2. SAMPLES

We investigated three different kinds of ZnO single crystals. One kind was produced by seeded chemical vapor transport (SCVT) by Eagle Picher Technologies. Two single crystals analyzed here were grown by hydrothermal vapor phase epitaxy (HVPE) one of them purchased from Crystec (labeled from now on HVPE I) the other was obtained from MaTeck (referred to as HVPE II). The thickness of these single crystals is 500 µm. In addition we probed samples grown by PLD on sapphire substrates. For that we used the 248 nm line of a KrF excimer laser to ablate polycrystalline ZnO targets produced by standard ball milling, pressing, and sintering. After the growth of a low temperature nucleation layer a about 1 µm thick ZnO layer was deposited at about 750°C at an oxygen partial pressure of 0.016 mbar. Details about the growth and the properties of the ZnO thin films are published in.[5-7]

3. OHMIC CONTACTS ON THIN FILMS

The contact resistivities ρ_c of different ohmic contacts were determined with the transmission line model. We investigated Ti, Al, and Ti-Au ohmic contacts produced by thermal evaporation of the contact metal. Ti contacts result in poor ohmic contacts with $\rho_c = 3.2\ \Omega\text{cm}^2$. Annealing these contacts at 300°C doubles ρ_c due to the formation of titanium oxide at the interface. The contact structure becomes insulating after annealing at temperatures of about 600°C. As-deposited Al contacts have with $\rho_c = 0.14\ \Omega\text{cm}^2$ a lower contact resistivity than Ti-contacts. Annealing these contacts at 700°C decreases ρ_c to $0.028\ \Omega\text{cm}^2$ due to the in diffusion of Al forming a highly doped surface layer that electrons may pass by tunneling. The lowest contact

resistivity was obtained for Ti-Au contacts. As-deposited contacts have ρ_c = 0.01 Ωcm^2 which decreases after annealing in vacuum at about 400°C to ρ_c = 2.4 x 10^{-3} Ωcm^2. If the contacts are annealed in a N_2 ambient ρ_c does not change compared to the as-deposited contacts. Annealing at higher temperatures increases ρ_c as depicted in Fig. 1.

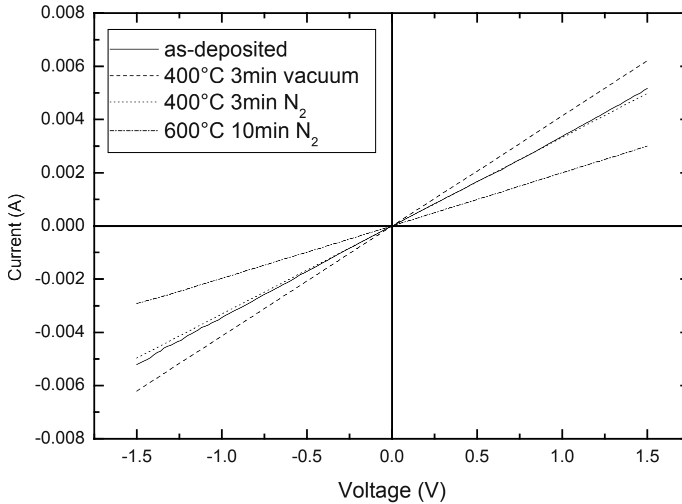

Figure 1. Current-voltage characteristic of as-deposited and annealed Ti-Au contacts

4. LOCK-IN THERMOGRAPHY ON THIN FILMS

In lock-in thermography[8] the surface temperature of a sample is imaged by an infrared (IR) camera and Joule heat is periodically created by injecting a pulsed current flow. The output signal of the IR camera is digitally processed according to the lock-in principle to convert the periodic surface temperature modulation into an image of the local temperature modulation amplitude. This amplitude image can be interpreted to visualize the local dissipated power density. If in a homogeneous conducting thin film with sheet resistivity of R_s a local current density of $j(x,y)$ flows, the local dissipated power density is $p(x,y) = R_s\,(j(x,y))^2$. If the current flows between two contacts in opposite corners of a square Hall sample, the current density decreases in the vicinity of the contacts proportional to the distance to the contact. Hence, we expect an increase of the lock-in thermography signal towards the current injecting contacts as shown in Fig. 2a. This pattern is the same if the injecting contacts are exchanged, or if the sample is rotated by

90°. Any deviation of the C_{2v}-symmetry is an indication of a spatial inhomogeneity of the electric properties of the conducting film.

We found, that the current paths are usually not homogeneous for samples grown using a fixed substrate holder. Often the current flows along an edge indicating regions with lower resistance (Fig. 2b). Such kinds of samples are not appropriate for Hall measurements in the van der Pauw geometry. A substantial improvement of the reliability of Hall measurements of PLD thin films in the van der Pauw geometry is obtained if the outer 2 mm of the sample are mechanically removed. The current paths show the desired behavior after the removal (Fig. 2c) and Hall measurements on samples prepared in that manner like the PLD thin films investigated in this study are reliable. If the substrates are mounted to a rotating substrate holder as-grown samples can be used directly (Fig. 1a).

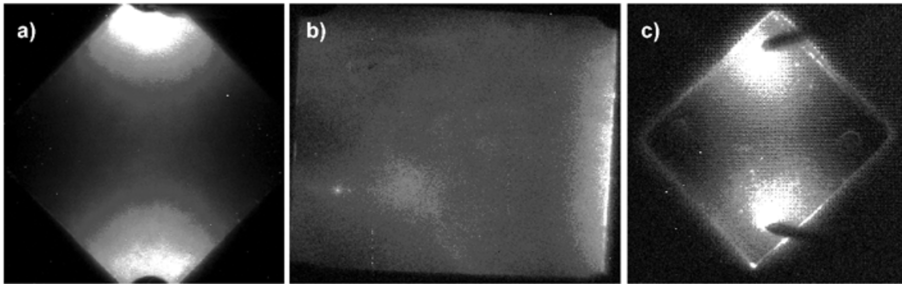

Figure 2. Lock-in thermography images of PLD sample grown with a) rotating substrate holder, b) fixed substrate holder, and c) fixed substrate holder but the outer 2 mm of the sample where removed. In (a, c) the circular contacts are in the top and bottom corners. In part (b) the contacts are stripe-like at the top and the bottom edge.

5. HALL MEASUREMENTS ON SINGLE CRYSTALS AND THIN FILMS

We investigated the transport properties of ZnO single crystals and PLD thin films by Hall measurements using the van der Pauw method.[9]

5.1 Room Temperature Measurements on thin films

The Hall mobility μ_H of the thin films is highest within a narrow region of free electron concentrations n ranging from about 2 to 5 x 10^{16} cm^{-3} as depicted in Fig. 3. In general, the Hall mobility of the thin films is lower

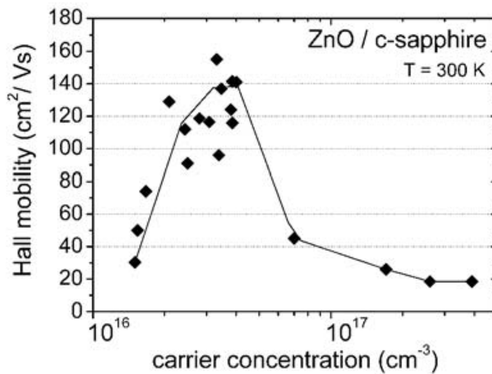

Figure 3. Dependence of the Hall mobility on the free electron concentration.

than expected by considering intrinsic scattering mechanisms and ionized impurity scattering only. The reason is grain boundary scattering, which occurs at potential barriers at the grain walls. The potential barriers arise from the occupation of acceptor states at the grain walls leading to depletion zones around these walls. Free carriers have to overcome these barriers, which reduces the mobility. The shape of Fig. 3 can be explained by considering the dependence of grain boundary scattering on the grain size and on the density of donors (which determines the depletion width, if the density of traps at the grain walls is assumed to be in average similar for all samples). As the carrier concentration increases the grain size decreases leading to a larger number of scattering events and with that to a reduction of the mobility. For low carrier concentrations the depletion width around the grain walls increases and the amount to which a grain is depleted increases. The peak in Fig. 3 corresponds to a regime where these two processes are comparatively small and grain boundary scattering is least important for the investigated thin films. The maximum Hall mobility of 155 cm^2/Vs defines the present state of the art for heteroepitaxial grown thin films on c-plane sapphire.

5.2 Temperature dependent measurements on single crystals and thin films

To model the temperature dependence of the Hall data we first fitted the Hall mobility accounting the intrinsic scattering mechanisms piezoelectric scattering and deformation potential scattering on longitudinal acoustic phonons and polar optical scattering (for them we used material constants, no fitting parameters are needed for the intrinsic scattering mechanisms) as

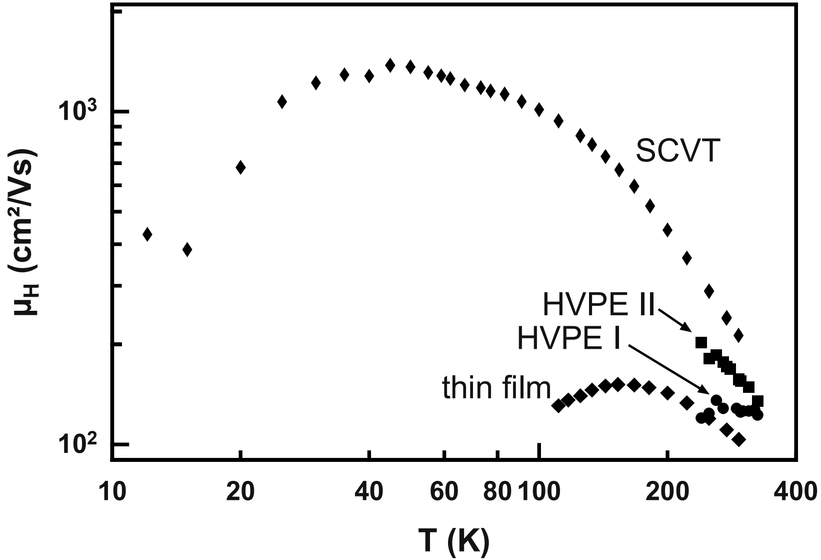

Figure 4. Hall mobility of single crystals and a thin film.

well as the extrinsic scattering at ionized impurities containing the fitting parameter N_A the concentration of compensating acceptors. For the thin films we also accounted grain boundary scattering containing two more fitting parameters, namely the barrier potential E_B and the grain size L_G. Matthiesen's rule was applied for the fits and the obtained density of compensating acceptors was used as input for the fit of *n(T)*.

Figure 4 shows the Hall mobility of the single crystal grown by SCVT, of the two hydrothermally grown single crystals (HVPE I and HVPE II), and a PLD thin film. The single crystal grown by SCVT has the highest μ_H at room temperature. This is due to a low concentration of compensating acceptors. The samples HVPE I and HVPE II are compensated for temperatures lower than 240 K. This originates in higher values of N_A that explains also the lower values of μ_H at room temperature. The Hall mobility of the thin films has a different temperature dependence compared to the single crystal grown by SCVT. The reason is the additional scattering at the grain boundaries this sample contains. From the fit we find that grain boundary scattering is the dominant scattering mechanisms in thin films up to room temperature.

A one donor charge balance equation considering compensating acceptors was used to model *n(T)*. Figure 5 depicts the experimental data and the corresponding fits. The shallowest dominating donor level with a density of N_D = 1.3 x 10^{17} cm^{-3} is found in the single crystal grown by SCVT. The thermal activation energy of about 37 meV is due to hydrogen donors at interstitial site. Effective mass donors as Al and Ga with lower concentration

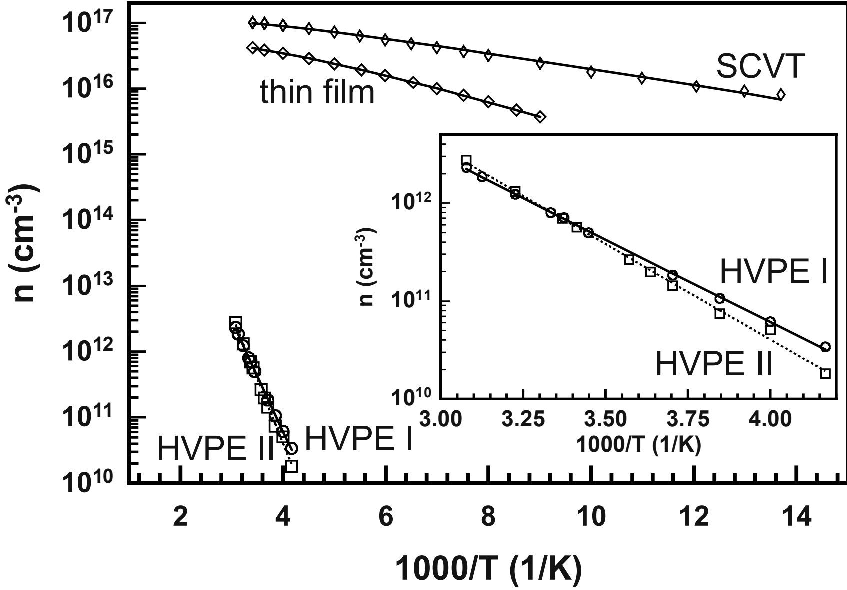

Figure 5. Free electron concentration (markers) and corresponding fits (lines) of single crystals and a thin film. The inset shows *n(T)* of HVPE I and HVPE II.

are also present in this sample as photoluminescence (PL) measurements suggest. The dominant donor in the HVPE grown samples is much deeper than the one in the SCVT grown sample. The activation energies are 299 meV or 352 meV for the samples HVPE I and HVPE II, respectively. An electron trap with an activation energy of 300 meV was also found in the SCVT grown single crystal and in PLD thin films by deep level transient spectroscopy as discussed in 6.2. The existence of this level in samples grown by three different methods suggests that it is an intrinsic defect probably the oxygen vacancy. The thin film has a donor level 65 meV below the conduction band which corresponds to the expected thermal activation.

Table 1. Parameters obtained from fits of the temperature dependent Hall measurements for single crystals and a PLD thin film.

	SCVT	HVPE I	HVPE II	PLD thin film
N_D (10^{16} cm^{-3})	13 ± 2	19 ± 0.6	12 ± 0.6	6 ± 1
E_D (meV)	37 ± 2	299 ± 5	352 ± 6	65 ± 2
N_A (10^{16} cm^{-3})	0.3 ± 0.07	18 ± 0.04	8 ± 0.04	0.15 ± 0.06
γ	0.021	0.945	0.69	0.024
L_G (nm)	-	-	-	40 ± 5
E_B (meV)	-	-	-	13 ± 2

energy of effective mass donors. The most probable cause of this level is Al diffusing during growth from the sapphire substrate in to the thin film. The lowest compensation ratio γ of about 0.02 have the single crystal grown by SCVT and the PLD thin film. This is a very low ratio indicating the high quality of present state of the art grown ZnO. The parameters of the Hall analysis are summarized in table 1.

6. SCHOTTKY CONTACTS ON SINGLE CRYSTALS AND THIN FILMS

Schottky contacts on ZnO were realized by the thermal evaporation of Ag, Au, Ni, or Pd, respectively. We used different surface preparation techniques prior to the deposition of the contact metal. For the single crystals a front-back contact configuration was used while a front-front configuration has to be used for thin films grown on insulating sapphire substrates. The homogeneity of the Schottky contacts depends on the surface preparation as revealed by electron beam induced current (EBIC) measurements (Fig. 6).

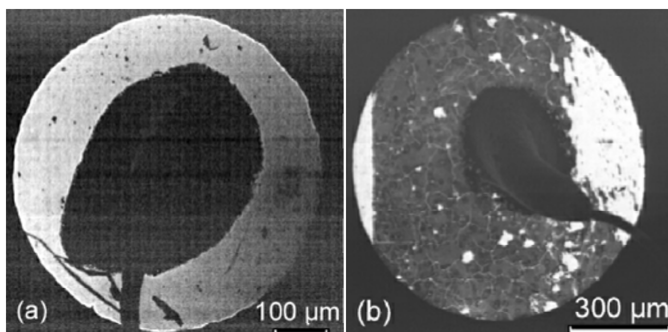

Figure 6. Electron beam induced current scans on a) a sample treated with N_2O plasma and b) a sample treated with HCl prior to the metal deposition.

The dependence of the Schottky barrier height on the metal work function is weak[10] and the ideality factors of the diodes are far from ideal indicating the presence of surface states, recombination in the space charge region, or diffusion limited currents. Etching the surface with HNO_3 leads to Schottky contacts of good quality on thin films as we found recently. The current density at –5V is about 4 x 10^{-5} A/cm² and the ideality factor determined for voltages between 0.05 V and 0.22 V is 1.3. The current density vs. voltage for this diode is depicted in Fig. 7.

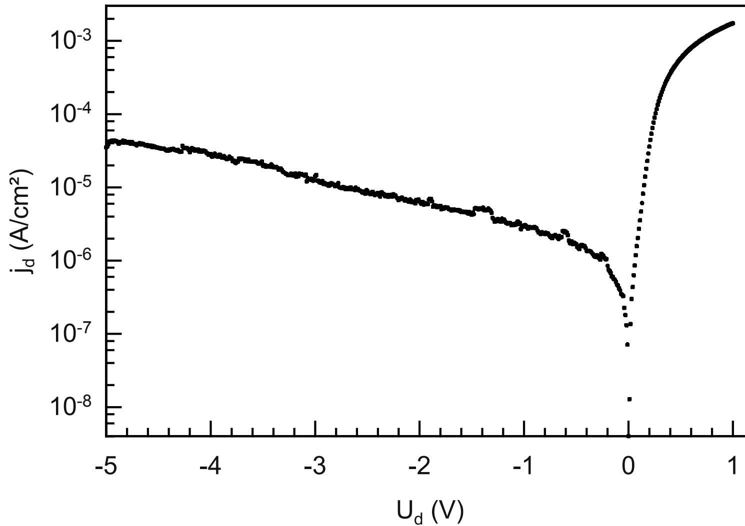

Figure 7. Current density in dependence on the voltage for a Schottky diode realized on a ZnO PLD thin film with Pd after etching with HNO_3.

6.1 Photocurrent Measurements on Single Crystals

We have measured the photocurrent of a Pd Schottky diode on a single crystal grown by SCVT in a temperature range from 4 K to 300 K. The spectra are shown in Fig. 8. The band edge shifts to lower energies as the temperature increases. For $T < 175$ K the spectra exhibit two peaks in the near band edge region. Their intensity ratio changes with temperature. The peak lower in energy is dominant for $T > 50$ K (this is the temperature where both peaks have about the same intensity) and for $T < 50$ K the higher energetic peak is most intense. To explain this behavior further investigations are on the way.

We have also realized interdigital metal-semiconductor-metal (MSM) contacts. We found a strong increase of the current through the structure by illuminating it with UV-light. If the stability under reverse bias of regular Schottky diodes (see Fig. 7) is achieved for interdigital structures we are confident that MSM structures are well suited for the realization of solar-blind UV-detectors.

6.2 Deep Level Transient Spectroscopy on single crystals and thin films

Deep level transient spectroscopy (DLTS) measurements were carried out between 4 K and 300 K. We investigated single crystals grown by SCVT

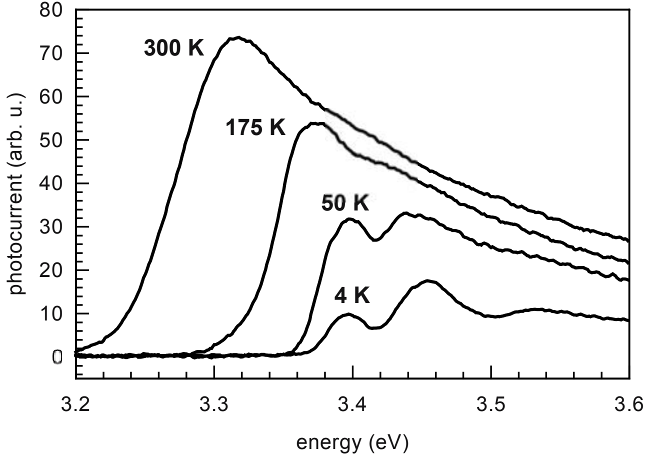

Figure 8. Photocurrent of a Pd Schottky contact on a single crystal grown by SCVT.

and PLD thin films. The series resistance of the samples HVPE I and II is too large for measuring DLTS with a capacitance bridge working at 1 MHz which we have at our disposal. We applied rate windows between 64 and 10725 Hz and found two traps in the single crystal and one trap in the thin film. Arrhenius plots of the temperature shift of the peak maximums with changing rate window are shown in Fig. 9. The slope in this plot corresponds

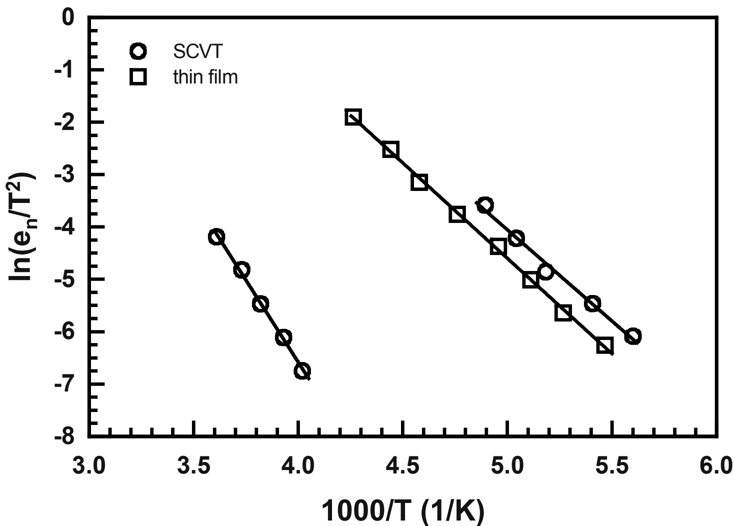

Figure 9. Arrhenius plot for deep levels found in the single crystal grown by SCVT and the thin film

to the activation energy E_t. A defect with E_t = 300 meV is found in both samples and was also found in HVPE I and II by the TDH experiments. The existence of the defect in all samples suggests that it is an intrinsic defect likely the oxygen vacancy. A deeper trap with an activation energy of 540 meV is contained in the SCVT sample.

7. SUMMARY

In summary we have reviewed the progress in the characterization of electrical properties of ZnO. Improved ohmic and Schottky contacts have been fabricated, the latter suitable for depletion layer spectroscopy. The shallow and deep donor levels have been identified for ZnO from various sources. Further control of deep donors seems necessary for achieving p-conductivity.

REFERENCES

1. D. C. Look, *Mater. Sci. Eng.*, B **80**, 383 (2001).
2. R. Schmidt, B. Rheinländer, M. Schubert, D. Spemann, T. Butz, J. Lenzner,E. M. Kaidashev, M. Lorenz, A. Rahm, H. C. Semmelhack, and M. Grundmann, *Appl. Phys. Lett.* **82**, 2260 (2003).
3. E. M. Wong and P. C. Searson, *Appl. Phys. Lett.* **74**, 2393 (1999).
4. M. J. Vellekoop, C. C. G. Visser, P .M . Sarro, A. Venema, *Sensors and Actuators*, **A21-A23**, 1027 (1990).
5. M. Lorenz, E. M. Kaidashev, H. v. Wenckstern, V. Riede, C. Bundesmann, D. Spemann, G. Benndorf, H. Hochmuth, A. Rahm, H.-C. Semmelhack und M. Grundmann, *Solid-State Electronics* **47**, 2205 (2003).
6. C. Bundesmann, M. Schubert, D. Spemann, T. Butz, M. Lorenz, E. M. Kaidashev, N. Ashkenov, H. Neumann, and M. Grundmann, *Appl. Phys. Lett.* **81**, 2376 (2002).
7. E. M. Kaidashev, M. Lorenz, H. v. Wenckstern, A. Rahm, H.-C. Semmelhack, K.-H. Han,G. Benndorf, C. Bundesmann, H. Hochmuth und M. Grundmann, *Appl. Phys. Lett.* **82**, 3901 (2003).
8. O. Breitenstein, M. Langenkamp: *Lock-in Thermography - Basics and Use for Functional Diagnostics of Electronic Components*, Springer-Verlag, Berlin, 2003.
9. L. J. van der Pauw, "A Method of Measuring Specific Resistivity and Hall Effect of Discs of Arbitrary Shape", *Philips Research Reports* **13**, No. 1, pp. 1-9 (1958).
10. H. von Wenckstern, E. M. Kaidashev, M. Lorenz, H. Hochmuth, G. Biehne, J. Lenzner, V. Gottschalch, R. Pickenhain, and M. Grundmann., *Appl. Phys. Lett.* **84**, 79 (2004).

Chapter 6

STRUCTURE, MORPHOLOGY, AND PHOTOLUMINESCENCE OF ZnO FILMS

V. A. Karpina[1], V. D. Khranovskyy[1], V. I. Lazorenko[1], G. V. Lashkarev[1], I. V. Blonsky[2] , and V. A. Baturin[3]

[1]Institute for Problems of Material Science, National Academy of Sciences of Ukraine,3, Krzhyzhanovsky str., Kyiv, 03142, Ukraine, [2]Institute of Physics, National Academy of Sciences of Ukraine, 46, Prospect Nauky, Kyiv, 03650, Ukraine, [3]Institute of Applied Physics, National Academy of Sciences of Ukraine, 40034, 58 Petropavlowska str., Sumy, Ukraine

Abstract: Thin films of ZnO were deposited by reactive thermal evaporation, r.f. magnetron sputtering and PEMOCVD. Crystal structure, surface morphology as well as ultraviolet photoluminescence at optical excitation were investigated. It is determined that ZnO films especially deposited by reactive thermal evaporation exhibit strong ultraviolet luminescence. We suggest that observed luminescence is obliged to recombination of excitons bound on two different defects.

Key words: PEMOCVD, magnetron sputtering, AFM, photoluminescence

1. INTRODUCTION

ZnO is a wide band gap semiconductor, which is used for various applications. Based on textured ZnO films one can build highly effective piezo field emitters. On the other hand ZnO is a very effective electron-excited phosphor. ZnO films easily withstand electron fluence more than 1 W/cm^2.[1] ZnO films doped with Al, Ga, or In have a low resistivity of about 10^{-4} Ωcm and a high transparency of about 90%. This is sufficient for applications as a front contact in solar cells, liquid crystal displays etc. Dielectric ZnO films have a high electromechanical coupling factor that allow using ZnO in various surface acoustic wave (SAW) devices such as delay lines, delay-line filters, resonators, transducers and SAW convolvers.

N.H. Nickel and E. Terukov (eds.),
Zinc Oxide – A Material for Micro- and Optoelectronic Applications, 59–68.
© 2005 *Springer. Printed in the Netherlands.*

Besides that, ZnO has some interesting properties, which make it very perspective for functional devices nowadays. ZnO is recognized as a promising optoelectronic material. Due to a large exciton binding energy the effective excitonic generation in ZnO could be achieved at and above room temperature. Indeed, optically pumped stimulated emission and lasing have been demonstrated at room temperature.[4-6] There are papers devoted to the deposition of p-type ZnO.[7,8] Hence, we can expect that effective light-emitting devices based on ZnO will be available in the near future.

As semiconductor ZnO can be used for detection of UV-A (300-400 nm) radiation. By doping with Mg the range can be tuned to the UV-B and UV-C (200-280 nm) regions. Such a wide interval of sensing spectra makes $Zn_xMg_{1-x}O$ UV detectors to be used in many applications such as solar UV radiation monitoring, ultra-high temperature flame detection, and airborne missile warning systems. There are reports on the design of photoconductive as well as Schottky types of ZnO UV detectors.[2,3]

Single crystal ZnO films have a strong optical anisotropy and can be used for modulation of UV radiation. ZnO modulators with a contrast of 70:1 and an operation speed of 100 ps have been designed already.[9]

ZnO appears to be a ferroelectric material upon doping with non-central ions such as Li^+, Mg^{2+}.[10,11] The Curie temperature can be increased to 340 K when ZnO is simultaneously doped with Li and Mg. Recently, ferroelectric thin films have been used for random access memory and other integrated ferroelectric devices. So, ZnO can be one of the candidates for such systems.

ZnO is recognized as the best candidate for diluted magnetic semiconductor in the recently emerged new field of electronics – spintronics. Spintronics (spin + electronics) focuses on the creation of functional devices based on the control of ferromagnetic ordering by an electric field or light. According to several theoretical predictions ZnO doped with transition metals is expected to be ferromagnetic with a high Curie temperature.[12,13] Therefore, a transparent ferromagnetic could be created. This shows that ZnO is a promising material for the development of a variety of functional devices.

2. EXPERIMENTAL PROCEDURE

ZnO films were obtained by evaporation of zinc metal from a special cell in oxygen atmosphere. The deposition was carried out on mica and glass substrates. The deposited films were annealed at 400 °C in air and at higher temperatures. For RF magnetron sputtering we used pure Zn as a target and a gas mixture of $Ar+O_2$ for the working gas. These samples were deposited on glass and sapphire substrates. Zinc acetylacetonate $Zn(AA)_2$ was used as a

precursor for PEMOCVD depositions. The base system was equipped by additional device with a resistive evaporator, to which small portions of $Zn(AA)_2$ powder were introduced periodically. The argon carrier gas transports the vapor into the chamber that contains an oxygen-argon plasma. The $Zn(AA)_2$ vapor is decomposed under plasma discharge and reacts with oxygen. Polycrystalline ZnO thin films were deposited at substrate temperatures in a range of 150 °C - 300 °C. The crystal structure was examined by XRD analysis and the surface morphology by AFM and SEM. UV photoluminescence was measured at high excitation with a nitrogen laser (337 nm, 10 ns, 100 Hz). The measurements were carried out at room temperature and at 77K.

3. RESULTS AND DISCUSSION

3.1 Structure and morphology of ZnO films

Fig. 1 shows XRD spectra of ZnO films deposited by reactive thermal evaporation (RTE), magnetron sputtering (MS) and PEMOCVD. As can be seen from Fig. 1(a) ZnO films deposited by RTE have no preferred crystallite orientation. It may be assumed that the ZnO films are not textured due to a high growth rate of 0.3-0.5 µm/min. At such deposition rates ZnO films have excess of Zn and their structure is not perfect. Thus, these films require subsequent annealing. On the contrary, ZnO films deposited by MS (Fig 1(b)) can be textured under certain conditions with the c-axis perpendicular to the substrate. It is known that increasing substrate temperature leads to high quality textured ZnO films. In our experiments we obtain highly oriented ZnO films deposited by MS at 300 °C and 20% O_2 for films deposited on glass substrate and at 200 °C, 20% O_2 for films deposited on sapphire substrates. Thin films, prepared by PEMOCVD showed some texture (Fig 1(c)), and the optimal growth conditions the following: $T_S = 200$ - 250 °C, $W_p = 300$ W, $Q_{Ar} = 40$ ml/min, P = 0.3 Torr.

Fig. 2 represents the surface morphology of ZnO films deposited by RTE and MS. It can be seen that films deposited by RTE have a large grain size of 0.7-1 µm. The samples deposited by MS have a smoother surface. AFM images of these films are shown on Figs. 3 and 4. ZnO films deposited by MS have a maximum grain size of about 100 nm and an average roughness of 2 nm. As the substrate temperature increases within 100-300 °C the average roughness increases from 0.7 to 3 nm. Simultaneously, the average grain size increases from 40 to 60 nm. AFM analysis demonstrates that the grain size of ZnO films deposited by PEMOCVD in the same temperature

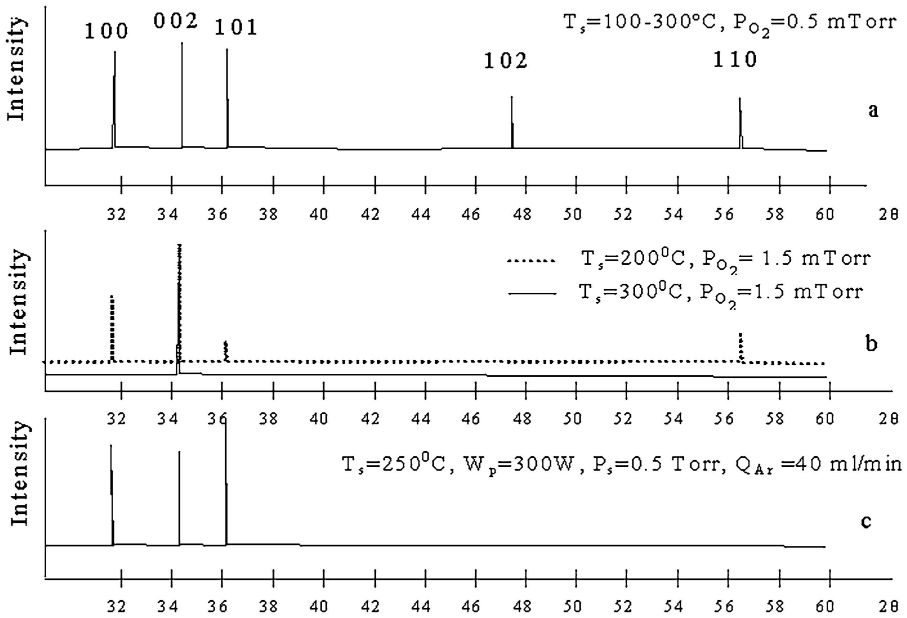

Figure 1. XRD spectra of ZnO/glass films deposited by RTE (a), MS (b), PEMOCVD (c). ZnO films deposited by RTE and PEMOCVD were annealed at 500 °C for two hour in ambient air.

range amounts to 25 – 75 nm for T_s=200 °C, 30 – 60 nm for T_s=250 °C, and 25 - 70 nm for T_s=300 °C. The average roughness was minimal at T_s=250 °C and changes slightly with increasing temperature. From it we conclude that that T_s=250 °C is the optimal temperature to obtain high quality ZnO films using PEMOCVD.

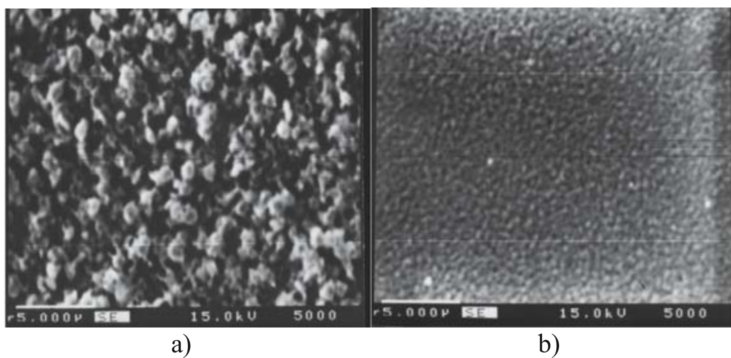

Figure 2. SEM images of ZnO deposited by RTE (a) and MS (b) and annealed at 500 °C.

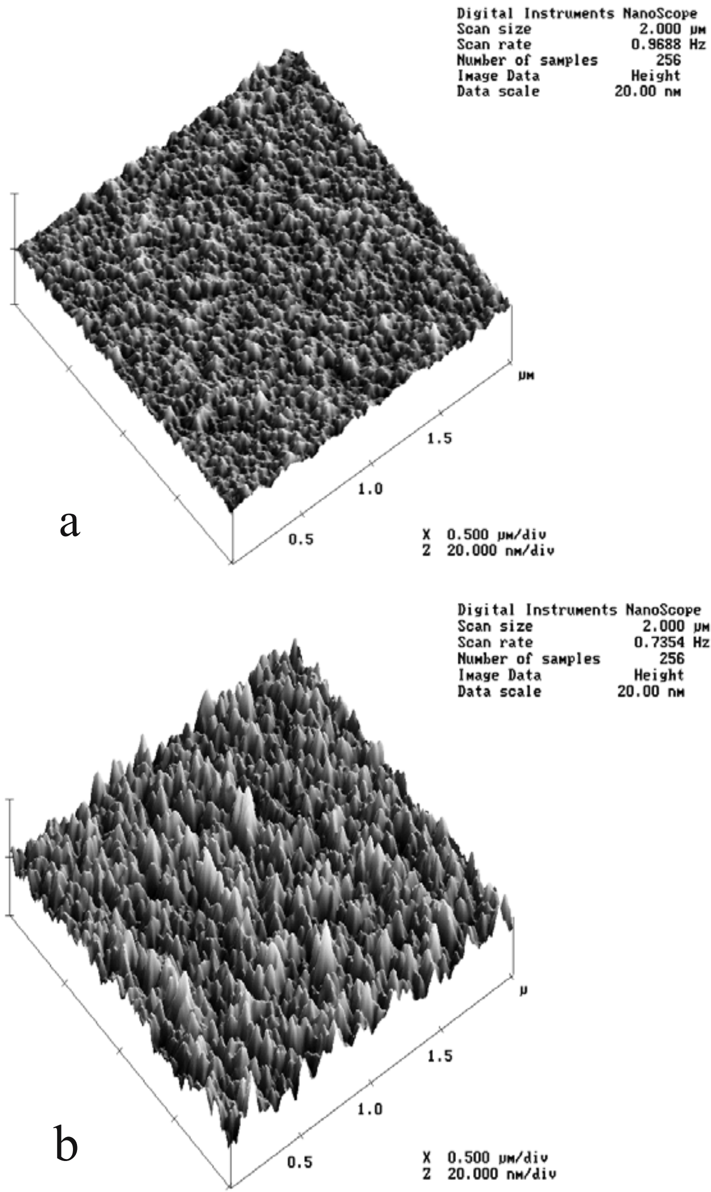

Fig. 1

Figure 3. AFM images of ZnO films deposited by MS at T_s=150 °C (a) and T_s=300 °C (b).

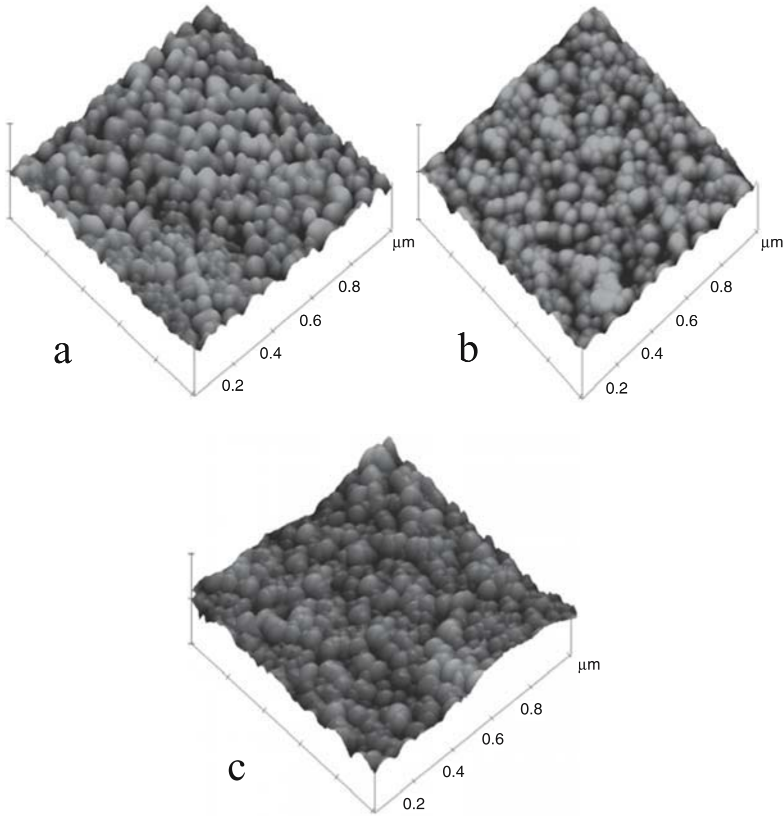

Fig. 2
Figure 4. AFM images of ZnO deposited by PEMOCVD at T_s=200 °C (a), T_s=250 °C (b), and T_s=300 °C (c).

3.2 Optical properties and UV photoluminescence

All deposited ZnO films show an optical transmittance of 65-85% in the range of 400 –800 nm. High transparency and an abrupt edge of absorption (at 380 nm) indicate a high optical quality of ZnO films. Fig. 5 shows RT PL spectra of ZnO films deposited by MS and RTE. It should be noted that we have observed UV PL in all deposited ZnO films only after thermal annealing at 500 °C or at higher temperatures. It is surprising that ZnO films deposited by RTE exhibit a stronger UV PL than ZnO films deposited by MS. The excitation density at which we clearly observed UV PL was not higher than 1.2 MW/cm^2 for films deposited by RTE and 9 MW/cm^2 for films deposited by MS. PL spectra taken at 77 K under the same excitation source are shown on Fig. 6(a). Fig. 6(b) shows the PL spectrum at low

excitation using a cw He-Cd laser (325nm, 6 mW). Super linear integrated PL intensity was observed (Fig. 6(c)).

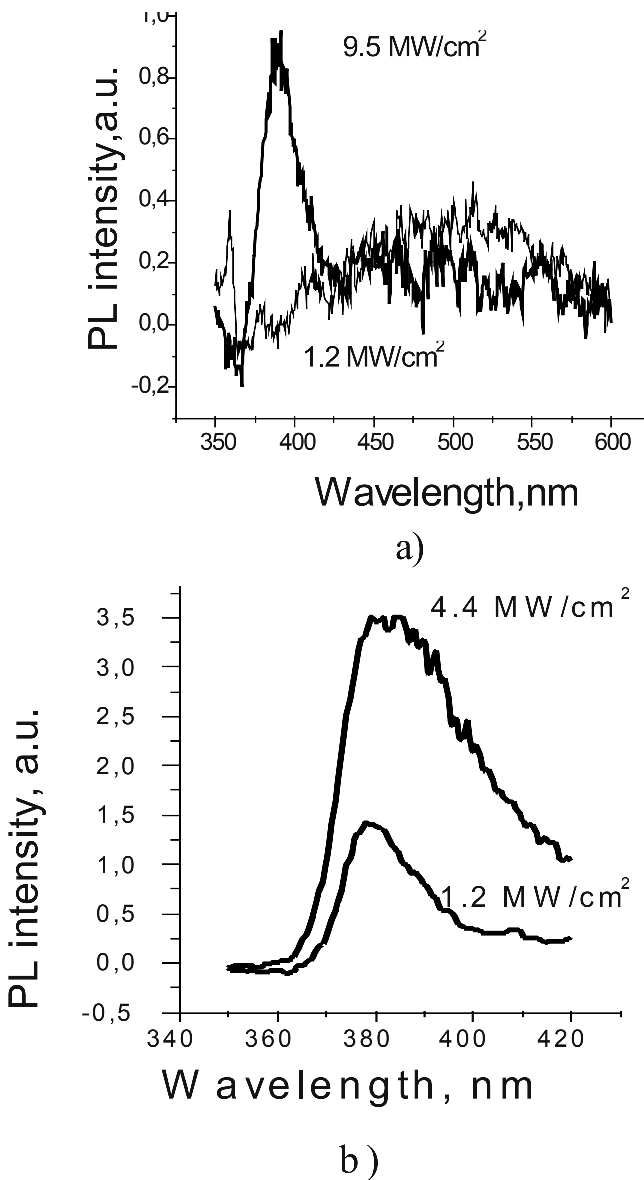

Figure 5. RT PL spectra of ZnO films deposited by MS on sapphire (a) and RTE on mica (b). ZnO films were annealed at 500 °C.

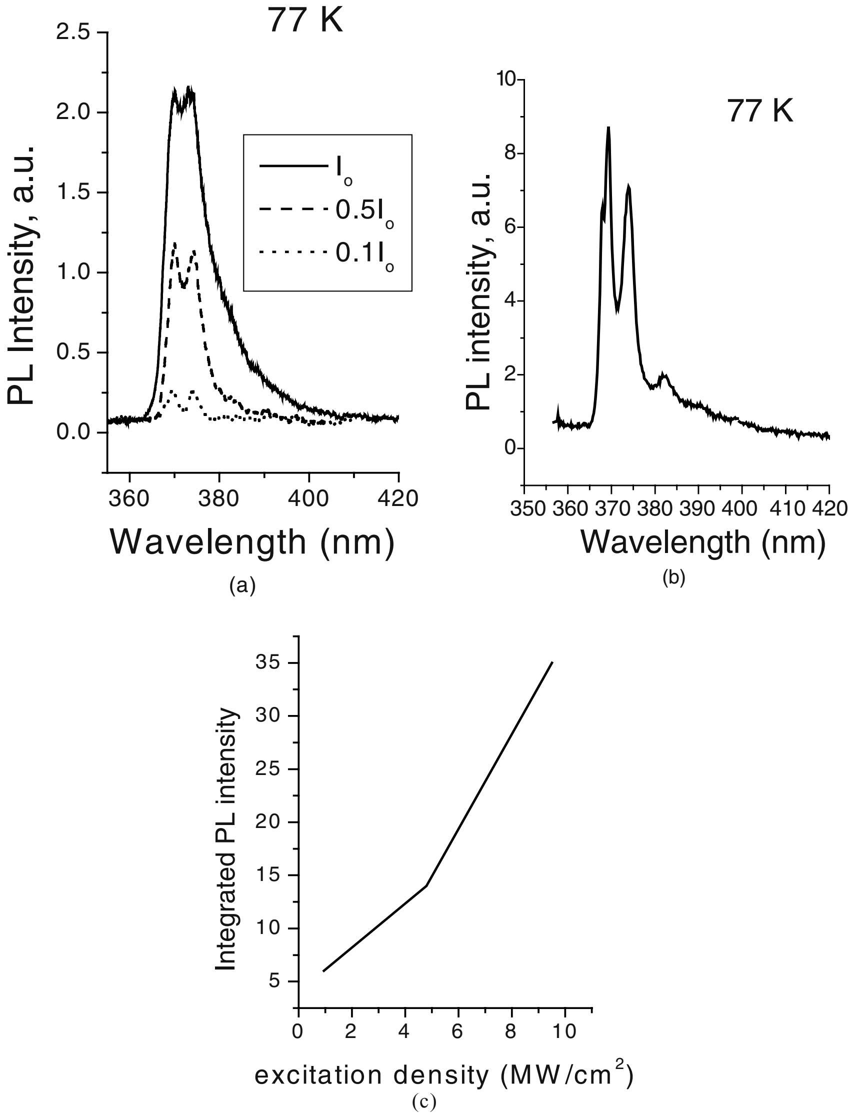

Figure 6. PL spectra of ZnO films deposited on mica by RTE and annealed at 500 °C (a), at high excitation by an N_2 laser (b), and at low excitation with a He-Cd laser (c). PL integrated intensity at N_2 excitation.

At low intensity there are two PL lines located at 369 and 374 nm (Fig. 6a). As the excitation intensity increases the intensity of the peaks also increases. These two bands widen and overlap. Besides, the long-wave part of the spectra strongly widens. At low excitation using a He-Cd laser we

observed three lines (Fig. 6b). Two lines are located at the same positions and the third line is positioned at 382.5 nm. The energy difference between the second and third line is 73 meV, what corresponds to LO phonon replica. Whereas we observed a broadening of the line at increasing of pumping intensity it could be supposed that stimulated emission with simultaneously generation of acoustic phonons occurs. Besides that we also suggest that twofold line is obliged to the recombination of excitons bound on two different types of defects.

Finally, we have measured the time-dependent behavior of the PL spectra at 77 K. At a delay time of 0-2 ns we observed strong UV PL (Fig. 7). At steady state conditions a deep-level yellow-red emission connected with defect luminescence is observed. So it could be concluded that exciton recombination is a faster process than recombination via deep levels.

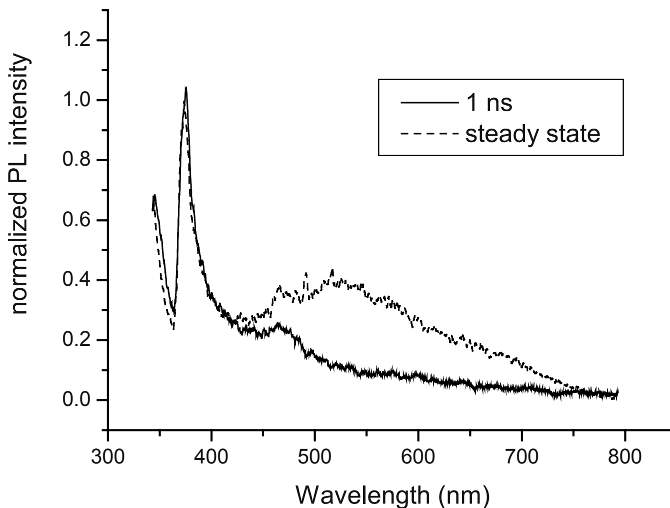

Figure 7. Normalized time-dependent PL spectra of ZnO films deposited by PEMOCVD.

4. SUMMARY

ZnO films were deposited by RTE, MS, and PEMOCVD. In the case of RTE the ZnO films have a large-grained structure with no preferred crystallite orientation. On the contrary, ZnO films deposited by PEMOCVD and MS have fine-grained structure with an average grain-size of 40-60 nm. Under certain growth conditions ZnO films show a preferred orientation with the c-axis normal to the substrate. However, ZnO films prepared by

RTE have larger RT UV photoluminescence. The UV PL peaks at 383 nm at RT. At 77K this peak splits into two located at 369 and 374 nm. Their intensity increases super linearly with increasing excitation. We suggest that the observed UV PL is due to recombination of excitons bound to two different centers. A long-wave tail is observed at high-level excitation. Such behavior testifies to the lasing effect accompanied by the generation of acoustic phonons. The transition time of the excitonic radiative process is in the range of sub nanoseconds.

ACKNOWLEDGEMENTS

We are thankful to A. Yu. Pyryatinsky, V. N. Kadan, A. N. Komarov, V. M. Vereschyak, and P. M. Lytvyn for their interest and input to this paper. We are indepted to the Institute of Single Crystals of the National Academy of Sciences of the Ukraine for providing us with sapphire substrates. This work is partially supported by the program "Nanosystems, nanomaterials, nanotechnologies" (project H27-04).

REFERENCES

1. P. P. Gorbick, A. A. Dadykin, and I. V. Dubrovin, *Reports of The National Academy of Science of Ukraine*, **1**, 84 (2001).
2. W. Yang, R. D. Vispute, S. Choopun, R. P. Sharma, T. Venkates, and H. Shen, *Appl.Phys.Lett.* **78,** 2787 (2001).
3. S. Liang, H. Sheng, Y. Liu, Z. Huo, Y. Lu, and H. Shen, *J. Cryst. Growth*, **225**, 110 (2001).
4. Z. K. Tang, G. K. L. Wong, P. Yu, M. Kawasaki, A. Ohtomo, H. Koinuma, and Y. Segawa, *Appl. Phys. Lett.* **72**, 3270 (1998).
5. H. Cao, Y. G. Zhao, H. C. Ong, S. T. Ho, J. Y. Dai, J. Y. Wu, and R. P. H. Chang, *Appl. Phys. Lett.* **73**, 3656 (1998).
6. Y. Chen, H. Ko, S. Hong, and T. Yao, *Appl. Phys. Lett.* **78,** 1469 (2001).
7. Y. R. Ryu, S. Zhu, D. C. Look, J. M. Wrobel, H. M. Jeong, and H. W. White et al., *J. Cryst. Growth*, **216**, 330 (2000).
8. M. Joseph, H. Tabata, and T. Kawai, *Jpn.J.Appl.Phys.* **38,** L1205 (1999).
9. M. Wraback, H. Shen, S. Liang, C. R. Gorla, and Y. Lu, *Appl.Phys.Lett.* **74**, 507 (1999).
10. A. Onodera, N. Tamaki, Y. Kawamura, T. Sawada, and H. Yamashita, *Jpn. J. Appl. Phys.* **35,** 5160 (1996).
11. M. Joseph, H. Tabata, and T. Kawai, *Appl. Phys. Lett.* **74**, 2534 (1999).
12. T. Dietl, H. Ohno, F. Matsukura, J. Gibert, and D. Ferrand, *Science* **287, 1019** (2000).
13. K. Sato and H. Katayama-Yoshida, *Jpn. J. Appl. Phys.* **39**, L555 (2000).

Chapter 7

OPTICS AND SPECTROSCOPY OF POINT DEFECTS IN ZnO

Vladimir Nikitenko
Moscow State Transport University, Obraztsova str. 15, 103055 Moscow, Russia

Abstract: This work investigates spectra of luminescence and photo-electron spin resonance (EPR) of zinc oxide single crystals, powders and films. We used single crystals of zinc oxide produced by the hydrothermal method and by the method of gas-transport reactions. The samples were subjected to irradiation of electrons (E = 4 MeV, f = 7.5×10^{18} cm^{-2} and f = 1.2×10^{19} cm^{-2}) and protons (E = 7.7 MeV, f = 10^{15} cm^{-2}). Using both thermoluminescence and EPR electron-hole processes are investigated (T = 4 - 450 K), which cause luminescence and decharging of self and impurity point defects. The mechanism of violet, green, yellow-orange and red (and accompanying it infra-red: λ = 11000 - 12000 Å) luminescence is discussed.

Key words: Point defects, photoluminescence, photo-EPR, single crystals, hydrothermal method, exciton, donor, acceptor, thermoluminescence

1. INTRODUCTION

Among the well-known semiconducting materials employed in various technical solutions, a unique position is held by zinc oxide, which is applied in electronic and space engineering, chemical industry, and medicine.[1-3]

Despite such different applications, there is no general agreement regarding the problem of the involvement of the intrinsic and extrinsic point defects in the optical, electrophysical, and radiative properties of this material. The mechanism underlying the photoexcitation and luminescence of zinc oxide is still a matter of debate. The simultaneous implementation of spectral luminescence and photo-EPR (electron paramagnetic resonance) methods has led to considerable improvement of this situation. This report is devoted to review our data obtained by these methods.

N.H. Nickel and E. Terukov (eds.),
Zinc Oxide – A Material for Micro- and Optoelectronic Applications, 69–81.
© 2005 *Springer. Printed in the Netherlands.*

2. EXPERIMENT

In the present work, we investigated powders, films and single crystals of ZnO produced by the hydrothermal method at the Institute of Crystallography of the Russian Academy of Sciences and by the method of gas-transport reactions at the Institute for the Physics of Semiconductor of the Siberian Branch of the Russian Academy of Science.[3]

The use of a helium flow cryostat in the our spectrometer made it possible to carry out EPR measurements within the temperature range 4-300 K with a rapid change in the sample temperature. In most cases of low temperatures, an identical initial state of the crystal before illumination was achieved by annealing the sample in a cryostat at room temperature for 5-10 min. The concentration N(T) of paramagnetic centers in thermally stimulated processes of charge transfer in the crystal under investigation was determined by the EPR – signal intensity in the pulsed heating mode.[3]

3. INVESTIGATION OF POINT DEFECTS IN ZnO

Typical luminescence spectra of as-grown crystals show ultra-violet emission due to free excitons (including their longitudinal optical phonons-LO replicas) as well as typical bands of green and yellow-orange luminescence (the temperature is 77-80 K). When the temperature is 4.2 K, the luminescence of bound excitons (including their LO – replicas) dominates.[1-3]

An exciton bound to a shallow neutral donor of interstitial zinc (Fig 1 a) and of interstitial lithium (Fig. 1b) is presented, for example, in our spectra. In some instances the radiative recombination of an exciton bound to a neutral defect may not lead to the ground state of the respective defect but to an excited state of the carrier at this occupied center (2 – electron transition). In a hydrogenic model we can calculate an ionization energy of the neutral donor state of interstitial zinc to 0.05 eV and of interstitial lithium to 0.033 eV.

In zinc oxide, various impurities of both substitution and interstitial type act as shallow donor centers with an ionization energy $E_d = 0.03 - 0.05$ eV (for example, interstitial hydrogen, the substitutional impurities of the 3-rd group of the periodic table of elements and so on).

The lithium dopant in ZnO may occupy interstitial sites (Li_i) or may substitute for the Zn site (Li_{Zn}) acting as a shallow donor or as an accepter, respectively. The optical depth, measured from the edge of the valence band, amounts to about 1 eV and the thermal depths to 0.2 - 0.4 eV.[3]

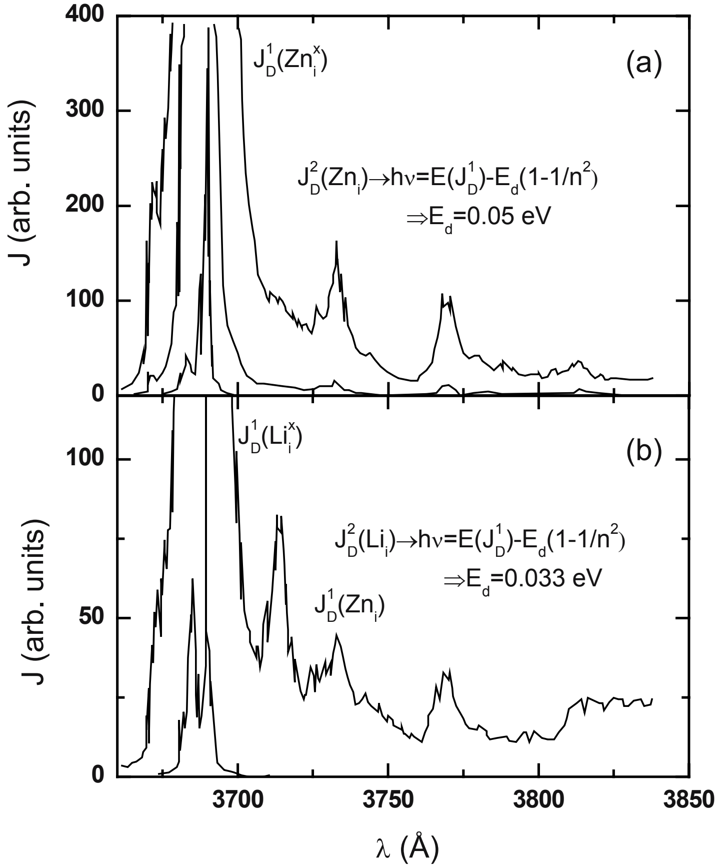

Figure 1. Photoluminescence spectra of a hydrothermally grown ZnO single crystal (a) before and (b) after Li-doping by heat treatment in Li_2CO_3 at 700 °C; T=4.2 K; laser excitation at λ=2950 Å.

The formation of defects of the first type is favored by reducing conditions for the doping of crystals while acceptors are created in oxidizing regimes. In order to investigate the lithium acceptor microstructure in ZnO, the photo – EPR method was used, which turned out to be very efficient in this respect.[3,4]

It was found that the EPR of lithium ions is observed only on optical excitation (mainly by UV light) and at low temperature (< 200 K). The resonance possesses axial symmetry with respect to the hexagonal C axis of a crystal. In a magnetic field directed normally to the C axis, the signal of the axial center is a quartet of closely spaced lines with g – factor $g_{\perp}$=2.0260, which corresponds to the hyperfine interaction of the unpaired electron spin

moment of the oxygen ion $O^|$ with the magnetic moment of the nucleus of isotope ^7Li (j = 3/2).

In a non-excited crystal, the substituting lithium ion is surrounded by four oxygen ions $O^{||}$ (with two electrons). The center becomes paramagnetic $Li^{\times}_{Zn}$ (in a more complete notation $[Li^{+}_{Zn} - O^|]$ when a hole is trapped (or an electron is released) by one of the nearest neighbor oxygen ions (or by one of the four oxygen ligands).

As an example needed for further discussions we give Fig. 2. Optical transitions (3) and (4) during excitation of the sample form paramagnetic states of lithium at T = 30 K. The capture of free electrons by the traps keeps

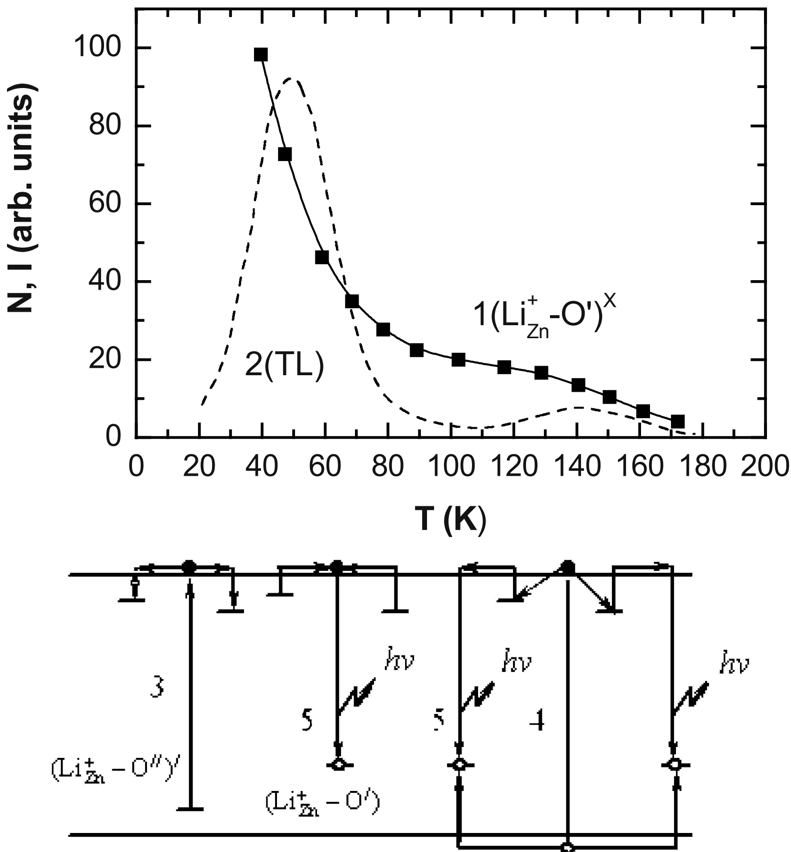

Figure 2. Dependence of the concentration of lithium paramagnetic centers (Li_{Zn}^{+}-$O^|$), shortened to $Li_{Zn}^{\times}$, at T = 30 K on the temperature of annealing the ZnO-Li single crystal (1), the intensity of thermoluminescence (2) at λ_{exe} = 380 nm, and the schematic diagram of optical transitions during excitation of the luminophor (3 and 4) and radiation (5).

a paramagnetic state of lithium. Vacating of the electron traps during heating (first at T_1 = 50 K, then at T_2 = 145 K) leads to the appearance of electrons in the conduction band. The subsequent capture of these electrons by the lithium acceptor is accompanied not only by a decrease in the concentration of the paramagnetic lithium states (curve 1) but also by yellow-orange thermoluminescence (curve 2 and transition 5). As a result, clearly observed is the mechanism of the yellow-orange luminescence of ZnO and the lithium nature of the corresponding luminescence centers (Li^{+}_{Zn}–$O^{|}$), which have been subject of lasting discussions. An analysis of thermoluminescence curves by various methods[3] showed that the detected electron traps have depths of E_1 = 0.03 - 0.05 eV and E_2 = 0.18 eV.

Heat treatment of as-grown crystals in Li_2CO_3 at 400 to 700°C for 2 to 7 days causes a partial substitution of lithium for Zn sites causing considerable growth of resistivity to $\rho \sim 10^8$-10^{10} Ωcm because of the Li^{+}_{I} = $Li^{|}_{Zn}$ and noticeable lowering of the Fermi level. The luminescence spectra of such samples are characterized by enhanced yellow-orange emission noticeable quenching of emission due to excitons bound to neutral shallow donors.

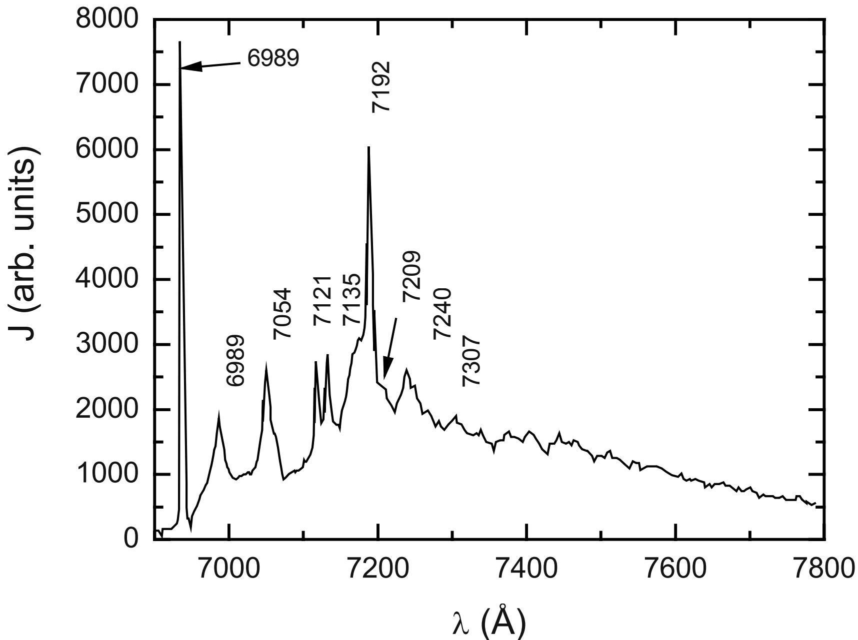

igure 3. Red photoluminescence spectrum of grown hydrothermally ZnO(Fe) single crystal annealed in Li2CO3 at 973 K for seven days; T=4.2 K; excitation with a DKSSh-3000 lamp (λ=3500 Å).

Li_2CO_3, their luminescence spectra show a composite violet band, which was attributed to donor-acceptor pairs is which the acceptors are not isolated $Li^{|}_{Zn}$ defects (as in the case of the yellow-orange luminescence) but associates including shallow donors, such as (Zn^{+}_{i} $Li^{|}_{Zn}$), (In^{+}_{Zn} $Li^{|}_{Zn}$) so on.[2,5]

Characteristic red luminescence is observed for ZnO crystals doped with iron and then heat-treated in Li_2CO_3 (iron doping can be accomplished during hydrothermal growth, yielding black ZnO crystals) (see Fig. 3).

The strong EPR signal, which is observed in these crystals, corresponds to the g-factor $g_{||} = 2.006$. It is associated with transition $M = -1/2 \rightarrow +1/2$ of the fine structure of the EPR spectrum of the Fe^{3+} ions. The EPR of the Fe^{3+}_{Zn} ($3d^5$) ions in zinc position is not observed in the dark in low-ohmic as-grown ZnO single crystals. This is attributed to the fact that as the Fermi level raises, three – valent iron ions go over into the two-valent diamagnetic state of Fe^{2+}_{Zn} with the configuration $3d^6$. Therefore, to observe the EPR signal of the Fe^{3+} ions, low-ohmic single crystals are often exposed to a preliminary thermal treatment, which lowers the Fermi level. Or, alternatively, the specimens can be irradiated with elementary particles in

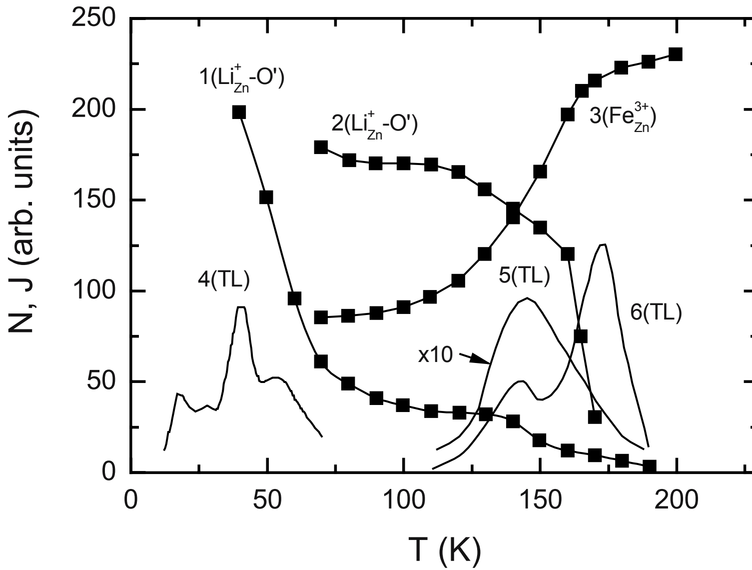

Figure 4. Dependence of the spin density N of the paramagnetic centers and of the thermoluminescence intensity (TL): (Li_{Zn}^{+}-$O^{|}$) at T=30 K (1) and at T=70 K (2), Fe_{Zn}^{3+} at T=70 K (3) on the annealing temperature of the hydrothermal ZnO single crystal and TL curves – the temperature of excitation T=5 K (4) and 80 K (5) – TL at λ=5900 Å; at T=70 K and λ=7200 Å (6). The original single crystal (1,4,5); ZnO:Fe single crystal annealed in Li_2CO_3 at T = 973 K for seven days (2,3,6). $\lambda_{exc.}$ = 3800 Å.

regimes causing an increase in their specific resistance. A systematic relation between the intensity of the red luminescence and the intensity of EPR signal of the Fe^{3+}_{Zn} ions was noticed.

In other ZnO single crystals, we observed the appearance of an isotopic EPR signal with the factor g = 2.0134, in which hyper fine structure was discovered (6 lines of identical intensity). Such an EPR signal was ascribed to the $^2S_{1/2}$ state of Pb^{3+}_{Zn} ions.

At low temperatures, the EPR signal of Fe^{3+} ions and Pb^{3+} ions in zinc oxide is photosensitive. We observed this signal in relatively low-ohmic single crystals of ZnO. A pronounced photo excitation band shows up.[3] It can be related to the photo ionization of the deep donor Fe^{2+} ions. The analysis of the form of the photo ionization spectrum allows to calculate the optical ionization energy, which turned out to be equal to 1.4 eV for Fe^{2+}_{Zn} ions and 1.65 eV for Pb^{2+}_{Zn} ions.

Fig. 4 shows the dependence of spin density of the paramagnetic centers and thermoluminescence intensity on the annealing temperature of the used single crystals. We should note the possibility of observing the Fe^{4+}_{Zn} state in crystals, which have an artificially lowered Fermi level. The transition $Fe^{4+}_{Zn} + e \rightarrow Fe^{3+}_{Zn}$ manifests itself in an increase of the concentration of paramagnetic Fe^{3+}_{Zn} states in the process of the release of electrons from electron traps (at 110 to 160 K; Fig. 4, curve 3). This leads to a simultaneous decrease in the concentration lithium paramagnetic states (curve 2) and appearance of the yellow-orange (curve 5) and red termoluminescence (curve 6).

As is seen in Fig. 4, the concentration of Li induced paramagnetic states drops in the range 160-200 K (the yellow-orange luminescence is absent). Taking into account the hole character of the process, this indicates that the electrons are transferred from the valence band to lithium paramagnetic states ($Li^{\times}_{Zn}+kT \rightarrow Li^{|}_{Zn}+e^{+}$). Therefore, the lithium paramagnetic centers can be identified with the hole traps responsible for red thermoluminecseence and, in some cases, for green thermoluminescence with a peak at T=180 K. A strong peak of red TL appears at 160-200 K in our crystals (curve 6). The concentration of paramagnetic Fe^{3+}_{Zn} ions increases at this moment (curve 3). This result can be accounted for by the reaction ($Fe^{2+}_{Zn}+e^{+} \rightarrow Fe^{3+}_{Zn}$), which is highly probably for the Fe center in ZnO.[3] It should be noticed that the thermal degradation of Li paramagnetic states in the range 160-200 K is also confirmed by the absence of the corresponding EPR signal for T>200 K.

Numerous measurements show that the traps responsible for the thermoluminescence peak at = 180 K are located 0.35-0.45 eV above the edge of the valence band. According to a model of yellow-orange

luminescence, the optical depth of the lithium level is 1-1.3 eV above the valence band.[1-4] Thus, thermal and optical measurement yield different defect ionization and neutralization energies for ZnO which is a natural consequence of the high bond ionicity and may result from a charge-transfer-induced polarization of the crystal lattice.

The spectrum of the red luminescence has a complex structure. We were able to separate three components of red luminescence that each have their own kinetics and that differ by the character of excitation. The radiation band at 7300-7800 Å is predominantly excited by light with λ_1 = 3700-4800 Å and has a three – exponential time dependence of afterglow with time constants of 3 msec, 15 msec, and 75 msec. The relatively strong emission line at 7175 Å has maxima in the excitation spectrum at 3700 and 5200 Å. It is characterized by an afterglow time constant of τ = 33 μsec. Several narrow lines in the 6900-7200 Å region are well excited with λ=4000-4800 Å and are characterized by $\tau_1 = 3$ and $\tau_2 = 22$ msec.

The red luminescence extends into the infra – red region (Fig. 5). The results obtained point to the requirement of further refinements of the emission transition scheme in the case of the red luminescence of ZnO.

The model, according to which the red luminescence of ZnO represents luminescence of ions Fe^{3+}_{Zn} ($3d_5$ – configuration) is the most encompassing

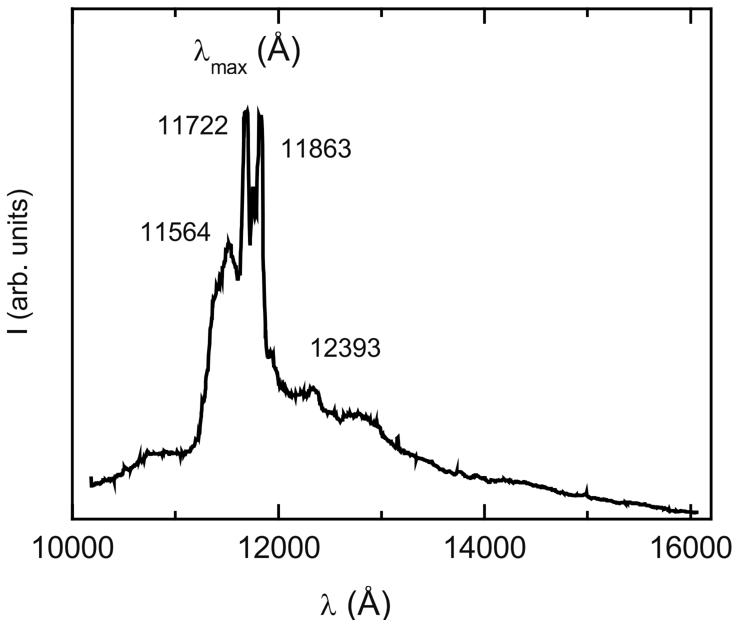

Figure 5. The infra-red photoluminescence spectrum of a ZnO-Fe,Li single crystal at T=4.2 K; excitation at 4880 Å (argon laser).

on our view now. The red luminescence of ZnO is the analogue of the well-known orange-red luminescence of manganese ions Mn^{2+} (for example, in ZnS), which have the same configuration $3d^5$ or the red luminescence of ions Fe^{3+}_{Zn} in ZnS. This radiation corresponds to the optical transitions $^4T_1(^4G) \rightarrow {}^6A_1(^6S)$.

Irradiation of the ZnO – Li samples by protons leads to the appearance of a photosensitive EPR signal (f – signal) which corresponds to the center with an axial symmetry and g-factor $g_{||} = 1.9948$ and $g_{\perp} = 1.9963$. This signal is very important for understanding the processes of defect formation, since it leads to gives rise to two alternative interpretations for the microscopic structure of the intrinsic defects that determine the deviation from the stoichiometry in ZnO.[6]

According to the one viewpoint, the f-signal should be assigned to the oxygen vacancies V^+_O (F^+ – center) that are formed by capture of one electron by anionic vacancies with double positive charge. In this case the detected hyperfine structure of the signal is explained by the interaction of the unpaired spin of the electron with the nuclei of the ^{67}Zn isotope (content is 4.1%, spin I=5/2). The condition for photoexcitation of the f-signal of EPR is such that the oxygen vacancy $V^{\times}_O$ (F – center) represents a deep donor with a photoionization energy of 2.3 eV. In this case the low resistivity in ZnO is determined by shallow donors of the interstitial zinc $Zn^{\times}_i$ with an ionization energy $E_d = 0.05$ eV, which by forming the impurity band or by recoiling the electrons to the empty band, are responsible for the specific EPR signal with the factor g=1.96.

From another viewpoint the recorded f-signal of EPR should be attributed to the interstitial oxygen in the paramagnetic state $O^{|}_i$ or $O^{\times}_i$, and $V^{\times}_O$ should be considered as the shallow donor specifying the EPR signal with the factor $g \approx 1.96$ (there is an anisotropy $g_{||} = 1.9557$ and $g_{\perp} = 1.9573$ at low temperature) and high electrical conductivity of ZnO.

The investigations of the processes of the charge exchange of the centers by the EPR method in the mode of pulsed heating made it possible to determine the temperature dependence of the relative concentration of the paramagnetic centers that specify the f-signal of EPR and of the reference $Li^{\times}_{Zn}$-centers in the ZnO-Li single crystals irradiated with protons. Concurrently, we studied thermoluminescence (Fig. 6). The spectra of the photoluminescence of crystals and those of the excitation of the F^+ and $Li^{\times}_{Zn}$ paramagnetic centers are shown in Ref. 6.

An important feature of the results obtained is the recapture of the electrons released from traps at $T_1 \approx$ 30-60 K and $T_2 \approx$ 110-150 K by the paramagnetic centers that form the f-signal of EPR (Fig. 6, curves 1). Only when these centers «finish their work» does the transformation of the lithium paramagnetic centers into the diamagnetic state begin ($T_2 \approx$ 150-180 K,

curve 2); this is accompanied by yellow-orange thermoluminescence (Fig. 6, curve 3). This fact indicates that the paramagnetic centers responsible for the f-signal with $g_{\|} = 1.9948$ and $g_{\perp} = 1.9963$ have a much greater effective cross section for the capture of mobile electrons than the neutral paramagnetic centers of the form ($Li^{\times}_{Zn}$–$O^{|}$), which is characteristic just for the F^{+}-centers. The $O^{\times}_{i}$ states must behave in the same way as the lithium paramagnetic centers, and the $O^{|}_{I}$ states must be substantially less effective in the capture of the electrons than the centers of the ($Li^{\times}_{Zn}$–$O^{|}$) type.

The concept of the F^{+}-center in interpreting the f-signal of EPR is confirmed by a theoretical model of the F^{+}-centers in ZnO and by the data for other A_2B_6 compounds.[3] The absence of the EPR-signal with the factor $g \approx 1.96$ in the crystals irradiated with proton (the resistance of a sample increases by 2-3 orders of magnitude) supports the argument in favor of the description of the signal by free carriers in the conduction band (or electrons in the band of shallow donors) and also confirms the conclusion about the vacancy nature of the f-signal of EPR. The valence band electrons fill the lithium paramagnetic centers in the 180-200 K temperature range. The holes formed in the valence band are captured by the F-centers following the reaction $F^{x} + e^{+} > F^{+}$, which leads to an increase in the intensity of the f-signal of EPR (Fig. 6, curve 1). A similar filling of the F^{+} states by the valence band electrons in the temperature region of about 250 K leads to the complete disappearance of the f-signal (Fig. 6).

Attention is drawn to the radiation-less character of the transition of electrons from the conduction band to the F^{+}-centers (a decrease in the concentration of the paramagnetic states F^{+} does not cause thermoluminescence, Fig. 6). This contradicts rather widespread models attributing the green luminescence of ZnO just to that sort of process.

Quenching of the complex band of the green-orange luminescence and redistribution of its maximum to the long-wavelength side are observed in ZnO single crystals irradiated with protons. This is related with the presence of a green-radiation absorption band in the spectrum of photoexcitation of F^{+}-centers.[3] This appears to be also an explanation of the absence of the green thermoluminescence which is typical for ZnO. Irradiation of initial ZnO-Li single crystals with electrons is also accompanied by the appearance of the f-signal of EPR. The character of the spectrum of the visible luminescence of these crystals corresponds to that in Fig. 6. An interesting feature of the ZnO-Li single crystals irradiated with electrons is the existence of the EPR signal from F_A-centers,[6,7] which is an additional argument in favor of the selected model of the f-signal of EPR.

The centers of F_A type have deeply been studied in alkali-earth oxides and have recently been detected in ZnS.[7] Unlike F^{+}, this center contains an impurity ion in the immediate neighborhood with the anionic vacancy (for

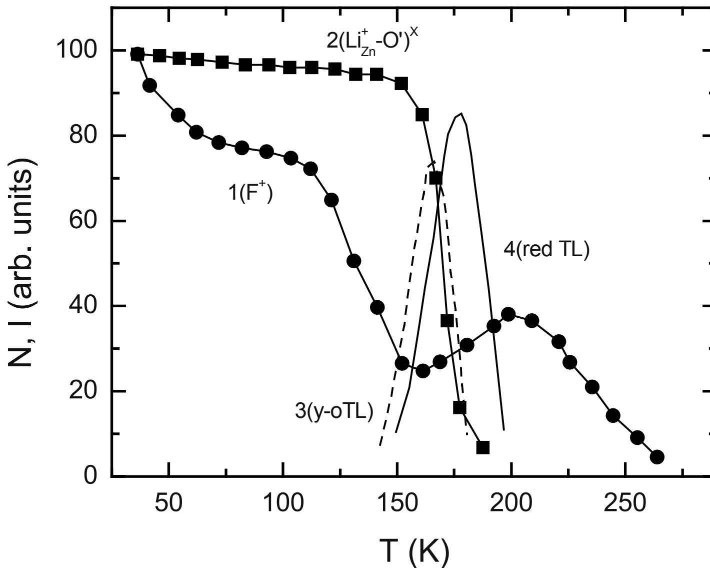

Figure 6. Dependence of the concentration of paramagnetic centers N at T = 30 K (full symbols) and of the intensity of thermoluminescence (curves 3,4) on the temperature of annealing of the ZnO single crystal irradiated with protons (E = 7.7 MeV. T_{dose} 10^{15} protons/cm^2): 1) F^+-centers; 2) paramagnetic states $Li_{Zn}{}^{\times}$; 3 and 4) the intensity of thermoluminescence at $\lambda = 6000$ and 7200 Å (the excitation $hv = 2.6$ eV).

example, $[F_{Mg}]^+$ and $[F_{Li}]^{\times}$ in CaO or $[F_{Cu}]$ in ZnS). The presence of the impurity in the F_A-center is usually confirmed by the hyperfine interaction of the spin moment of the unpaired electron with the magnetic moment of the impurity nucleus, which is fixed in the ZnO-Li crystals irradiated with electrons.[6,7]

The values of the g-factor ($g_{\|} = 1.9951$ and $g_{\perp} = 1.9956$), hyperfine interaction constants, and the electron wave function for F_A-centers in ZnO correlate well with similar parameters for the F_A- and F^+-centers in CaO and ZnS. Here, Li_{Zn} seems to be the impurity in the F_A-center in the crystals we have investigated. This assumption is based on the fact that the investigated hydrothermal single crystals were doped with lithium with a concentration of $N_{Li} \approx 10^{17}$ cm^{-3} during the process of growing. The unpaired electron of the F_A-center interacts with the impurity having nuclear spin J = 3/2, which is also well satisfied for lithium, which in the natural state contains 92.58% of the isotope ^{7}Li with J = 3/2.

In the temperature range 530-660 K in the investigated ZnO crystals, thermally stimulated ionic processes were detected, at the first stage of which (T = 530-630 K) "pure" anionic vacancies disappear and at the second

of which (T = 610-660 K) the F_{Li}-centers also are healed. A similar behavior was observed for the F- and F_{Cu}-centers in ZnS.[7]

The green luminescence is typical for ZnO-Cu.[1-3] An interesting feature of the isovalent impurity of copper in ZnO is that the photoexcitation of a valence electron into the impurity d-shell is accompanied by the formation of a hole which on the hydrogen like large-radius orbit is bound with the impurity atom onto which the electron has gone over. Thus, as a result of the

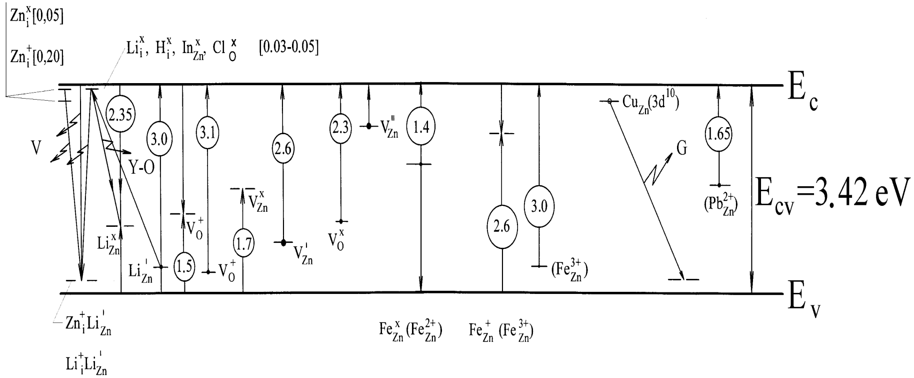

Figure 7. Energy scheme of basic point defects in zinc oxide. The figure shows the energy level position relative to the edge of the conduction and valence band; the optical and thermal depths of the corresponding level are given in parentheses and square brackets, respectively (eV); T = 77 K. Luminescence: violet (V), yellow-range (YO) and green (g). The unbroken line is the energy level occupied with one electron; the dotted line is the energy level of the empty state.

optical transition on the impurity, the exciton - like state of two particles is formed, $3d^{10}(Cu^{+})h$, the so-called «acceptor» exciton, whose formation and breakup leads to the appearance of the characteristic structure of edge absorption (the α, β and γ lines) and of green multi phonon luminescence.[8-10] It should be noted that in recent years the concept of «acceptor» and «donor» excitons bound with the impurities of transition metals in semiconductors has found theoretical and experimental justification for a variety of compounds A_2B_6.

The given model is confirmed by the application of green emission intensity in low voltage cathodoluminescent phosphors, single crystals and ZnO films doped with Cu.[11]

4. CONCLUSION

In conclusion, the simultaneous application of the photo-EPR and luminescence methods is extremely useful for studying the role of point defects in thermo- and photo stimulated electron-hole processes in crystals. As a result of the investigations, the energy position and the microstructure of basic local centers that influence the optical and electro physical properties of zinc oxide have been determined. Fig 7 summarizes our results and interpretations by showing the energy scheme of the defects and the assignments of luminescence transitions. It is shown that when constructing the energy scheme of optical transitions with participation of point defects in ZnO it is necessary to take into account the nonequivalence of the position of occupied and "awaiting" energy levels of the center and also the difference between the optical and thermal energies of the ionization of defects.

ACKNOWLEDGMENT

The author is grateful to K. E. Tarkpea (investigations of EPR), A. Freiberg, I. P. Kuz'mina, S. V. Mukhin and I. V. Pykanov for their help in this work.

REFERENCES

1. W. Hirschwald, P. Banasewicz, L. Ernst, *Curr. Top. Mater. Science.* **7**, 143 (1981).
2. J. P. Kuz`mina, V.A. Nikitenko, *Zinc Oxide. Production and Optical Properties* [in Russian], Moscow (1984).
3. V. A. Nikitenko, *J. Appl. Spectroscopy* , **57**, 783 (1992).
4. D. Zwingel, *J. Luminescence*. **5**, 385 (1972).
5. V. A. Nikitenko, S. V. Mukhin, J. P. Kuz`mina, V. G. Galstyan, S. G. Stoyukhin, *Inorganic Materials*, **31**, 1243 (1995).
6. V. A. Nikitenko, K. E. Tarkpea, I. V. Pykanov, S. G. Stoyukhin, *J. Appl. Spectroscopy*, **68**, 502 (2001).
7. K. Tarkpea, A. Ots, V. A. Nikitenko, *J. Phys. Chem. Sol.* **55**, 1353 (1994).
8. R. Dingle, *Phys. Rev. Lett.* **23**, 579 (1969).
9. D. J. Robbins, S. G. Bishop, J. A. Savage, P. Porteous, *J. Phys. C.* **14**, 2847 (1981).
10. D. J. Robbins, D. C. Herbert, P. J. Dean, *J. Phys. C.* **14**, 2859 (1981).
11. Ya.J. Alivov, M. V. Chukichev, V. A. Nikitenko, *Phys. and Tech. Semiconductors*, **38**, 34 (2004).

Chapter 8

WHISPERING GALLERY MODES IN HEXAGONAL ZINC OXIDE MICRO- AND NANOCRYSTALS

Thomas Nobis, Evgeni M. Kaidashev, Andreas Rahm, Michael Lorenz, and Marius Grundmann
Universität Leipzig, Fakultät für Physik und Geowissenschaften, Institut für Experimentelle Physik II, Linnéstraße 5, D-04103 Leipzig, Germany

Abstract: The resonator properties of zinc oxide (ZnO) micro- and nanocrystals grown by a novel high pressure pulsed laser deposition process have been investigated at room temperature by cathodoluminescence (CL), spatially resolved CL-imaging and polarization resolved micro-photoluminescence (μ-PL) within the visible spectral range. The spectra exhibit a series of comparatively sharp and almost equidistant resonance lines. Using a simple plane wave interference model and taking into account the spectral characteristic $n(\omega)$ of the refractive index of ZnO, we can unambiguously attribute those lines to whispering gallery modes (WGMs) of a two dimensional hexagonal resonator. The predicted resonator diameters agree well with the measured crystal sizes. Tapered, high aspect ratio ZnO nanoneedles furthermore allow systematic investigations of the WGMs as a function of cavity diameter D down to zero. Hence, the transition from a multi-mode to a single mode cavity is directly observed. μ-PL experiments demonstrate that the WGMs are mainly TM polarized.

Key words: Whispering gallery modes, nanostructure, microcrystal, nanocavity, polarization

1. INTRODUCTION

If as mechanical, acoustical, electrical, or optical ones, resonators have always been part and parcel of unique kinds of technical applications. As an integral part of semiconductor lasers, e.g., optical cavities are essential

N.H. Nickel and E. Terukov (eds.),
Zinc Oxide – A Material for Micro- and Optoelectronic Applications, 83–98.
© 2005 *Springer. Printed in the Netherlands.*

home-electronic devices and therefore even entered people's daily life. In the last decades, as a result of miniaturization within the field of electronics and photonics, very small optical resonators strongly gained importance. In this context, an interesting type of resonator is the so called dielectric whispering gallery resonator, e.g. shaped as a microdisc[1-4], microcylinder[5] or microsphere.[6,7] Inside such a resonator, the light wave can be considered to circulate around due to multiple total internal reflection (TIR) at the resonator's boundary. This effect typically leads to high Q-factors and low laser threshold power. In recent years, particularly in the course of analysing and employing wurtzite structured materials, research focussed on hexagonally shaped resonators, and whispering gallery mode (WGM) lasing has been successfully demonstrated also in hexagonal cavities.[8,9]

However, the size of all afore mentioned cavities is typically much larger than the emitted light wavelength λ. Characteristic cavity diameters usually exceed 5 µm. In order to create nano-sized and laterally single mode devices, the prospering branch of nanophotonics requires resonators whose lateral size is at least comparable to or even smaller than λ.

In this paper we present the systematic investigation of WGMs in hexagonal resonators within the micro- *and* nanometer regime for small mode numbers N down to $N = 1$. Single zinc oxide (ZnO) microcrystals and high aspect ratio ZnO nanoneedles have been analysed, together covering the range from $D \approx 3$ µm down to $D = 0$. The needles' tapered cross section furthermore easily allows direct studies of resonator properties in dependence of the cavity diameter. In our measurements, the continuous transition from a multi mode to a single mode cavity is observed. Surprisingly, a simple plane wave interference model without free parameters agrees well with our experimental data for all N.

2. THEORY OF HEXAGONAL WHISPERING GALLERY MODES

2.1 Dielectric resonators

From a general point of view a dielectric resonator is a transparent body of certain shape consisting of a substance with a high refractive index n, usually surrounded by air. Such a structure has the ability to confine light inside, e.g. utilized in any kinds of optical fibers or waveguides. To explain this phenomenon in terms of classical electrodynamics, and any similar problem respectively, it is necessary to solve the tree-dimensional wave

equation for the given geometry. Steady state solutions of this equation are then usually called eigenmodes of the considered resonator.

In the case of a hollow metallic resonator as an example for a so-called *closed* cavity, a discrete set of eigenmodes exists related to a discrete spectrum of eigenmode energies.[10] This is due to the boundary conditions for the electric and magnetic field that lead to a complete suppression of wave propagation outside the resonator. Hence, no energy is radiated from the hollow resonator; the whole radiation field is restricted inside the metallic cavity.

In contrary, a dielectric resonator is an *open* cavity. Because of the continuity conditions for the electric and magnetic field at the cavity's boundary, the radiation field is not exclusively restricted to the resonator itself, but actually extended to infinity. This results in a permanent radiation loss of energy and hence, every imaginable field distribution decays exponentially with a lifetime τ, therefore not representing a steady state solution.[11] The actual solutions of this problem form a continuum of so-called scattering states consisting of an incoming plane wave and an outgoing scattered wave. Therefore, the eigenmodes of a dielectric cavity appear as maxima within the continuous spectrum of the total scattering cross section in dependence of the energy of the incoming wave. Those maxima, i.e. those incoming wave energies that exhibit the strongest interaction with the given resonator, are usually called resonance energies or *resonances* of the dielectric cavity.[11] Due to the above mentioned finite lifetime, all resonances exhibit a finite line width. The larger the losses of a given resonance the shorter is the life time and the larger is the resonance's line width.

2.2 Two-dimensional hexagonal resonator

An important class of dielectric resonators are two-dimensional cavities, i.e. their in-plane dimensions are much larger compared to their height. In this case, wave propagation parallel to the longitudinal axis $\boldsymbol{c}$ is negligible. The light can be assumed to circulate around only within the resonator's cross section. The respective mode patterns are so-called whispering gallery modes (WGMs), obtained by solving the wave equation in its two-dimensional form. Hence, two decoupled types of polarizations occur,[11] namely TE polarized modes ($\boldsymbol{E} \perp \boldsymbol{c}$), and TM polarized modes ($\boldsymbol{E} \parallel \boldsymbol{c}$), as explained in Figs. 1b,c.

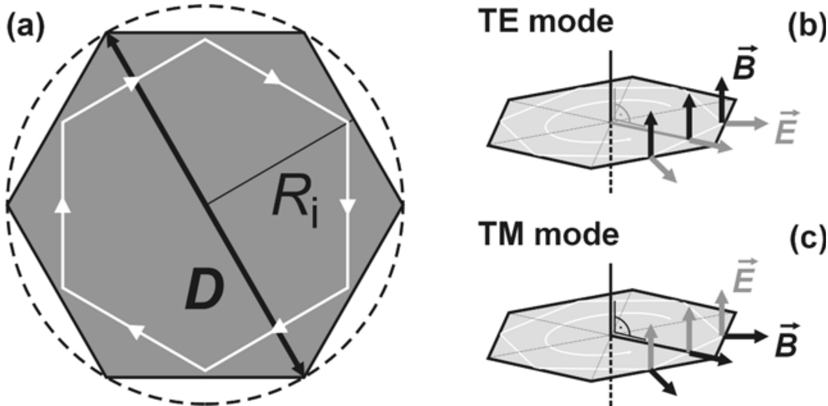

Figure 1. (a) The light confined within a hexagonal cross section can be assumed to circulate inside the cavity as indicated by the white arrows. The geometry of the cavity can be described by the radius of the incircle R_i, by the radius of the circumscribing circle R, or by its related diameter $D = 2R$ using the geometric relation $R = 2R_i/\sqrt{3}$. Note that the circumference of the inscribed white hexagon has a length of $6R_i$. (b), (c) Two possible types of polarization of two-dimensional whispering gallery modes, exemplary given for a hexagonal resonator. For TE modes the electric field is transverse to the longitudinal axis of the resonator, for TM modes the magnetic field is.

Eigenmodes of such two dimensional whispering gallery resonators have been calculated in the past; the solutions for a circular cavity can be expressed in an analytical way.[12] Other kinds of geometries have been subject to present literature, as e.g. deformed circles,[13,14] rectangles[15] or hexagons,[16] that necessarily have to be calculated numerically.[16,17] A scheme of the geometry of the two-dimensional hexagonal cavity is given in Figure 1a.

The results of theoretical modeling show,[16] that the eigenmodes of such a hexagonal cavity can be numbered by an integer mode number N. Additionally, the modes can be distinguished concerning their symmetry, e.g. leading to pairs of degenerated modes N^+ and N^-, related to their respective chirality. In Ref 16, hexagonal WGMs have been calculated for a fixed $n = 1.466$ and in the mode number range of about $N = 20$ to 70.

2.2.1 Plane wave model

For large mode numbers $N > 70$ a simple plane wave model (PWM) has been deduced.[16] Its main idea is, that the light wave circulates around exploiting the process of multiple total internal reflection (TIR, see Fig. 1a) and finally interferes with itself when having completed one full circulation within the resonator. To enforce constructive interference the total phase

shift of the wave along its path has to be an integer multiple of 2π, i.e. only entire wave trains are allowed to perform multiple circulations generating a standing wave. Taking into account the polarization-dependent negative phase shift that occurs during the process of TIR,[10] we obtain the following equation:

$$6\ R_{\mathrm{i}} = \frac{h\ c}{n\ E}\left[N + \frac{6}{\pi}\ \arctan\left(\ \beta\ \sqrt{3\ n^2 - 4}\ \right)\right] \tag{1}$$

The factor β regards polarization, for TM-polarization, $\beta = \beta_{\mathrm{TM}} = n^{-1}$ has to be used; TE-polarization leads to $\beta = \beta_{\mathrm{TE}} = n$. Due to the spectral dependence of the refractive index $n = n(E)$, eq. (1) is an implicit equation to determine the discrete resonance energies $E = E_N\ (R_{\mathrm{i}})$ in terms of the geometric parameter R_{i}, Planck's constant h and vacuum speed of light c. The first factor of the right side of eq. (1) corresponds to the wavelength in matter. The integer $N \geq 1$ characterizes the interference order of the resonance, which is in this case identical with the respective WGM number.[16] The following term containing β refers to the additional phase shift mentioned above. Furthermore, since ZnO is uniaxial, $n = n_{\|}(E)$ and $n = n_{\perp}(E)$ have to be applied for TM- and TE-polarisation, respectively. We note that eq. (1) for TM-polarisation and n = const. is identical with eq. (17) of Ref. 16. Neglecting the spectral dependency of n, eq. (1) leads to

$$E_N \propto \frac{1}{R_{\mathrm{i}}} \tag{2}$$

and thus, WGMs generally shift to higher energies with decreasing cavity diameter. Note that, although TIR suggests no way for the light to leave the resonator, emission nevertheless occurs at the corners of the hexagon.[16] After all, radiation losses are always allowed due to the reasons given in part 2.1. Therefore it is possible to optically detect WGMs. Since the geometrical model leading to eq. (1) is a combination of basic ray and plane wave optics, it is expected to be valid only for $R >> \lambda$, i.e. for $N >> 1$.[16] Anyhow, we show in this work, that eq. (1) describes the experimentally found WGMs even down to mode number $N = 1$.

3. EXPERIMENTAL DETECTION OF HEXAGONAL WHISPERING GALLERY MODES

3.1 Sample properties

3.1.1 Growth

As a model system for the investigation of hexagonal cavities we use zinc oxide micro- and nanocrystals naturally exhibiting a hexagonal cross section due to their wurtzite structure. Those crystals have been grown self-assembled on *a*-plane sapphire substrates by high pressure pulsed laser deposition (PLD) utilizing a gold assisted growth mechanism similar to Morales and Lieber.[18] For this purpose the substrates have been sputtered partially or fully by a few nanometer thin gold film. When heating up to the growth temperature of about 870°C to 950°C the gold is melting and subdividing into small clusters that provide the seed for columnar nanocrystal-growth. Within the PLD chamber a KrF excimer laser is used to evaporate the ZnO target, and argon acts as transport gas, set under a background pressure ranging from about 1 mbar to 100 mbar. More detailed information about this technique will be published elsewhere.[19] Depending on the respective growth conditions the PLD process provides a variety of differently shaped ZnO micro- and nanocrystals shown in Figure 2.

3.1.2 Luminescence

ZnO is a direct semiconductor with a band gap of about 3.4 eV at room temperature. Its room temperature luminescence typically consists of two bands, the first (UV) around 3.25 eV, the second (visible, VIS) around 2.35 eV. The UV band is associated with free-exciton emission. The latter is also called “green band” in the literature; its exact nature, involving deep levels, is still under debate. Since the luminescence of our PLD grown micro- and nanocrystals is dominated by VIS emission, and furthermore since VIS emission provides a bright and broad-band light source, it can easily be utilized in cathodoluminescence (CL) experiments to excite the micro- or nanocavities. Within the VIS range ZnO is optically transparent and exhibits a refractive index of $n \approx 2$,[20] i.e. ZnO micro- and nanocrystals represent an interesting system to investigate resonator properties in a wide spectral range.

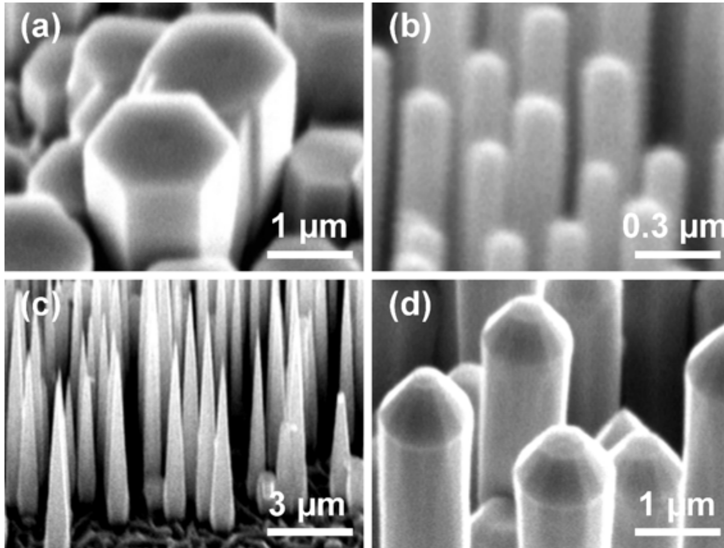

Figure 2. Different shapes of PLD grown ZnO micro- and nanocrystals. (a) Hexagonal microcrystals with diameters of about 2 µm. (b) ZnO nanowires with diameters around 100 nm. (c) Needle like nanostructures. (d) Microcrystals exhibiting a dodecagonal cross section.

3.2 Whispering Gallery Modes in hexagonal ZnO microcrystals

3.2.1 Detection of Whispering Gallery Modes

Figure 3 shows a typical VIS emission CL spectrum from a ZnO microcrystal. An electron microscopy image of the crystal is given in the inset. In comparison to the broad and unstructured VIS emission of thin films or bulk material, VIS emission of the microcrystal is accompanied by a series of comparatively sharp peaks.

Using the PWM, those peaks can unambiguously be attributed to WGMs of a hexagonal cavity. Therefore it is necessary to determine the correct mode number N of every single detected peak. Provided that this mode number is known, eq. (1) enables to calculate the theoretical diameter of the crystal $D = 4R_i/\sqrt{3}$ out of every single detected peak energy. Fortunately, since the peaks have to be numbered in ascending order, one only has to find the correct mode number to start. The best fitting and therefore the final peak numbering is found, if every single peak predicts *the same* radius as all the

other resonance peaks, or at least if the variations in the predicted radius become smallest. This procedure is explained more detailed in Fig. 4.

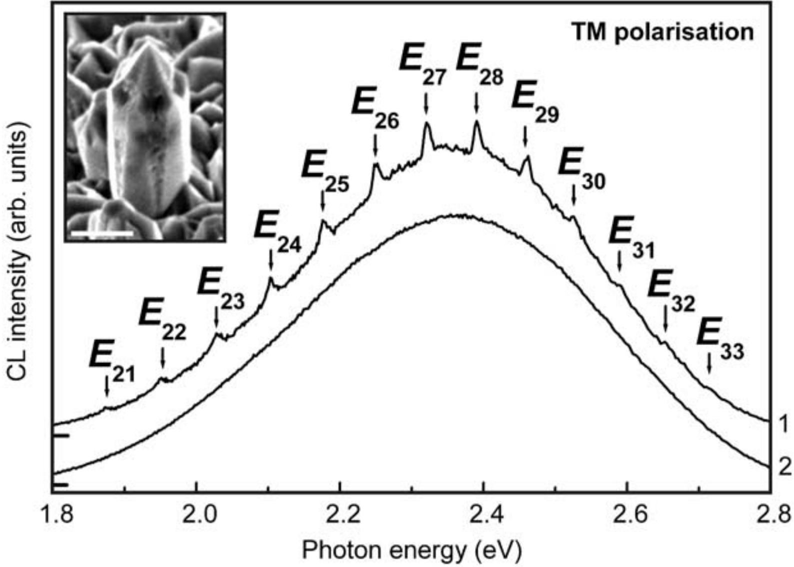

Figure 3. Room temperature VIS emission CL spectra of a ZnO microcrystal (curve 1) and of thin film material (curve 2) scaled to the same intensity and vertically shifted for clarity. Arrows mark theoretical energetic positions of WGMs due to eq. (1) for TM polarization and $D = 2.86$ μm. The inset shows a SEM image of the investigated microcrystal. The scalebar has a length of 2 μm. The experimental cavity diameter is $D_{\text{exp}} = (2.90 \pm 0.06)$ μm.

3.2.2 Theory vs. Experiment

For the investigated crystal, the correct mode numbering is shown also in Fig. 3, the respective theoretical diameter yields to $D_{\text{theory}} = 2.86$ μm with a small minimum-maximum spreading of less than 10 nm. Although theory predicts both TM and TE polarization, all calculations have been performed for TM type, since polarization-dependent micro-photoluminescence experiments showed, that WGMs are preferentially TM polarized (see Figure 7 below). The required data for $n_{\|}(E)$ were obtained from ellipsometry measurements on PLD grown ZnO thin film samples.[20]

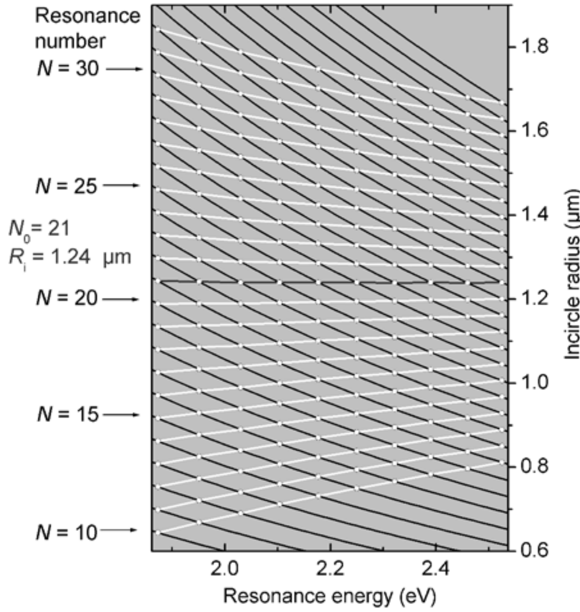

Figure 4. Diagram $R_\mathrm{i}(E)$ to determine the correct mode numbering for the spectrum of Figure 3. Equation (1) enables to calculate the radius of the cavity-incircle $R_\mathrm{i}=R_\mathrm{i}(E,N)$ out of a given resonance number N and resonance energy E. The resulting set of curves is given here for N = 10…41 as a set of black lines approximately exhibiting a hyperbolic shape (as expected from eq. 2). The index of the curves, i.e. the respective resonance number, is shown on the left side of the scheme marked by black arrows. The experimentally detected resonance energies are given as white circles. Since the resonances have to be numbered in ascending order, every white line represents a possible peak numbering. As can be seen from the diagram there exists only one peak numbering that results in an energy-independent incirlce radius, denoted by the horizontal line. Hence, the starting number for the peak numbering of the spectrum in Figure 3 yields to N_0=21 with R_i = 1.24 µm, this leads to a respective cavity diameter D=2.86 µm.

The experimentally determined cavity diameter obtained from electron microscopy amounts to D_exp = (2.90 ± 0.06) µm. Hence, the deviations between theory and experiment are in the range of only 2%! This means, that the simple PWM fits very well, even if N is in the range of only 20 to 30. To emphasize this fact, the theoretical values E_N calculated for fixed diameter $D = D_\mathrm{theory}$ are given as black arrows in Figure 3; they appear very close to the measured peaks. We note, that if $n \neq n(E)$ = const. is used, the agreement between theory and experiment becomes worse.

3.3 Whispering Gallery Modes in ZnO nanostructures

Although the simple PWM obviously is valid for WGMs with mode numbers in the range of about $N = 20\ldots30$, i.e. for optical cavities in the micrometer regime, it does not necessarily need to be valid for nanostructures. Furthermore, prism-shaped microcrystals only enable analysis of WGMs for fixed cavity diameter given by the cross section of the particular microcolumn. Those restrictions can be vanquished by focusing on nanostructures with a *needle-like* shape.

3.3.1 ZnO nanoneedles

An example of an array of PLD-grown ZnO nanoneedles is shown in Figure 5a. As can be seen in Figs. 5b-d, the width of the hexagonal cross section of a selected needle is continuously tapered when approaching the needle's top. Since the aspect ratio of this structure is very high, every plane perpendicular to the needle's longitudinal axis creates a hexagonal cavity and actually, those structures allow for systematic investigations of WGMs in the nanometer regime from $D = 800$ nm down to $D = 0$!

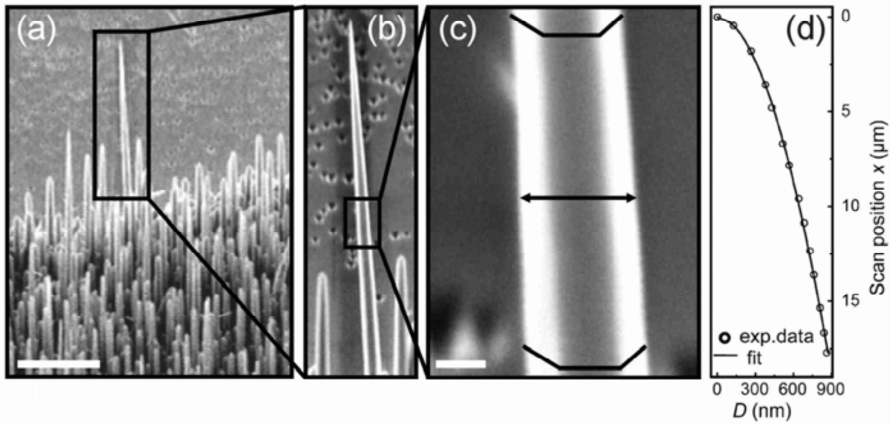

Figure 5. SEM image of the investigated nanoneedle. All images have been obtained at 45° perspective. (a) SEM image of an array of ZnO nanoneedles containing the reported one marked by a black rectangle. The scale bar has a length of 10 µm. (b) Larger scale SEM image of the investigated nanoneedle. The needle's diameter is continuously tapered approaching zero at the top. (c) High resolution SEM image indicating the hexagonal cross section of the needle. The scale bar has a length of 300 nm. (d) Experimentally determined shape of the needle. The obtained characteristic of the diameter D vs. scan position x can be fitted using a potential law $D \propto x^{0.523 \pm 0.007}$, leading to a square root like shape of the needle.

3.3.2 Detection

For this purpose, we performed spatially resolved CL experiments,[21,22] i.e., point wise CL spectra have been recorded across the whole needle using a scan grid of 16 × 150 points. Typical spectra and their interpretation are given in Fig. 6. As in the case of microcrystals, the broad VIS band of luminescence again is modulated due to a preferred constructive interference of light whose photon energy again fulfills the resonance condition of eq. (1). For decreasing diameter, approaching the top of the needle, these maxima continuously shift to higher energies. This effect supplies the unambiguous proof that the measured spectral modulation actually originates from WGMs. When the dominating WGM with number N is blue shifted so far that it leaves the VIS range, the next lower resonance N-1 occurs at lower energies indicated by a *discontinuous* red shift of the spectral maximum in Fig. 6c and 6d. This process continues until $N = 1$ is reached referring to the last resonance that can be observed.

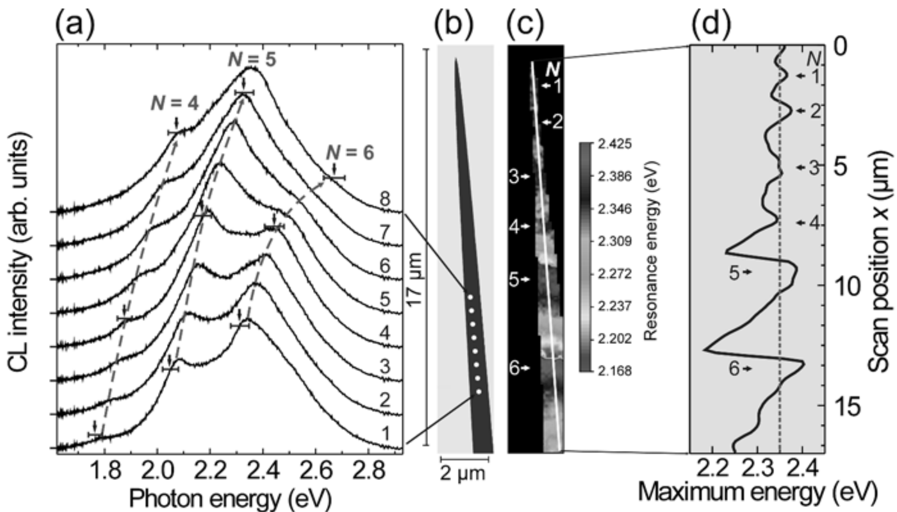

Figure 6. Spatially resolved CL investigation of a single tapered ZnO nanoneedle. (a) CL spectra shifted vertically for clarity collected at 8 equidistant locations marked on the needle's longitudinal axis by white dots in Fig. 6b. The VIS band of ZnO is modulated such that maxima can clearly be distinguished from each other and attributed to WGMs labelled according to eq. (1). Since the radius of the needle decreases along the longitudinal axis, the spectral maxima continuously shift to higher energies as indicated by the red dashed lines. Blue arrows and error bars mark selected TM resonance energies obtained from eq. (1) and their error. (b) Experimentally determined shape of the needle. (c) Map of the energy of the spectral maximum within the visible spectral range. (d) Line scan along the white line shown in Fig. 6c. The red dashed line gives the maximum position of the unstructured VIS band in bulk material.

3.3.3 Polarization

To obtain essential information about the state of polarization of the detected WGMs we performed local polarization-dependent micro-photoluminescence experiments. These show that the WGMs are preferentially TM polarized, since detecting TE polarization causes an almost complete suppression of WGM modulations (see Fig. 7). The remaining spectrally unstructured emission occurs due to the unpolarized character of ZnO photoluminescence originating from the needle's center. However, this result is consistent with former investigations of lasing in hexagonal cavities within the micrometer regime that are reported to only emit TM modes.[8] Hence, in comparison to TE modes, TM modes obviously exhibit lower losses. This can be generally understood since, leaving the regime of TIR, the reflection coefficient for TM polarized waves due to Fresnel's equations is always larger than that for TE polarized ones.

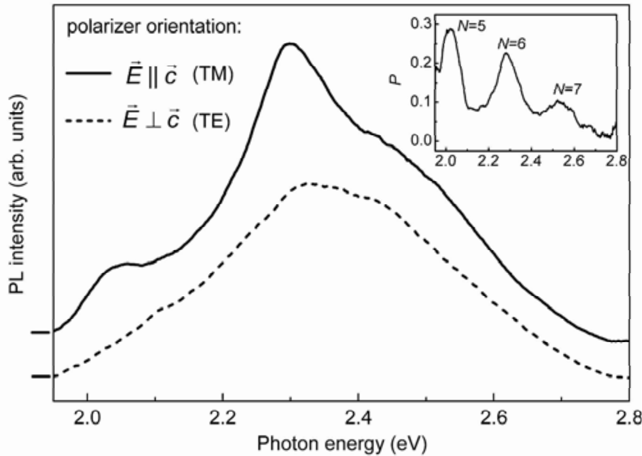

Figure 7. Micro-photoluminescence spectra of the nanoneedle of Fig. 5 for $D \approx 790$ nm at two different polarizer azimuth orientations shifted vertically for clarity. The modulation of the VIS band almost disappears when detecting the TE mode. Thus, the resonances are mainly TM polarized. The inset shows the ratio $P = (I_{TM} - I_{TE}) / (I_{TM} + I_{TE})$, that visualizes the TM-WGMs as distinguishable peaks. The polarization effect has been found to be independent of the polarization of excitation.

3.3.4 Theory vs. Experiment

To compare the measured energies of the WGMs in nanostructures with theoretically predicted ones for both types of polarization, a spectral line

scan along the needle's longitudinal axis is given in Fig. 8. In grey scales, the resonances appear as a set of bright lines, that actually exhibit a curvature as expected from eq. (2). The theoretical values are shown with dots and cross symbols in Fig. 8. They are directly calculated without free parameter using the experimentally determined shape of the needle, i.e. $R_i(x)$, see Fig. 5, and the above mentioned thin-film data for $n_{\|}(E)$ and $n_{\perp}(E)$.[20] The dots (TM) match the measured resonance energies with a very good agreement. Additionally, the well fitting blue arrows within Fig. 6a confirm, that the simple PWM gives a good description of the basic physics of WGMs even in nano-sized crystal geometries within the limits of the resonance line widths.

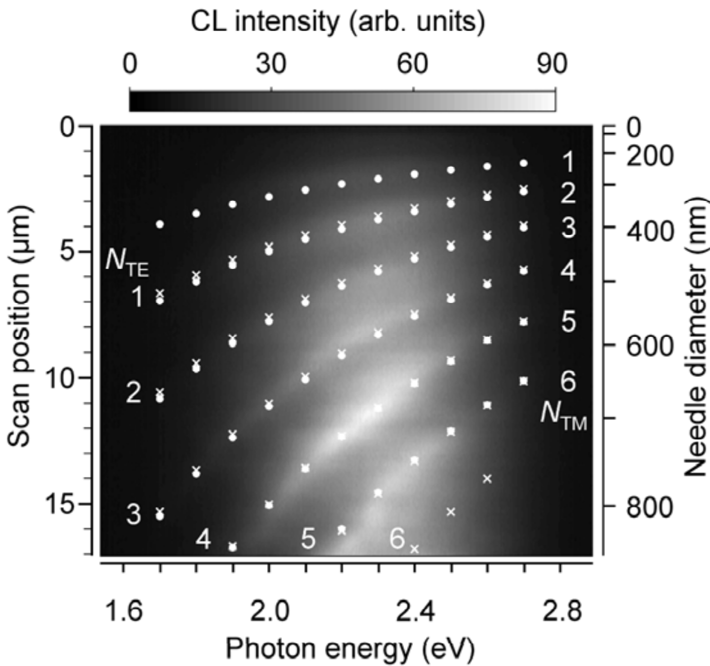

Figure 8. Two dimensional plot of spectra recorded along a line scan on the needle's longitudinal axis. The left vertical axis shows the line scan position x, the right one refers to the respective needle diameter D. The grey scales refer to the spectral CL-intensity. The spectral maxima, i.e. the measured WGM energies, appear as bright belts going from the bottom left corner to the right upper one. With decreasing diameter all resonances shift systematically to higher energies. The white dots give theoretical TM-resonance energy positions obtained from eq. (1), white crosses give the same for TE-polarisation. Without adjusting free parameters there is a very good agreement between experiment and theory.

3.3.5 Line broadening effects

As shown in Figure 6, compared to microcavities, nano-sized crystals show broadened WGMs due to the increase of losses with decreasing cavity diameter. Nevertheless, CLI of the broad VIS band still enables the visualization of WGMs in the ZnO nanoneedle even at diameters $D < \lambda/n \cong 270$ nm. For mode numbers $N \geq 4$ single TM-WGMs can be detected unambiguously as distinguishable maxima modulating the broad VIS band. For smaller mode numbers $N \leq 3$ WGMs can only be visualized as a continuous blue shift of the intrinsic VIS maximum, and the discontinuities in Fig. 6c and 6d become smooth. This is due to the extreme line broadening of both types of WGMs with decreasing cavity diameter. Theory[16] predicts line broadening by loss processes due to boundary waves that are scattered out of the resonator and due to light paths whose angle of incidence is slightly deviating from 60°. A relation $FWHM \propto E^{-1} R^{-2}$ is obtained, that explains the dramatic broadening of the measured resonances. For TM polarization and $N = 6$ (spectrum 1 of Fig. 6a) a *FWHM* of about 350 meV is predicted. Considering that the underlying theory again is prepared for $N \gg 1$, the obtained spectrum verifies this value within the limits of resolution. For resonance $N = 3$ the theoretical *FWHM* is about 900 meV, which exceeds even the intrinsic line width of the VIS band. This explains the difficulty to obtain distinct WGM peaks for $N \leq 3$. Nevertheless, VIS emission is still affected when a WGM crosses the VIS range, as Fig. 8 clearly shows intensity modulations at the respective line scan positions. We note that losses due to surface roughness of the cavity faces could also lead to line broadening. However, as the high resolution SEM image of Fig. 5c shows well shaped resonator faces, we do not adopt this loss process to be the dominating one.

3.3.6 Discussion

As mentioned above, there is an energy difference between predicted TM- and TE-modes. This difference is mostly due to β in eq. (1), since the ZnO birefringence $(n_{\parallel} - n_{\perp})/(n_{\parallel} + n_{\perp}) \approx 1.2\%$ is small.[20] However, TE-mode with mode number N is predicted (coincidentally, due to the particular value of n) to appear very close to the spectral position of TM-mode N+1 (Fig. 8), and hence, this could be one reason for the missing TE mode series. Possible TE-WGM maxima should always lie beyond higher ordered TM maxima, and as the former ones suffer larger losses, they lead to much broader resonance peaks hardly detectable in the VIS band.

Certainly there are, however, small deviations between the detected peak energies and the predicted TM-WGMs according to eq. (1). (See Figs. 6a

and 8.) These deviations probably reveal the limits of the simple PWM. To discuss this fact more in detail we note, that the application of numerical methods to predict resonance energies at the end always depends on a precise determination of the considered geometry, e.g. R_i, and a good knowledge of the refractive index n. SE microscopy measurements of the cavity diameter D is performed with an error of at least 1%. The ellipsometrically determined values for $n_{||}$ for bulk material yield an error in n of about 2%. The actual refractive index of the nanocrystals may possibly differ additionally. These effects lead to an error in E of about 3%, i.e. 50 - 80 meV in the considered spectral range, which is indicated as error bars in Fig. 6a. Compared to the line widths of the WGMs, eq. (1) for TM polarization gives a very good description of the spectral position of the resonant modes.

4. CONCLUSION

In conclusion we investigated the resonant optical behavior of ZnO micro- and nanocrystals, giving detailed insight into optical whispering gallery modes within the micro *and* nanometer regime. In particular, for the first time we analyzed hexagonal WGMs in nanocavities for mode numbers in the range from $N = 1$ to $N = 6$. The energy shift and broadening of the modes for cavity diameter decreasing to zero is well described without free parameter by eq. (1) from a plane wave model.

ACKNOWLEDGMENTS

This work was supported by the Deutsche Forschungsgemeinschaft within FOR 522 (Project Gr 1011/12-1).

REFERENCES

1. S.L. McCall, A.F.J. Levi, R.E. Slusher, S.J.Pearton, and R.A. Logan, *Appl. Phys. Lett.* **60**, 289 (1992).
2. S. Chang, N.B. Rex, R.K. Chang, G. Chong, and L.J. Guido, *Appl. Phys. Lett.* **75**, 166 (1999).
3. K.J. Luo, J.Y. Xu, H. Cao, Y. Ma, S.H. Chang, S.T. Ho, and G.S. Solomon, *Appl. Phys. Lett.* **77**, 2304 (2000).
4. X. Liu, W. Fang, Y. Huang, X.H. Wu, S.T. Ho, H. Cao, and R.P.H. Chang, *Appl. Phys. Lett.* **84**, 2488 (2004).

5. A.F.J. Levi, R.E. Slusher, S.L. McCall, S.J. Pearton, and W.S. Hobson, *Appl. Phys. Lett.* **62**, 2021 (1993).
6. S.M. Spillane, T.J. Kippenberg, and K.J. Vahala, *Nature* **415**, 621 (2002).
7. M. V. Artemyev, U. Woggon, R. Wannemacher, *Appl. Phys. Lett.* **78**, 1032 (2001).
8. I. Braun, G. Ihlein, F. Laeri, J.U. Nöckel, G. Schulz-Ekloff, F. Schüth, U. Vietze, Ö. Weiss, and D. Wöhrle, *Appl. Phys. B* **70**, 335 (2000).
9. U. Vietze, O. Krauß, F. Laeri, G. Ihlein, F. Schüth, B. Limburg, and M. Abraham, *Phys. Rev. Lett.* **81**, 4628 (1998).
10. J. D. Jackson, *Classical electrodynamics* (Wiley, New York, 1999).
11. J.U. Nöckel, "2-d Microcavities: Theory and Experiments", in *Cavity-Enhanced Spectroscopies,* edited by R.D. van Zee and J.P.Looney, (Academic Press, San Diego, 2002) pp. 185-226.
12. N.S. Kapany and J.J. Burke, "*Optical Waveguides*", (Academic Press, New York, 1972)
13. S.-B. Lee, J.H. Lee, J.S. Chang, H.J. Moon, S.W. Kim, and K. An, *Phys. Rev. Lett* **88**, 033903 (2002).
14. C. Gmachl, F. Capasso, E.E. Narimanov, J.U. Nöckel, A.D. Stone, J. Faist, D.L. Sivco, and A.Y. Cho, *Science* **280**, 1556 (1998).
15. M.Lohmeyer, *Opt. Quant. Electron.* **34**, 541 (2002).
16. J. Wiersig, *Phys. Rev. A* **67**, 023807 (2003).
17. J. Wiersig, *J. Opt. A.* **5**, 53 (2003).
18. A. M. Morales and C. M. Lieber, *Science* **279**, 208 (1998).
19. M. Lorenz *et al.*, *unpublished.*
20. R. Schmidt, B. Rheinländer, M. Schubert, D. Spemann, T. Butz, J. Lenzner, E.M. Kaidashev, M. Lorenz, A. Rahm, H.C. Semmelhack, and M. Grundmann, *Appl. Phys. Lett.* **82**, 2260 (2003).
21. J. Christen, M. Grundmann, and D. Bimberg, *J. Vac. Sci. Technol. B* **4**, 2358 (1991).
22. Th. Nobis, E.M. Kaidashev, A. Rahm, M. Lorenz, J. Lenzner, and Marius Grundmann, *Nano Lett.* **4**, 797 (2004).

Chapter 9

PROPERTIES OF DISLOCATIONS IN EPITAXIAL ZnO LAYERS ANALYZED BY TRANSMISSION ELECTRON MICROSCOPY

E. Müller[1], D. Livinov[1], D. Gerthsen[1], C. Kirchner[2], A. Waag[3], N. Oleynik[4], A. Dadgar[4], and A. Krost[4]

[1]Laboratorium für Elektronenmikroskopie, Universität Karlsruhe (TH), 76128 Karlsruhe, Germany; [2]Abteilung Halbleiterphysik, Universität Ulm, Albert-Einstein Allee 45, 89081 Ulm, Germany; [3]Institut für Halbleitertechnik, Universität Braunschweig, Hans-Sommer-Straße 66, 38106 Braunschweig, Germany; [4]Otto von Guericke Universität Magdeburg, FNW-IEP, Postbox 4120, 39016 Magdeburg, Germany

Abstract: The dislocation configuration in epitaxial ZnO layers grown by metal organic vapor phase epitaxy (MOVPE) was analyzed by transmission electron microscopy. Misfit dislocations and the majority of threading dislocations are characterized by Burgers vectors of the type 1/3 <11-20>. First results on the electrical activity of dislocations are presented which are obtained by electron holography in a transmission electron microscope. The evaluation of the phase change of the electron wave in the vicinity of a dislocation yields a negative line charge of approximately 3 e/nm.

Key words: Metal organic vapor phase epitaxy (MOVPE), dislocations, electrical activity of dislocations, transmission electron microscopy, electron holography

1. INTRODUCTION

ZnO was rediscovered some years ago as a promising material for optoelectronic devices because ZnO could be grown epitaxially at that time by metal organic vapor phase epitaxy (MOVPE) and molecular beam epitaxy (MBE). Although significant progress has been achieved in improving the structural quality of epitaxial ZnO layers, the defect density has to be further reduced before the fabrication of optoelectronic devices becomes feasible. Apart from point defects, which determine the electrical properties of the material, high concentrations of extended defects like

N.H. Nickel and E. Terukov (eds.),
Zinc Oxide – A Material for Micro- and Optoelectronic Applications, 99–111.
© 2005 *Springer. Printed in the Netherlands.*

dislocations and stacking faults are present which are known to be detrimental for light-emitting devices. It is therefore of considerable interest to study the configuration of extended defects in ZnO epilayers and correlate the microstructure with the growth procedure. For this purpose, transmission electron microscopy (TEM) has proven to be a suitable technique because it allows the analysis of extended defects down to the atomic scale. Despite the strongly increasing activity in epitaxial ZnO growth, only few TEM studies have been devoted to a detailed study of the defect structure in ZnO. Narayan et al. (1998) have analyzed defects in ZnO deposited by pulsed layer deposition on (0001)Al_2O_3. The defect structure in MBE-grown ZnO layers was studied by Hong et al. (2000) and Vigué et al. (2001). For ZnO deposited directly on Al_2O_3(0001) substrates, a 30° rotation of the in-plane orientation was observed independent of the growth technique, which reduces the lattice-parameter mismatch from 32 % to 15 %.

The possible influence of dislocations on the overall electrical properties of epilayers was recognized recently when electron holography in a transmission electron microscope was used to reveal the electrical activity of edge dislocations in epitaxial GaN layers (Cherns and Jiao, 2001). It is known already for a long time that the electrical activity of dislocations can be described by electronic states in a partially filled band acting as donors or acceptors depending on the position of the Fermi energy with respect to the occupation limit of the dislocation band (see review of Alexander and Teichler, 1991). If present at a high density, dislocations – in particular charged dislocations - act as scattering centers which strongly reduces the charge carrier mobility (Gerthsen, 1986). In addition, the charge carrier concentration can be modified by several orders of magnitude. In a review by Ossip'yan et al. (1986), the electronic properties of dislocations in several II-VI semiconductors are summarized and a negative line charge of 1.5 e/nm was assigned to 60° Zn(glide) dislocations on the basal plane of n-ZnO.

The present study is focused on dislocations in ZnO epilayers grown by MOVPE. The distribution of edge, mixed and screw dislocations was analyzed for layers grown under different MOVPE conditions using TEM. Electron holography was applied to study the electrical activity of threading dislocations.

2. EXPERIMENTAL TECHNIQUES

The TEM investigations were performed in a 200 keV Philips CM 200 FEG/ST microscope which is equipped with a field emission gun. Dislocation Burgers vectors **b** were analyzed on the basis of the **b g** = 0 extinction criterion using different imaging vectors **g**. The weak-beam

technique was applied to improve the resolution compared to conventional bright-field and dark-field images (see e.g. Williams and Carter, 1996). Cross-section samples along the <11-20>- and <1-100>-zone axes were prepared applying the technique described by Strecker et al. (1993) using 3.5 keV Xe^+ ions for the final ion milling to minimize radiation damage with an ion current of 1 mA and an incidence angle of 14 degrees.

For electron holography, the microscope is equipped with a Möllenstedt biprism, which is installed in the selected-area aperture holder. The electrostatic potential of the biprism was set at approximately 180 V leading to an interference fringe distance of 0.2 nm. Holograms were obtained by orienting a straight dislocation line parallel to the biprism whereas the reference wave is transmitted through the undisturbed crystal on the other side of the biprism. The reconstruction procedure for the amplitude and phase of the electron wave is outlined in detail by Lehmann and Lichte (2002).

All investigated samples were grown by MOVPE on Al_2O_3(0001) substrates. Details of the growth procedure can be found in context with the analyzed samples in chapter 3.

3. DISLOCATIONS IN EPITAXIAL ZnO LAYERS

3.1 Structural and morphological properties

Dislocations are characterized by a Burgers vector and line direction, which determine the dislocation type. Perfect dislocations in hexagonal crystals have Burgers vectors $\mathbf{b_a}$=1/3<11-20>, $\mathbf{b_c}$=[0001] and $\mathbf{b_{a+c}}$=1/3<11-23> (Hull, 1975). Misfit dislocations are generated at the interface between the substrate and epitaxial layers, if they are grown on a substrate with a different lattice parameter. The density of misfit dislocations depends on the lattice-parameter mismatch and - during the early stages of the growth – on the layer thickness. The threading dislocation density is correlated with the density of misfit dislocations but can be minimized by optimizing the epitaxial growth.

Figure 1 shows cross-section TEM images of a MOVPE-grown ZnO layer on Al_2O_3(0001) with a 40 nm GaN buffer layer deposited prior to the ZnO growth. Isopropanol and Diethylzinc were used as precursors for the ZnO deposition with a VI/II-flux ratio of 36 at total reactor pressure of 400 mbar and hydrogen as a carrier gas. The substrate temperature was 380 ^{o}C.

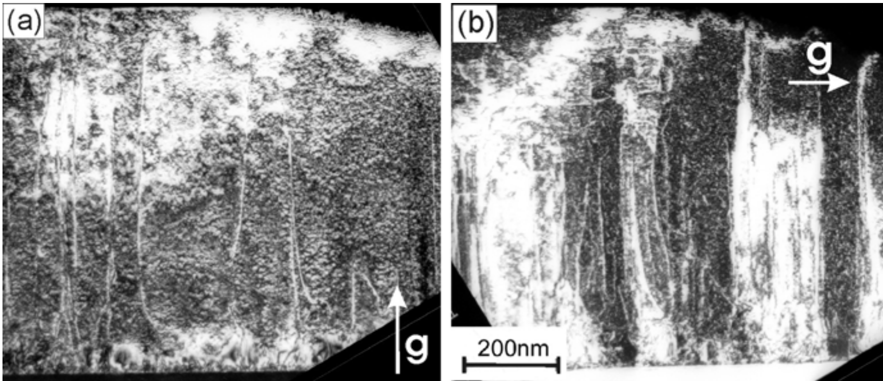

Figure 1. Cross-section weak-beam images of the same area of a MOVPE-grown ZnO layer on Al_2O_3(0001) with a 40 nm GaN buffer layer taken with (a) g = {0002} under g,3g conditions and (b) g = {11-20} under g,3g conditions.

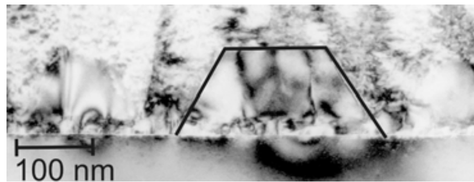

Figure 2. Bright-field image of the interface between the GaN/Al_2O_3(0001) interface and the ZnO layer taken with g = {11-20}. The black line marks a GaN island.

Threading dislocations extend typically along the [0001] direction in epilayers with a hexagonal crystal structure, which has been also observed for MBE-grown ZnO epilayers (Hong et al., 2000). One possible origin of this preferred line direction was attributed to the fact that the dislocations form small angle grain boundaries between columnar grains (Vigué et al., 2001) slightly twisted around the [0001] direction which is visible in Fig.1(b) by contrast variations in the ZnO layer. Figure 1(a) was taken with **g** = {0002} where edge dislocations with $\mathbf{b}_a$ = 1/3<11-20> do not show any contrast. The contrast of screw dislocation is extinct in Fig. 1(b) taken with **g** = {1-100}. It is obvious from Fig. 1, that the majority of dislocations exhibit edge-type character while the density of dislocations with $\mathbf{b}_c$ and $\mathbf{b}_{a+c}$ is relatively low.

Imaging the interface region (Fig.2) shows, that the GaN buffer layer consists of relatively large islands (a GaN island is indicated by the black line in Fig.2), which could contribute to the mosaicity of the ZnO film.

The threading dislocation configuration depends significantly on the buffer layer morphology and growth procedure, which can be inferred from Fig. 3. This ZnO film was grown on a thick GaN buffer layer using a procedure outlined in detail by Dadgar et al. (2004). A high-temperature annealing treatment was applied after the buffer layer growth and again after the deposition of the ZnO. Due to the thick GaN buffer layer, the mismatch between the Al_2O_3(0001) and ZnO is reduced from 15 % to 1.8 % which is accompanied by a reduction of the threading dislocation density. It is remarkable that the threading dislocations in the GaN buffer layer do not continue in the ZnO film but annihilate at the ZnO/GaN interface. The dislocation lines in the ZnO deviate frequently from the [0001] direction indicating a low degree of mosaicity, which is supported by the homogeneous contrast of the ZnO layer. The extinction of the dislocation contrast in Fig.2(a,b) shows that the majority of the dislocations is characterized by Burgers vectors of the type $\mathbf{b_a}$=1/3<11-20> as in the layer shown in Fig.1. However, different dislocation types are the result of the random dislocation line orientations.

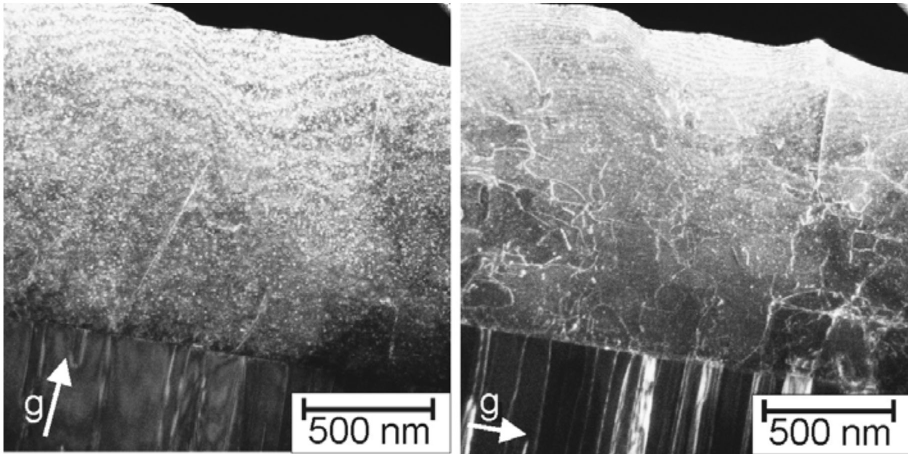

Figure 3. Cross-section weak-beam images of the same area of a MOPVE-grown ZnO layer on Al_2O_3(0001) with a thick GaN buffer layer taken with (a) g = {0002} and (b) g = (11-20) taken under g,3g conditions.

The large fraction of threading dislocations with $\mathbf{b_a}$ can be understood by analyzing the misfit dislocations at the interface between the buffer layer and the ZnO film. Figure 4(a) displays a <11-20> zone-axis high-resolution TEM (HRTEM) image of the interface of the sample depicted in Fig.3. The {1-100} Fourier-filtered image Fig.3(b) shows that the misfit dislocations

are characterized by one {1-100} plane inserted from below as expected due to the larger a lattice parameter of the ZnO.

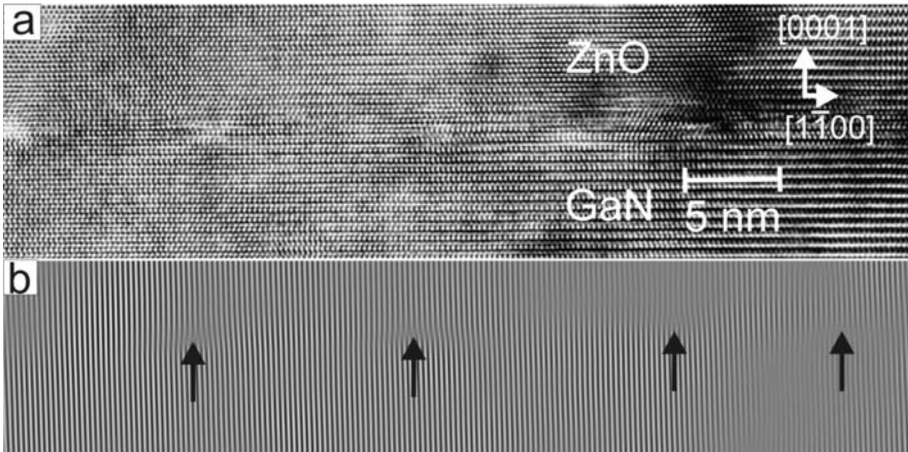

Figure 4. (a) HRTEM image of the interface between the GaN buffer layer and ZnO along the <11-20>-zone axis and (b) Fourier-filtered image showing only {1-100} lattice fringes. The arrows indicate {1-100} fringes inserted from the substrate side.

Figure 5 shows schematically the misfit dislocation orientation and possible Burgers vectors (grey vectors). The electron-beam direction and dislocation lines are aligned parallel to the [11-20] direction. 60° or 120° misfit dislocations are characterized by $\mathbf{b_a}$ = 1/3 [-12-10] and 1/3 [-2110]. The edge component $\mathbf{b_e}$ = ½ [1-100] is compatible with an inserted (1-100) plane as observed in Fig.4(b). It can assumed that three set of misfit dislocations along the three <11-20> directions are present in the (0001) interface plane.

The generation of misfit dislocations with $\mathbf{b_a}$ can be understood by considering the efficiency of the different possible Burgers vectors to relax the lattice-parameter mismatch. Dislocations with $\mathbf{b_a}$ are most efficient because they are characterized by the longest Burgers vector edge component $\mathbf{b_e}$ in the (0001) interface plane among all possible dislocation Burgers vectors. In addition, the strain energy of dislocations is ~ b^2 which favors the formation of dislocations with the shortest overall Burgers vector $\mathbf{b_a}$. Since dislocations cannot end inside a perfect crystal and the Burgers vector is conserved along the dislocation line, the threading segments of misfit dislocations are also characterized by $\mathbf{b_a}$ as observed is Fig.1 and Fig.3. The above analysis suggests that improving the structural quality of the interface and using a thick GaN buffer layer should minimize threading dislocations with Burgers vectors of the type 1/3 <11-20>.

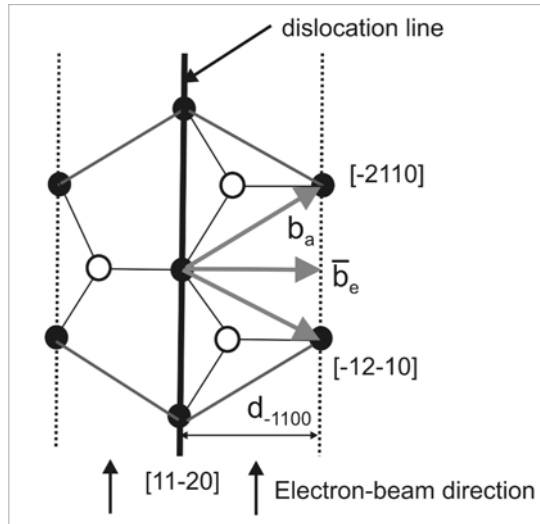

Figure 5. Schematic representation of the orientation of a misfit dislocation (bold black line) and possible Burgers vectors (grey vectors) in the (0001) interface plane

3.2 Electrical activity of dislocations

Due to the strong disturbance of the translational symmetry of the crystal, dislocations with an edge component are expected to generate deep electronic states in the energy gap of a semiconductor. If the Fermi level does not coincide with the occupation limit of the band of electronic states the dislocation will be charged. To maintain the overall neutrality of the material, a charged dislocation is required to be shielded by a space charge region of opposite sign. The resulting potential V at a distance r from the dislocation line was already calculated by the Read (1954),

$$V(r) = \frac{Q}{4\pi\varepsilon\varepsilon_0}\left[\ln\left(\frac{R^2}{r^2}\right) - \left(\frac{r^2}{R^2}\right) + 1\right] \tag{1}$$

where Q=q e is the charge per dislocation length and ε = 8.4 the dielectric constant of the material (Viswanatha et al., 2004). The Read radius $R = \sqrt{q/(\pi \quad N_{sc})}$ describes the radius of space charge region where N_{sc} is density of compensating charges available for screening.

Electron holography is a TEM technique that allows the retrieval of the phase of the electron wave. This provides the possibility to study the interaction of the incident electrons with the electrostatic potential of a charged dislocation with high spatial resolution. Fig.6 indicates the

orientation of the dislocation with respect to the electron-beam direction, which has been used in our study.

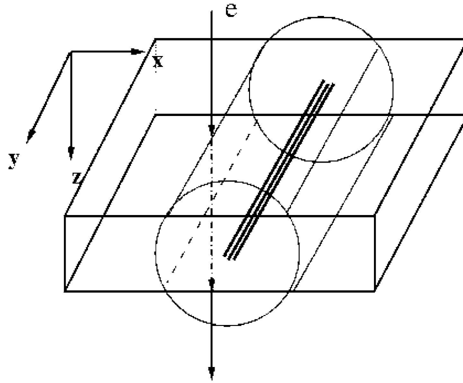

Figure 6. Geometry used for electron holography investigations: the electron beam is oriented along the z direction and the dislocation along y perpendicular to the electron-beam direction.

After passing a sample with a thickness t, the phase of the transmitted beam $\Delta\varphi$ is shifted with respect to the vacuum. If a charged dislocation is present, the mean inner potential V_0 of the material is locally modified by the potential *V(r)* ($r = \sqrt{x^2 + z^2}$) which induces a phase shift given by Eq.(2).

$$\Delta\varphi = C_E \int_0^t (V_0 + V(r))\ dz \qquad (2)$$

The constant $C_E = 7.29 \cdot 10^6$ is determined by the electron energy which was measured precisely for our electron microscope by convergent beam electron diffraction (Kruse et. al., 2003). Equation (2) only applies if kinematical diffraction conditions are chosen. To eliminate the influence of dynamical electron diffraction, the sample was tilted out of the zone axis by minimizing the excitation of the Bragg reflections in the diffraction pattern.

In previous work (Cherns and Jiao, 2001) dislocations with [0001]-line directions were aligned parallel to the electron beam, which is adequate to maximize the contribution of the line charge to the phase shift of the electron wave. However, the formation of pits at the intersection line of the dislocation with the surface due to ion etching of the sample is difficult to avoid and to detect. By analyzing embedded dislocations, thickness modifications, which also shift the phase with respect to the surrounding material according to Eq.(2), can be eliminated definitely. In addition, dynamical contributions to the phase shift are more difficult to exclude if

dislocations and electron beam are parallel. The dislocation strain field can locally tilt the lattice such that dynamical diffraction conditions apply in the vicinity the dislocation, i.e. Bragg reflections are strongly excited, even if kinematical conditions are chosen for the undisturbed crystal. The contribution of dynamical phase shifts can be minimized in our approach as will be shown later in this section.

On the basis of Eq.(2), a comparison of the phase shift measured by electron holography and the calculated $\Delta\phi$ yields the line charge *q*. Figure 7 shows the evaluated amplitude and phase of an electron hologram for the transmitted beam. The dislocation line direction is indicated by the dashed line in the amplitude image. Due to the noise, the position of the dislocation is visible only by a weak dark contrast in the phase image.

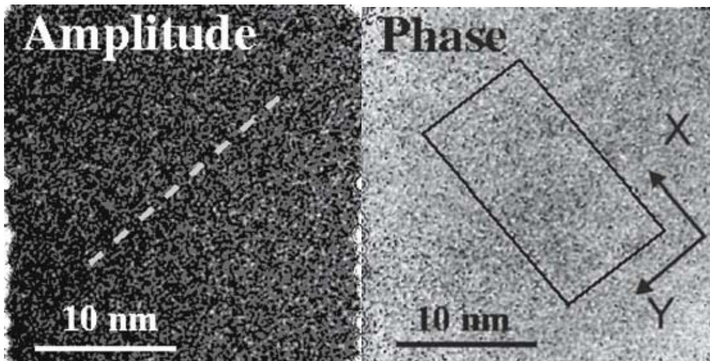

Figure 7. Reconstructed amplitude and phase of the electron wave in an area containing a dislocation indicated by the dashed line in the reconstructed amplitude.

To reduce the noise, the phase profile perpendicular to the dislocation line along the x direction was obtained by averaging the phase along the y direction inside the dark frame indicated in the phase image. The resulting phase profile is plotted in Fig.8. The line represents the best fit of the expected phase shift from Eq. (1) and (2) using the line-charge density as a fit paramter. The best fit was obtained for a line charge q = 3 e/nm^{-1}. The calculation was carried out iteratively by optimising both, the line charge q and R, because the Read radius R also depends on the line charge. Since the density of positive screening charges N_{SC} is not exactly known we have varied N_{sc} in the range from 10^{17}cm^{-3} to 10^{18}cm^{-3}, which yields Read radii between 98 nm and 30 nm. The error due to the variation of N_{sc} corresponds to Δq = ± 0.024 e/nm^{-1}. The retardation of the electron wave at the dislocation indicates that the dislocation is negatively charged. As only the electrical field induced by the charged dislocation contributes to the

measured phase change with respect to the undisturbed crystal, the thickness integration interval in Eq.(2) was chosen to be twice the Read radius. Therefore, an accurate value for the sample thickness is not required.

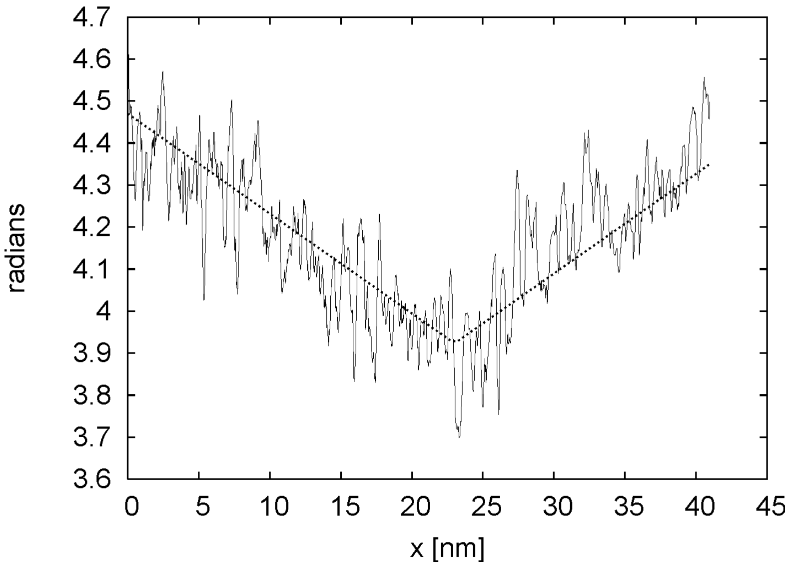

Figure 8. Measured phase change perpendicular to the dislocation line and fit according to Eq.(1) and Eq.(2).

The value for the line charge is reliable only if the effects of dynamical diffraction can be neglected. To assess the influence of dynamical diffraction on the phase shift, the 'worst' case was considered by assuming that the dislocation locally tilts the crystal from kinematical into {0002} or {11-20} two-beam conditions. The resulting dynamical phase shift was calculated using the Bloch wave formalism of the EMS program package (Stadelmann, 1987). Figure 9 shows the phase difference for the transmitted beam in the undisturbed crystal as a function of the thickness comparing the phase under kinematical conditions and for {0002} or {11-20} two-beam conditions. For the tilt angle the experimental values (1.5° perpendicular and 5° along the dislocation line with respect to the <1-100> zone axis) were taken into the account. It follows from Fig. 9, that dynamical diffraction is negligible if the distorted region in Bragg condition is smaller than 7 nm. With the experimental geometry with a dislocation orientation perpendicular to the electron-beam direction the assumption of a laterally limited distortion field is more likely to be satisfied compared to a parallel orientation.

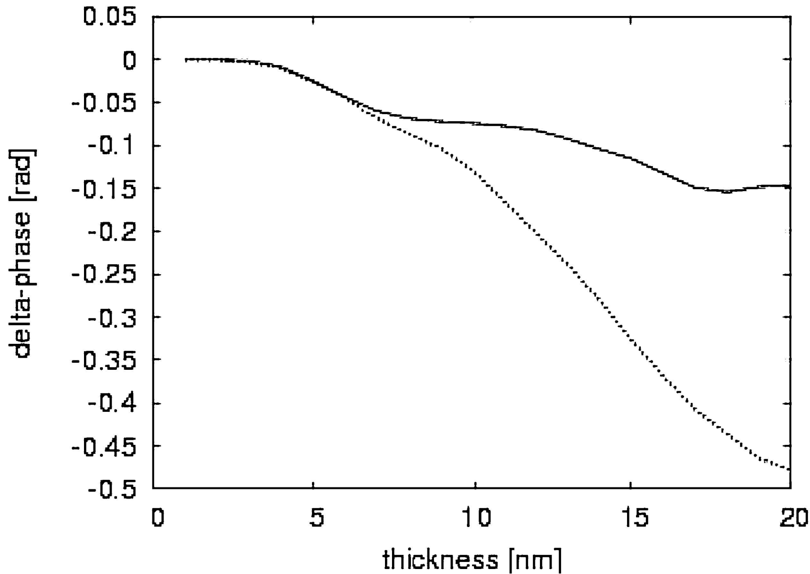

Figure 9. Phase difference for the transmitted beam in the undisturbed crystal comparing the phase under kinematical conditions and for (lower curve) {0002} or (upper curve) {11-20} two-beam conditions as a function of the thickness.

Regarding the accuracy of the determined line charge, it has to be taken into account that the fit of the phase profile strongly depends on the dielectric constant of ZnO with significantly differing values published in the literature (Landolt Börnstein, 1987). Another source of error is the sample thickness. If the sample thickness is smaller than the diameter of the Read cylinder (2 R) the electrical field of the line charge leaks into the vacuum region. Thus the effective dielectric constant decreases, leading to a smaller value of q. For an accurate treatment of this situation the field distribution outside the sample has to be calculated requiring an additional parameter for the fit of the measured phase curve.

The determined value for q is large, but it agrees with the trend towards high line charges in ZnO according to Ossip'yan et al. (1986). The discrepancy between our measured value and the value published for 60° (Zn)gilde dislocation can be explained by the different core structure of threading dislocations which do not lie on the (0001) plane. In our case, we did not analyse the dislocation Burgers vector because the dislocation could not be identified anymore after taking electron holograms. It has to be noted that the electrical activity of dislocations is not necessarily induced by intrinsic electronic dislocation states but can be also due to a high

concentration of point defect accumulated in the vicinity of the dislocation core.

The high negative dislocation line charge in n-ZnO indicates that dislocations can provide acceptor states with a high concentration if the dislocation density is high. This will lower the free electron concentration. Due to the amphoteric nature of the dislocation states they act as donors, if the Fermi energy is located below the occupation limit of the dislocation states. Pinning of the Fermi energy at the occupation limit of the band is expected if the concentration of shallow donors is reduced and the shallow acceptor density is increased. Therefore, dislocation states could contribute to the difficulty of obtaining p-type ZnO with low resistivity.

4. SUMMARY

The morphology and Burgers vectors of threading and misfit dislocations in MOVPE-grown ZnO heterostructures grown on Al_2O_3(0001) substrates were analyzed by transmission electron microscopy. Most threading dislocation are characterized by 1/3 <11-20> Burgers vectors which can be considered as threading segments of misfit dislocations with the same Burgers vectors. The line directions of threading dislocations extend typically along the [0001] growth direction yielding a high fraction of edge dislocations. High-temperature annealing treatments during the ZnO growth lead to different line directions and consequently different threading dislocations types. The threading dislocation density can be reduced by the growth of a thick GaN buffer layer and the optimization of the interface quality between the GaN buffer and the ZnO film. Analyzing the phase of the transmitted beam by electron holography, indications for a high negative line charge at threading dislocations are found. This observation emphasizes that dislocations can have a strong influence on the mobility and concentration of charge carriers in ZnO if they are present at a high density.

REFERENCES

Alexander, H., and Teichler, H., Dislocations, 1991, in: Materials Science and Technology, Vol. 4, chap.6, W. Schröter, ed., North-Holland Pub. Company, pp. 249.

Cherns, D., and Jiao, C.G., 2001, *Phys. Rev. Lett.* **87**, 205504.

Dadgar, A., Oleynik, N., Forster, D., Deiter, S., Witek, H., Bläsing, J., Bertram, F., Krtschil, A., Diez, A., Christen, J., and Krost, A., 2004, *J. Cryst. Growth* **267**, 140 .

Gerthsen, D., 1986, *phys. stat. sol. (a)* **97**, 527.

Hong, Soon-Ku, Ko, Hang-Ju, Chen, Y., Yao, T, 2000, *J. Cryst. Growth* **209**, 537.

Hull, D., Introduction to Dislocations, 1975, 2nd edition, Pergamon Press, pp.122.

Kruse, P., Rosenauer, A., and Gerthsen, D., 2003, *Ultramicroscopy* **96**, 11.
Landolt Börnstein, 1987, Springer-Verlag, Heidelberg, 165
Lehmann, M., and Lichte, H., 2002, *Microscopy and Microanalysis* **8**, 447.
Narayan, J., Dovidenko, K., Sharma, A.K., and Oktyabrsky, 1998, S., *J. Appl. Phys*. **84**, 2597.
Osip'yan, Yu. A., Petrenko, V.F., Zaretski, A.V., and Whitworth R.W., 1986, *Adv. Phys*. **35** 115.
Read, W.T., 1954, *Phil. Mag*. **45**, 775.
Stadelmann, P.A., 1987, *Ultramicroscopy* **21**, 131.
Strecker, A., Salzgeber, U., and Mayer, J., 1993, *Prakt. Metallographie* **30,** 482.
Vigué, F., Vennéguès, P., Vézian, S., Laügt, M., and Faurie, J.-P., 2001, *Appl. Phys. Lett.* **79**, 194.
Viswanatha, R., Sapra, S., Satpati, B., Satyam, P.V., Dev, B. N., and Sarma, D.D., 2004, *J. Mater. Chem.* **14**, 661.
Williams, D.B., and Carter, C.B., Transmission Electron Microscopy, 1996, Plenum Press, New York.

PART III: ROLE OF HYDROGEN

Chapter 10

MUON SPIN ROTATION MEASUREMENTS ON ZINC OXIDE

E. A. Davis
Department of Materials Science and Metallurgy, University of Cambridge, Pembroke Street, Cambridge CB2 3QZ, United Kingdom

Abstract: The theoretical suggestion that hydrogen might form shallow donor states in zinc oxide – and hence account for the n-type conductivity normally found in undoped samples – has been confirmed by experimental studies using mounium, a light pseudo-isotope of hydrogen. Characteristic frequencies in muon spin rotation experiments yield a hyperfine constant that is ~10^4 times smaller than that of vacuum-state muonium, indicating an extended orbital and a shallow centre. Temperature-dependence studies yield an ionization energy of about 30 meV. Band-offset diagrams and measurements on other semiconductors suggest that hydrogen forms shallow donor centres when the electron affinity of the host material is more than about 4 eV; otherwise the hydrogen level lies deep in the energy gap.

Key words: Hydrogen, muons, muonium, shallow donors

1. INTRODUCTION

The simulation of hydrogen by muons has proved to be extremely valuable in the identification of potential sites for hydrogen in semiconductors and insulators. Although the muon has a mass one-ninth that of the proton, its interaction with the host lattice, both electronically and chemically, is virtually identical to that of a proton. During its 2.2 microsecond lifetime (experiments are frequently undertaken over a timescale of up to ten lifetimes), the muon can diffuse, interact with, and adopt positions in the lattice that protons themselves would occupy. If the temperature is sufficiently low, muons can capture electrons to form muonium atoms. The reduced mass of muonium is within 0.5% of that of

N.H. Nickel and E. Terukov (eds.),
Zinc Oxide – A Material for Micro- and Optoelectronic Applications, 115–123.
© 2005 *Springer. Printed in the Netherlands.*

hydrogen and so its Bohr radius and ionization energy are essentially the same as those of hydrogen.

Experiments using muons are generally easier and more direct than experiments[1] using hydrogen itself. One reason for this is the high sensitivity of the technique, by which one can essentially 'see' individual muons. Another and more fundamental aspect is that hydrogen frequently forms 'a negative-*U* system', making the neutral state inaccessible under thermal equilibrium conditions. Such conditions do not apply in the muon experiments, permitting observation of both the ionized (charged) and unionized (neutral) states.

The theoretical prediction[2] that hydrogen forms a shallow donor state in ZnO has been confirmed by muon implantation studies[3,4]. Below 40 K a distinctive beating of the muon precession signal provides the required signature. Fourier transformation reveals a central line at the muon Larmor frequency accompanied by two symmetrically disposed satellites, the separation of which yields a hyperfine constant about 10,000 times smaller than that for vacuum-state muonium. Confirmation that this signal represents the extended orbital of a shallow centre has been obtained by studies as a function of temperature, which reveal the disappearance of the satellites with an ionization energy of approximately 30 meV. More recent measurements[5] in longitudinal magnetic fields provide further evidence for these findings.

2. EXPERIMENTAL DETAILS AND RESULTS

The experiments were undertaken at the ISIS pulsed muon facility at the Rutherford Appleton Laboratory situated near Oxford in England. Positive muons of energy 4 MeV and 100% spin polarized are brought to rest within a few tenths of a millimetre in powder or single-crystal samples mounted within a cryostat.

The technique of muon spin rotation involves applying a magnetic field perpendicular to the direction of the incoming beam of muons (transverse to their spin) and monitoring the resulting precession signal via the emission of positrons that are emitted preferentially in the direction of the muon spin at the moment of its radioactive decay. For the bare muons this is simply the Larmor frequency but for muonium several frequencies are observed. In the case of a small hyperfine constant, one can easily reach the so-called Paschen-Back regime in moderate fields and then a triplet of lines is seen in a Fourier transform of the raw data.

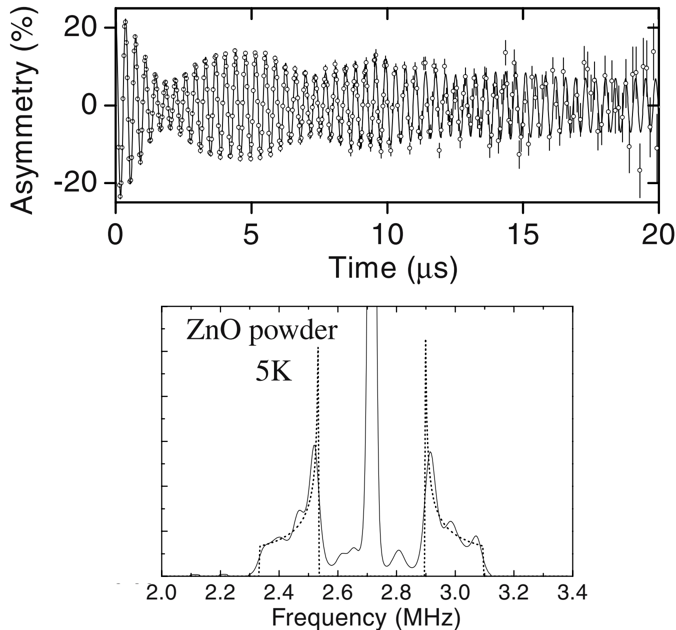

Figure 1. Muonium spin precession signal for a ZnO powder sample at 5 K. The upper plot is the raw time-domain spectrum (corrected for the muon decay) while the lower plot is the corresponding frequency spectrum. The central line corresponds to the Larmor frequency of the bare muon (ionized muonium) and the two symmetrically disposed satellites are associated with muonium. The dotted curve is a theoretical fit using a powder-pattern lineshape.

The triplet of frequencies gives rise to a beating in the time-domain spectrum as seen for a powder sample of ZnO in Figure 1.The separation of the two satellite lines provides a direct measure of the hyperfine coupling constant between the muon and the electron. This is 500 ± 20 kHz, which is 0.011% of the free-muonium value of 4463 MHz, indicating immediately a small electron spin density at the site of the muon and an extended wavefunction associated with a shallow donor state.

Studies of the temperature dependences of the lines reveal that, as the temperature is raised, the central line increases in amplitude at the expense of the satellites. This is to be expected for ionization of the donor state. The corresponding Arrhenius plots, shown in Figure 2, produce activation energies for the central (diamagnetic) line of ~ 26 meV and of the satellite (paramagnetic) lines of ~ 33 meV. The results imply that muonium in ZnO ionizes above ~ 40 K with an activation energy of about 30 ± 3 meV.

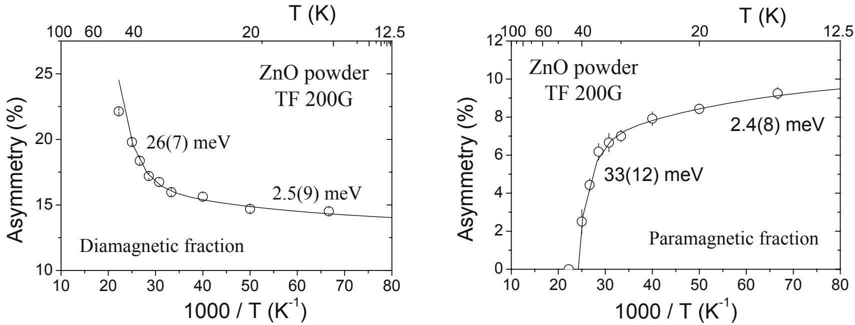

Figure 2. Arrhenius plots of the temperature dependences of the amplitudes of the lines shown in Figure 1. (Courtesy of J M Gil.)

The smaller activation energies seen at lower temperatures are probably associated with an exchange of electrons between muonium and other donors (hydrogen?) already present in the samples.

One might question whether the energy of 30 meV represents the depth of the donor level below the conduction band edge? Under conditions of thermal equilibrium, carrier activation energies yield the donor depth if compensating acceptors are present but one-half the donor depth for the case of no compensation. In the case of implanted muons, thermal equilibrium is not reached and the correct interpretation is a matter for debate. Doubling our activation energies would imply a donor depth for muonium or hydrogen of ~ 60 ± 6 meV, which is closer to the theoretical 'hydrogenic' value – see next section.

Investigations by others have yielded a variety of possible values for the depth of hydrogen donors in ZnO. Hall effect studies[6] have been analysed in terms of the ionization of two donors having energies of 31 meV and 61meV, with the authors preferring to associate the *lower* of these two values with hydrogen donors. Hofmann *et al.*[1], as part of their ENDOR investigations, also made Hall effect measurements and found two activation energies with values 35 and 66 meV. Early photoluminescence data[7] gave 52 meV as the depth of a hydrogen donor. More recent photoluminescence studies[8] suggests a lower value of 40 meV.

3. FURTHER ANALYSIS

Assuming for the sake of simplicity an isotropic centre, the effective Bohr radius a^* can be obtained directly from the hyperfine constant A^*, since this scales as the third power of the radius:

$$a^* = a_0 \left(A_0 / A^* \right)^{1/3} \tag{1}$$

where A_0 is the free-muonium hyperfine constant and a_0 is the Bohr radius. Taking A_0 = 4463 MHz and a_0 = 0.053 nm, we find a^* = 1.1 nm. This can be compared with the value estimated from a 'hydrogenic' model:

$$a^* = a_0 \varepsilon \left(m_e / m^* \right) \tag{2}$$

where ε is the relative permittivity and m^* the effective mass for electrons in ZnO. Using the values ε = 8 and m^*/m_e = 0.24, gives a^* = 1.7 nm, in fair agreement with the value deduced from the data.

In a similar vein we can estimate the ionization energy from the hyperfine constant:

$$I^* = I_0 \left(A^* / A_0 \right)^{1/3} / \varepsilon \tag{3}$$

where I_0 is the Rydberg = 13.6 eV. This yields I^* = 51 meV, which can be compared with the 'hydrogenic' value, given by:

$$I^* = I_0 \left(m^* / m_e \right) / \varepsilon^2 \tag{4}$$

of 50 meV. The agreement is good, bearing in mind the assumptions in the hydrogenic model – no central-cell corrections for example.

4. SINGLE-CRYSTAL STUDIES

The experiments described above were made on powder samples of 99.999% purity from Alfa Aesar. Single-crystal studies have also been undertaken[5]. Figure 3 shows spectra of an Eagle-Picher sample taken at two different orientations of the crystallographic c-axis with respect to the muon beam; the inset gives the orientation dependence of the separation of the main satellite lines.

For an anisotropic centre this splitting is given by

$$\Delta \nu = A^* + \frac{D}{2} \beta \left(3\cos^2 \theta - 1 \right) \tag{5}$$

where A^* is the isotropic part of the hyperfine tensor and D is a dipolar term. These data yield a very similar value of A^* (namely 490 ± 10 kHz) to the powder sample studies but confirm an anisotropy of the centre with D = 260 ± 20 kHz. From the angular dependence one can deduce that the symmetry axis of the centre is parallel to the c-axis.

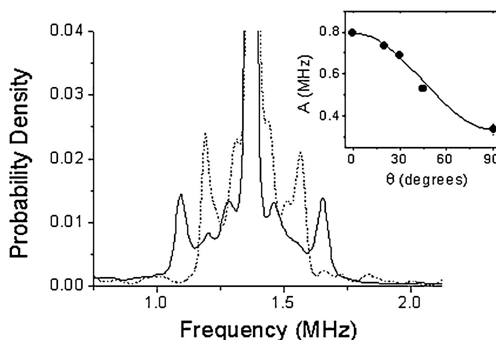

Figure 3. Frequency spectrum derived from muonium spin rotation measurements on a single-crystal sample of ZnO as a function of orientation (from reference 5).

Of the possible sites that hydrogen (muonium) can occupy in the wurtzite lattice (see Figure 4) the BC_{par} site has been shown theoretically to have the lowest energy, i.e. to be the most stable site[9]. Experimentally we cannot distinguish between this site and the site antibonding to oxygen along the c-axis.

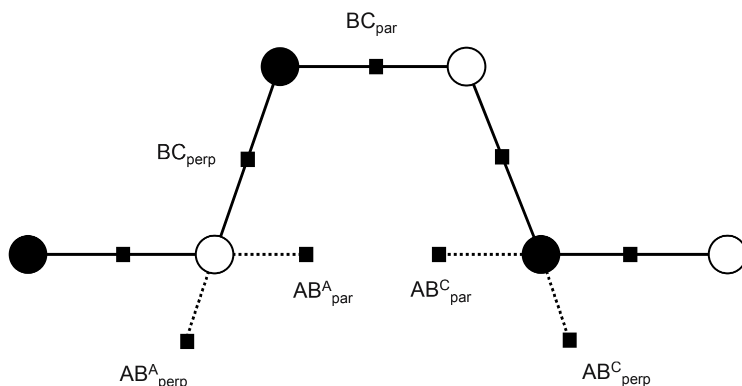

Figure 4. Six principal sites for hydrogen in the wurtzite structure. BC = bond centre and AB = antibonding. Superscripts denote sites adjacent to the cation(C) and anion (A). ‘Perp’ and ‘par’ refer to directions perpendicular (not exactly) and parallel to the c-axis (from ref. 11).

Shimomura *et al.*[10] have also made muonium studies on single crystals of ZnO and claim to have identified two distinct shallow centres, one associated with each of the above sites.

5. SHALLOW VERSUS DEEP

The reason why muonium (and by implication hydrogen) acts as a shallow centre in some materials and as a deep centre in others is intriguing. It appears that the electron affinity of the host is a crucial parameter, as revealed by the plot shown in Figure 5.

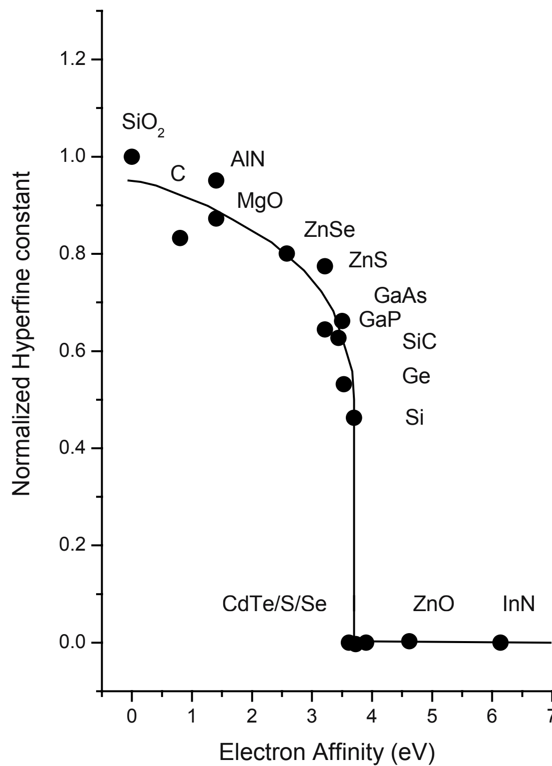

Figure 5. Correlation of the normalized muonium hyperfine constant with electron affinity. (Courtesy of S F J Cox – reference 11.)

Here the muonium hyperfine constant, relative to the vacuum-state value, is plotted versus electron affinity for a variety of materials, from insulators

such as SiO_2 and diamond on the left (for which A^*/A_0 is close to unity) to semiconductors in the middle of the plot. The five semiconductors with an effectively zero (on this scale) hyperfine constant are those in which muonium forms shallow centres. It is evident that the 'dilation of the wavefunction' from atomic-like to extended occurs rather suddenly on this plot, corresponding to an electron affinity of about 3.7 eV.

The concept of the electron affinity of the host being the all important factor influencing the deep to shallow transition is implicit in the band-offset diagrams proposed by Van de Walle[12]. An example is shown in Figure 6 for a few materials. In this diagram E_c represents the energy of the bottom of the conduction band and E_v the top of the valence band, both plotted on an absolute energy scale, i.e. with respect to the vacuum level. The dashed line marked +/- gives the energy at which the formation energies of the positively and negatively charged states of hydrogen are equal. This represents the position at which the Fermi level would be pinned in a negative U system.

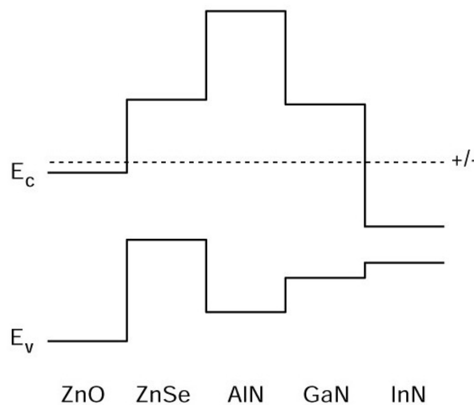

Figure 6. Band-offset diagram for several semiconductors (from reference 13).

If this level lies in the conduction band (as in ZnO and InN) hydrogen forms a shallow donor level. If the level lies in the band gap (as for the other three materials) then hydrogen forms a deep centre. The predictive nature of this model is currently being tested for other semiconductors, in particular oxides other than ZnO.

Peacock and Robertson[14] have questioned whether the hydrogen level really does lie at a constant depth below the vacuum level. A subtle point relevant to this question is that the donor state actually lies at the level +/0, i.e. the energy through which the Fermi level would pass when the centre ionizes, changing from the neutral to the positively charged state. This level differs by $U/2$ from the +/- level and so, even if the +/- level is invariant, the

+/0 level is not expected to be so. Under thermal equilibrium conditions the Fermi level is pinned at +/- (for a –ve *U* system). Such conditions do not apply in the muonium experiments and so we are able to explore the higher +/0 level directly, without the need to illuminate the sample to reveal the neutral state, as required for, say, ENDOR experiments using hydrogen itself[1].

ACKNOWLEDGEMENTS

The author wishes to acknowledge fruitful and enjoyable collaboration with several colleagues during the experimental work reported here. These are S F J Cox (Rutherford Appleton Laboratory and University College London), P J C King, J S Lord and S P Cottrell (Rutherford Appleton Laboratory), J M Gil, H Alberto, R Vilão, J Piroto Duarte and N Ayres de Campos (Coimbra University, Portugal), and R Lichti (Texas Tech University, USA).

REFERENCES

1. D. M. Hofmann, A. Hofstaetter, F. Leiter, H. Zhou, F. Henecker, B. K. Meyer, S. B. Orlinskii, J. Schmidt, and P. G. Baranov, *Phys Rev Lett*. **88**, 045504 (2002).
2. C. G. Van de Walle, *Phys. Rev. Lett*. **85**, 1012 (2000).
3. S. F. J. Cox, E. A. Davis, S. P. Cottrell, P. J. C. King, J. S. Lord, J. M. Gil, H. V. Alberto, R. C. Vilão, J. Piroto Duarte, N. Ayres de Campos, A. Weidinger, R. L. Lichti, and S. F. C. Irvine, *Phys. Rev. Lett*. **86**, 2601 (2001).
4. J. M. Gil, H. V. Alberto, R. C. Vilão, J. Piroto Duarte, P. J. Mendes, L. P. Ferreira, N. Ayres de Campos, A. Weidinger, J. Krause, E. A. Davis, S. P. Cottrell, and S. F. J. Cox, *Phys. Rev. B* **64**, 075205 (2001).
5. H. V. Alberto, R. C. Vilão, J. Piroto Duarte, N. Ayres de Campos, R. L. Lichti, E. A. Davis, S. P. Cottrell, and S. F. J. Cox, *Hyperfine Interact*. **136/137**, 471 (2001).
6. D. C. Look, D. C. Reynolds, J. R. Sizelove, R. L. Jones, C. W. Litton, G. Cantwell, and W. C. Harsch, *Solid State Commun*. **105**, 399 (1998).
7. D. C. Reynolds and T. C. Collins, *Phys. Rev*. **185**, 1099 (1969).
8. D. C. Look, C. Coskun, B. Clafin, and G. C. Farlow, *Physica* B **340-342**, 32 (2003)
9. E V. Lavrov, J. Weber, F. Börrnert, C. G. Van de Walle, and R. Helbig, , *Phys. Rev*. B **66**, 165205 (2002).
10. K. Shimomura, K. Nishiyama, and R. Kadono, *Phys Rev Lett*. **89**, 255505 (2002).
11. S. F. J. Cox, *J. Phys.: Condens. Matter* **15**, R1727 (2003).
12. C. G. Van de Walle and J. Neugebauer, *Nature* **423**, 626 (2003).
13. E. A. Davis, S. F. J. Cox, R. L. Lichti, and C. G. Van de Walle, *Appl. Phys. Lett*. **82**, 592 (2003).
14. P. W. Peacock and J. Robertson, *Appl. Phys. Lett*. **83**, 2025 (2003).

Chapter 11

HYDROGEN DONORS IN ZINC OXIDE

M. D. McCluskey and S. J. Jokela
Department of Physics, Washington State University, Pullman, WA 99164, U.S.A.

Abstract: Zinc oxide (ZnO) has emerged as a leading material for micro- and optoelectronic applications. Although the fabrication of ZnO, from nanocrystals to bulk single crystals, is well established, a major roadblock for fabricating optoelectronic devices is the lack of reliable *p*-type doping. The presence of compensating donors inhibits the growth of *p*-type ZnO. In this paper, studies pertaining to the microscopic structure and doping properties of hydrogen in ZnO are described. Results from infrared (IR) spectroscopy are consistent with a model where the hydrogen attaches to a host oxygen atom, in an anti-bonding orientation, which is not aligned along the *c* axis. These hydrogen complexes are unstable, however, perhaps due to the formation of H_2 molecules.

Key words: IR spectroscopy, infrared, hydrogen, vibrational modes, H donors, O-H complexes

1. INTRODUCTION

Zinc oxide (ZnO) has a wide range of industrial applications. An environmentally friendly, wide-bandgap semiconductor, ZnO may prove to be a valuable material for blue lasers and light-emitting diodes.[1] The lack of reliable *p*-type doping, however, is major roadblock to the realization of such devices. Compensating donors play a detrimental role in preventing *p*-type conductivity. Early work by Mollwo[2] and Thomas and Lander[3] showed that the diffusion of hydrogen into ZnO could increase the electrical conductivity. The more recent theoretical work by Van de Walle,[4] which showed that hydrogen should be a shallow donor in ZnO, re-ignited interest in this subject. Subsequent experiments involving muonium in ZnO[5] and electron-nuclear double resonance (ENDOR) spectroscopy[6] verified that hydrogen is a shallow donor in ZnO. In this paper, we review results from

N.H. Nickel and E. Terukov (eds.),
Zinc Oxide – A Material for Micro- and Optoelectronic Applications, 125–132.
© 2005 *Springer. Printed in the Netherlands.*

infrared (IR) spectroscopy of hydrogen diffused into ZnO.[7-9] Preliminary Hall-effect and high-pressure results are also presented.

2. EXPERIMENTAL TECHNIQUES

Single crystal, *c*-cut ZnO samples were purchased from Cermet, Inc. Samples were sealed in quartz ampoules along with hydrogen or deuterium gas. In addition, ZnO powder was placed in the ampoule, in order to prevent the decomposition of the ZnO crystal due to hydrogen reduction. Hydrogen diffusion occurred at a temperature of 700-800°C for 10-100 hr, followed by a rapid quench to room temperature by immersion of the ampoule in water. The sample was then retrieved by breaking the ampoule.

IR spectra were taken at room temperature (300 K) and liquid-helium temperatures (5-15 K), using a Bomem DA8 Fourier transform infrared (FTIR) spectrometer and an InSb detector. For the low-temperature measurements, a Janis continuous-flow liquid-helium cryostat with wedged, IR-transparent windows was utilized. Hall-effect measurements, in the Van der Pauw geometry, were performed at room temperature using a system from MMR Technologies. Wires were attached to the ZnO using silver paint, which provided adequate Ohmic contacts for the electron concentrations (10^{17} cm^{-3}) in these samples.

3. RESULTS

3.1 IR spectroscopy and Hall-effect measurements

At liquid-helium temperatures, hydrogenated ZnO samples exhibit an O-H stretch mode at a frequency of 3326 cm^{-1} at liquid-helium temperatures (Fig 1). The IR peak corresponding to this mode broadens and shifts to higher frequency when the sample is warmed to room temperature. Deuterated ZnO samples, at liquid-helium temperatures, have an O-D stretch mode at 2470 cm^{-1}.[7] The ratio of the O-H and O-D frequencies are in good agreement with a simple diatomic model. More importantly, the frequency ratio is nearly identical to that of O-H and O-D complexes in GaP.[10] Our observed O-H mode is different from those observed by Lavrov *et al.*[11] and Nickel and Fleischer.[12]

At a temperature of 300 K, the O-H complexes are unstable. Over the course of a few months, the intensity of the IR peak decreases substantially. In order to quantify this decay process, we prepared two identical

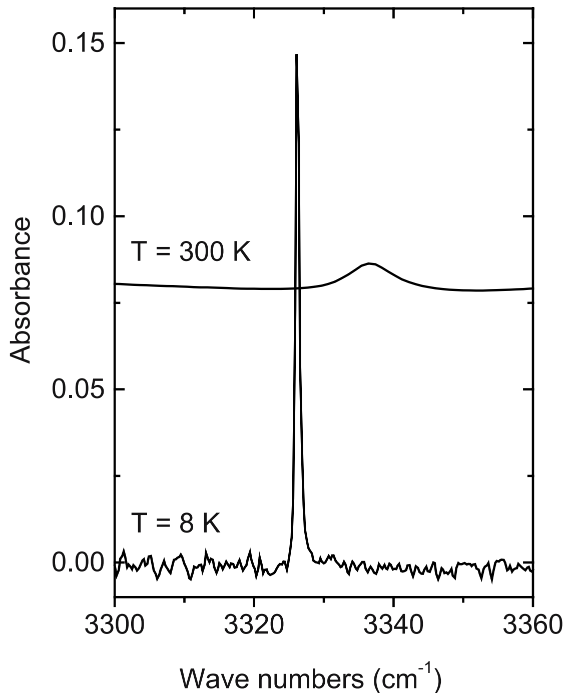

Figure 1. IR spectra of O-H complexes in ZnO at room- and liquid-helium temperatures.

hydrogenated samples. For one sample, the electron concentration was determined as a function of time, using room-temperature Hall-effect measurements. For the other sample, room-temperature IR spectroscopy was used to measure the intensity of the O-H peak as a function of time. The results of these measurements are plotted in Fig. 2. The circles and squares refer to the Hall-effect and IR measurements, respectively.

In Fig. 2, there are two features worth noting. First, the decay of the O-H peak and the decay of the free-electron concentration are correlated, providing evidence that the O-H complexes are shallow donors. Second, the data were fit using a biexponential decay model,

$$N = \frac{1}{1/N_0 + At}, \tag{1}$$

where N is the number of O-H complexes, N_0 and A are adjustable parameters, and t is time. This model is consistent with the idea that hydrogen donors may form H_2 molecules.[13] Since H_2 molecules are

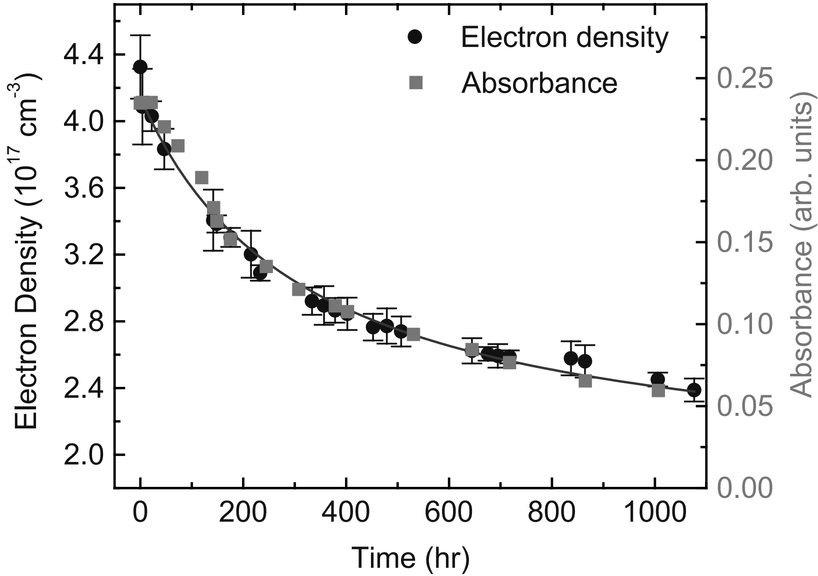

Figure 2. Electron density (circles) and IR absorbance of the O-H peak (squares) as a function of time, in hydrogenated ZnO.

essentially IR inactive, and electrically neutral, the formation of H_2 molecules results in a decrease in the O-H IR mode *and* free-electron concentration.

3.2 Polarized IR spectroscopy

The IR measurements described in the previous section were performed in a normal incidence geometry on *c*-cut ZnO samples. Since the polarization of the light is perpendicular to the *c* axis, it follows that the O-H complexes that we observed are *not* aligned along the *c* axis. This observation contradicts some theoretical reports, which claim that the lowest energy orientation of the hydrogen is parallel to the *c* axis.[4] The calculated energy differences are small, however, on the order of 0.1 eV.

To check this result, we performed polarized IR spectroscopy on an *a*-cut sample. For light that was polarized along the *c* axis, the O-H absorption is reduced as compared to light perpendicular to the *c* axis. As discussed in Ref. 8, our results are consistent with O-H dipoles that are aligned at an angle of ~112 ° to the *c* axis.

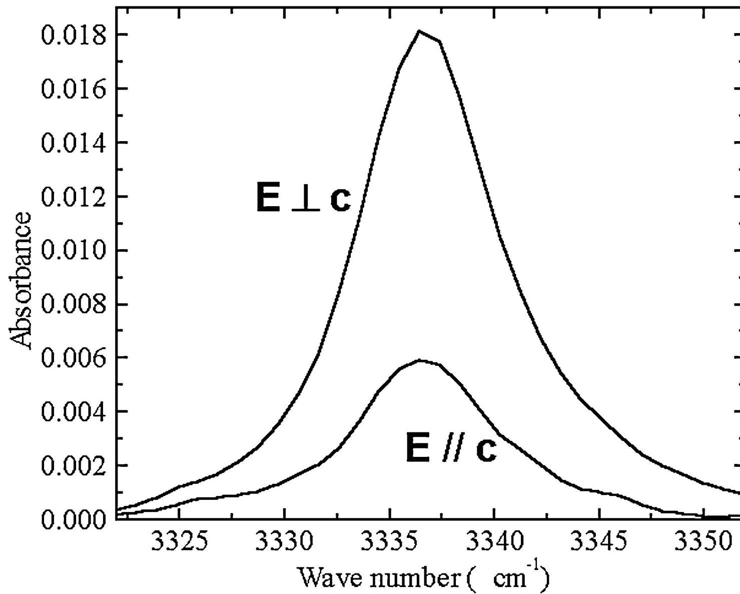

Figure 3. Polarized IR spectra of O-H complexes in ZnO, at room temperature.

3.3 High-pressure measurements

Regarding the structure of the O-H complexes, one question remains: is the configuration bond-centered or anti-bonding? Since both structures have identical symmetry, it is not obvious how to distinguish between them. One possible method involves measuring the O-H stretch-mode frequency as a function of hydrostatic pressure. By comparing the results with predictions of *ab initio* calculations, it should be possible to determine the structure with reasonable certainty.

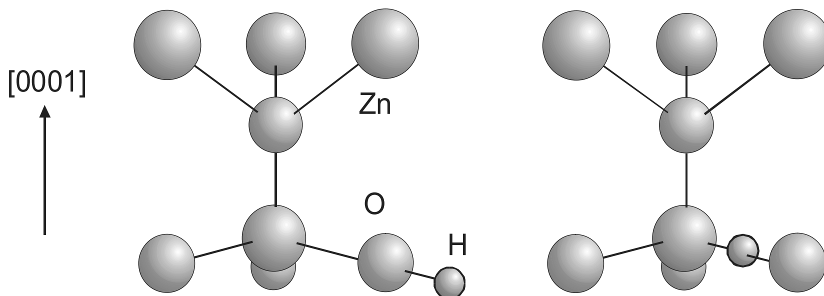

Figure 4. Ball-and-stick diagrams of the antibonding (left) and bond-centered (right) models for hydrogen donors in ZnO.

High-pressure measurements were performed at room temperature, using a moissanite-anvil cell. As shown in Fig. 5, there is only a very slight shift with pressure, approximately -1 cm^{-1}/GPa. Qualitatively, this small shift would seem to favor the antibonding orientation, in which the hydrogen is not crowded by neighboring atoms. However, it will be necessary to compare our results with first-principles calculations. In addition, IR measurements over a larger range of pressures will be performed.

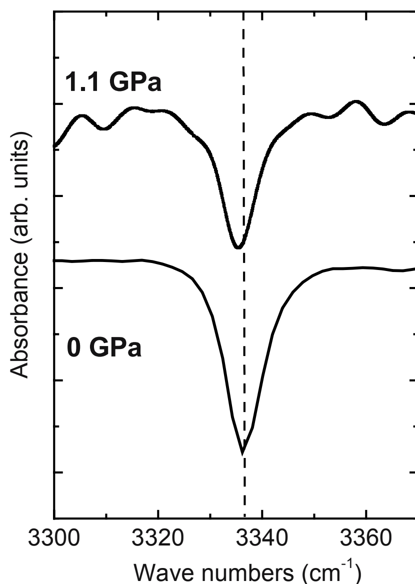

Figure 5. IR spectra of hydrogenated ZnO, at room temperature, at hydrostatic pressures of 0 and 1.1 GPa.

4. UNSOLVED MYSTERIES

In addition to the bond-centered versus antibonding question, there are two results that do not have good explanations. First, as shown in Fig. 6, hydrogenated samples from Cermet show a much stronger peak than identically treated samples from Eagle-Pitcher. This may be due to a higher concentration of oxygen vacancies in Eagle-Picher material, which could trap hydrogen atoms. The second mystery is the larger intensity of the O-H peak as compared to the O-D peak (Fig. 7). The larger intensity may be related to hydrogen's faster diffusion and larger vibrational amplitude, but the size of the difference (x10) is puzzling.

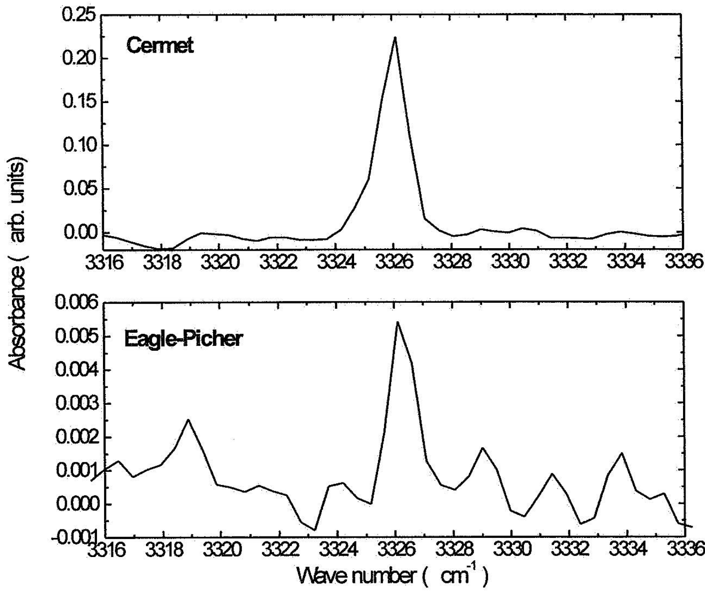

Figure 6. IR spectra of hydrogenated ZnO, at liquid-helium temperatures, for samples purchased from Cermet and Eagle-Picher.

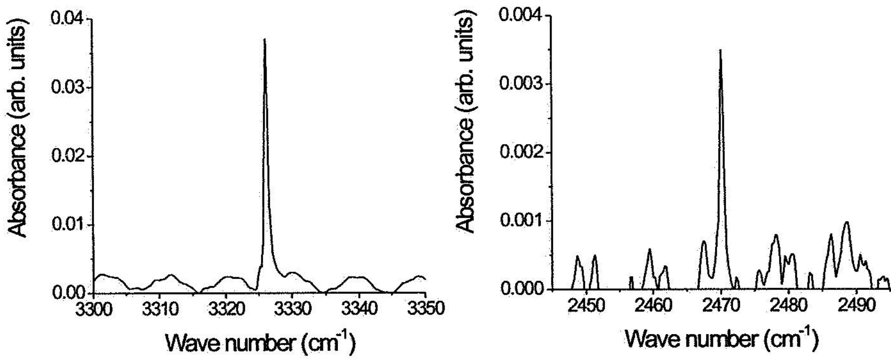

Figure 7. IR spectra of O-H (left) and O-D (right) complexes in ZnO.

5. CONCLUSIONS

Hydrogen donors can be introduced by annealing ZnO in a hydrogen ambient, resulting in O-H complexes. These donor complexes are unstable, however, and decay away in a few months at room temperature. It is likely that most of the O-H complexes form H_2 molecules in the sample. Results of IR spectroscopy are consistent with an O-H complex that is in an antibonding configuration, oriented at some angle to the *c* axis.

ACKNOWLDGMENTS

The authors would like to thank S. Limpijumnong, M. Stavola, C.G. Van de Walle, and S.B. Zhang for helpful discussions. This work was supported by NSF Grant No. DMR-0203832.

REFERENCES

1. D. C. Look, *Mater. Sci. Eng. B* **80**, 383 (2001).
2. E. Mollwo, *Z. Phys.* **138**, 478 (1954).
3. D. G. Thomas and J.J. Lander, *J. Chem. Phys.* **25**, 1136 (1956).
4. C. G. Van de Walle, *Phys. Rev. Lett.* **85**, 1012 (2000).
5. S. F. J. Cox, E. A. Davis, S. P. Cottrell, P. J. C. King, J. S. Lord, J. M. Gil, H. V. Alberto, R. C. Vilão, J. Piroto Duarte, N. Ayres de Campos, A. Weidinger, R. L. Lichti, and S. J. C. Irvine, *Phys. Rev. Lett.* **86**, 2601 (2001).
6. D. M. Hoffman, A. Hofstaetter, F. Leiter, H. Zhou, F. Henecker, B. K. Meyer, S. B. Orlinskii, J. Schmidt, and P. G. Baranov, *Phys. Rev. Lett.* **88**, 045504 (2002).
7. M. D. McCluskey, S. J. Jokela, K. K. Zhuravlev, P. J. Simpson, and K. G. Lynn, *Appl. Phys. Lett.* **81**, 3807 (2002).
8. S. J. Jokela, M. D. McCluskey, and K. G. Lynn, *Physica B* **340-342**, 221 (2003).
9. M. D. McCluskey and S. J. Jokela, in MRS Proc. Vol. **813**, edited by N. H. Nickel, M. D. McCluskey, and S. B. Zhang (Materials Research Society, PA, 2004).
10. W. Ulrici, M. Czupalla, and M. Siefert, *Phys. Status Solidi B* **210**, 551 (1998).
11. E. V. Lavrov, J. Weber, F. Börrnert, C. G. Van de Walle, R. Helbig, *Phys. Rev. B* **66**, 165205 (2002).
12. N. H. Nickel and K. Fleischer, *Phys. Rev. Lett.* **90**, 197402 (2003).
13. G. Alvin Shi, M. Saboktakin, M. Stavola, and S. J. Pearton (unpublished).

Chapter 12

HYDROGEN-RELATED DEFECTS IN ZnO STUDIED BY IR ABSORPTION SPECTROSCOPY

E.V. Lavrov,[1,2] F. Börrnert,[1] and J. Weber[1]
[1]Technical University Dresden, 01062 Dresden, Germany; [2]Institute of Radioengineering and Electronics of RAS, 101999 Moscow, Russia

Abstract: Most of the ZnO growth techniques result in *n*-type conductivity of the crystal, which hinders the progress of ZnO applications for electronic devices. Hydrogen incorporated during the process of crystal growth is now considered as a likely source of the *n*-type conductivity of ZnO. Infrared absorption spectroscopy provides detailed insights into the physical properties of the light impurities in the semiconductor matrix and is, therefore, an excellent tool to explore the structure of the hydrogen-related defects embedded in ZnO. We report a number of hydrogen-related defects observed in hydrothermally grown ZnO and ZnO grown from the vapor phase studied by Fourier transform infrared absorption spectroscopy. Three IR absorption lines at 3611.3, 3349.6, and 3312.2 cm^{-1} at 10 K are observed after hydrogenation of the vapor phase grown ZnO. The line at 3611.3 cm^{-1} is tentatively assigned to a bond-centered hydrogen, whereas the other two are identified as a Zn vacancy decorated with two hydrogen atoms. The nature of a hydrogen center responsible for the 3577.3 cm^{-1} line observed at 10K in *as-grown* hydrothermal ZnO is discussed.

Key words: Hydrogen, hydrogen-related defects, IR absorption, Zn vacancy

1. INTRODUCTION

Due to recent progress in crystal growth[1] and the unique piezoelectric, optical, and electrical properties, ZnO is considered at the moment as a serious alternative to GaN for use in optoelectronic devices.[2] ZnO nearly always exhibits *n*-type conductivity. The nature of this conductivity has been discussed for years and is normally attributed to native defects, such as the Zn-on-O antisite (Zn_O), the Zn interstitial (Zn_i), and the O vacancy (V_O).[3]

N.H. Nickel and E. Terukov (eds.),
Zinc Oxide – A Material for Micro- and Optoelectronic Applications, 133–144.
© 2005 *Springer. Printed in the Netherlands.*

However, a new cause for the *n*-type conductivity of ZnO has recently been proposed: First-principles investigations based on density functional theory suggest that hydrogen in ZnO occurs exclusively in the positive charge state, i.e., it always acts as a donor.[4] Recent muon spin rotation (μSR)[5] and EPR[6] studies confirmed the presence of hydrogen-related shallow donors. However, the molecular structure of these defects remains unknown.

Local vibrational mode (LVM) spectroscopy is a tool suited to study this problem. The knowledge about LVMs supplies a detailed information about the physical properties of light impurities embedded in ZnO. The frequencies of the LVMs reveal directly the chemical binding of hydrogen with its neighbors due to the dependence on the atomic structure of the hydrogen-related defects.

To our knowledge, the first infrared absorption study of hydrogen-related LVMs in ZnO was made in the end of the 70th by Gärtner and E. Mollwo.[7,8] They investigated copper doped ZnO annealed in a hydrogen atmosphere and identified a set of LVMs originating from different copper-hydrogen defects.

Interest for hydrogen behavior in ZnO stimulated further studies of LVMs hydrogen-related defects. McCluskey *et al.* reported an O-H stretch mode at 3326.3 cm^{-1} observed at 8 K in ZnO samples that were annealed at 700 ^{o}C in hydrogen atmosphere.[9] The 3326.3 cm^{-1} line was assigned to a hydrogen atom in an antibonding configuration oriented at an angle of 100° to the *c* axis.

Recently, Nickel and Fleischer reported a Raman scattering study of as-grown state-of-the-art ZnO. A number of Raman lines were detected, which were ascribed to LVMs of N-H and $C\text{-}H_n$ complexes with n=1,2,3.[10]

Here, we summarize our results of an infrared absorption study of hydrogen-related centers in ZnO grown by different techniques.[11,12] A number of O-H LVMs has been detected. The lines at 3611.3, 3349.6, and 3312.2 cm^{-1} are observed after hydrogen plasma treatment in nominally undoped ZnO grown from the vapor phase. The 3611.3 cm^{-1} line is tentatively identified as a LVM of bond centered (BC) hydrogen, whereas the other two modes are assigned to LVMs of a zinc vacancy decorated with two hydrogen atoms. The origin of an IR absorption line at 3577.3 cm^{-1} detected at 10 K *in as-grown* hydrothermal ZnO is discussed.

2. EXPERIMENTAL DETAILS

Two types of ZnO crystals have been employed in the current study. Nominally undoped *n*-type ZnO crystals grown from the vapor phase (VP) at

the Institute for Applied Physics, University Erlangen (Germany) with resistivity of 10-100 Ω cm had a shape of hexagonal prisms with a diameter of ~2 mm and a length of ~20 mm.[13,14] Hydrothermally grown (HT) *n*-type (1120) ZnO substrates supplied by CrysTec GmbH had sizes of 5x5x1 mm^3 with the *c* axis parallel to one of the edges of the substrate. The carrier concentration at RT was 10^{17} cm^{-3}.

For hydrogenation the samples were exposed for 1-19 h to a remote hydrogen and/or deuterium dc plasma in a parallel plate system, with a plate voltage of 1000 V. The samples were mounted on a heater block held at a temperature of 150-380 °C and placed 10 cm downstream from the plasma with a bias voltage of about 300 V, which fixed the bias current to ~40 μA. The gas pressure was held at ~1 mbar.

In order to study the annealing behavior of the hydrogen-related defects, infrared absorbance spectra were recorded at 10 K after each step in a series of isochronal heat treatments (annealings) at temperatures in the range 400-1200 °C. The annealings were performed in a furnace purged with argon gas and the duration of each treatment was 30 min.

Infrared absorbance spectra were recorded with a BOMEM DA3.01 Fourier transform spectrometer equipped with a globar light source, a KBr beam splitter, and a liquid-nitrogen-cooled mercury cadmium telluride (MCT) detector. The samples were free standing in the sample compartment of an exchange-gas cryostat, where the temperature was measured with a platinum resistor. The measurements were performed in the temperature range 9-120 K. Polarized light was produced by placing a wire-grid polarizer with KRS-5 substrate in front of the cryostat.

3. VAPOR PHASE GROWN ZnO

3.1 Results

Figure 1 shows typical infrared absorption spectra measured at 9 K for a VP ZnO sample after exposure to a hydrogen and/or deuterium plasma at 350 °C for two hours.[11] The spectra have been measured with the *c* axis of the crystal perpendicular to the beam. Three IR absorption lines at 3611.3, 3349.6, and 3312.2 cm^{-1} are seen in the hydrogen treated sample (top spectra).[11] When hydrogen is substituted by deuterium (mid spectra), the lines shift downwards in frequency to 2668.0, 2486.3, and 2460.7 cm^{-1}, respectively. The frequency ratio of the hydrogen- and deuterium-related lines is 1.35, which is close to the value expected for a harmonic oscillator comprising a hydrogen atom bound to an oxygen atom, $(D_r/H_r)^{1/2}$=1.37,

where H_r and D_r are the reduced masses of the ^{16}O-H and ^{16}O-D species, respectively. The LVM frequencies strongly suggest that the new lines are stretch LVMs of the O-H species. When the sample is treated with a mixed hydrogen and deuterium plasma, four additional lines at 3346.6, 3315.2, 2484.6, and 2463.0 cm^{-1} are observed (bottom spectra in Fig. 1). No extra lines are seen near the 3611.3 and 2668.0 cm^{-1} lines. This implies, that two different defects are responsible for the 3611.3, 3349.6, and 3312.2 cm^{-1} lines. The LVM at 3611.3 cm^{-1} belongs to a defect containing one hydrogen atom, whereas the LVMs at 3349.6 and 3312.2 cm^{-1} originate from a defect containing two *nonequivalent* hydrogen atoms. We label these defects H-I and H-II.

Figure 2 shows the results of isochronal annealing experiments on ZnO samples treated with a hydrogen plasma at 350 °C. It follows from the figure that the H-I defect anneals out at 500 °C, whereas H-II is more stable and disappears from the spectra at 600 °C. Parallel to the annealing of H-I and H-II, another line at 3191.6 cm^{-1} grows in the spectra. It represents a stretch LVM of the well-known Cu-H defect.[7,8] It reaches its maximum intensity at 600 °C, when both H-I and H-II are already gone from the spectra.

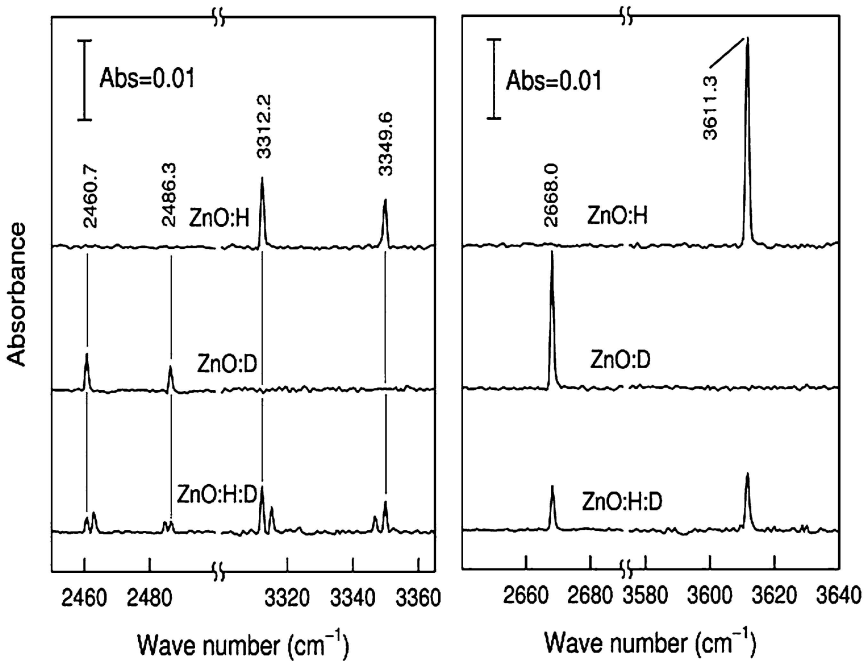

Figure 1. Absorption spectra measured for vapor phase grown ZnO samples at 10 K after: H-, D-, and H+D-plasma treatments at 350 °C. Unpolarized light.

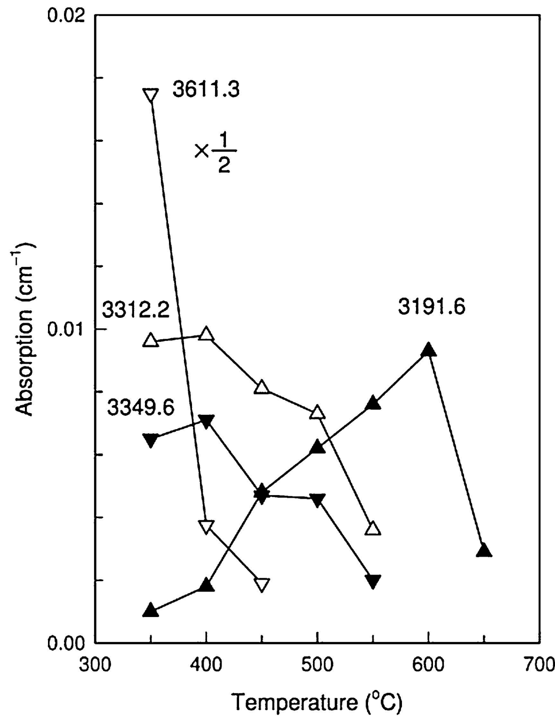

Figure 2. The intensity (integrated absorbance) of the 3191.6, 3312.2, 3349.6, and 3611.3 cm^{-1} lines measured at 10 K for a vapor phase grown ZnO sample vs. the annealing temperature. The sample was exposed to a hydrogen plasma at 350 °C.

Bond angles of the O-H species comprising the H-I and H-II defects with respect to the *c* axis of the crystal may be obtained from the polarized IR absorption spectra. For the stretch modes, the direction of the dipole moment should coincide with the bond direction, provided each bond vibrates independently.

The H-I defect contains only one O-H bond, therefore the assumption that its direction coincides with the induced dipole moment is fulfilled automatically. The H-II defect contains two O-H species and according to the isotope substitution data (see bottom spectrum in Fig. 1), the coupling between the two LVMs of the defect is rather weak, i.e. substitution of one hydrogen atom comprising the defect with deuterium does not change the LVM frequency of the second O-H bond considerably. Thus, the O-H bonds of H-II vibrate independently, and from the polarized absorption spectra we get directly the bond angles.

The results of polarization dependent absorption measurements are presented in Fig.3. It shows the normalized intensities of the LVMs

belonging to the H-I and H-II defects as a function of the polarizer angle (ϑ) with respect to the *c* axis of the sample. As one can see from the figure, the LVM of H-I and the LVM of H-II at 3312.2 cm^{-1} are polarized along the *c* axis, while the LVM of H-II at 3349.6 cm^{-1} is polarized perpendicular to *c*.

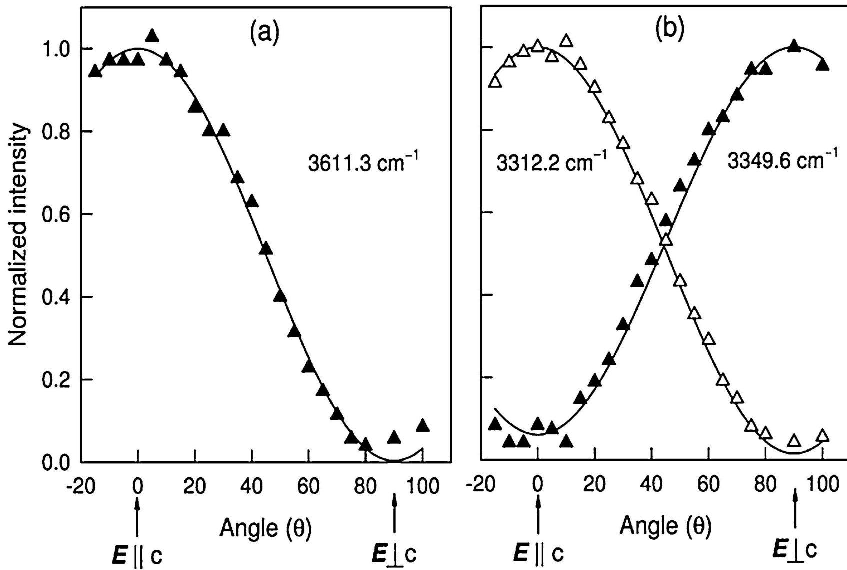

Figure 3. Normalized LVMs intensities of the H-I (a) and H-II (b) defects measured at 10 K as a function of the angle ϑ between polarizer and the *c* axis of the sample.

The best fit to the experimental data shown in Fig. 3 by the solid lines is achieved when the O-H bond of the H-I defect is parallel to the *c* axis with the accuracy of 10°. The same result is obtained for the O-H bond responsible for the 3312.2 cm^{-1} line of H-II, whereas the O-H bond giving rise to the 3349.6 cm^{-1} line is nearly perpendicular to the *c* axis, i.e.: $\vartheta = 100^o$.

3.2 Molecular models

3.2.1 H-I complex

The experimental observations indicate that this defect has one hydrogen atom primarily bound to an oxygen atom with the O-H bond aligned close to the *c* axis. H-I is observed in all our nominally undoped VP ZnO samples. We propose that interstitial hydrogen at the $BC_{||}$ site is the most likely candidate for this center. Here, the symbol "||" stands for the configuration

with the O-H unit parallel to the *c* axis; the other bond directions are denoted by the symbol "⊥". Indeed, the first-principles calculations indicate that in this configuration hydrogen is strongly bound to an oxygen atom, with the neighboring Zn atom relaxing outward by almost 40 % of the bond length.[4] The results of Ref. 4 showed that the $BC_{\parallel}$, $BC_{\perp}$, $AB_{\parallel}$ and $AB_{\perp}$ configurations all have very similar formation energies, although calculations with increased convergence and additional relaxation indicate that $BC_{\parallel}$ may be lower than the others by about 0.1 eV.[11] The experimental results conclusively indicate a configuration oriented parallel to *c*, but experiment alone cannot distinguish between $BC_{\parallel}$ and $AB_{\parallel}$. Both the calculated formation energies[4] and the calculated vibrational frequencies[11] strongly favor $BC_{\parallel}$, indeed, the calculated LVM for $BC_{\parallel}$ is about 300 cm^{-1} lower than the LVM at $BC_{\parallel}$. All these findings point to interstitial hydrogen at $BC_{\parallel}$ (H^{+}_{BC}) as the most likely candidate for the H-I defect.

Nonetheless, we cannot exclude that this interstitial hydrogen might be bound to an impurity. Indeed, the fact that the H-I signal is stable up to about 350 ^{o}C in the annealing experiments (see Fig. 2) may point to a configuration that is more strongly bound than isolated interstitial hydrogen, which has a diffusion barrier of about 0.9 eV.[15] Interstitial hydrogen bound to an isoelectronic or acceptor impurity could account for the H-I line, provided the hydrogen would still be in the $BC_{\parallel}$ configuration.

It is known that the conductivity of ZnO crystals exposed to hydrogen increases.[16] With our samples we have found that the resistivity is reduced from 50 to 5 Ωcm after hydrogen plasma treatment. This finding is definitely consistent with hydrogen being introduced as an interstitial and acting as a shallow donor. However, the resistivity data alone cannot help to distinguish between hydrogen being present as an isolated donor (H^{+}_{BC}) or passivating an acceptor impurity or native defect, since both scenarios increase the *n*-type conductivity of ZnO.

3.2.2 H-II complex

The defect has two non-equivalent hydrogen atoms primarily bound to oxygen atoms. It is observed in all our nominally undoped ZnO samples. One of the two O-H bonds comprising H-II is close to the *c* axis, whereas the other one is nearly perpendicular to *c*. Two interstitial hydrogen atoms, both acting as shallow donors, are unlikely to spontaneously come together, pointing strongly towards involvement of another defect. We believe that V_{Zn} is the most likely candidate. Indeed, the Zn-H bond is much less stable as compared to the O-H bond, and the Zn-H stretch LVM frequencies should be in the range 1500-1700 cm^{-1}, which is too far away from what we see in our spectra.[17] Thus, among the native defects only V_{Zn}, O_i or O_{Zn} decorated

with two hydrogen atoms may explain our data. Interstitial oxygen and oxygen antisites are ruled out by the weak coupling between the two LVMs of H-II. Therefore, we propose that a zinc vacancy decorated with two hydrogen atoms, $V_{Zn}H_2$, is the most probable model for H-II.[11]

This assignment is also supported by the results of cathodoluminescence studies of ZnO after hydrogen plasma treatment. Sekiguchi *et al.* have shown that such a treatment made at 400 ^{o}C fully suppresses the, so-called, "green" luminescence band centered around 2.2 eV.[18] We have observed the same behavior by means of photoluminescence for our ZnO samples. On the other hand, based on first-principles pseudopotential calculations, Kohan *et al.* suggested that V_{Zn} is involved in the "green" luminescence in ZnO.[19] Thus, passivation of V_{Zn} with two hydrogen atoms leads to a reduction of the "green" luminescence, and appearance of the H-II LVMs.

As mentioned above, the resistivity of our ZnO samples is reduced from 50 to 5 Ω cm after hydrogen plasma treatment, which is also in favor of the $V_{Zn}H_2$ model. Indeed, passivation of V_{Zn} acting as an acceptor in ZnO should increase the *n*-type conductivity of the samples.

4. HYDROTHERMALLY GROWN ZnO

We found that hydrogen influences on the *n*-type conductivity of the VP ZnO and suggested molecular structures responsible for this observation. It follows from these findings that hydrogen does not seem to be the *main* source for the *n*-type conductivity of ZnO because all hydrogen-related centers found in VP ZnO appear only after intentional hydrogenation. However, this situation changes in the case of hydrothermally grown material.

Figure 4 shows typical IR absorption spectrum of an as-grown HT ZnO sample.[12] The lines at 4216.2, 4240.0, and 4246.6 cm^{-1} were previously identified as internal transitions of substitutional Ni^{2+} split by the local crystalline field.[20,21] The new lines at 3335.6, 3482.9, 3516.3, and 3577.3 cm^{-1} are located in the region characteristic of O-H stretch modes.[17]
An additional deuterium plasma treatment at 350 ^{o}C results in one additional IR absorption line at 2644.4 cm^{-1}. The frequency ratio of the 3577.3 cm^{-1} line and the line at 2644.4 cm^{-1} is 1.35, which is close to the value expected for a harmonic oscillator consisting of a hydrogen atom bound to an oxygen atom (1.37). Based on this, we identify the 3577.3 cm^{-1} line as a LVM of an O-H bond. No extra lines appear in the spectra after H+D plasma treatment. This strongly indicates that the defect responsible for the 3577.3 cm^{-1} line includes a single hydrogen atom.

Thus, in contrast to ZnO grown from the vapor phase, *as-grown* hydrothermal ZnO contains hydrogen. Note that we could not find any deuterium replica of the 3335.6, 3482.9, and 3516.3 cm^{-1} lines. Hence, the nature of these remains unknown.

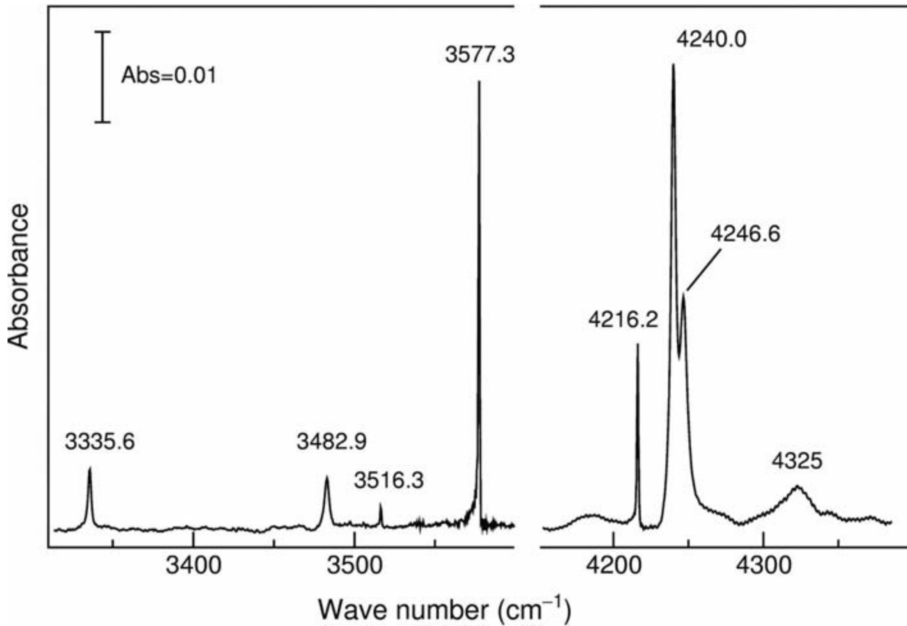

Figure 4. Absorption spectra measured at 10 K for an as-grown hydrothermal ZnO sample.

All the lines presented in Fig. 4 display distinct polarization properties, which is demonstrated in Fig. 5. The figure shows the IR absorption spectra measured for an as-grown HT ZnO sample with the polarization vector of the absorbed light parallel (top spectrum) and perpendicular (bottom spectrum) to the *c* axis of the crystal. The polarization properties of the Ni-related lines at 4216.2, 4240.0, and 4246.6 cm^{-1} are identical to those reported in Ref. 21. It follows also from the figure that the 3577.3 cm^{-1} line is predominantly polarized with the *c* axis of the crystal, which implies that the O-H bond of the defect is aligned close to *c*. We label this defect as $H\text{-}I^*$. The $H\text{-}I^*$ defect is extremely stable: The 3577.3 cm^{-1} line does not change its intensity even after annealing at 1100 ^{o}C for 30 min. Only thermal treatment at 1200 ^{o}C for several hours eliminates the signal from the spectra. Interestingly, subsequent hydrogen plasma treatment at 350 ^{o}C does not result in the formation of this defect. No changes in the Ni^{2+} signals occur

after thermal and hydrogen plasma treatment. The last finding strongly indicates that the H-I* defect does not include a substitutional Ni atom, as tentatively suggested in Ref. 12.

We could not establish a correlation/anticorrelation between the 3577.3 cm^{-1} line and any other spectroscopic signal of HT ZnO. We take this as an indication that the center giving rise to this line is related to the presence of native defects. The LVM frequency of the center points to V_{Zn}, O_i, or O_{Zn} as possible candidates. Of these three, we rule out V_{Zn} because, as we have seen

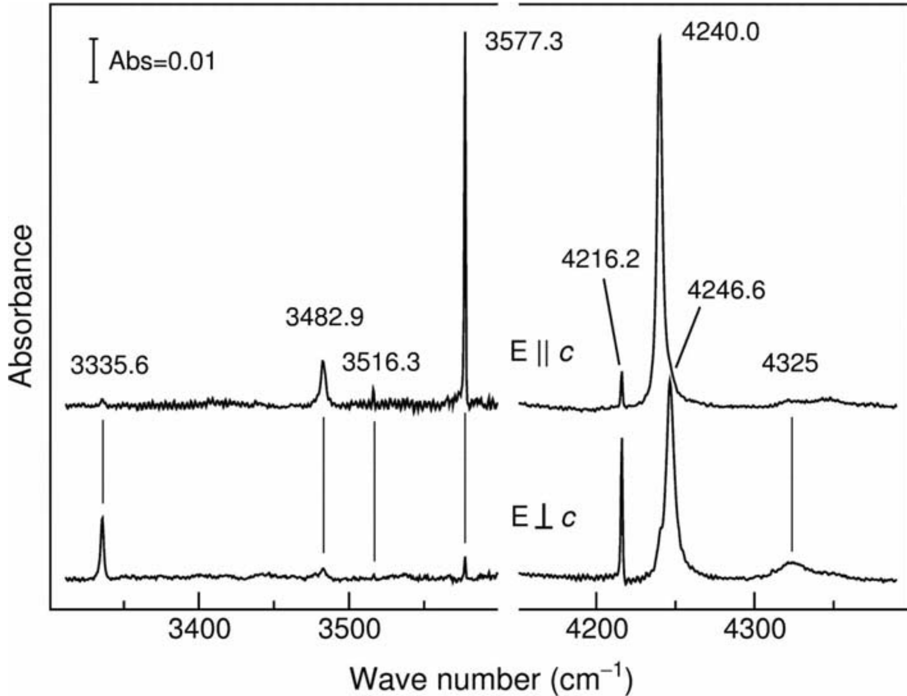

Fig. 3

Figure 5. Polarized absorption spectra measured at 10 K for a virgin hydrothermally grown ZnO sample: top E || *c*, bottom E ⊥ *c*.

in the previous section, zinc vacancies tend to bind two hydrogen atoms resulting in $V_{Zn}H_2$ defects, which are not stable at annealing temperatures above 600 ^oC.

Indirect indication that O_i or O_{Zn} might be responsible for H-I* is the annealing temperature of this center. It is known that ZnO crystals, when heated in air at temperatures above 1000 ^oC become nonstoichiometric in composition through formation of excess zinc atoms resulting from the more rapid loss of oxygen atoms.[22] It means that of all native defects O_i and O_{Zn}

should be destroyed first at elevated temperatures. This may explain why HT ZnO annealed at 1200 ^{o}C for several hours and subsequently treated with a hydrogen plasma does not reveal the 3577.3 cm^{-1} line in the IR absorption spectra.

Nonetheless, participation of some other impurity is not excluded. Further theoretical studies in combination with other experimental techniques such as EPR, electron-nuclear double resonance (ENDOR), etc., are needed to establish microscopic structure of the H-I* defect.

5. CONCLUSIONS

Vibrational spectroscopy has been employed to study hydrogen-related defects in ZnO samples grown by different techniques. Hydrogenation of vapor phase grown ZnO results in three IR absorption lines at 3611.3, 3349.6, and 3312.2 cm^{-1}. The 3611.3 cm^{-1} line corresponds to a defect labeled H-I that contains a single hydrogen atom. We tentatively assign H-I to an interstitial H at a $BC_{||}$ site. The lines at 3349.6 and 3312.2 cm^{-1} are associated with a defect labeled H-II that contains two hydrogen atoms. The H-II defect is identified as a hydrogenated Zn vacancy ($V_{Zn}H_2$).

Absorption spectra of as-grown hydrothermal ZnO samples reveal a number of lines located in the region characteristic of O-H stretch LVMs. Based on the isotope substitution experiments as well as on the polarization studies, it is shown that at least one of these lines, at 3577.3 cm^{-1}, originates from a defect containing one O-H bond primarily aligned with the *c* axis of the crystal and labeled as H-I*. The presence of a native defect is tentatively suggested.

ACKNOWLEDGMENTS

The authors greatly acknowledge C. G. Van de Walle, and B. Bech Nielsen for helpful discussions, R. Helbig for supplying the ZnO samples, and the Russian foundation for Basic Research (Grant No. 02-02-16030).

REFERENCES

1. D.C. Look, D.C. Reynolds, J.R. Sizelove, R.L. Jones, C.W. Litton, G. Cantwell, and W.C. Harsch, *Solid State Comm.*, **105**, 399 (1998).
2. M. Joseph, H. Tabata, and T. Kawai, *Jpn. J. Appl. Phys.*, **38**, L1205 (1999).

3. D. C. Look, J. W. Hemsky, nad J. R. Sizelove, *Phys. Rev. Lett.*, **82**, 2552 (1999) and references therein.
4. C. G. Van de Walle, *Phys. Rev. Lett.*, **85**, 1012 (2000).
5. S.F.J. Cox, E.A. Davis, S.P. Cottrell, P.J.C. King, J.S. Lord, J.M. Gil, H.V. Alberto, R.C. Vilão, J. Piroto Duarte, N. Ayres de Campos, A. Weidinger, R.L. Lichti, and S.J.C. Irvine, *Phys. Rev. Lett.*, **86**, 2601 (2001).
6. D.M. Hofmann, A. Hofstaetter, F. Leitner, H. Zhou, F. Henecker, B.K. Meyer, S.B. Orlinskii, J. Schmidt, and P.G. Baranov, *Phys. Rev. Lett.*, **88**, 45504 (2002).
7. F. G. Gärtner and E. Mollwo, *phys. status solidi B*, **89**, 381 (1978).
8. F. G. Gärtner and E. Mollwo, *phys. status solidi B*, **90**, 33 (1978).
9. M. D. McCluskey, S. J. Jokela, K. K. Zhuravlev, P. J. Simpson, and K. G. Lynn, *J. Appl. Phys.*, **81**, 3807 (2002).
10. N. H. Nickel and K. Fleischer, *Phys. Rev. Lett.*, **90**, 197402 (2003).
11. E. V. Lavrov, J. Weber, F. Börrnert, C. G. Van de Walle, and R. Helbig, *Phys. Rev. B*, **66**, 165205 (2002).
12. E. V. Lavrov, *Physica B*, **340-342**, 195 (2003).
13. G. Müller and R. Helbig, *J. Phys. Chem. Solids*, **32**, 1971 (1971).
14. R. Helbig, *J. Cryst. Growth*, **15**, 25 (1972).
15. D. G. Thomas and J. J. Lander, *J. Chem. Phys.*, **25**, 1136 (1956).
16. E. Mollwo, *Z. Phys.*, **138**, 478 (1954).
17. *CRC Handbook of Chemistry and Physics, 82nd edition*, David R. Lide (ed.), CRC Press LLC, 2001-2002, p. **9**-77.
18. T. Sekiguchi, N. Ohashi, and Y. Terada, *Jpn. J. Appl. Phys.*, **36**, L289 (1997).
19. A. F. Kohan, G. Ceder, D. Morgan, and C. G. Van de Walle, *Phys. Rev. B*, **61**, 15019 (2000).
20. U. Kaufmann, P. Koidl, and O. F. Schirmer, *J. Phys. C*, **6**, 310 (1973).
21. H. J. Schulz and M. Thiede, *Phys. Rev. B*, **35**, 18 (1987).
22. H. E. Brown, *Zinc Oxide: Properties and Applications*, New York, Int. Lead Zinc Research Organization, 1976.

Chapter 13

INFLUENCE OF THE HYDROGEN CONCENTRATION ON H BONDING IN ZINC OXIDE

N. H. Nickel
Hahn-Meitner-Institut Berlin, Kekuléstr. 5, 12489 Berlin, Germany

Abstract: Despite of the recent developments the properties of hydrogen in ZnO are not fully understood. While in some ZnO single crystals the amount of H detected by gas effusion experiments is similar in concentration to the number of free electrons, a large number of samples exhibits much higher H concentrations. Raman backscattering experiments reveal that a significant amount of H is accommodated at sites that do not give rise to enhanced conductivity; a large amount of H is bound to carbon and nitrogen impurities forming $C–H_X$ and N–H complexes. Depending on the method of the sample preparation H concentrations as high as 3.0×10^{21} cm^{-3} have been observed. To gain further insight into the properties of H in ZnO data obtained from H effusion measurements of single crystal and sputter deposited ZnO have been analyzed to deduce the hydrogen binding energy as a function of the H chemical potential. In samples with a low H content six peaks were observed in the H density-of-states distribution. With increasing H concentration the peaks broaden. In addition, an increase of the H concentration results in a pronounced increase of the average H binding energy. This observation indicates that the properties of H expand well beyond the formation of donors and the neutralization of impurities and deep defects.

Key words: Hydrogen binding energy, hydrogen local vibrational modes, hydrogen concentration, hydrogen density-of-states distribution

1. INTRODUCTION

Recently, there has been a significant increase of research in the field of zinc oxide. This is mainly driven by its extraordinary electrical and optical properties that enable a variety of applications ranging from piezoelectrical

N.H. Nickel and E. Terukov (eds.),
Zinc Oxide – A Material for Micro- and Optoelectronic Applications, 145–155.
© 2005 *Springer. Printed in the Netherlands.*

devices, transparent conducting layers for solar cells, transparent thin-film transistors to ultra violet light emitting diodes and lasers. Almost all of these applications require the control of the conductivity from n-type to p-type. While n-type doping can be controlled easily the reproducible fabrication of p-type ZnO is a major obstacle that has to be overcome to allow for the successful development of LEDs and UV lasers. The major drawback is the fact that zinc oxide generally exhibits n-type conductivity that has been attributed to the presence of native defects, traditionally. However, recent theoretical and experimental investigations have identified a new source that can easily account for the observed n-type conductivity. Van de Walle[1] suggested that hydrogen atoms can act as shallow donors. This prediction has been confirmed experimentally by muon spin rotation[2] and electron nuclear double resonance measurements.[3] In addition, Hall-effect measurements revealed the presence of a second shallow donor.[3]

Thus, to achieve p-type doping of ZnO a number of aspects have to be considered. First of all the formation of hydrogen shallow donors has to be prevented or their concentration has to be minimized. Recently it has been shown that a simple post anneal of state-of-the-art ZnO at 850 °C causes the dissociation of hydrogen shallow donors which results in a decrease of the free carrier concentration from 1×10^{17} cm^{-3} to 6×10^{16} cm^{-3}.[4]

A suitable acceptor for ZnO is nitrogen. In fact, substitutional nitrogen incorporated at an oxygen site has been observed using electron-paramagnetic-resonance (EPR) measurements.[5] Although nitrogen can be incorporated as an acceptor the presence of hydrogen could give rise to the formation of N-H complexes that are electrically neutral. Hence it is of great importance to investigate the properties of hydrogen in ZnO.

In this paper, we present information on hydrogen bonding and hydrogen concentration in state-of-the-art single crystal and sputter deposited ZnO thin films. Raman backscattering measurements reveal 6 H-related local vibrational modes in the wave number range between 2800 and 3150 cm^{-1}. Hydrogen effusion measurements clearly show that the observed local vibrational modes are due to the presence of H in ZnO. From the effusion data the H density-of-states (DOS) distribution is derived, which provides detailed insight into H binding energies. In single crystal ZnO reveals six peaks in the H DOS. On the other hand, in sputtered ZnO thin films the total H concentration increases by up to 5 orders of magnitude. This is accompanied by a pronounced increase of the average H binding energy.

2. EXPERIMENTAL

Two sets of samples were used in this investigation. The first set consists of commercially available ZnO single crystals with a (0001) orientation and an "O" face. These crystals were fabricated by Eagle-Picher. The second set of samples were Al-doped ZnO thin-films. These specimens were grown on quartz substrates by dc magnetron sputtering at a power density of 22.6 W/cm^2 and a substrate temperature of 150 °C. The ZnO films had a thickness ranging from 0.11 µm to 3.83 µm. From a structural point of view the sputtered ZnO samples were composed of columnar grains with an average grain diameter of about 0.16 µm. The length of the grains is only limited by the thickness of the film. The samples were characterized with Raman backscattering experiments in a conventional macro-Raman setup using the 488 nm laser line of an Ar^+ ion laser. Information on hydrogen content and H bonding was obtained from H effusion measurements. For this purpose the samples were placed in an ultrahigh vacuum system and heated to a temperature of up to 950 °C with a constant heating rate of 20 K/min. During the temperature ramp the flux of molecular hydrogen was measured with a quadrupole mass spectrometer. Prior to each measurement background spectra were taken and subsequently subtracted from the sample data. To obtain absolute values for the H_2 flux the effusion spectra were calibrated by measuring the know neon flux through a capillary.

3. HYDROGEN LOCAL VIBRATIONAL MODES

Raman backscattering measurements were performed in the wave number range between 200 and 4300 cm^{-1}. Besides the well known phonon modes that are located between 200 and 800 cm^{-1} additional lines were observed at wave numbers ranging from 2800 to 3150 cm^{-1} (see spectrum (a) in Fig. 1). At higher wave numbers Raman lines were not observed.

The local vibrational modes (LVMs) shown in Fig. 1 are due to the presence of hydrogen. This is supported by Raman backscattering experiments performed after hydrogen effusion experiment. Spectrum (b) in Fig. 1 was obtained after the sample was heated up to 950 °C in an effusion experiment. The measured molecular hydrogen flux as a function of temperature is plotted in Fig. 2. The background signal taken in a separate measurement was subsequently subtracted from the data. The spectrum shows a maximum H_2 flux at a temperature of 473 °C. From the H_2 flux the total hydrogen concentration can be determined by integration and taking into account the heating rate and sample thickness. The H concentration

amounts to 5.2×10^{16} cm^{-3}. This value is remarkably close to the concentration of shallow donors that was attributed to the presence of hydrogen donor states in state-of-the-arte undoped ZnO [6]. After the diffusion experiment the sample is depleted of hydrogen and a second scan merely yields the background data taken without a sample. Raman backscattering measurements performed on H depleted specimens did not show any local vibration modes. This clearly indicates that the LVMs observed between 2800 and 3150 cm^{-1} are due to the presence of H atoms. However, when H acts as a donor in ZnO it has to be accommodated in a bond center site or anti bonding site forming an O-H bond and the local vibration modes should occur at 3680 cm^{-1} and 3550 cm^{-1}, respectively.[1] These values for the LVMs are close to those of free O-H molecules and were recently observed in single crystal ZnO.[7,8] This raises the question regarding the origin of the observed hydrogen LVMs.

Local vibrational modes between 2800 and 3150 cm^{-1} (see Fig. 1) have been observed in a number of semiconductors such as amorphous silicon carbide,[9] GaAs,[10] and GaN.[11] In these materials the vibrational modes are assigned to symmetric and antisymmetric stretching modes of CH_X complexes with x = 1, 2, 3. Therefore, the vibrational modes located at 2854 cm^{-1}, 2890 cm^{-1}, 2918 cm^{-1}, 2948 cm^{-1}, and 2988 cm^{-1} should be due to the

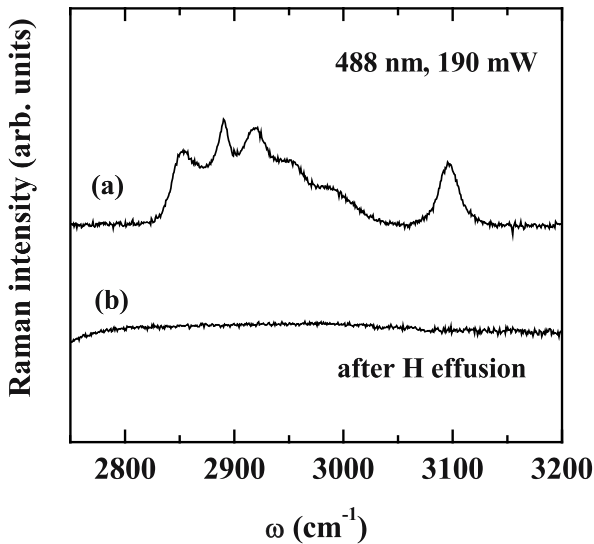

Figure 1. Raman backscattering spectra of single crystal ZnO before (a) and after hydrogen effusion (b). The measurements were performed using the 488 nm line of an Ar^+ laser and a laser power of 190 mW. Background data were subtracted.

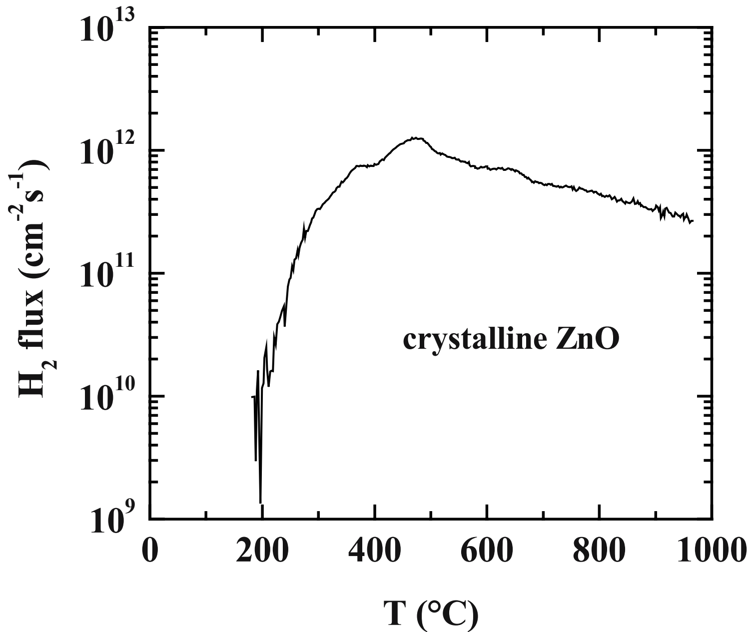

Figure 2. Molecular hydrogen flux of single crystal ZnO as a function of temperature. The sample was heated with a heating rate of 20 K/min.

stretching modes of C-H, symmetric stretching modes of $C\text{-}H_3$, symmetric stretching modes of $C\text{-}H_2$, antisymmetric stretching modes of $C\text{-}H_3$, and antisymmetric stretching modes of $C\text{-}H_2$, respectively. The measured LVMs (see Fig. 1) are in excellent agreement with CH_X stretching modes except for the local vibrational mode located at 2988 cm^{-1} that is shifted to higher wave numbers by about 65 cm^{-1}.

The H local vibrational mode at 3096 cm^{-1} has been assigned to N-H centers. This assignment is consistent with a recent theoretical investigation by Van de Walle[12] who calculated a vibrational frequency of approximately 3100 cm^{-1} for the N-H center. It is interesting to note that this frequency deviates by about 10 % from the value observed for the N-H vibration in ammonia molecules.

The results of this section clearly demonstrate that hydrogen does not only form shallow donors in ZnO. The properties of H and the underlying chemistry are manifold. Apparently a high concentration of H atoms can be accommodated in single crystal ZnO without the need to form a significant number of shallow donors. The presence of impurity-hydrogen complexes is one important aspect that has to be investigated further.

4. HYDROGEN DENSITY OF STATES DISTRIBUTION

From hydrogen effusion spectra as shown in Fig. 2 a variety of information such as the H concentration, diffusion coefficient, and hydrogen binding energies can be obtained. This section will focus on the H binding energies. However, to avoid errors in the analysis it is important to know if H transport from the bulk to the surface is governed by molecular or atomic hydrogen diffusion. This question can be solved either by changing the heating rate of the effusion experiment or by measuring samples of various thicknesses. In both cases peaks observed in the effusion spectra should shift to different temperatures; with decreasing heating rate and increasing sample thickness the maxima of the H_2 flux should move to higher temperatures. Fig. 3 shows H effusion spectra obtained on sputter deposited ZnO thin films with thicknesses varying from 0.11 to 3.83 μm.

The effusion spectra of the sputter deposited ZnO films reveal two pronounced maxima around 420 °C and 600 °C. A detailed analysis of the spectra yielded the thickness dependence of the maxima (see Fig. 4). Both

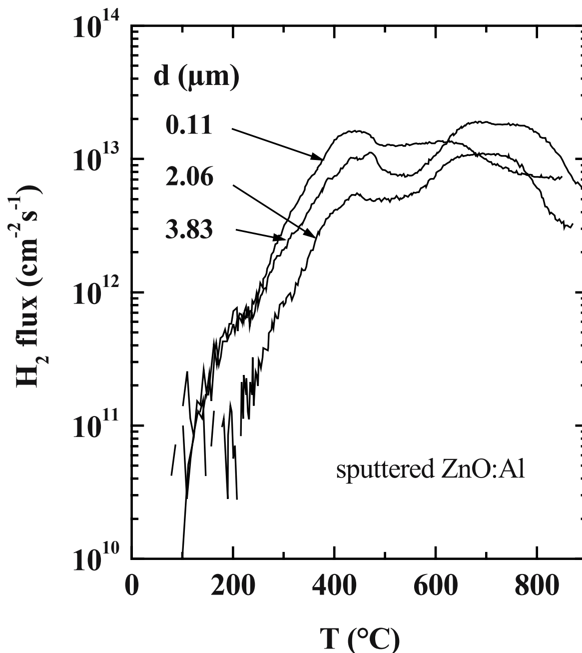

Figure 3. Molecular hydrogen flux vs temperature for sputter deposited ZnO thin films. The experiments were performed with a heating rate of 20 K/min. For clarity only three effusion spectra are plotted.

Table 1. Hydrogen concentration in single crystal and sputter deposited ZnO. The asterisk marks single crystal ZnO.

Thickness (μm)	H concentration (cm^{-3})
0.11	3.3×10^{21}
0.5	7.9×10^{20}
2.06	1.0×10^{20}
3.83	1.0×10^{20}
500 (*)	5.2×10^{16}

effusion peaks shift to higher temperatures as the sample thickness increases. This behavior indicates that the effusion process is governed by atomic hydrogen diffusion from the bulk to the surface.[15]

When comparing the data of Fig. 3 with the H_2 flux of the single crystal ZnO (Fig. 2) it is obvious that the total H concentration in sputtered ZnO is significantly enhanced. A summary of the H concentration of the investigated specimens is given in Tab. 1. The highest H content is observed in the thinnest ZnO film. A more detailed investigation revealed that the H concentration does not vary with thickness. This effect is observed only because the ZnO thin-films were deposited in a single run without breaking the vacuum and starting with the thinnest sample. The large amount of H incorporated in the thin films originates from the residual water vapor in the vacuum system that dissociates upon electron impact during sputtering.[13, 14]

Since the effusion experiment is governed by the diffusion of monatomic H, the hydrogen binding energy can be deduced from effusion spectra applying the following formalism. The total H content, C_{H}, is related to the hydrogen density-of-states distribution, $N_{\mathrm{H}}(E)$ by

$$C_H = \int_{-\infty}^{\infty} N_H(E) f(T, E, \mu_H) dE \tag{1}$$

where E is the H binding energy, T the temperature, f is the occupation function, and μ_{H} is the hydrogen chemical potential. Since $\partial f/\partial \mu_{\mathrm{H}}$ has its maximum value at $E \approx \mu_{\mathrm{H}}$ the H DOS distribution can be estimated by[16]

$$N(\mu_H) \approx \frac{\partial C_H}{\partial \mu_H}. \tag{2}$$

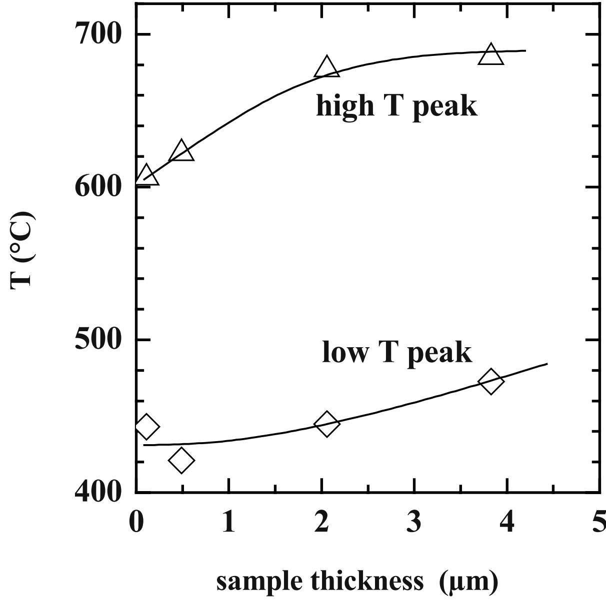

Figure 4. Temperature of the effuson peaks as a function of the sample thickness of sputtered ZnO thin films.

The hydrogen chemical potential can be estimated using the following equation

$$E - \mu_H = -kT \ln\left(\frac{F}{F_0}\right) \tag{3}$$

where k is Boltzmann's constant, T the temperature, F the molecular hydrogen flux, and F_0 a prefactor. The prefactor can be estimated using the equation $d \times F_0 = 2\nu a N_{\mathrm{surface}}$, where a is the mean free path, ν is an attempt frequency, and N_{surface} is the concentration of H surface states. With reasonable values of $a \approx 3\times10^{-8}$ cm, $\nu \approx 10^{13}$ Hz, and $N_{\mathrm{surface}} \approx 10^{15}$ cm^{-3}, a value of $d \times F_0 \approx 6\times10^{20}$ s^{-1}cm^{-1} is obtained. This prefactor represents an average value. However, since F_0 is in the argument of logarithm when computing the H chemical potential even an order of magnitude error results in an error of only 0.1 eV in the absolute energy scale.

Fig. 5 shows the H density-of-states distribution derived from effusion spectra. The lowest H DOS is obtained for single crystal ZnO (Fig. 5a). Deconvolution of the N_H reveals that the distribution is composed of six peaks; the peak positions are marked in the figure by arrows

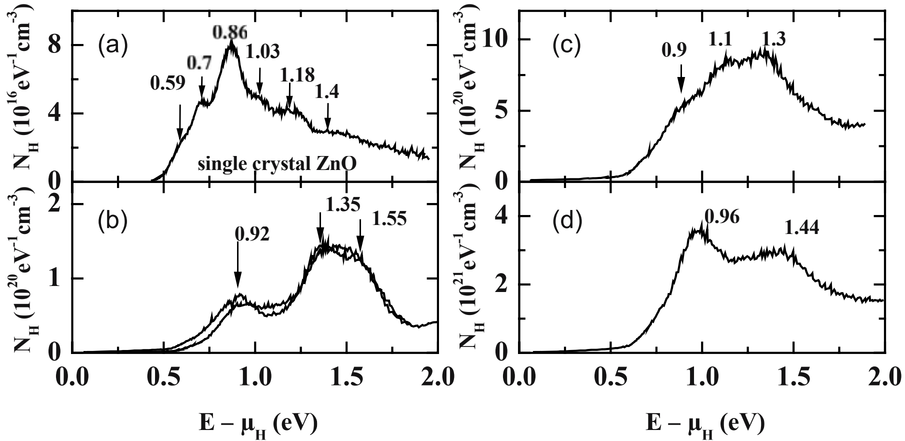

Figure 5. Hydrogen density-of-states distribution in single crystal ZnO (a) and Al doped ZnO thin films (b) – (d). Zero energy corresponds to the H transport site.

For sputter deposited ZnO the H content and thus N_H increases up to 8×10^{21} $cm^{-3}eV^{-1}$ (see Fig. 5d). The data plotted in Fig. 5(b) show an important result. The H effusion spectra were obtained on 2 different samples with different thickness and the analysis yielded identical density-of-states distributions indicating that the method to derive the H DOS is reproducible and reliable.

Further analyzing the data in Fig. 5 reveals a striking observation. While in single crystal ZnO about 45 % of all H atoms are accommodated with binding energies of less than 1.0 eV with respect to the H transport site an increase of the H concentration is accompanied with an increase of N_H in the energy range 1.0 eV < $E - \mu_H$ < 1.8 eV. With increasing H content the amount of H atoms accommodated with binding energies of less than 1.0 eV decreases to about 25 %. This suggests that H creates larger clusters presumable in a similar way as it has been observed in other semiconductors.[17]

5. SUMMARY

In summary, Raman backscattering measurements showed the presence of C-H_X and N-H local vibrational modes in single crystal ZnO. Heating the specimens to temperatures of up to 950 °C caused hydrogen out diffusion. After dehydrogenation the local vibrational modes disappeared indicating that they are related to the presence of H. From H effusion measurements the

total H concentration of the samples was determined. Single crystal ZnO exhibits the lowest H concentration while sputter deposited ZnO thin-films contain H concentrations of up to $3\times10^{21}cm^{-3}$. The H content depends on the precondition of the deposition chamber; e.g.: the amount of residual water vapor. From the effusion spectra the H density-of-states distribution was derived. Single crystal ZnO reveals a H DOS that deconvolutes into six peaks. With increasing H concentration an pronounced increase of the H binding energies is observed. In sputtered ZnO about 75 % of the H atoms are incorporated with binding energies larger than 1.0 eV while in single crystal ZnO only about 55 % of the accommodated H atoms reveal binding energies larger than 1.0 eV.

ACKNOWLEDGEMENT

The author is grateful to C. Klimm for the preparation of the ZnO thin films and to K. Brendel for stimulating discussions and his constant interest in the topic.

REFERENCES:

1. C. G. Van de Walle, *Phys. Rev. Lett.* **85**, 1012 (2000).
2. S. F. Cox, E. A. Davis, S. P. Cottrell, P. J. C. King, J. S. Lord, J. M. Gil, H. V. Alberto, R. C. Vilão, J. Pironto Duarte, N. Ares de Campos, A. Weidinger, R. L. Lichti, and S. J. C. Irving, *Phys. Rev. Lett.* **86**, 2601 (2001).
3. D. M. Hofmann, A. Hofstaetter, F. Leiter, H. Zhou, F. Henecker, B. K. Meyer, S. B. Orlinskii, J. Schmidt, and P. G. Baranov, *Phys. Rev. Lett.* **88**, 045504 (2002).
4. B. K. Meyer, H. Alves. D. M. Hofmann, W. Kriegseis, D. Forster, F. Bertram, J. Christen, A. Hoffmann, M. Straßburg, M. Dworzak, U. Haboeck, and A. V. Rodina, *phys. stat. sol (b)* **241**, 231 (2004), and references therein.
5. N. Y. Garces, N. C. Giles, L. E. Halliburton, G. Cantwell, D. B. Eason, D. C. Reynolds, and D. C. Look, *Appl. Phys. Lett.* **80**, 1334 (2002).
6. D. C. Look, J. W. Hemsky, and J. R. Sizelove, *Phys. Rev. Lett.* **82**, 2552 (1999).
7. M. D. McCluskey, S. J. Jokela, K. K. Zhuravlev, P. J. Simpson, and K. G. Lynn, *Appl. Phys. Lett.* **81**, 3807 (2002).
8. E. V. Lavrov, J. Weber, F. Börrnert, C. G. Van de Walle, R. Helbig, *Phys. Rev. B* **66**, 165205 (2002).
9. S.-Y. Lin, *J. Appl. Phys.* **80**, 1399 (1996), and references therein.
10. D. M. Joseph, R. Balagopal, R. F. Hicks, L. P. Sadwick, and K. L. Wang, *Appl. Phys. Lett.* **53**, 2203 (1988).
11. M. O. Manasreh, J. M. Baranowski, K. Pakula, H. X. Jiang, and J. Lin, *Appl. Phys. Lett.* **75**, 659 (1999).
12. C. G. Van de Walle, presentation at the MRS Spring Meeting in San Francisco 2004.
13. J. W. Bozzelli and R. B. Barat, *Plasma Chem. Plasma Proc.* **8**, 293 (1983).

14. S. Roychowdhury, U. K. Roychowdhury, and M.Venugopalan, *Plasma Chem. Plasma Proc.* **2**, 157 (1982).
15. W. Beyer, in *Hydrogen in Semiconductors II*; Vol. **61**, edited by N. H. Nickel (Academic Press, San Diego, 1999), p. 165.
16. W. B. Jackson, A. J. Franz, H.-C. Jin, J. R. Abelson, and J. L. Gland, *J. Non-Cryst. Sol.* **227-230**, 143 (1998).
17. *Hydrogen in Semiconductors II*, edited by N. H. Nickel (Academic Press, San Diego, 1999), Vol. 61. p. 165.

PART IV: FUNDAMENTAL PROPERTIES

Chapter 14

VALENCE BAND ORDERING AND MAGNETO-OPTICAL PROPERTIES OF FREE AND BOUND EXCITONS IN ZnO

A.V. Rodina[1], M. Strassburg[2], M. Dworzak[2], U. Haboeck[2], A. Hoffmann[2], H. R. Alves[3], A. Zeuner[3], D. M. Hofmann[3], and B. K. Meyer[3]
[1]A.F. Ioffe Physico-Technical Institute, St.-Petersburg, Russia; [2]Institute of Solid State Physics, Technical University of Berlin, Berlin, Germany; [3]I. Physics Institute, Justus-Liebig-University Giessen, Giessen, Germany

Abstract: The Zeeman splitting of free and bound excitons is analysed theoretically for both Γ_7 and Γ_9 symmetries of the upper valence band. The Zeeman splitting of the Γ_7 (Γ_9) holes in magnetic field parallel to the hexagonal ***c*** axes of the crystal is found to be smaller (larger) than the Zeeman splitting of the electrons. The magnetic-field dependence of the bound exciton optical transition energies measured in the Faraday geometry with right and left circular polarized light can be well described with Γ_7 as well as with Γ_9 holes. However, the fitting of the experimental dependence of the Zeeman splitting on the angle between magnetic field and ***c*** axis proves the Γ_7 symmetry of the holes involved in all low temperature transitions and thus of the upper valence band in bulk ZnO. The determined parameters are in excellent agreement with known experimental data on the fine structure of the free exciton ground state in ZnO. The hole *g*-factors determined for excitons bound to an ionized and neutral impurity centers are close to each other and to the *g*-factor calculated for the Γ_7 hole in the free exciton ground state. This points to a donor character of the neutral impurity centers. This conclusion is confirmed by temperature dependent magneto-transmission and magneto-luminescence measurements.

Key words: Photoluminescence, magneto-luminescence, Zeeman effect, g-factor, excitons, valence band symmetry

1. INTRODUCTION

Bulk ZnO is a direct band gap wurtzite semiconductor with the valence band maximum split by the crystal field and spin-orbit interaction. The

N.H. Nickel and E. Terukov (eds.),
Zinc Oxide – A Material for Micro- and Optoelectronic Applications, 159–170.
© 2005 *Springer. Printed in the Netherlands.*

symmetry of the upper valence subband (A-subband) has been the subject of controversy (Γ_9 or Γ_7 character) for more than 40 years.[1-15] Based on the polarization properties of the free exciton transitions, the inverted ordering of the valence subbands as shown in Figure 1(a) was first suggested by Thomas[1] and supported later in many articles.[3-7,11-18,21] However, different argumentation led some researches[2,8-10,19,20] to the conclusion that the ordering of valence subbands in ZnO is the same as in other wurtzite semiconductors like GaN, CdSe, CdS (see Figure 1(b)).

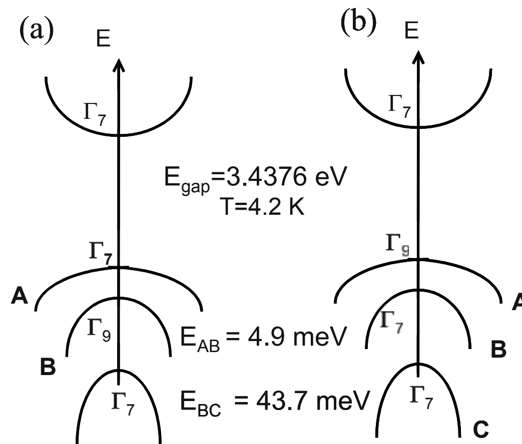

Figure 1. Energy band structure and the symmetry of the free exciton ground state in wurtzite-type semiconductors for (a) ZnO and (b) GaN, CdSe, CdS.

Magneto-optical studies are a powerful tool to distinguish the symmetry of the free and bound exciton states.[5-8,14-21] Unfortunately, most of the magneto-optical investigations in ZnO were incomplete and allowed both interpretations concerning the symmetry of the holes involved. For example, recent magneto-optical studies[8] of the free A exciton fine structure were interpreted with the assumption of the Γ_9 symmetry for the valence band maximum, while the more elaborated theoretical analysis[11] enabled the explanation of the same date applying the Γ_7 symmetry for the A valence band. To resolve this controversy, detailed theoretical and experimental studies of the magneto-optical properties of bound excitons in bulk ZnO were undertaken.[14] In this paper we show that the detailed comparison between the theoretical predictions and the experimentally observed Zeeman behavior of free excitons and bound exciton complexes in bulk ZnO confirms the Γ_7 symmetry of the upper valence subband.

2. THEORY

The inverted ordering of the valence subbands (Fig. 1(a)) can be understood in terms of an effective negative spin-orbit splitting. The first-principles band structure calculations of Ref. 11 confirmed the inverted ordering in bulk ZnO. It was found that the negative spin-orbit coupling arises from the contribution of the lower lying Zn *3d* bands. The optimal value for the Zn *3d* bands position was derived which gives good agreement with the basic valence band splittings.[11] A self consistent set of the effective mass parameters obtained from these band structure calculations was used in the analysis of the exciton binding energies and effective *g* values.[11]

In Figure 2 we sketch all possible transitions from the free exciton and from the exciton bound to the ionized impurity center corresponding to the calculated values[11] of the hole effective *g*-factors. We consider the holes from the Γ_7 (case (a)) and Γ_9 (case (b)) valence bands. We take in account only the short-range exchange interaction in Fig. 2 and do not consider the long range exchange interaction or polariton effects. The zero field exchange splitting between the Γ_1 and Γ_2 exciton states is neglected in Fig. 2 (a) as it is known to be small in ZnO.[11] The zero field spin-exchange splitting of the Γ_1/Γ_2 and Γ_5 exciton states (case (a)) or Γ_6 and Γ_5 exciton states (case (b)) is about 0.95 meV[23] and governs the Zeeman behavior in the magnetic field perpendicular to the ***c*** axis. In the magnetic field parallel to the ***c*** axis the linear Zeeman splitting of the Γ_5 exciton state is expected. The Γ_6 state and the Γ_1/Γ_2 states mixed by the magnetic field also show the linear splitting. The splitting is given by

$$\mu_B B g_{exc} = \mu_B B(g_h^{//} \pm g_e), \quad (1)$$

where μ_B is the (positive) value of the Bohr magneton, $g_e=1.95$ is the electron (isotropic) effective g-factor and the calculated values of the hole effective *g* factor are $g_h^{//}(\Gamma_7) = -1.4\pm0.15$ for the Γ_7 hole in the exciton ground state and $g_h^{//}(\Gamma_9) = 3.0\pm0.15$ for the Γ_9 hole. The resulting values of the exciton effective *g*-factors g_{exc} for all states are shown in the Figure 2. For the transitions allowed with $\boldsymbol{E} \perp \boldsymbol{c}$ the g_{exc} values are positive in both (a) and (b) cases. Therefore in the $\boldsymbol{B} // \boldsymbol{c} // \boldsymbol{k}$ configuration the upper-energy state is expected to be active for the right-circular polarized light σ^+. In the $\boldsymbol{k} \perp \boldsymbol{c}$ configuration, the transitions with $\boldsymbol{E} // \boldsymbol{c}$ are allowed in the case (a); in the case (b) they are forbidden but might be observed due to high-order perturbations. The calculated g_{exc} values for the Γ_7 hole (case (a)) in $\boldsymbol{B} // \boldsymbol{c}$ describe well the experimental data reported in Ref. 8 for the free exciton ground state in both $\boldsymbol{E} \perp \boldsymbol{c}$ and $\boldsymbol{E} // \boldsymbol{c}$ polarization. We discuss the

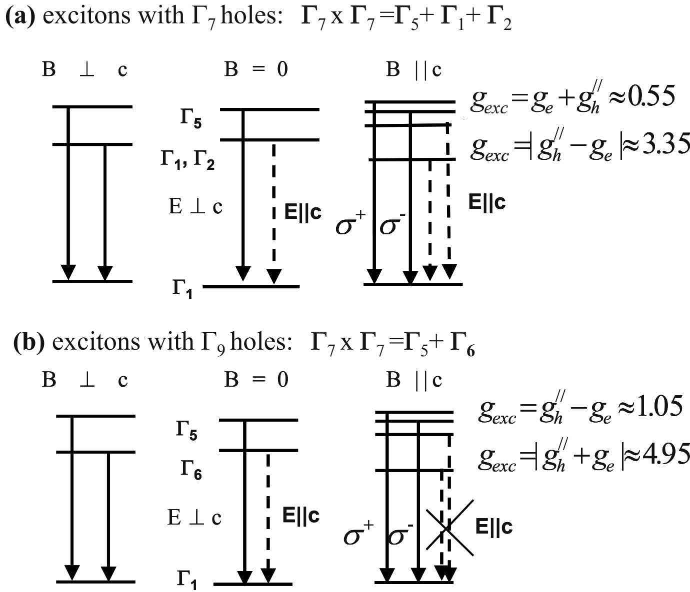

Figure 2. Level schemes and selection rules for the ionized bound exciton transitions.

experimentally Zeeman splitting of the ionized donor bound exciton complex in the next section.

In Figure 3 we sketch all possible transitions for excitons bound to neutral impurities considering the holes from the Γ_7 (cases (a), (c)) and Γ_9 (cases (b), (d)) valence bands. In the case of a donor bound exciton complex (Fig. 3 (a) and (b)), the spins of two electrons are anti-parallel and the Zeeman splitting of the excited (D_0,X) state is determined by the anisotropic hole effective g factor (g_h), while the splitting of the ground D_0 state is given by g_e. In the case of an acceptor bound exciton complex (Fig. 3 (c) and (d)), two holes have the same symmetry and anti-parallel spins. Hence, the splitting of the excited $(A_0;X)$ state is determined by g_e, while the ground A_0 state splits according to g_h. For the holes in the exciton states we use in Fig. 3 (a) and (b) the g values calculated in Ref. 11. For the holes in the acceptor ground states we use in Fig. 3 (c) and (d) the values calculated using the theory developed in Ref. 24 with effective mass Luttinger parameters from Ref. 11.

Our calculations show that the Zeeman splitting of the Γ_7 (Γ_9) holes in ***B//c*** determined by $|g_h^{//}|$ is smaller (larger) than the Zeeman splitting of the electrons determined by g_e. For the arbitrary angle Θ between the ***c*** axis and the direction of the magnetic field the absolute value of the hole anisotropic g factor is given by[22]

$$g_h(\Theta) = \sqrt{|g_h^{//}|^2 \cos^2\Theta + |g_h^{\perp}|^2 \sin^2\Theta} \quad (2)$$

Therefore, for the Γ_7 holes the Zeeman splitting in any magnetic field remains always smaller than the Zeeman splitting of the electrons. In contrary, for the Γ_9 holes some critical angle Θ_{cr} should exist so that $g_h(\Theta_{cr})=g_e$, and $g_h(\Theta)>g_e$ for $0^{\circ} \leq \Theta < \Theta_{cr}$ and $g_h(\Theta)< g_e$ for $90^{\circ} \geq \Theta > \Theta_{cr}$. Examination of the selection rules for optical transitions in the ***B // c // k*** configuration shows that the upper-energy transition is expected to be active for the right-circular polarized light σ^+ for all cases presented in Fig. 3 cases.

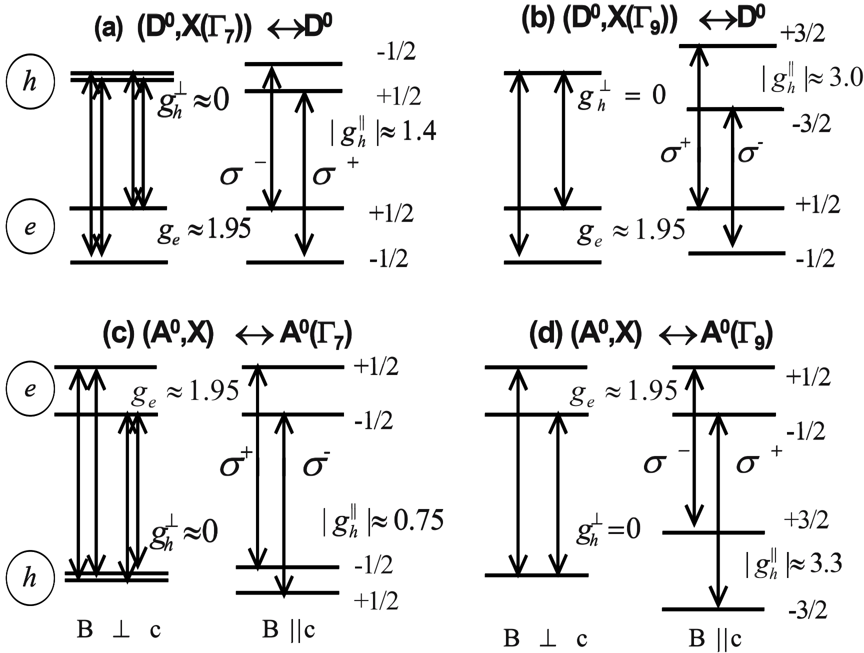

Figure 3. Level schemes and selection rules for neutral bound exciton transitions.

3. EXSPERIMENTAL SETUP AND SAMPLE CHARACTERIZATION

We used nominally undoped (as grown from Eagle-Picher, see for details Ref. 15) and nitrogen doped bulk ZnO crystals. A nitrogen doped ZnO:N sample was prepared from the as grown one by ion implantation (2 MeV,10^{13} cm^{-2}) followed by a thermal annealing process at 900 °C for 15 min (see also Ref. 15).

The magneto-PL measurements were performed at liquid helium temperature in a split-coil magnetocryostat allowing the variation of both temperature (2–300 K) and magnetic field (0–5 T). For some measurements, a second split-coil magnetocryostat was applied providing magnetic fields up to 15 T. Photoluminescence was excited by the 325 nm line of a HeCd laser. A 450 W XBO lamp was used as excitation source for the transmission investigations. The spectral resolution of the detection system was better than 0.15 meV for the 5 T cryostat and >0.3 meV for the 15 T cryostat.

The magneto-PL and magneto-PT measurements were performed in Faraday configuration (magnetic field $\boldsymbol{B}$ parallel to the $\boldsymbol{c}$ axis of the crystal and parallel to the $\boldsymbol{k}$ vector of the detected light) and in Voigt configuration ($\boldsymbol{B} \perp \boldsymbol{k}$). Additionally, the angles between $\boldsymbol{B}$ and $\boldsymbol{c}$ axes were varied from 0 to 90° at fixed magnetic field of 5 T. The circular polarization of the light (σ^+ and σ^-) in the Faraday configuration was analyzed using l/4 plate and linear polarizer. Additionally, PL spectra with $\boldsymbol{B} \perp \boldsymbol{c}$, $\boldsymbol{k} \perp \boldsymbol{c}$ and $\boldsymbol{E} \parallel \boldsymbol{c}$ were recorded for the ZnO:N. Temperature-dependent measurements reveals the thermalization behavior of the Zeeman split components in the emission and transmission spectra.

The zero-field PL spectra of the as grown (nominally undoped) ZnO and nitrogen doped ZnO:N are shown in Figs. 4(a) and 4(b), respectively. Only the lines that will be discussed in this paper in details are marked (for other lines see Ref. 14,15). The strongest line in the as grown ZnO (see Fig. 4 (a)) is the I_4 (368.59 nm or 3.3628 eV). We attribute the I_4 transition as an exciton bound to a neutral shallow H donor that can be easily removed by an annealing process.[15,25] Indeed, the I_4 PL line is absent in ion implanted ZnO:N (see Fig. 4(b)). This is because of the post annealing processes at 900 °C included in the doping procedure. The PL spectrum of ZnO:N is dominated by two lines: a new line I_2 (368.07 nm or 3.3676 eV) and the I_9 transition. The latter considerably gains in intensity compared to the undoped ZnO. The wavelengths of the lines are given here in air with an accuracy of 0.02 nm and have been transformed into the respective wavelength values in vacuum before calculating the transition energies.

4. ZEEMAN BEHAVIOR OF THE BOUND EXCITON COMPLEXES: EXPERIMENTAL DATA AND DISCUSSION

Figure 5 presents the magneto-PL spectra in the energy region of the I_2 transition for the ZnO:N for Faraday configuration (a), Voigt configuration (c) and for the different angles between the magnetic field direction and the

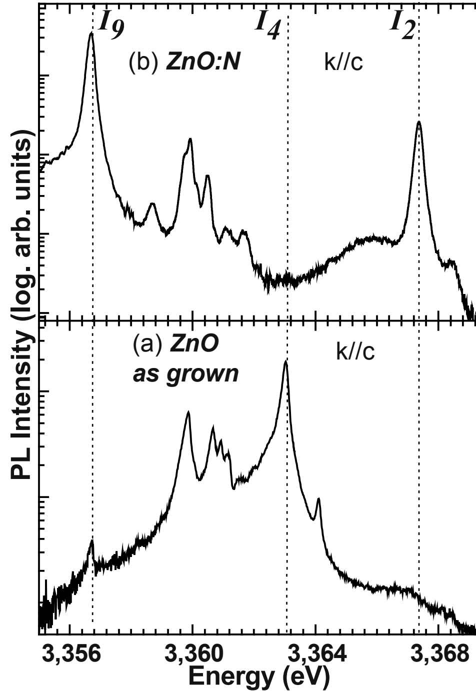

Figure 4. Photoluminescence spectra of undoped as grown ZnO (a) and nitrogen doped ZnO:N (b) at 4.2 K.

c axis at $B = 5$ T (b). The most important feature of the spectra in Figures 2 (b) and (c) is the appereance of a new transition line at an energy about 1 meV below I_2. This I_3 transition (368 18 nm or 3 3666 eV in zero field as determined by the extrapolating procedure) is forbidden in $\boldsymbol{B}$ // k // $\boldsymbol{c}$, $\boldsymbol{E} \perp \boldsymbol{c}$ geometry but has been also observed in parallel magnetic field with the light polarized along the c axis ($\boldsymbol{E}$ // $\boldsymbol{c}$, $\boldsymbol{k} \perp \boldsymbol{c}$ configuration). Such behavior leads to the conclusion that the I_2 and I_3 transitions originate from excitons bound to an ionized impurity. The stability of such complex in semiconductors strongly depends on the ratio of electron and hole effective masses.[26] In the case of ZnO, the single band isotropic mass approximation predicts the existence of the excitons bound to ionized donors.[23] Next, the presence of acceptors in the ZnO:N may induce the ionization of the shallow donors[26] as in the case of Li and Na doped ZnO.[19] Therefore, we attribute the I_2 and I_3 lines in the doped ZnO:N to transitions of excitons bound to respective ionized donors (($D^+, X(\Gamma_7)$) complex). The value of the zero-field spin-exchange splitting is 0.98 meV, in a good agreement with Refs. 19,23.

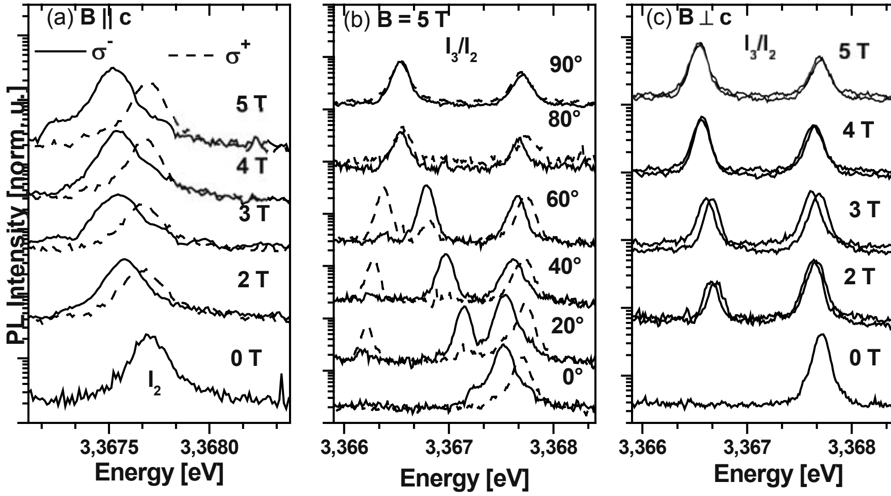

Figure 5. Photoluminescence spectra of ZnO:N in the energy region of the I2/I3 lines at 4:2 K for different magnetic fields in Faraday configuration (case (a): B // k // c, E ⊥ c) and Voigt configuration (case (c): B ⊥ c, k // c, E ⊥ c), and for different angles between the c axis and the direction of the magnetic field B at 5 T (case (b)).

The magnetic field and angular dependencies of the emission lines I_2 and I_3 allow us to determine the symmetry and the g values of the valence band hole involved in the corresponding bound excitons.[14,15] The magnetic field ***B // c*** linearly splits the I_2 transition (allowed in ***E ⊥ c*** configuration) as well as the I_3 transition (allowed in ***E // c*** configuration). The upper-energy component of the I_2 line is active for the right-circular polarized light (see dashed line in Fig. 5 (a)) as predicted in Fig. 2. The linear splitting of the I_2 line in ***B // c*** can be described with the positive exciton effective g- factor $g_{exc} = 0.71$ that is close to the calculated values in Fig.2 (a) and (b). However, the experimental value $g_{exc} = 2.66$ determined for the I_3 line is in better agreement with the expected value for the Γ_7 holes (case (a) in Fig. 2) and differs significantly from the respective value in case (b). Furthermore, from the fitting of the angular dependence of the transition energies[14,15] we obtained $g_h^{//} = -1.24$ in the excellent agreement with the calculated value for the Γ_7 hole in the exciton ground state. This demonstrates that the hole in the lowest exciton state and thus the upper A valence subband in ZnO also have the Γ_7 symmetry.

The Zeeman behavior of the emission lines from I_4 to I_9 is different from that of the I_2/I_3 lines. Their linear splitting in ***B ⊥ c*** indicates transitions originating from excitons bound to neutral impurities. We discuss the emission lines I_9 and I_4 in detail. These lines represent the dominant

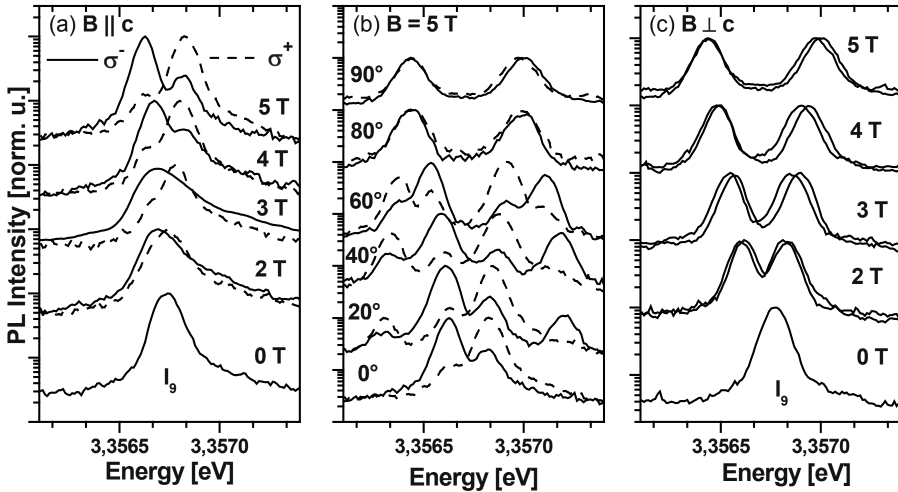

Figure 6. Photoluminescence spectra of ZnO:N in the energy region of the I9 line at 4:2 K. Cases (a), (b) and (c) are the same as in Fig. 5.

recombination in ZnO:N and as grown ZnO bulk crystals, respectively, and are spectrally resolved from the other observed emission lines. Figure 6 presents the magneto-PL spectra in the energy region of the I_9 transition for the ZnO:N, the Zeeman behavior of this line and the I_4 in the undoped ZnO is very similar. The transitions allowed for $\boldsymbol{E} \perp \boldsymbol{c}$ split with magnetic fields parallel and perpendicular to the $\boldsymbol{c}$ axis. The upper Zeeman split energy component in $\boldsymbol{B} \,//\, \boldsymbol{c} \,//\, \boldsymbol{k}$ configuration is active in σ^+ polarization (see Fig. 6 (a)) as predicted for all cases in Fig. 3 (a-d). Four transition components can be distinguished for an arbitrary angle Θ between the direction of the magnetic field and the $\boldsymbol{c}$ axis.

The B-field dependencies up to 5 T of the I_4 transition energies in $\boldsymbol{B} \perp c$ and $\boldsymbol{B} \,//\, \boldsymbol{c}$ are shown in Figure 7 together with the angular dependence at B = 5 T. These dependencies can be described as

$$E(B,\Theta) = E_0 \pm 1/2\mu_B B(g_e \pm g_h(\Theta)), \tag{3}$$

where E_0 is the zero field transition energy and $g_h(\theta)$ is given by Eq. (2). For the Γ_9 holes the $g_h^{\perp} = 0$ by the symmetry and the Eq. (3) leads to the linear dependence of $E(B,\Theta)$ on $cos(\Theta)$ (see dashed lines in Fig. 7 (b)). For the Γ_7 holes in ZnO the value of $g_h^{\perp} \approx 0$ and the nonlinear behavior of $E(B,\Theta)$ on $cos(\Theta)$ can not be detected as well (see solid lines in Fig. 7 (b)). However, the symmetry of the holes can be unambiguously established by the analysis of the angular dependence in Fig. 7 (b). Indeed, no critical

angle θ_{cr} corresponding to $g_h(\Theta_{cr})=g_e$ and no respective crossing of the transition energies expected for the Γ_9 holes (see dashed lines in Fig. 7 (b)) was observed. The excellent agreement between experimental data and theoretical modeling is possible if and only if we assume that the hole *g* factor is smaller than electron's *g* factor: $|g_h^{//}| < g_e$. Together with the selection rules observed in ***B // c // k*** configuration this corresponds to the holes of the Γ_7 symmetry. The values of the electron and hole effective *g* factors used for the fitting (solid curves) are $g_e = 1.97$, $g_h^{//} = -1.21$ and $g_h^{\perp} = 0.1$ for the I_4 in Fig. 7 and $g_e = 1.86$, $g_h^{//} = -1.27$ and $g_h^{\perp} = 0.06$ for the I_9 line[14].

The values of $g_h^{//}$ derived for the I_4 and I_9 lines are very close to the $g_h^{//} = -1.24$ obtained for the hole involved in the exciton bound to ionized donor and to the *g* factor of the hole in 1*S* free exciton state.[5,7,11] On the other hand, the expected $g_h^{//}$ values of the holes involved in the acceptor bound exciton transitions differ significantly from the *g* values of the holes involved into excitons bound to ionized or neutral donors. This is similar to the situation found in CdS.[22] Therefore we conclude that both I_4 and I_9 transitions should be assigned to the $(D_0;X_A(\Gamma_7))$ complex rather than to the $(A_0(\Gamma_7);X_A(\Gamma_7))$.

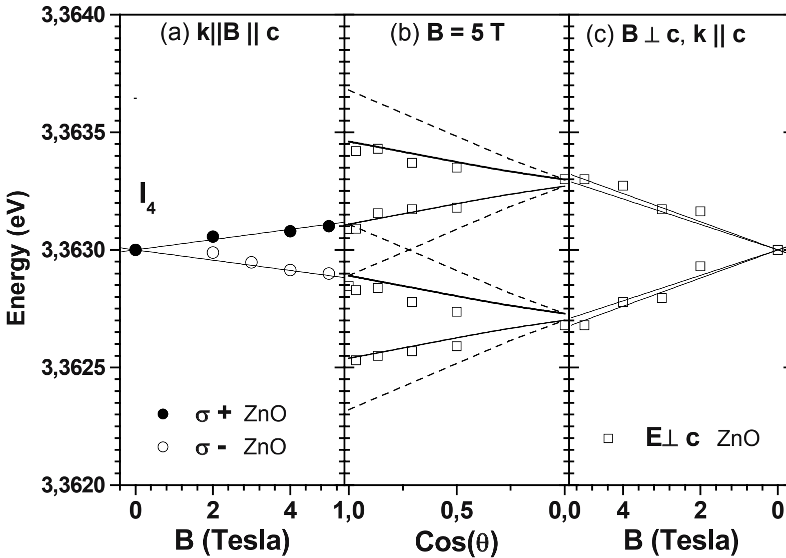

Figure 7. Zeeman splitting of the bound exciton line I4. Case (a): B // k // c, E ⊥ c. Case (c): B ⊥ c, k // c, E ⊥ c. Case (b): the angular dependence for B = 5 T. Symbols are experimental data measured with circular polarized light (σ^+ and σ^-) and with unpolarized light (E ⊥ c) as denoted in the Figure, and lines are fits. For the fits the hole is assumed to be of Γ7 symmetry with $|g_h^{||}| < g_e$ (solid lines) and of Γ9 symmetry with $|g_h^{||}| > g_e$ (dashed lines).

This conclusion is supported by the analysis of the thermalization properties of the I_4 and I_9 lines[14] in the temperature dependent emission and transmission spectra and by the observation of the two electron satellite transitions for these lines.[15,21,25]

5. CONCLUSION

The inverted $\Gamma_7(A)$, $\Gamma_B(B)$, $\Gamma_7(C)$ ordering of the valence subbands in bulk ZnO was confirmed by the detailed analysis of the Zeeman splitting of the free and bound excitons. The polarization properties and the angular dependence of the transition energies from excitons bound to ionized and neutral impurity centers indicated the Γ_7 character of the upper *A* valence band. The obtained Γ_7 effective *g* values are in good with theoretical calculations. We observed no low temperature PL transitions involving the Γ_9 hole states from the *B* valence subband.

ACKNOWLEDGEMENTS

The work of A. V. Rodina was carried out during the stay at the Institute for Solid State Physics, TU Berlin, and supported by the Deutsche Forschungsgemeinschaft (DFG).

REFERENCES

1. D. G. Thomas, *J. Phys. Chem.* **15**, 86 (1960).
2. Y. S. Park, C. W. Litton, T. C. Collins, and D. C. Reynolds, *Phys. Rev.* **143**, 512 (1966).
3. B. Segall, *Phys. Rev.* **163**, 769 (1967).
4. W. Y. Liang and A. D. Yoffe, *Phys. Rev. Lett.* **20**, 59 (1968).
5. K. Hümmer, *phys. stat. sol.* **56**, 249 (1973).
6. M. Rosenzweig, Diploma Thesis, TU Berlin, 1975.
7. G. Blattner, G. Kurtze, G. Schmieder, and C. Klingshirn, *Phys. Rev. B* **25**, 7413 (1982).
8. D. C. Reynolds, D. C. Look, B. Jogai, C. W. Litton, G. Cantwell, and W. C. Harsch, *Phys. Rev. B* **60**, 2340 (1999).
9. B. Gil, *Phys. Rev. B* **64**, 201310(R) (2001)
10. B. Gil, A. Lusson, V. Sallet, R. Triboulet, and P.Bigenwald, *Jpn. J. Appl. Phys. Lett.* **40**, L1089 (2001).
11. W. R. L. Lambrecht, A. V. Rodina, S. Limpijumnong, B. Segall, and B. K. Meyer, *Phys. Rev. B* **65**, 075207 (2002).
12. V. Val. Sobolev and V. V. Sobolev, *Lith. J. of Physics* **42**, 189 (2002).

13. K. Hazu, T. Sota, K. Suzuki, S. Adachi, SF. Chichibu, G. Gantwell, D. B. Eason, D. S. Reynolds, and C. W. Litton, Phys. *Rev. B* **68**, 033205 (2003).
14. A. V. Rodina, M. Strassburg, M. Dworzak, U. Haboeck, A. Hoffman, A. Zeuner, H. R. Alves, D. M. Hoffmann, and B. K. Meyer, *Phys. Rev. B* **69**, 125206 (2004).
15. B. K. Meyer, H. Alves, D. M. Hofman, W. Kriegseis, T. Riemann, J. Christen, A. Hoffmann, M. Strassburg, M. Dworzak, U. Haboeck, and A. V. Rodina, *phys. stat. sol. (b)* **241**, 231 (2004).
16. J. Gutowski, N. Presser, and I. Broser, *Phys. Rev. B* **38**, 9746 (1988).
17. G. Blattner, C. Klingshirn, R. Helbig, R. Meinl, *phys. stat. sol. (b)* **107**, 105 (1981).
18. P. Loose, M. Rosenzweig, and M. Wohlecke, *phys. stat. sol. (b)* **75**, 137 (1976).
19. D. C. Reynolds, C. W. Litton, and T. C. Collins, *Phys. Rev.* **140**, A1726 (1965).
20. D. C. Reynolds and T. C. Collins, *Phys. Rev.* **185**, 1099 (1969).
21. K. Thonke, N. Kerwien, A. Wysmolek, M. Potemski, A. Waag, and R. Sauer, *Mat. Res. Soc. Symp. Proc.* Vol. **719**, F2.4.1 (2002); K. Thonke, N. Kerwien, A. Wysmolek, M. Potemski, A. Waag, and R. Sauer, in Proc. 26th Int'l Conf. on the Physics of Semiconductors, edited by R. Long and J. H. Davies, Institute of Physics Publishing, Bristol (UK) and Philadelphia (USA), Institute of Physics Conference Series Number **171**, P22, (2003).
22. D. G. Thomas and J. J. Hopfield, *Phys. Rev.* **128**, 2135 (1962).
23. T. Skettrup, M. Suffczynski, and W. Gorzkowski, *Phys. Rev. B* **4**, 512 (1971).
24. A. V. Malyshev, I. A. Merkulov, and A. V. Rodina, *Fiz. Tverd. Tela* **40**, 1002 (1998) [*Physics of the Solid State* **40**, 917 (1998)].
25. H. Alves, D. Pfisterer, A. Zeuner, T. Riemann, J. Christen, D. M. Hofmann, and B. K. Meyer, *Optical Materials* **23**, 33 (2003).
26. M. A. Lampert, *Phys. Rev. Lett.* **1**, 450 (1958).
27. A. Zeuner, H. R. Alves, D. M. Hofmann, B. K. Meyer, A. Hoffmann, U. Haboeck, M. Strassburg, and M. Dworzak, *phys. stat. sol. (b)* **234**, R7 (2002).

Chapter 15

FUNDAMENTAL OPTICAL SPECTRA AND ELECTRONIC STRUCTURE OF ZnO CRYSTALS

V. Val. Sobolev and V. V. Sobolev
Udmurt State University, 426034 Izhevsk, Russia

Abstract: The analysis of ZnO exciton spectra is given. In the band and exciton theory, necessity of taking into account hybridization of O 2p and Zn 3d states is confirmed. Full sets of ZnO exciton spectra are obtained for 1.6, 4.2, and 90 K for the first time. The main parameters of the three exciton series are determined. Five variants of full sets of the fundamental polarized optical functions of ZnO crystal were determined in the energy range 0–26 eV for polarizations **E** ⊥ **c** and **E** || **c**. Three variants of dielectric permittivity and volume electron energy loss polarized spectra of ZnO crystal were decomposed into the transverse and longitudinal transition band components. The main features and parameters of the five variants of the optical functions spectra were established. A theoretical analysis of the obtained components was performed, based on the known theoretical band schemes.

Key words: Exciton, interband transition, optical spectra, reflectance, permitivity, polarization, band structure

1. INTRODUCTION

The polarization of the exciton spectra of ZnO does not follow the classical model. All the three exciton series are strongly polarized and can be observed only with **E** ⊥ **c** (A, B) and **E** || **c** (C). This has led to contradictory position schemes of the two highest valence bands (Γ_9, Γ_7) and values of Δ_{so}, Δ_{cr}. There are also certain discrepancies in the results of different papers on the nature of the lines of complex discrete reflectivity and absorption spectra of ZnO at 4.2 K, as well as on the bands and excitons parameters.[1–13]

Polarized reflectivity spectra of ZnO have long been measured in the wide energy region of fundamental absorption 0–26 eV, and some other optical functions have been calculated from them.[4,7,14,15] However, full sets

N.H. Nickel and E. Terukov (eds.),
Zinc Oxide – A Material for Micro- and Optoelectronic Applications, 171–182.
© 2005 *Springer. Printed in the Netherlands.*

of optical functions and their decompositions into the elemental components have not yet been determined, neither have the results of the three mentioned papers been compared with each other.

In the present report, three subjects are to be reviewed: (i) The triplet structure of excitons and the upper valence band; (ii) the full set of the fundamental optical functions in the 0–30 eV energy range for polarizations **E** || **c**, **E** ⊥ **c**, and their theoretical analysis; and (iii) the main parameters of the elementary transverse and longitudinal transition components in the 0–30 eV energy range for polarizations **E** || **c**, **E** ⊥ **c**, and their theoretical analysis.

2. CALCULATION TECHNIQUES

A full set of optical functions consists of reflectivity R and absorption coefficients, μ, the imaginary ε_2 and real ε_1 parts of the dielectric function ε, the absorption and refraction indices k and n, the product of the integral joint density of states (DOS) function and the transition probability, equal within constant factor to $\varepsilon_2 E^2$; the effective number of valence electrons $n_{ef}(E)$ participating in the transitions to given energy level E; the effective dielectric coefficient ε_{ef}, and the characteristic electron energy functions for volume ($-\mathrm{Im}\varepsilon^{-1}$) and surface ($-\mathrm{Im}(1+\varepsilon)^{-1}$) losses.

The fine structure of optical transitions is determined by several main parameters: the energy values of the maxima E_i and half-widths H_i of the component bands, oscillator strengths f_i, and the areas S_i of the bands which equal transition intensity, to within a universal constant factor, and the amplitudes I_i of the components maxima. The techniques used in the paper were discussed[16] and applied.[17,18]

3. ANALYSIS OF THE STRUCTURE OF EXCITON REFLECTIVITY, ABSORPTION AND EMISSION SPECTRA

The exciton transitions of three series with $n = 1, 2, 3$ were found in the reflectivity, absorption, and radiation spectra at a temperature $T \leq 5$ K, and their binding energies R were determined.[1–4] The ZnO samples were obtained using different techniques, and their surfaces were treated in different ways (cleavages, etched surfaces). The spectra were measured with photographic and photoelectric techniques. Despite these substantially different surface treatment and measurement techniques, a comparatively good agreement was reached between the results of many papers concerning

the positions of the exciton lines. This agrees well with the simple classical exciton model and contradicts the polariton model.

The problem has long been discussed of a connection between the differences in the exciton spectra and the triplet band structure of ZnO and other hexagonal crystals.[1–11] In all these papers, the simplest model is accepted on the assumption of invariability of the symmetry of the three bands: in some papers, inversion of two upper bands is assumed,[1,12] i.e.: the highest band is Γ_7 instead of Γ_9, while other papers propose to retain the conventional interleaving of bands Γ_9, Γ_7, and Γ_7.[2,3,10] This problem is theoretically considered.[9]

It was shown in the quasicubic approximation of the group theory that the relative energies of three upper valence bands with energies E_1, E_2, E_3 are determined by the values of Δ_{so} and Δ_{cr}:

$$E_2 = A + \sqrt{A^2 - 2B/3},\ E_3 = A - \sqrt{A^2 2B/3} \qquad (1)$$

where $2A = \Delta_{so} + \Delta_{cr}$; $B = \Delta_{so} \cdot \Delta_{cr}$; $E_1 = 0$; Δ_{so}, $\Delta_{cr} << E_g$. The values of Δ_{so} for ZnO obtained with Eq. (1) vary in their absolute values and even in their sign: –0.009,[1] –0.015,[12] 0.016[10] eV. The calculations of Δ_{so} and Δ_{cr} are known that use the classical model of band interleaving (Γ_9, Γ_7, Γ_7) and inversion (Γ_7, Γ_9, Γ_7). The values of Δ_{cr} proved to be almost identical in all the papers, regardless of the band model: Δ_{cr} = 0.041,[1] 0.0355[12] eV for Γ_7, Γ_9, Γ_7; 0.041,[3] 0.043[10] eV for Γ_9, Γ_7, Γ_7. However, the values of the second parameter (Δ_{so}) turned out to be mostly negative: Δ_{so} –0.009,[1] –0.015[12] eV for Γ_7, Γ_9, Γ_7; –0.005,[3] 0.016[10] eV for Γ_9, Γ_7, Γ_7. Large divergence of the calculation results for Δ_{so} seem to be due to too small a distance between two (A, B) exciton series and larger relative errors of $(B–A)/A$.

Two experimental results have been known, which show a possibility of considerable change of the parameters of all the three valence bands of ZnO. First, polarization of all the three exciton series of ZnO conceptually differs from their polarization in other A^2B^6 crystals that is in good agreement with the conventional band model. This fact undoubtedly shows that in ZnO, not only the symmetry of the second band changes, but the symmetry of the third band also. Second, according to the photoemission spectra (PES), the valence band of zinc d-states (Zn 3d) is located below the top of the valence band of ZnO by ~ 8 eV, while below its bottom only by ~ 3 eV.[19] Therefore, Zn 3d states can intermix with O 2p states and change the symmetry of the upper valence bands.

According to the theoretical calculations,[20] O 2p states form ~ 67 – 74% of the highest valence band, while Zn 3d states form the remaining almost

quarter of it. The analysis of the experimental X-ray photoemission spectra (XPS) showed a lower contribution of d-states – about 9%.[21]

Among the theoretical papers, the most interesting results are found by Wei, et al.[23] and Lambrecht et al.[11] Wei, et al.[23] show that interaction of oxygen p-levels with zinc d-levels, i.e.: p – d repulsion and hybridization, reduces the spin-orbital splitting and alters the sign of the crystal-field splitting; p – d coupling mixes d-character into the wave function at the valence-band maxima:

$$\Delta_{so} = \Delta_{so}(p\ \mathrm{O}) - a\Delta_{so}(d\ \mathrm{Zn}) \qquad (2)$$

According to the estimations, Δ_{so}(d Zn) ≈ –0.37 eV, a = 0.07. Oxides BeO and MgO, lacking d-bands, have Δ_{so}(p O) ≈ 0.034 eV. Hence, Δ_{so}(ZnO) ≈ (0.034–0.026) eV < 0.01 eV.

Lambrecht and his colleagues have theoretically shown[11] that the energies Δ_{so} and Δ_{cr} depend very strongly and almost linearly on the location of the d-levels of zinc (E_d). According to the authors, the most optimal variant is that with $E_d \approx 6.25$ eV together with the band inversion model. However, the experimental results give $E_d \approx 8.5 \pm 0.4$ eV.[19] Unfortunately, it is in the energy region $E > 6.7$ eV that the calculations of this paper are not reliable. Thus, both the theoretical and experimental results indicate that zinc d-states make a substantial contribution to the formation of the highest valence band of ZnO. It is the hybridization of O 2p and Zn 3d states that strongly changes the symmetry of the three valence bands and, consequently, the polarization of three exciton series *A*, *B*, *C*, as well as the splitting energies of the three bands.

4. CALCULATIONS OF OPTICAL FUNCTIONS AND EXCITON PARAMETERS

From the experimental polarized exciton reflectivity spectra of papers[2,4,5] and the reflectivity spectra in wide energy region up to 25 eV,[14] three full sets of optical fundamental functions of excitons were calculated at 1.6 K[4] (L), 4.2 K[2] (P), and 90 K[5] (K). For the sake of briefness, some of them are given in Figs. 1.

The analysis of the ε_2 and $-\mathrm{Im}\varepsilon^{-1}$ spectra allowed to determine the energy values of transverse and longitudinal exciton transitions, and to evaluate their band areas and oscillator strengths (Tab. 1); the values of *f*, given here, have been enlarged 10^5.

Table 1. Energy values E (eV) of ε_2 and –Im ε^{-1} maxima, bands areas *S*, and oscillator strengths $f \times 10^5$ of ZnO excitons, calculated from the *R*(*E*) spectra of papers Lagois, et al.[4] (L), Park, et al.[2] (P), and Klucker, et al.[5] (K)

N		A_1		B_1		C_1	
		ε_2	$-\text{Im}\varepsilon^{-1}$	ε_2	$-\text{Im}\varepsilon^{-1}$	ε_2	$-\text{Im}\varepsilon^{-1}$
L,	*E*	3.3766	3.3792	3.3830	3.3948	3.421	3.439
1.6 K	*S*	0.16	0.0005	0.20	0.008	0.32	0.007
	$f\times10^5$ (10^7)	7.5	2.4	9.4	38	15	33
P,	*E*	3.3746	3.3772	3.3796	3.3904	3.419	3.433
4.2 K	*S*	0.20	0.0006	0.16	0.006	0.50	0.006
	$f\times10^5$ (10^7)	9.4	2.8	7.5	2.8	23.5	28
K,	*E*	3.349	3.38	3.349	3.38	3.387	3.424
90 K	*S*	0.50	0.008	0.50	0.008	0.50	0.008
	$f\times10^5$ (10^7)	24	38	24	38	24	38
N		A_2		B_2		C_2	
		ε_2	$-\text{Im}\varepsilon^{-1}$	ε_2	$-\text{Im}\varepsilon^{-1}$	ε_2	$-\text{Im}\varepsilon^{-1}$
L,	*E*	3.43	3.43	3.44	3.43	3.47	3.47
1.6 K	*S*	0.02	0.0005	0.03	0.0005	0.05	0.0007
	$f\times10^5$ (10^7)	0.94	2.35	14	2.4	2.35	3
P,	*E*	3.42	3.42	3.43	3.43	3.46	3.47
4.2 K	*S*	0.04	0.04	0.02	0.001	0.1	0.003
	$f\times10^5$ (10^7)	1.9	1.9	0.94	4.7	4.7	1.4
K,	*E*	3.41	3.41	3.41	3.43	3.453	3.49
90 K	*S*	0.10	0.10	(0.10)	0.008	0.05	0.001
	$f\times10^5$ (10^7)	4.4	4.4	4.7	38	2.4	4.7

5. RESULTS OF CALCULATIONS OF OPTICAL FUNCTIONS IN THE 0 - 26 eV ENERGY RANGE

Using the *R*(*E*) spectra of the three papers,[5,14,15] we calculated three variants of sets of polarized spectra of all the optical functions (*A*, *B*, *C* from the *R* of papers[15,14,5]). Some of them are given in Figs. 1. The polarized reflectivity spectra of ZnO in the energy range 0–18 eV were calculated theoretically in three papers.[23,24,25] The results of Wei, et al.[23] differ very much from the experimental spectra.[5,14,15] Because of this, our calculations of polarized spectra of all the remaining optical functions are based on the theoretical *R*(*E*)[24] and $\varepsilon_2(E)$[25] spectra. Some of the calculated spectra are given in Fig. 1 (curves 4 and 5).

The most long-wavelength maximum of the experimental reflectivity curves at **E** ⊥ **c** and **E** || **c** and that of the other optical functions spectra, calculated from them (the experimental-calculated ones), is caused by free excitons. Therefore, there should be no such maximum in the theoretical spectra obtained from the bands.

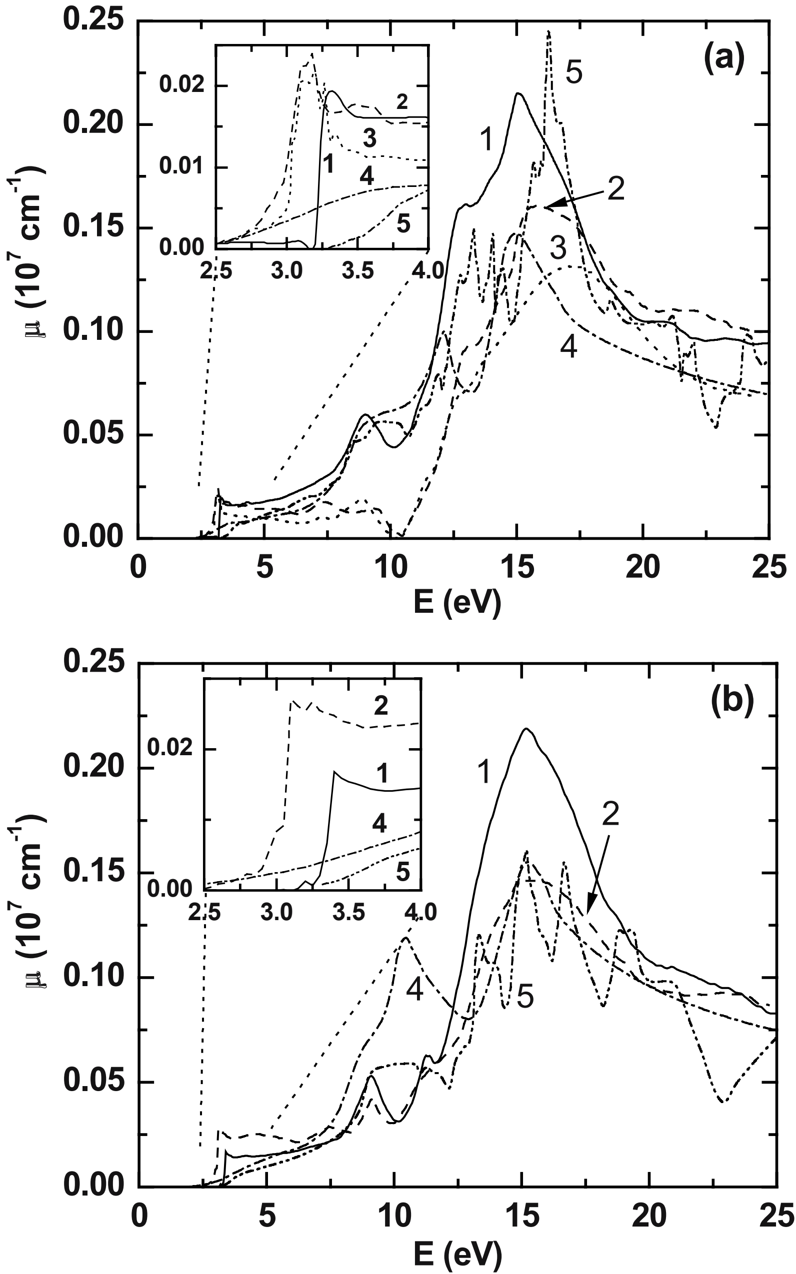

Figure 1. The μ (a, b) and $E^2\varepsilon_2$ (c, d) spectra of ZnO crystal for **E**⊥**c** (a, c) and **E**||**c** (b, d) in the range of 0–25 eV (in the inset – in the range of 2.5–4.0 eV), calculated from the experimental *R* spectra (1, 2, 3) and from the theoretical ε_2 and ε_1 spectra (4, 5)

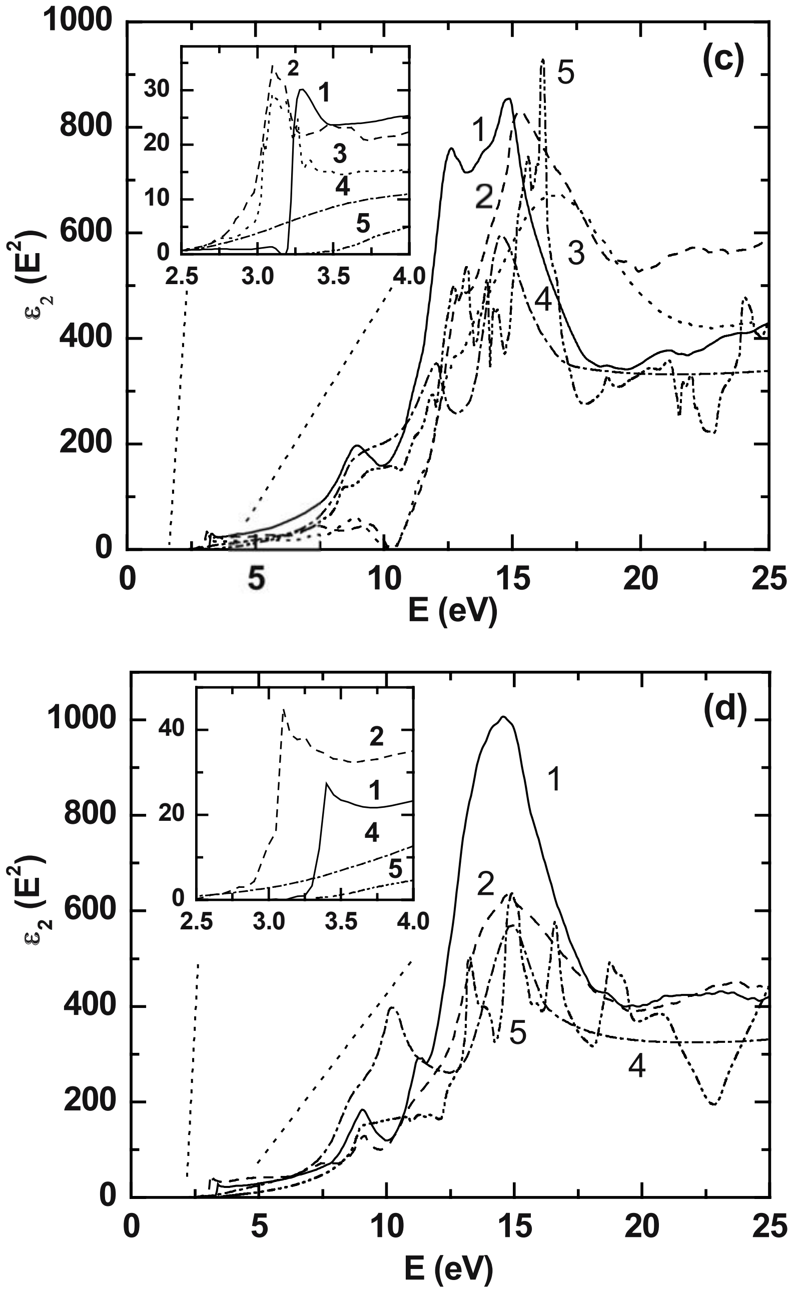

Figure 1. Continued: The μ (a, b) and $E^2\varepsilon_2$ (c, d) spectra of ZnO crystal for **E**⊥**c** (a, c) and **E**||**c** (b, d) in the range of 0–25 eV (in the inset – in the range of 2.5–4.0 eV), calculated from the experimental *R* spectra (1, 2, 3) and from the theoretical ε_2 and ε_1 spectra (4, 5)

The maxima of the theoretical $R(E)$ spectra of papers ref. 24 and 25 differ one from the other by ~ 0.2–1 eV, while the differences between these and the maxima from papers[5,14,15] come up to 1.5 eV, with the intensity distribution of the maxima remaining mostly similar. A noticeable general similarity was also discovered as a result of direct comparison of the remaining experimental and calculated, and theoretical spectra of the optical functions (Fig. 1). However, the detailed comparison of the theoretical and experimental spectra of the optical functions showed, naturally, substantial differences in the intensities and locations of the maxima.

In papers 33–36, the photoemission spectra of ZnO crystal were experimentally studied. According to the presented results Zn 3d electron energy levels of ZnO (E_d) are lower than the maximum of the valence bands for ~ 8.5 eV,[19] 7.5 eV,[34] and 7.5 eV,[21] while the total width of the highest valence band (ΔE_v) is equal to ~ 5.0 eV,[34] 8.0 eV,[19] and 6.0 eV.[21] From the theoretical band calculations, ΔE_v is equal to ~ 6 eV[24] and 4.2 eV,[25] while E_d ≈ 4.2 eV;[25] zinc d-levels being ignored in paper ref. 21. This means that both important band parameters of ZnO (ΔE_v and E_d) are undervalued in paper ref. 24 by ~ 2 eV and 4 eV for ΔE_v and E_d, respectively. This must have led, in the first place, to underestimation of the energy values of the theoretical transitions from the lower sub bands of the highest valence band and alteration of the transitions intensities.

6. THE ε_2 AND –Im ε^{-1} SPECTRA IN THE 0–26 eV ENERGY RANGE

Spectra of ε_2 and $-\text{Im}\varepsilon^{-1}$ of the three variants of optical functions sets (*A*, *B*, *C*) were deconvoluted by us into components. The main parameters of the obtained components are given in Tables 1, 2 (*A*), 3, 4 (*B*), and 5 (*C*), as well as in Fig. 1.

In Table 2, the calculated values of energy maxima E_i and band areas S_i of transverse transitions were compared for the three variants of calculations of optical function sets. These variants differ comparatively little in energy E_i. The principal inconsistencies are observed in the values of S_i. This is caused by the differences in the experimental $R(E)$ spectra, i.e. by using of ZnO samples of different quality and by different registration techniques for polarized reflectivity spectra. The determined components of ε_2 and $-\text{Im}\varepsilon^{-1}$ spectra are caused by direct interband transitions or metastable excitons, except for the most long-wavelength of them, which are associated with free excitons. The theoretical band calculations of ZnO[20,23–25] strongly differ in the bands dispersion and positions. This makes it difficult to propose a

model of specific and unambiguous connection between the determined components and transitions between pairs of bands. It is commonly accepted that transitions can be expected between those pairs of bands that are parallel in the largest portion of the Brillouin zone.[16] Using this simplified model, we estimated the energies of such transitions in the vicinity of points Γ, A, M, K, and L for the bands of papers[20,23–25] (Table 2,3). These results are in accordance with our calculations of the components energies (Tables 2,3).

Table 2. Energy (eV) of the maxima E_i, band areas S_i, oscillator strengths f_i of the transverse (ε_2) and longitudinal (ε^{-1}) transition components of ZnO crystal for **E** ⊥ **c** (⊥) and **E** || **c** (||) and theoretical interband transitions E_n

N	E_i				S_i		f_i		E_i, K
	⊥		||		⊥	||	⊥	||	
	ε_2	ε^{-1}	ε_2	ε^{-1}	ε_2	ε_2			
1	3.28	3.57	–	–	0.36	–	1.59	–	–
2	–	–	3.4	–	–	0.26	–	2.56	–
3’	3.58	–	–	–	0.62	–	1.01	–	–
3	–	–	3.7	3.7	–	0.84	–	1.9	–
4	4.34	4.42	–	–	1.11	–	0.9	–	3.8, Γ
5	–	–	4.7	4.9	–	1.11	–	1.01	5.0, Γ
6	6.2	6.1	–	–	2.67	–	1.21	–	7.5, Δ
7	–	–	6.7	6.7	–	2.36	–	1.2	
8	–	–	8.4	8	–	0.57	–	0.21	9.5, Δ, Σ
9	8.8	9.3	9	9.3	4.22	1.39	1.05	0.2	10, *U*
10	11.1	11.4	11.2	11.4	0.67	1.66	0.12	0.35	11.0, *S*
11	12.5	12.7	12.9	12.9	6.85	2.2	0.84	0.32	12.6, *U*
12	13.7	13.7	13.7	13.8	1.78	6.83	0.17	0.77	14.0, *S*
13	14.7	14.7	15	15	3.8	3.51	0.31	0.3	14.6, *U*
14	16	16	15.5	–	1.87	1.69	0.14	0.13	16.7, Δ
15'	–	–	16.4	16.3	–	1	–	0.07	
15	17.2	17.3	17.5	17.5	0.77	0.45	0.06	0.03	17.8, *U*
16	18.7	18.4	18.7	18.3	0.48	0.89	0.03	0.06	
16’	–	19.1	–	19.1	–	–	–	–	–
17'	–	20.1	–	19.7	–	–	–	–	20.3, *U*
17	20.7	21.5	20.9	20.9	1.47	1.89	0.11	0.28	
18	22.9	23.4	23.4	23.7	0.34	1.08	0.03	0.08	22.0, *U*
19	25.1	25.1	–	–	2.46	–	0.19	–	–
20	–	–	26.8	26.8	–	2.31	–	0.17	–

7. CONCLUSIONS

Thus, an analysis of the known polarized exciton reflectivity, absorption, and radiation spectra of ZnO crystal has been performed for the first time. High stability of the positions of the lines of three exciton series has been

found despite the substantial differences in the monocrystal's growing processes and the spectra recording techniques. This argues against the necessity of application of the polariton model in these papers.

The conventional or inverse model of triplet structure of the highest valence band applied to explanation of the exciton spectra of ZnO has been shown to be much too simplified. It is necessary to take into account

Table 3. Energy E_i (eV) of the maxima and band area S_i of the components of ε_2 spectrum decomposition at **E** ⊥ **c** (⊥) and **E** || **c** (||) in three variants of optical functions sets (*A*, *B*, *C*) of ZnO crystal

N	Ei					Si				
	⊥			||		⊥			||	
	A	B	C	A	B	A	B	C	A	B
1	3.28	3.10	3.10	–	3.10	0.36	0.44	0.15	–	0.35
2’	–	3.18	3.19	–	3.20	–	0.08	0.22	–	0.09
2	–	3.46	3.48	3.40	3.35	–	0.68	0.05	0.26	0.95
3’	3.58	–	–	–	–	0.62	–	–	–	–
3	–	–	3.69	3.70	3.70	–	–	0.91	0.84	0.05
4	4.34	4.10	4.25	-	4.15	1.11	0.75	0.14	–	2.16
5	–	4.60	–	4.70	4.80	–	0.63	–	–	0.13
6	6.20	5.38	5.13	–	5.25	2.67	0.39	0.96	–	1.19
7	–	7.20	7.3	6.70	7.40	–	1.10	0.22	2.36	1.91
8	–	–	8.2	8.40	–	–	–	0.06	0.57	–
9	8.80	–	8.8	9.00	9.1	4.22	–	0.53	1.39	0.65
10	11.1	–	11.4	11.2	11.1	0.67	–	0.21	1.66	1.08
11	12.5	12.8	12.3	12.9	12.0	6.85	2.74	0.35	2.20	0.67
12	13.7	13.7	12.7	13.7	13.7	1.78	0.38	1.68	6.83	6.77
13	14.7	15.1	14.0	15.0	14.8	3.80	7.58	1.20	3.57	0.38
14	16.0	–	15.5	15.5	16.0	1.87	–	4.32	1.69	–
15	17.2	17.3	17.6	17.5	17.9	0.77	3.75	3.88	0.45	1.46
16	18.7	19.5	18.8	18.7	–	0.48	1.42	0.16	0.89	–
17	20.7	21.9	20.4	20.9	21.9	1.47	2.60	2.26	1.89	5.05
18	22.9	23.3	–	23.4	23.3	0.34	0.24	–	1.08	–
19	25.1	24.7	24.3	–	24,7	2.46	1.09	2.50	–	0.05
20	–	–	–	26.8	–	–	–	–	2.31	–

hybridization of O 2p- and Zn 3d-states and change of symmetry of all the three valence bands, as well as the relative values of their splitting energy.

For the first time, the full sets of exciton optical fundamental functions of ZnO have been calculated at 1.6, 4.2, and 90 K. The most correct energy values of transverse and longitudinal exciton transitions of the three series, together with their areas and oscillator strengths, have been determined, as well as their characteristic features.

The spectra of full sets of optical functions of ZnO crystals in the range 0–24 eV were calculated for polarizations **E** ⊥ **c** and **E** || **c** from three

experimental reflectivity spectra[5,14,15] and from two theoretical $R(E)$[24] and $\varepsilon_2(E)$[25] spectra. Very complex structures and strong polarization of most transition band maxima were found for five sets of optical functions. Good general agreement was established between the experimental and the theoretical optical function spectra.

The differences between the experimental $R(E)$ spectra of ZnO for polarizations $\mathbf{E} \perp \mathbf{c}$ and $\mathbf{E} \parallel \mathbf{c}$ in the range 3–24 eV (together with the spectra of the other optical functions, calculated from them)[6–8] and the theoretical $R(E)$[21] and $\varepsilon_2(E)$[26] spectra (together with the spectra of the other optical functions, calculated from them) are caused mainly by simplifications of the theoretical band calculation models, as well as by not taking into account the competitiveness of the metastable excitons model.

Thus, for the first time, three variants of ε_2 and $-\mathrm{Im}\varepsilon^{-1}$ polarized spectra of ZnO crystal in the energy region 0–26 eV have been decomposed into elementary components. The main parameters of the transverse and longitudinal transition components were found. The main features of the transitions parameters were determined. Having analyzed the theoretical bands provided by seven calculations of the electronic structure of ZnO, performed using different techniques, we estimated the energy values of possible interband transitions and their localization in various points of the Brillouin zone in the range of 3–30 eV. These simplified estimations proved to be in good agreement with the calculated energy values of the $\varepsilon_2(E)$ spectra decomposition components.

The obtained results allow to study the electronic structure and optical properties of ZnO crystal on the basis of conceptually deeper and more detailed background, than it was previously available on integral reflectivity spectra, and to base theoretical calculations of the properties of zinc oxide upon new foundations.

ACKNOWLEDGEMENTS

The paper was supported by the Fundamental Natural Sciences Center, State University of Saint-Petersburg, Russia.

REFERENCES

1. D. G. Thomas, *J. Phys. Chem. Sol.* **15** (1), 86–96 (1960).
2. Y. S. Park, C. W. Litton, T. C. Collins, and D. C. Reynolds, *Phys. Rev.* **143**, 512 (1966).
3. W. Y. Liang and A. D. Yoffe, *Phys. Rev. Lett.* **20,** 59 (1968).
4. J. Lagois and K. Hummer, *phys. stat. sol. (b)* **72**, 393(1975).

5. R. Klucker, H. Nelkowski, Y. S. Park, M. Skibowski, and T. S. Wagner, *phys. stat. sol. (b)* **45**, 265 (1971).
6. V. V. Sobolev, V. I. Donetskich, and E. F. Zagainov, *Fizika i Tekhnika Poluprovodnikov* **12**, 1089 (1978).
7. V. Sobolev, (Stiintza, Kishinev, 1980).
8. P. Kuzmina and V. A. Nikitenko, *Poluchenie i opticheskie svoystva*, (Nauka, Moscow, 1984).
9. J. Hopfield, *J. Phys. Chem. Sol.* **15,** 97 (1960).
10. Reynolds, D. C. Look, B. Jogai, and C. W. Litton, *Phys. Rev. B* **60**, 2340 (1999).
11. L. Lambrecht, A. V. Rodina, and B. Segal, *Phys. Rev. B* **65**, 75207 (2002).
12. H. Yoshikawa and S. Adachi, *Jpn. J. Appl. Phys.* **36**, 6237 (1997).
13. G. E. Jellison and L. A. Boatner, *Phys. Rev. B* **58**, 3586 (1998).
14. J. L. Freeouf, *Phys. Rev.* **7,** 3810 (1973).
15. R. L. Hengehold, R. J. Almassy, and F. L. Pedrotti, *Phys. Rev. B* **1**, 4784 (1970).
16. V. V. Sobolev and V. V. Nemoshkalenko, Elektronnaya struktura poluprovodnikov (Naukova dumka, Kiev, 1988).
17. V. V. Sobolev, A. I. Kalugin, V. Val. Sobolev, and V. I. Kormilets, *Wide Bandgap Materials* **8**, 87 (2001).
18. V. Val. Sobolev and V. V. Sobolev, *Phys. Low Dim. Struct.* **5/6**, 65 (2003).
19. C. J. Vesely, R. L. Hengehold, and D. W. Langer, *Phys. Rev. B* **5**, 2296 (1972).
20. D. Vogel, P. Kruger, and J. Pollmann, *Phys. Rev. B* **54**, 5495 (1996).
21. S. A. Leontyev, S. V. Koshcheyev, V. G. Devyatov, A. E. Cherkashin, and E. P. Mikheyeva, *Zh. Strukturnoy Khimii* **38**, 867 (1997).
22. S. Bloom, and J. Ortenburger, *phys. stat. sol. (b)* **58**, 561 (1973).
23. S. B. Zhang, S.-H. Wei, and A. Zunger, *Phys. Rev. B* **37**, 8958 (1995).
24. J. R. Chelikowsky, *Solid State Commun.* **22**, 351 (1977).
25. J. Xu and W. J. Ching, *Phys. Rev. B* **48**, 4335 (1993).

Chapter 16

PHOTO-INDUCED LOCALIZED LATTICE VIBRATIONS IN ZnO DOPED WITH 3D TRANSITION METAL IMPURITIES

Alexey Kislov
Ural State Technical University, Mira Str. 19, 620002 Ekaterinburg, Russia

Abstract: The purpose of this work is twofold: to simulate vibrational spectra of ZnO crystals with nickel impurities in different charge states and to analyze vibrational structures of electroabsorption spectra of ZnO:Ni based on calculations of localized vibrations induced by the impurities.

Key words: Impurity exciton, electroabsorption spectra, molecular static method, vibrational density of states, recursion method

1. INTRODUCTION

The progress in development of optoelectronics demands the further investigation of new materials and new effects being a basis for the production of various optoelectronic systems. A special interest is focuses on II-VI semiconductor compounds containing 3d transition metals as impurities. Due to the unique combination of physical properties ZnO crystals are potential candidates for numerous industrial applications.

In recent years some researchers were attracted by the photorefractive effect in such systems. It is based on the photoionization of 3d impurities by light. Note that at the photoionization of these impurities a non-stationary charge with respect to the lattice is created. Owing to the change of an impurity charge there can be a lattice deformation around 3d impurities. Besides, in the distorted part of the lattice photo-induced localized modes connected to the charged impurity can appear. Such modes are difficult to observe with traditional methods such as infrared absorption and Raman light scattering because the concentration of the charged centers is small.

N.H. Nickel and E. Terukov (eds.),
Zinc Oxide – A Material for Micro- and Optoelectronic Applications, 183–194.
© 2005 *Springer. Printed in the Netherlands.*

Under illumination the 3d impurity can pass in excited states of a hydrogen-like type as well. When the impurity loses the electron from the 3d-shell it is positively charged with respect to the lattice and the electron is confined by the long-range Coulomb field of the 3d impurity to a hydrogen-like orbit (see Fig. 1a and Fig. 1c). As a result a donor exciton is formed:[1] $d^n + \hbar\omega_d \rightarrow [d^{n-1}e]$. The acceptor exciton is formed after the transition of the electron from the valence band to the impurity and the Coulomb field of the negatively charged impurity keeps the hole in the hydrogen-like orbit (see Fig. 1b and Fig. 1c). Schematically, the process of formation of the acceptor exciton is written as follows: $d^n + \hbar\omega_a \rightarrow [d^{n+1}h]$.

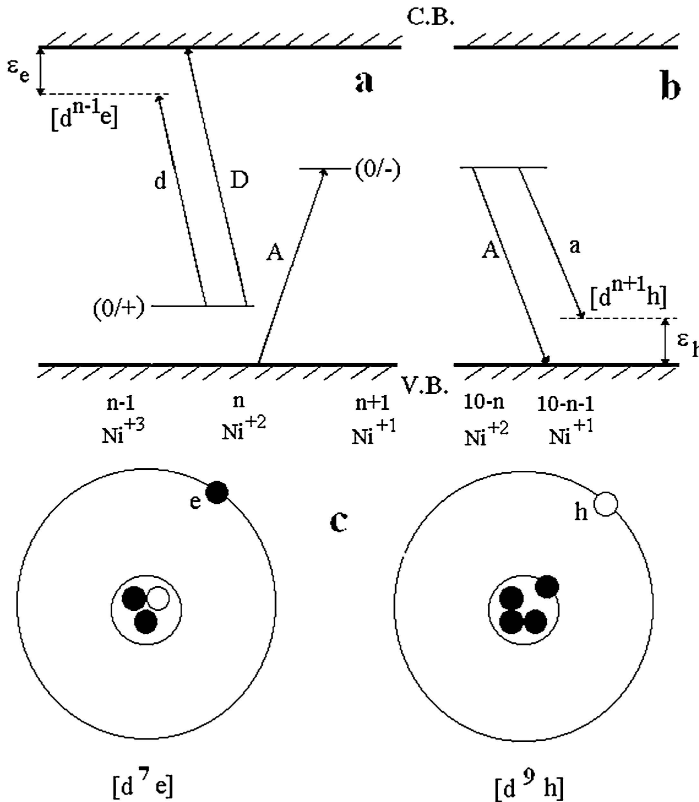

Figure 1. Diagrams of energy levels of a 3d impurity [(a) and (b)]: transitions involving an ionization of the impurity (D, A) and transitions to hydrogen-like states (d, a) are shown. Fig. 1(c) is an illustration of the transitions (d, a) in a space near a Ni impurity.

The formation of the impurity exciton leads to an appearance of photo-induced lattice vibrations. Sokolov[1] has offered an experimental electroabsorption (EA) method, which has a very high sensitivity for detecting such vibrations. However, the analysis of experimental data supposes a theoretical study of the vibrational spectrum of the defective crystal.

The purpose of our work was to simulate vibrational spectra of ZnO crystals containing nickel impurities in different charge states with respect to the lattice and also to analyze vibrational structures of EA spectra of ZnO:Ni based on calculations of localized vibrations induced by the impurities.

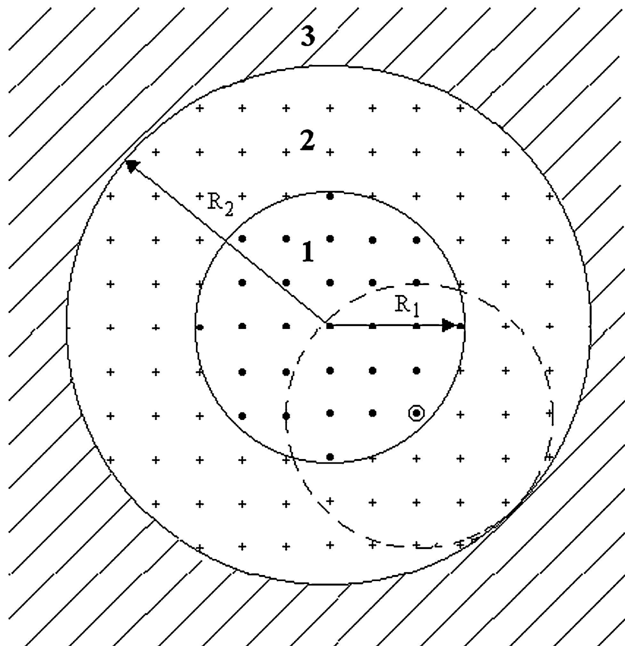

Figure 2. Illustrating the way the defective crystal is modeled.

2. METHODS OF CALCULATION

The lattice relaxation near the impurities was calculated on the basis of the molecular static method[2]. The crystal with the impurity was dividing into regions: an inner region 1 and an outer region 2+3 (see Fig. 2). The energy of the static lattice of this system can be written as[2]

$$E^{st} = E(\vec{x},\vec{\xi}) = E_1(\vec{x}) + E_2(\vec{x},\vec{\xi}) + E_3(\vec{\xi}) \quad (1)$$

where $E_1(\vec{x})$ is the energy of the region 1, $E_3(\vec{\xi})$ is the energy of region 3, and $E_2(\vec{x},\vec{\xi})$ is the interaction energy of regions 1 and 3. $\vec{x}$ is the coordinate describing the lattice configuration of region 1 while $\vec{\xi}$ is the displacement in region 3 and is formally distinguished from $\vec{x}$.

The ion displacements in region 1 can be determined by direct minimization of the defect energy with respect to $\vec{x}$, i.e.: by solving the equation

$$\sum_{\substack{i,\alpha \\ i\neq j}} \left. \frac{\partial E^{st}}{\partial x_{i\alpha}} \right|_{\vec{x}_{(n)}} + \sum_{\substack{i,j,\alpha,\beta \\ i\neq j}} \left. \frac{\partial^2 E^{st}}{\partial x_{i\alpha} \partial x_{j\beta}} \right|_{\vec{x}_{(n)}} u_{j\beta}^{st} = 0 \tag{2}$$

The defect formation energy is the difference in energy between the relaxed defective crystal and the ideal crystal: $\Delta E_d = E_d^{st} - E_{id}^{st}$.

The theoretical study of the lattice dynamics of the defective crystals conventionally makes use of the local vibrational density of states (LVDS)[3] $g_{i\alpha}(\omega)$[3]. It is related to the diagonal element of the Green's function $G_{ui\alpha}(\omega)$ by the expression[3]

$$g_{i\alpha}(\omega) = -\frac{2\omega}{\pi} \operatorname{Im} G_{u_{i\alpha}}(\omega) \ . \tag{3}$$

The latter in turn is determined by the dynamical matrix D of the crystal

$$G_{u_{i\alpha}}(\omega) = \langle u_{i\alpha} | [I(\omega^2 + i0) - D]^{-1} | u_{i\alpha} \rangle = \sum_{s=1}^{3N} \frac{|A_{i\alpha}^s|^2}{\omega^2 + \mathrm{i}0 - \omega_s^2} \ . \tag{4}$$

Using the recursive relationship,[4]

$$\mathbf{u}_{\mathbf{n+1}} = (\mathbf{D} - a_n)\mathbf{u}_{\mathbf{n}} - b_{n-1}\mathbf{u}_{\mathbf{n-1}} \tag{5}$$

we transform the dynamical matrix into tri-diagonal form

$$D = \begin{pmatrix} a_1 & b_1 & 0 & 0 & \dots & 0 \\ 1 & a_2 & b_2 & 0 & \dots & 0 \\ 0 & 1 & \dots & \dots & \dots & \dots \\ \dots & \dots & \dots & \dots & \dots & \dots \\ 0 & 0 & \dots & \dots & 1 & a_{3N} \end{pmatrix} . \tag{6}$$

In this case the diagonal element of the Green's function are described by the easily calculated continued fraction

$$G_{u_1}(\omega) = \cfrac{1}{\omega^2 - a_1 - \cfrac{b_1}{\omega^2 - a_2 - \cfrac{b_2}{\cfrac{\ddots}{\cfrac{b_{n-1}}{\omega^2 - a_n - b_n t(\omega)}}}}}, \qquad (7)$$

where t(ω) is a truncation function.

The well-known shell model[5] was used for modeling the local atomic structure and the lattice dynamics of the defective crystal. In this model, the lattice energy is written as

$$\begin{aligned} E_{lat} &= \frac{1}{2}\sum_{\substack{i,j \\ j\neq i}} \varphi(r_{ij}) + \frac{1}{2}\sum_i k_i \mu_i^2 \\ &= \frac{1}{2}\sum_{\substack{i,j \\ j\neq i}} [V^{Coul}(r_{ij}) + V^{Buck}(r_{ij})] + \frac{1}{2}\sum_i k_i \mu_i^2 \end{aligned} \qquad (8)$$

The structure and dynamics of the lattice were simulated by using empirical potentials of pair wise interactions. The interaction between ion cores is assumed to be long-range purely Coulombic. The interaction between electron shells has two components: a long-range purely Coulombic interaction and a short-range interaction described by the Buckingham potential.

$$V^{Coul}(r_{ij}) = \frac{X_i X_j}{r_{ij}^c} + \frac{X_i Y_j}{|\vec{r}_j^{\,s} - \vec{r}_i^{\,c}|} + \frac{Y_i X_j}{|\vec{r}_j^{\,c} - \vec{r}_i^{\,s}|} + \frac{Y_i Y_j}{|\vec{r}_j^{\,s} - \vec{r}_i^{\,s}|} \qquad (9)$$

$$V^{Buck}(r_{ij}) = A_{ij}\exp(-|\vec{r}_j^{\,s} - \vec{r}_i^{\,s}|/\rho_{ij}) - \frac{C_{ij}}{|\vec{r}_j^{\,s} - \vec{r}_i^{\,s}|^6}\ . \qquad (10)$$

3. RESULTS AND DISCUSSION

The parameters of the ion-ion interaction potentials in ZnO crystals are listed in Table 1. The values of the parameters were obtained by theoretical fits to the measured elastic and dielectric constants, the lattice constants, the lattice energy (see Table 2), and the phonon dispersion curves.

Table 1. The parameters A_{ij}, ρ_{ij} and C_{ij} of the Buckingham potential.

i – j ions	A_{ij} (eV)	ρ_{ij} (Å)	C_{ij} (eV/ Å) (Ref. 6)
Zn^{+2}–Zn^{+2}	890.0	0.300	0.0
Zn^{+2}–O^{-2}	1265.0	0.300	0.0
O^{-2}–O^{-2}	88760.0	0.149	0.0

Table 2. Potential charges and spring constants.

Ion	Y_i ($\lvert e \rvert$)	k_i (eV/ $Å^2$)
Zn^{+2}	3.749	116.4
O^{-2}	-2.930	51.8

Table 3. Calculated and observed crystal properties for ZnO.

Properties	Calculated	Observed
Lattice constants (Å)		
a	3.25	3.25 (Ref. 6)
c	5.21	5.21 (Ref. 6)
Lattice energy (eV)	40.8	42.2 (Ref. 7)
Elastic constants (GPa)		
C_{11}	237.4	209.7 (Ref. 8)
C_{12}	127.1	121.1 (Ref. 9)
C_{13}	115.8	105.1 (Ref. 9)
C_{33}	258.4	210.9 (Ref. 8)
C_{44}	60.2	42.47 (Ref. 8)
$C_{66} = (C_{11} - C_{12})/2$	55.2	44.29 (Ref. 8)
Dielectric constants		
$\varepsilon^0_\perp$	5.60	8.33 (Ref. 6)
$\varepsilon^0_\parallel$	6.10	8.84 (Ref. 6)
$\varepsilon^\infty_\perp$	3.82	3.94 (Ref. 8)
$\varepsilon^\infty_\parallel$	3.91	4.00 (Ref. 8)
Phonon spectrum gap (THz)	8.8 – 11.3	8.0 – 11.5 (Ref. 8)
ν_{max} (THz)	16.6	17.7 (Ref. 10)

As an example, Fig. 3 plots the phonon dispersion curves for three highly symmetric directions in the Brillouin zone of the perfect ZnO crystal. Comparison of the theoretical and experimental frequencies[8] shows good agreement for the acoustic branches. The densities of phonon states of the perfect ZnO crystal calculated by integrating over the Brillouin zone are displayed in Fig. 4. Comparison of the results of our calculation and a calcu-

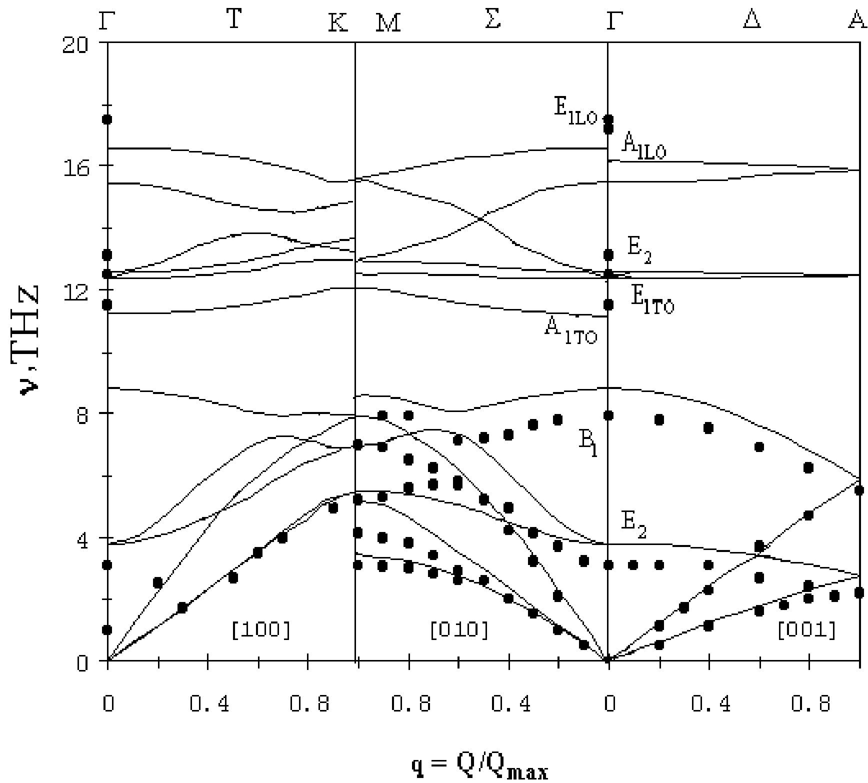

Figure 3. Phonon dispersion curves for ZnO crystals. The points denote experimental values.[8]

lation based on the valence force model[11] shows clearly that the approximation of pairwise central interactions is satisfactory. The difference in the position of the phonon forbidden region and of some maxima is due to limitations associated with the pairwise interaction approximation used in the calculations.

The formation of the nickel excitons results in the lattice distortion near them and the induced lattice vibrations. Conditions of their occurrence are defined by the charged impurity because the removed hydrogen-like type carrier practically does not influence the deformation of the lattice near the charged impurity. Thus, our analysis of the vibrational background of the zero phonon line of the EA spectrum of the nickel exciton is based on results of a simulation of the lattice dynamics of the ZnO crystal with Ni^{+1} or Ni^{+3} ions.

An important question is how to correctly describe the interaction between the defect and the remaining atoms of the crystal. The parameters of the short-range interaction potentials between the Ni impurities in various charge states and its surrounding ions being taken as the corresponding parameters

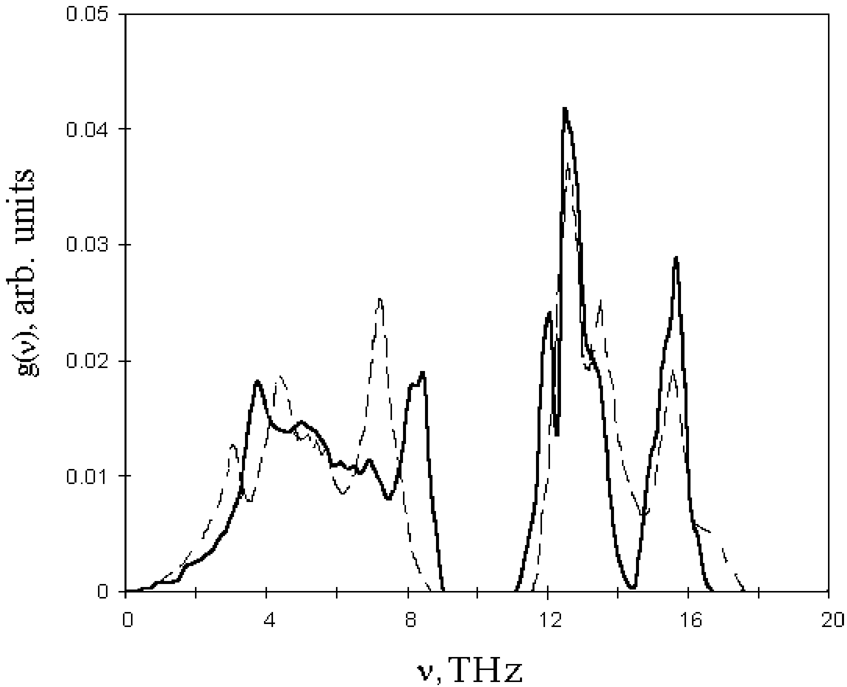

Figure 4. Total density of phonon states in ZnO crystals. Dashed line - result of the calculation from Ref. 11; solid line - our calculation.

for Zn ions. Of course, we took into account the change of mass and charge associated with the substitution of Ni^{+1} or Ni^{+3} for Zn.

Table 3 lists the displacements of nearest neighbors around the charged nickel. The calculations show that the nearest neighbors of the Ni^{+1} impurity are quite removed from it. For Ni^{+3} they shift toward the impurity.

The effect of charged nickel ions on the vibration spectrum of ZnO crystals was studied by calculating the symmetrized LVDS in perfect and defective crystals using a cluster of 1000 ions (region 1). For the calculation of the Coulombic component of the diagonal elements of the force constant matrixes of the ion-ion interactions by the Ewald method about 4000 ions were considered for region 2.

We have calculated the symmetrized LVDS projected onto a region containing two coordination spheres around a zinc ion or its nickel replacement. Nickel ions in ZnO crystals are in the positions with the symmetry point group C_{3v}. The 36-dimensional displacement space splits into the irreducible representations of the C_{3v} point group: $\Pi(36\times36) = 9A_1 + 3A_2 + 12E$.

Table 4. The defect formation energy and the displacements around the defect.

Defect	ΔE_d (eV)	Ion (coord. Sphere)	Displacement (Å)
Ni^{+1}	18.4	O^{-2} (1)	0.251
		Zn^{+2} (2)	-0.017
Ni^{+3}	-30.3	O^{-2} (1)	-0.240
		Zn^{+2} (2)	0.027

In Fig. 5 LVDS projected onto displacements with A_1-symmetry of the center ion and the O^{-2}(z) ion for ZnO:Ni crystals are presented. Specific features of the symmetrized LVDS in a defective crystal, which differ from those of the symmetrized LVDS in a perfect crystal, corresponded to both resonant vibrations and gap vibrations induced by defects. Local vibration frequencies were determined by observing the change of the sign of the real part of the Green's function. For example, the resonant vibration located in the acoustic band at the frequency 3.0 THz (see Fig.5a) is associated with motion of the Ni^{+1} impurity.

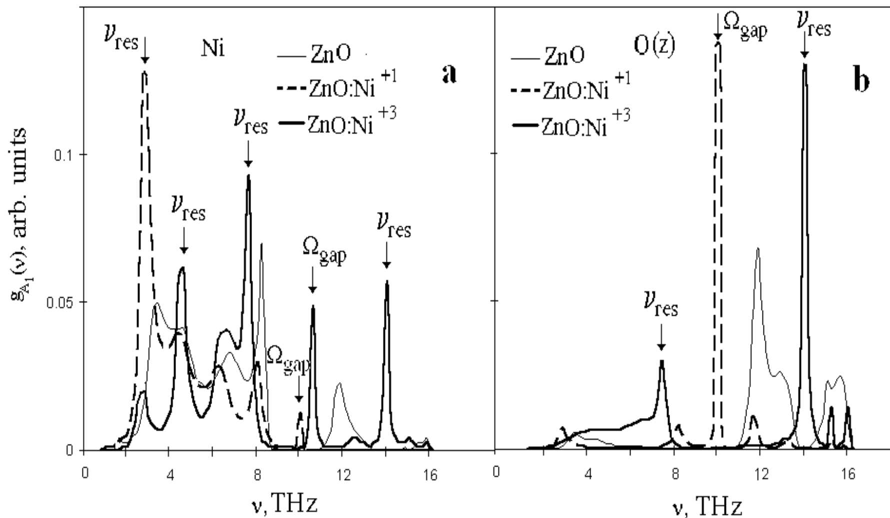

Figure 5. LVDS projected onto displacements with A1-symmetry of the center ion (a) and the O-2(z) ion (b).

Special attention is given to the localized vibrations with the symmetries A_1 and E. According to a group-theoretic analysis, they are active in the EA spectra of ZnO:Ni crystals. The frequencies of such localized vibrations induced by nickel impurities in ZnO crystals are listed in Table 4.

For ZnO:Ni the EA spectrum depicted in Fig. 6 (a) was measured at liquid-helium temperature T=4.2 K;[12] therefore, its vibrational part is shifted into the Stokes region of the spectrum and is associated with phonon creation.

Table 5. The frequencies of localized vibrations in ZnO with nickel impurities.

Defect	Type of mode	Type of symmetry	Frequency (THz)
Ni^{+1}	Resonance	A_1	3.0, 13.8
	Gap	A_1	10.0
	Local	A_1	16.8
	Resonance	E	3.0, 13.8
	Local	E	16.8
Ni^{+3}	Resonance	A_1	4.6, 6.8, 7.8, 14.0, 14.8
	Gap	A_1	10.8
	Local	A_1	17.4, 19.6
	Resonance	E	4.6, 6.8, 7.8, 14.0, 14.8
	Gap	E	9.8, 10.8
	Local	E	18.0

In the first-order phonon sidebands of the EA spectrum there are four features (arrows in Fig. 6(a)) that correspond to the maxima of the absorption spectrum. In our case, these features in the EA spectrum are zero-crossing points or points associated with the largest slope in the regions of fall-off of the absorption coefficient. These features correlate very well with the four strong peaks in the symmetrized LVDS projected onto displacements with A_1- and E-symmetries of the ions of two coordination spheres around a Ni^{+1} impurity (see Fig. 6(b)). These peaks correspond to the localized vibrations induced by the Ni^{+1} impurity.

Our calculation on defect vibrations enables the assignment of the EA spectrum features. For example, one is found at a frequency of 10.0 THz from the zero phonon line and falls in the region between the acoustic and optical bands of the phonon spectrum of the ZnO crystal. Perhaps it is due to an A_1-motion of the Ni^{+1} ion, the O^{-2} ions of the first sphere and the Zn^{+2} ions of the second sphere. According to our calculation, the EA spectrum for ZnO:Ni corresponds to the nickel acceptor exciton [d^9h].

4. CONCLUSIONS

The effect of charged nickel ions on the vibrational spectra of ZnO crystals was investigated by the recursion method using the shell model. The frequencies of localized vibrations of different symmetries were calculated with allowance for the atomic displacements in the vicinity of the charged impurities. These data on defect vibrations were applied to the interpretation

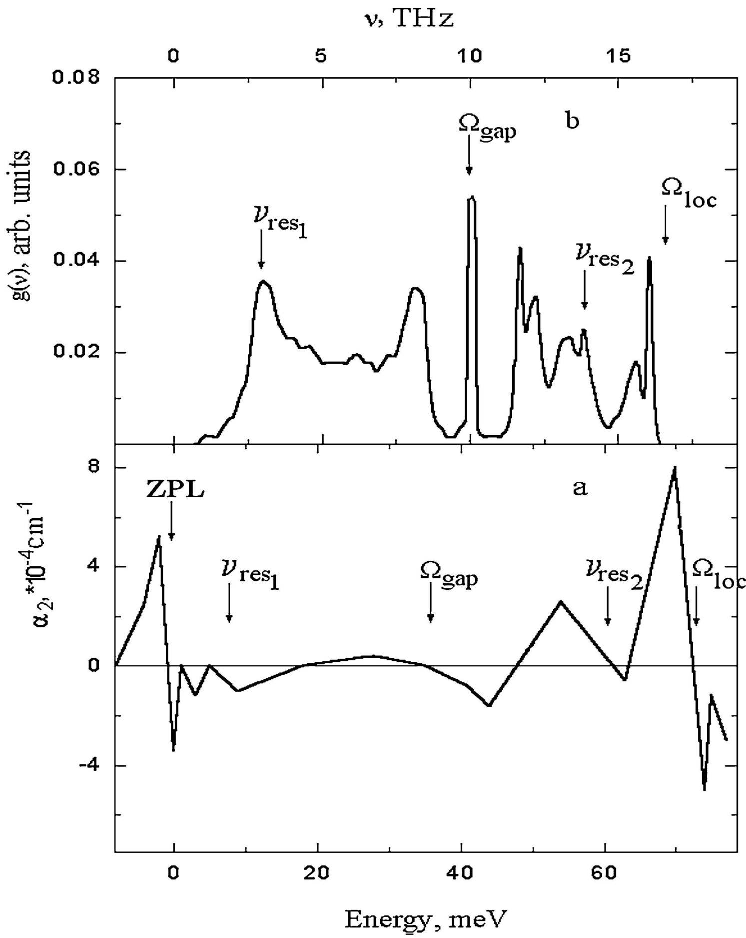

Figure 6. Spectral dependence of the EA second harmonic α2 for ZnO:Ni (a). Symmetrized LVDS projected onto displacements with A1- and E-symmetries of the ions of two coordination spheres around a Ni+1 impurity (b).

of the vibrational background of the zero phonon line of the EA spectrum of ZnO:Ni. The analysis of the EA spectrum based on model calculations of localized modes near a Ni^{+1} charged impurity has advanced our understanding of the vibrational structure of the EA spectrum. It was shown that the EA spectrum for ZnO:Ni corresponds to the nickel acceptor exciton.

REFERENCES

1. V. I. Sokolov, *Semiconductors* **28,** 329 (1994).
2. M. P. Puls, C. H. Woo, and M. J. Norgett, *Phil. Mag.* **36**, 1457 (1977).
3. P. E. Meek, *Phil. Mag.* **33**, 897 (1976).
4. S. K. Bose, *Phil. Mag. B* **49,** 631 (1984).
5. B. G. Dick, A. W. Overhause, *Phys. Rev.* **112**, 90 (1958).
6. P. P. Kuz'mina and V. A. Nikitenko, (Nauka, Moscow, 1984).
7. G. V. Lewis and C. R. A. Catlow, *J. Phys. C: Solid State Phys.* **18,** 1149 (1985).
8. K. Thoma, B. Dorner, G. Duesing, and W. Wegener, *Solid State Commun.* **15**, 1111 (1974).
9. T. B. Bateman, *J. Appl. Phys.* **33**, 3309 (1962).
10. J. M. Calleja and M. Cardona, *Phys. Rev. B* **16,** 3753 (1977).
11. S. V. Mel'nichuk, V. I. Sokolov, T. P. Surkova, and V. M. Chernov, *Phys. Sol. State.* **33**, 1833 (1991).
12. A. N. Kislov, V. G. Mazurenko, V. I. Sokolov, and A. N. Varaksin, *Phys. Sol. State.* **41,** 897 (1999).

PART V: DEVICE APPLICATIONS

Chapter 17

ZnO WINDOW LAYERS FOR SOLAR CELLS

Walther Fuhs
Hahn-Meitner-Institut Berlin, Kekuléstraße 5, D-12489 Berlin, Germany

Abstract: ZnO layers are very frequently used as window layers in photovoltaic solar cell structures. In this application high electrical conductivity σ should be combined with a low value of the optical absorption constant α in the visible range. Thus an appropriate measure of the performance is the ratio $r = \sigma/\alpha$ and the optimization consists in realizing high σ by high carrier concentration and mobility with a minimum optical loss due to free carrier absorption at long wavelength. Such layers can be prepared by numerous techniques most frequently by magnetron sputtering either from compound targets or reactively from metallic targets. Optimized doped ZnO-layers have resistivities of 1.5-2×10^{-4} Ωcm with Hall mobilities of up to 60 cm^2/Vs, refractive indices of approximately 2.0 and an average transmittance of 85 % in the visible range. It appears that for the value of μ the physical limit as defined by ionized impurity scattering has been reached for homogeneously doped thick layers. This paper will discuss various aspects of the application of ZnO window layers in photovoltaic solar cells.

Key words: Polycrystalline films, heterointerface window layers, electrical transport, doping, light trapping

1. INTRODUCTION

Transparent, electrically conducting films (TCO) have been prepared from a large variety of materials such as semiconducting oxides of Sn, In, Zn, and Cd.[1] The uses of such materials are manifold. Particularly important are low emissivity glass for building applications, energy-saving windows, front electrodes in flat-panel displays, thermal solar collectors, solar cells or smart windows. In such applications high electrical conductivity σ should be combined with a low value of the optical absorption constant α in the visible range. Thus an appropriate measure of the performance is the ratio $r = \sigma/\alpha$ and the optimization consists in realizing high σ by high carrier

N.H. Nickel and E. Terukov (eds.),
Zinc Oxide – A Material for Micro- and Optoelectronic Applications, 197–209.
© 2005 *Springer. Printed in the Netherlands.*

concentration and mobility with a minimum optical loss due to free carrier absorption at long wavelength. However, for a particular application this figure of merit is not the only parameter that has to be considered. Further aspects may become important such as physical, chemical and thermal durability, stability, homogeneity, chemical etchability, workfunction, method of preparation, toxicity, availability of the materials or simply cost factors. So far tin oxide, SnO_2, prepared by chemical vapor deposition (CVD) is most commonly used in low-energy windows and indium tin oxide (ITO) made by spray pyrolysis or sputter deposition is the preferred material for flat panel displays.[1] ZnO films are used in particular for transparent contacts in photovoltaic solar cells (window layers). However, due to potentially lower cost, material availability and easy chemical etchability ZnO may become attractive also for display applications in the future.

This article deals with various aspects of ZnO window layers in photovoltaic cells. The copper indium diselenide $CuInSe_2$ (CIS) thin-film solar cell uses a ZnO window with a thickness of about one μm. Here ZnO forms a heterojunction with a CdS buffer layer.[2] In the superstrate configuration of the amorphous silicon a-Si:H pin solar cell light enters through the glass substrate which is covered by a thick ZnO layer. This layer is chemically structured to enhance light scattering to enable the efficient use of sun light.[3] A third example is a solar cell on basis of a silicon wafer which uses a heterojunction formed between a highly doped thin a-Si:H emitter layer an the crystalline silicon wafer. In this case the task of the window layer is twofold: enhancement of the lateral conductivity and reduction of the reflection losses. The latter limits the thickness to 80 nm only.[4] These examples demonstrate the various aspects in the application: high lateral conductivity, formation of heterojunctions (ZnO/CdS, ZnO/a-Si:H) and the generation of textures for enhanced light trapping by chemical etching.

2. PREPARATION AND STRUCTURE

The research on polycrystalline ZnO layers so far has been performed on an empirical basis mainly. ZnO films on glass substrates have been prepared by a variety of techniques such as chemical vapor deposition (CVD), magnetron sputtering (MS), spray pyrolysis, metal organic chemical vapor deposition (MOCVD), or pulsed laser ablation.[1] Of particular importance has been magnetron sputtering due to a number of advantages: low process temperatures, high deposition rate, reasonable controllability of the process, potentially low cost and scalability to large areas. Highly conducting n-type films can be made either in argon atmosphere from compound targets (ZnO/Al_2O_3) or by sputtering reactively in argon/oxygen atmosphere from

metallic targets (Zn/Al). The dependence of the physical properties of the films on the most important deposition parameters substrate temperature, pressure and oxygen flow rate has been studied intensively.[5,6] The growth can qualitatively be described in a modified structure zone model as developed by Thornton.[7] This model predicts that with increasing substrate temperature and decreasing pressure there is a transition from a porous structure (tapered crystallites with voids) to a densely packed film (columnar structure). A qualitative explanation of this trend may be that the reduction of pressure results in an increase of the mean free path to values close to the substrate/target separation and thus to a higher energy of the species impinging on the growing surface.

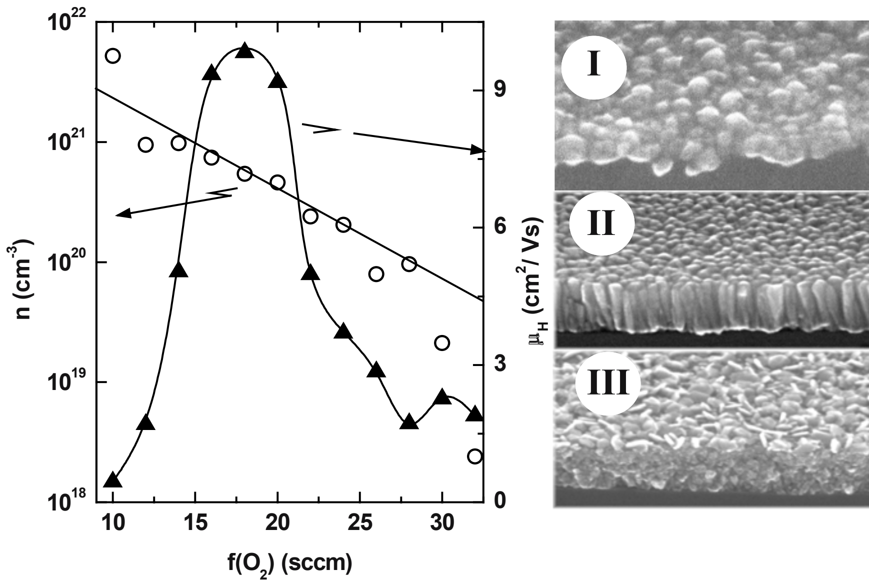

Figure 1. Electron concentration n and electron mobility μ measured by Hall effect of ZnO films prepared by reactive magnetron sputtering as a function of the oxygen flow rate $f(O_2)$. SEM micrographs taken on samples in the three regions of low, medium and high $f(O_2)$.[8,9]

In a reactive sputtering process the oxygen flow rate $f(O_2)$ is the most relevant parameter. Fig.1 displays a typical example of the influence of $f(O_2)$ on physical properties and structure. Hall effect measurements show that the free carrier concentration n decreases continuously with $f(O_2)$ whereas the electron mobility attains a maximum at medium values of $f(O_2)$. This variation of the n and μ clearly reflects the change from metallic behavior at low $f(O_2)$ (region I) to oxide formation (region III) at high $f(O_2)$ which is related with an increase of the optical transmission T. These changes are accompanied by structural variations in the ZnO layers. The SEM

micrographs taken on samples in the three regions show granular morphology with high surface roughness in region I and a flaky morphology in region III. Around $f(O_2)$ = 15 sccm (range II) where the mobility attains a maximum value the films are compact with columnar structure which has preferential orientation of the c-axis perpendicular to the glass substrate.[9]

Independent of the deposition method used ZnO films contain a high amount of hydrogen. Fig. 2 displays photoelectron spectra (XPS-O1s-spectra) that have been obtained on layers prepared by magnetron sputtering in the UHV.[10] The structure at E_B = 533 eV in the O1s-spectrum of the as-deposited layer has been assigned to $Zn(OH)_2$. Annealing at 400 °C in O_2 atmosphere results in hydrogen effusion and a reduction of the hydrogen content to values below of the XPS detection limit. Fig. 2b shows the hydrogen profiles of the same samples determined with the nuclear reaction technique (^{15}N-profiling). The hydrogen concentration in the bulk of the layers is as high as $10^{21}cm^{-3}$ and decreases upon annealing by about two orders of magnitude. The presence of hydrogen in such high amounts in ZnO window layers has been ignored so far. At present it is not clear whether the hydrogen is homogeneously distributed in the bulk of the films or whether the hydrogen terminates grain boundaries. It is also an open question whether hydrogen is directly or indirectly responsible for n-type conduction of nominally undoped films. In single crystalline ZnO hydrogen has been shown to form a flat donor state.[11] It appears also reasonable that hydrogen in such high concentrations affects the defect structure considerably and forms complexes with intrinsic defects and/or impurities.

3. TRANSPORT PROPERTIES

The transport properties of polycrystalline ZnO films have mainly been studied on an empirical basis focused by the requirement of high conductivity and high transparency for conducting window layers. ZnO films in general exhibit n-type conduction with values for the resistivity strongly dependent on the deposition conditions and/or doping level.[6,12] The influence of the preparation conditions is rather confusing. The scatter in the data from various laboratories often prevents general conclusions. An example is the influence of the substrate temperature. If one compares data from various laboratories no trend can be observed. However, the resistivity clearly decreases with increasing substrate temperature within one preparational set from a single laboratory. Among the preparation methods magnetron sputtering appears to be superior. Besides of practical and cost

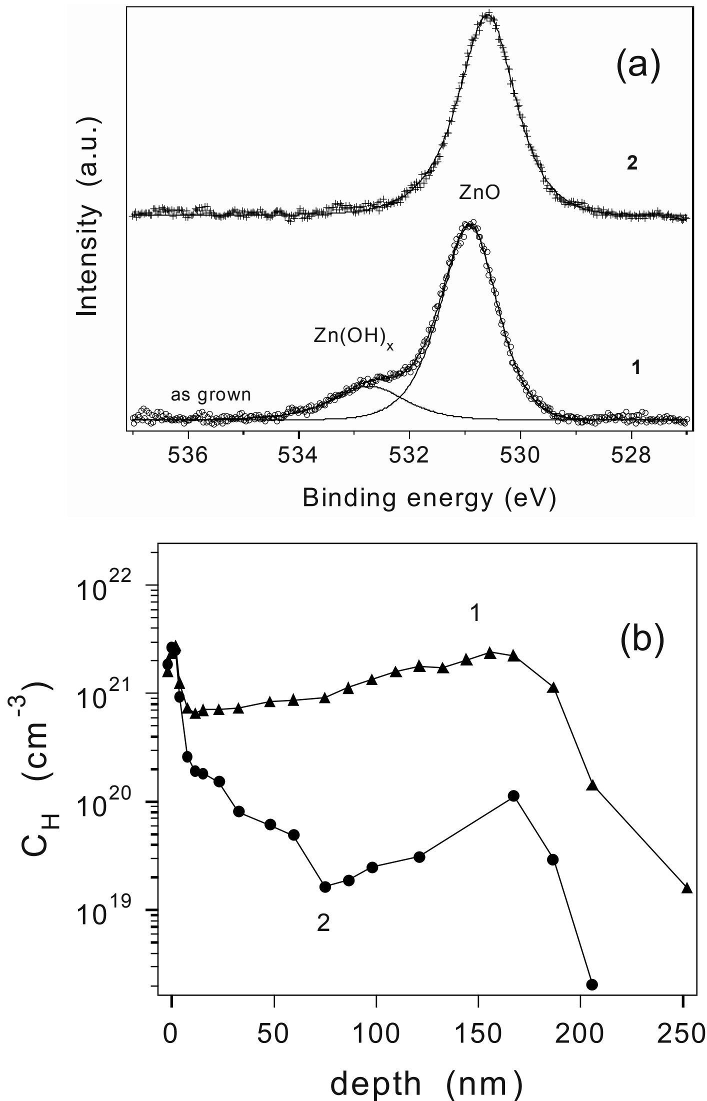

Figure 2. (a) XPS-Photoelectron spectra of ZnO deposited by magnetron sputtering taken with an excitation energy of E_{ex} = 1486 eV (O1s-spectra): (1) as deposited, (2) after annealing at 400 °C; (b) Depth profile of the hydrogen concentration CH determined by nuclear reaction technique (^{15}N). Same ZnO samples as in (a).[10]

arguments it has been emphasized that the physical advantage lies in the incorporation of particle energy from the plasma into the growing film. Two directions have been pursued to obtain the low resistivity values at room temperature:

1. Creation and control of intrinsic donor levels by defects such as oxygen vacancies or Zn atoms on interstial sites. Undoped ZnO films with resistivities of less than 5×10^{-4} Ωcm have been prepared by magnetron sputtering without adding impurities but were found to be unstable at T > 150 °C.[13]
2. Impurity doping with group III elements (Al, Ga, In, B) or with group IV elements (Si,Ge, Ti; Zr, or Hf) incorporated substitutionally on Zn-sites. Alternatively also group VII elements have been used such as F incorporated on an O-site. The lowest values achieved today range at 1.5 - 2×10^{-4} Ωcm rather independent of the method of preparation.

Fig. 3 summarizes literature data on the resistivity ρ and Hall mobility μ from various laboratories with different techniques for preparation and doping.[6] ρ and μ are plotted as a function of the carrier concentration n. The figure includes results for undoped and doped ZnO single crystals for comparison. As one expects, ρ decreases monotonously with n. The lowest values reached are 1.5-2×10^{-4} Ωcm at about 1.5×10^{21}cm^{-3}. Most interestingly these values are reached almost independently of the kind of dopant used. It is obvious that there is an intrinsic limitation to the dopability which is given by the solubility of the dopants which for all elements used is in the order of a few at%.

The scatter in the data for μ is more pronounced than for ρ and probably due to the influence of structural defects such as grain boundaries on the scattering mechanism. At $n < 10^{19}$ cm^{-3} scattering at structural defects appears to be dominant. The results obtained without impurity doping where μ increases with n fall in this range. It is interesting to notice that at $n > 10^{19}$ cm^{-3} the mobility values of single crystals and polycrystalline ZnO films are of very similar magnitude and both decrease with increasing carrier concentration. This supports the view that the mobility in highly doped material is not limited by the crystalline structure. Scattering at ionized impurities has been proposed as the dominant scattering process in this doping range. The dashed curve shows the result of the theoretical estimate for impurity scattering basing on parabolic bands.[14] Clearly, the mobility calculated from this approach is considerably too high. Various corrections to this theory have been proposed such as additional contribution of grain boundary scattering, non-parabolic bands, multiply charged scattering centers, or cluster formation at higher doping levels. In most applications thick ZnO layers (typically 1 μm) are used for window layers. However, there are also situations where thin ZnO layers are required in order to meet two demands: high lateral conductivity and low reflectivity. The latter requires very thin ZnO layers (about 80 nm). It has been reported quite generally that the physical properties of ZnO depend on the layer thickness.

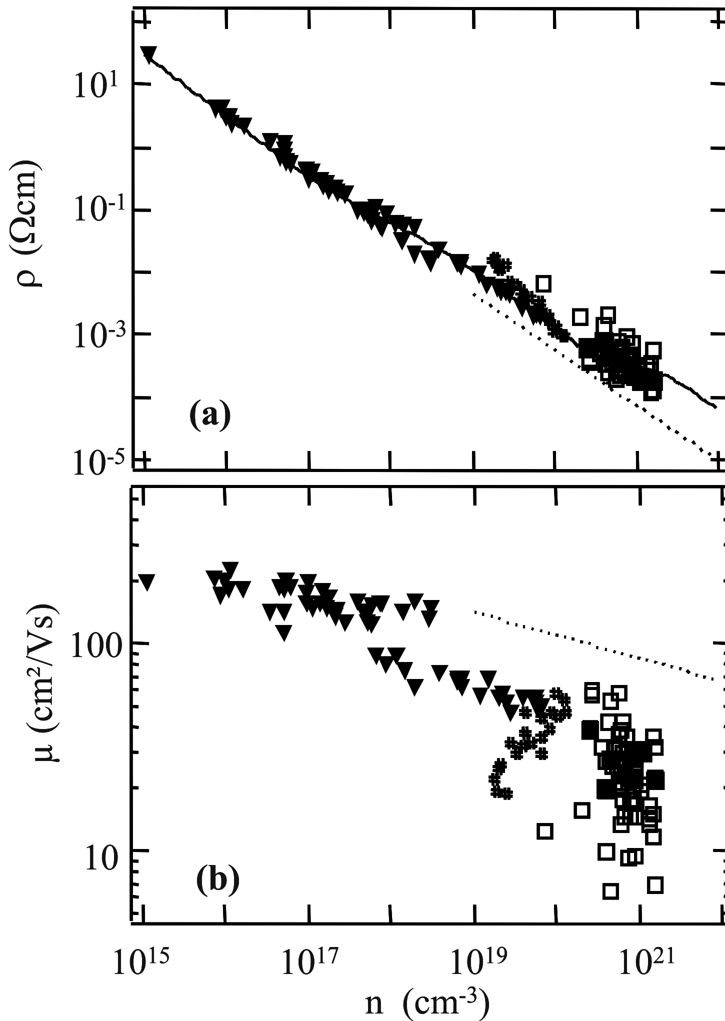

Figure 3. Resistivity ρ (a) and Hall mobility μ (b) as a function of the carrier concentration n.[6] Data from various laboratories: ▼ ZnO single crystals, (■,□) magnetron sputtering impurity doped, # magnetron sputtering without impurity doping. The dashed line is the result of a theoretical estimate for impurity scattering.[14]

Using glass substrates it has been observed that the resistivity increases appreciably with decreasing layer thickness at values below of 100-300 nm mainly due to a decrease of the electron mobility. A possible reason for such behavior is the different growth and morphology in the early stages of film growth.[15]

4. ZnO/SEMICONDUCTOR INTERFACE

In many applications not only the bulk properties of the ZnO layers are important but also the morphology and electronic structure of the ZnO/semiconductor interface which may have influence on the band profiles of the solar cells, losses by contact resistance and instability.

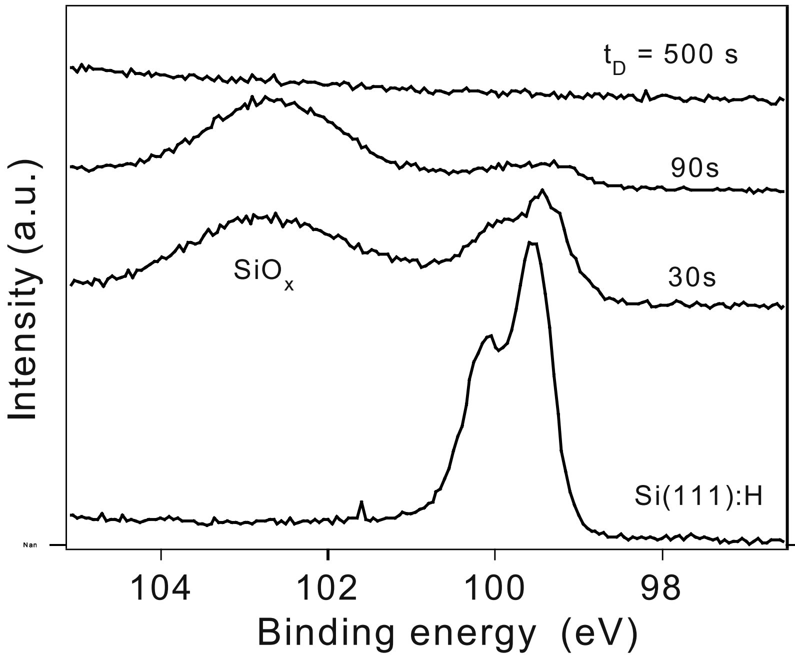

Figure 4. Photoelectron spectra (Si 2p core levels) of magnetron sputtered ZnO layers after different deposition times t_D (different thickness).[10]

For PV-applications the stability of the cell efficiency is a very critical parameter. Therefore CIS solar cells have to pass a test, a so called damp-heat-test, where the modules are held in an atmosphere with a humidity of 85 % at a temperature of 85 °C. For non-encapsulated Cu(In,Ga)Se_2 cells under such conditions in particular the open circuit voltage and the fill factor degrade as a function of time causing severe performance loss.[16] The physical background of this effect is quite unclear. The observed small increase of the sheet resistance of the ZnO window apparently is not sufficient to explain this effect. Some investigations suggest that the degradation is strongly related with the use of CdS as bufferlayer which may react with ZnO and thus cause an increase of the contact resistance of the window.[16]

The ZnO/Si heterointerface has been of particular interest in photovoltaics. The preparation of interfaces with high electronic quality is complicated by the problem that oxidation of the surface of the Si substrate may be induced by the deposition process. The photoelectron spectra (Fig. 4) show that indeed oxide formation occurs in the early stages of film growth when the films are deposited by magnetron sputtering.[10] The finger print of SiO_x are the bands at a binding energy of about 103 eV. For the H-terminated Si(111) surface no structure is found in this spectral range. Clearly the suboxide band develops at small deposition times. Concomitantly the Si-2p bands decrease due to the decreasing sensitivity to the surface of the Si wafer (1-2 nm). This is also the reason why no structure from neither the Si-wafer nor the oxide surface layer can be observed when after longer deposition time (t_D = 500 s) a thicker ZnO layer has grown. Besides of the oxidation of the Si substrate reduction of Zn is observed. Surface sensitive photoelectron spectroscopy clearly reveals a neutral Zn°-phase as well as Zn_2SiO_4 phases at the interface.

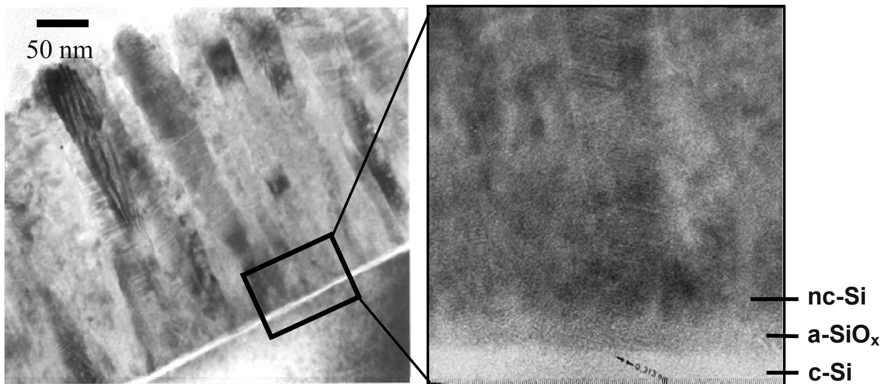

Figure 5. Cross sectional TEM micrographs of the ZnO/c-Si interface.[17]

The complex structure of the ZnO/Si interface has also directly been observed in cross-sectional TEM micrographs. An example is given in Fig. 5. This micrograph clearly reveals the formation of a thin amorphous film on the Si-surface (suboxide phase), the formation of nano-crystalline phases followed by columnar ZnO growth.[17]

The above results showed that the ZnO/Si interface prepared by magnetron sputtering is of high complexity and difficult to control. This explains why all attempts to develop photovoltaic devices with reasonable performance on basis of sputtered ZnO/Si heterojunctions have failed. This may be a particular problem of the deposition method used. Recently it was

shown that the formation of silicon suboxides at the interface does not occur when the ZnO film is deposited by metal organic chemical vapor deposition (MOCVD) from diethylzinc/H_2O vapor on a heated substrate.[10] The different result obtained from these two methods may be explained by the fact that in case of MOCVD only thermal energy is involved while magnetron sputtering is characterized by additional energy input from the plasma into the growing film. The quality of the interface may therefore strongly depend on the energy of the species, which are responsible for film growth, and on the ion-to-neutral ratio in the plasma.

5. LIGHT TRAPPING

Silicon thin-film solar cells on basis of hydrogenated amorphous silicon, a-Si:H, and microcrystalline silicon, µc-Si:H, are one of the most promising technology options for cost effective photovoltaic modules. A common device structure for such cells uses a superstrate configuration (glass/ZnO/p-i-n/Al) where the light penetrates in through the glass. Effective light trapping is essential to achieve high cell efficiencies with absorber layers the thickness of which is in the range of one µm only. This can be achieved by an optimized surface texture of the window layer which results in light scattering and a back reflector for the transmitted part of the light which often consists of a ZnO/Al double layer.[3] In the superstrate configuration used, ZnO is required as window layer forming the front contact and has to combine high conductivity (low series resistance) with high transparency and excellent surface texture (milky appearance). The required surface texture can be realized with sputtered ZnO:Al films by a combination of a proper choice of the process parameters of the sputter process and post-deposition wet chemical etching in diluted hydrochloric acid HCl.[7] With increasing substrate temperature and decreasing pressure there is a transition from a porous structure (tapered crystallites with voids) to a densely packed film (columnar structure). In the same direction the etching rate decreases. Films which, are prepared at low substrate temperature and high deposition pressure, have a porous rough surface structure and are homogeneously etched without surface texturing. For optimized surface texture resulting in optimized light scattering over a wide wavelength range the starting structure has to be densely packed with a smooth surface. Fig. 6 shows an example for an optimized surface texture and the resulting optical properties. The layer is highly transparent and the reflection amounts to less than 10 % in the entire visible spectral range.[3] Fig. 7 compares the external quantum efficiencies of µc-Si:H solar cells prepared as glass/ZnO/pin-structures on

smooth (as deposited) and textured ZnO (short HCl-dip, optimized) window layers. The cells had been prepared in the same run with an absorber layer

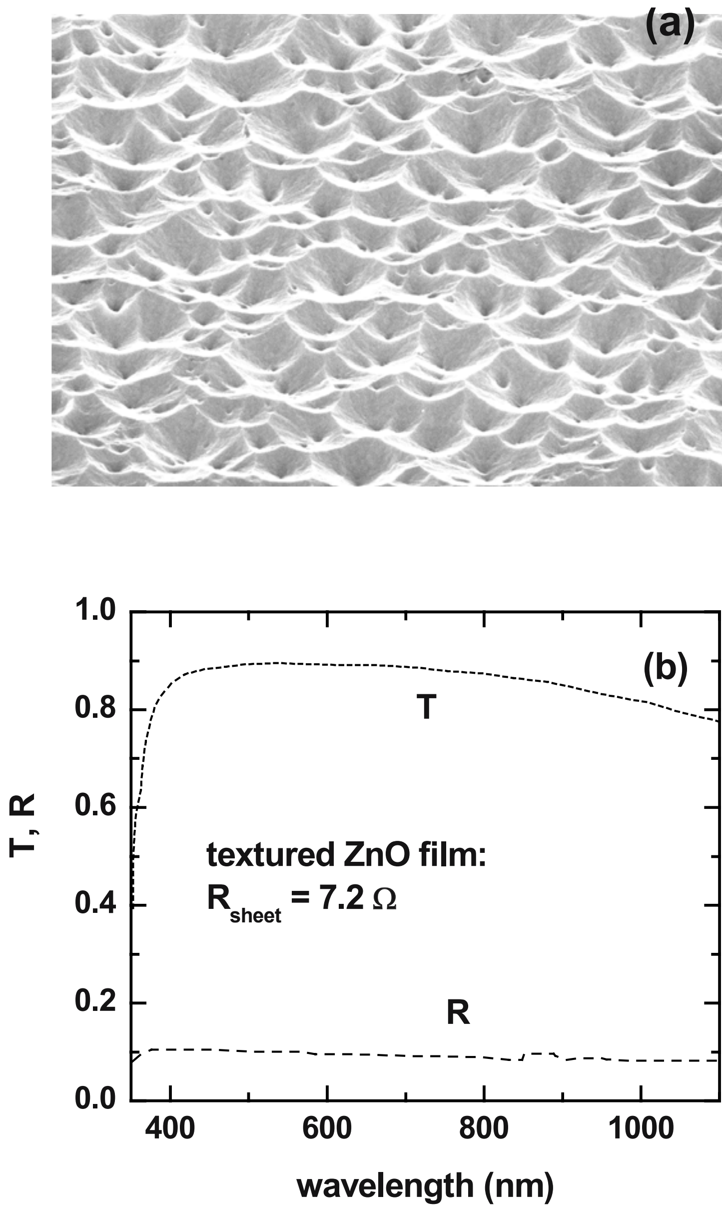

Figure 6. Optimized surface texture of ZnO-layer (a) and optical properties: transmission T and reflectivity R (b).[3]

thickness of 1.1 μm. Texturization enhances the external quantum efficiency in the entire spectral range. On the short wavelength side this is due to a reduction of the reflection of the cells. The enhancement at long wavelengths is mainly due to an enhancement of light trapping. From a comparison of the

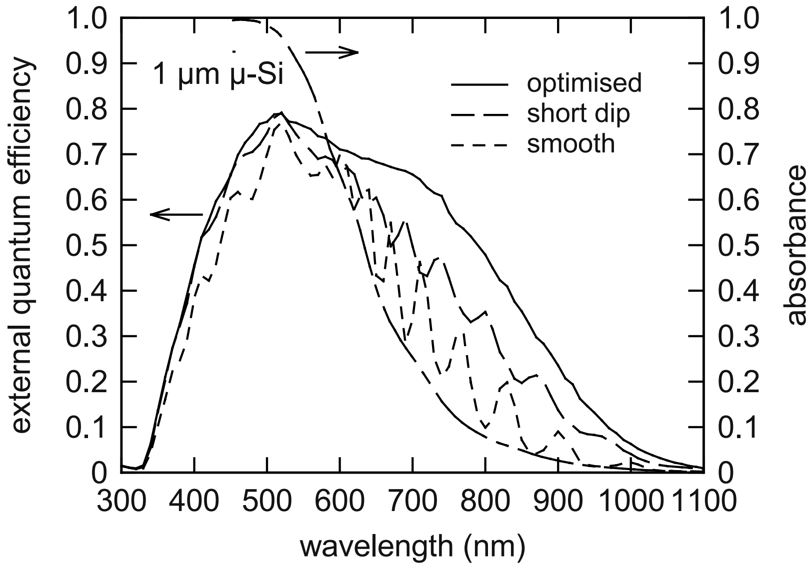

Figure 7. External quantum efficiency of μc-Si:H solar cells, glass/ZnO(textured)/pin/ZnOAl, co-deposited on smooth, shortly etched and optimized ZnO window layer. For comparison the absorbance of a 1 μm thick μc-Si:H layer is shown.[3]

absorbance of a 1 μm thick μc-Si:H layer with the quantum efficiency it has been concluded that the effective light path through the i-layer must be larger than 10 μm.[3] Although at present the a-Si:H based solar modules quite commonly use tin oxide (SnO_2:F) coated glass substrates, doped ZnO prepared by sputtering and post deposition etching presents a promising alternative for the future.

6. CONCLUSION

Polycrystalline ZnO for window layers in solar cells are most frequently prepared by magnetron sputtering. Optimized layers have resistivities of $1.5\text{-}2\times10^{-4}$ Ωcm with Hall mobilities of up to 60 cm^2/Vs, refractive indices of approximately 2.0 and an average transmittance of 85 % in the visible range. The best values of the mobility in optimized films have reached the

intrinsic limit set by ionized impurity scattering. Optimized films grow with columnar structure with the c-axis oriented perpendicular to the substrate. Depending on the type of solar cell various aspects have to be considered: high lateral conductivity, formation of heterojunctions (ZnO/CdS, ZnO/a-Si:H) and the generation of textures for enhanced light trapping by chemical etching.

ACKNOWLEDGMENT

The author gratefully to C. Pettenkofer for allowing the use of so far unpublished results (Figs. 2 and 4) and to Ina Sieber and Frank Fenske for fruitful discussion.

REFERENCES:

1. D. S. Ginley and C. Bright (guest editors), *MRS Bulletin*, 15 (2000).
2. J. Hedström, H. Ohlsen, M. Bodegard, A. Kylner, L. Stolt, D. Hariskos, M. Ruckh, and H. W. Schock, *Proc. 23rd IEEE PVSC* (1993).
3. B. Rech, J. Müller, T. Repmann, O. Kluth, T. Roschek, J. Hüpkes, H. Stiebig, and W. Appenzeller, *Mat. Res. Soc. Symp. Proc*. **762**, A 3.1. (2003).
4. M. Schmidt, A. Schöpke, O. Milch, T. Lussky, and W. Fuhs, *Mat. Res. Soc. Symp. Proc.* **762**, A19.11.1. (2003).
5. K. Ellmer, *J. Phys. D: Appl. Phys.* **33**, R1 (2000).
6. K. Ellmer, *J. Phys. D: Appl. Phys*. **34**, 3097 (2001).
7. O. Kluth, G. Schöpe, J. Hüpkes, C. Agashe, J. Müller, and B. Rech, *Thin Solid Films* **442**, 80 (2003).
8. S. Brehme, F. Fenske, W. Fuhs, E. Neubauer, M. Poschenrieder, B. Selle, and I. Sieber, *Thin Solid Films* **342**, 167 (1999).
9. F. Fenske, W. Fuhs, E. Neubauer, A. Schöpke, B. Selle, and I. Sieber, *Thin Solid Films* **343**, 130 (1999).
10. U. Meyer, *Dissertation Universität Cottbus* (2004), U. Meyer and C. Pettenkofer, unpublished.
11. S. F. J. Cox, E. A. Davis, S. P. Cottrell, P. J. C. King, J. S. Lord, J. M. Gil, H. V. Alberto, R. C. Vilao, J. Pironto Duarte, N. Ayres de Campos, A. Weidinger, R. L. Lichti, and S. J. C. Irvine, *Phys. Rev. Lett.* **86**, 2601 (2001).
12. T. Minami, *MRS Bulletin*, 38 (2000).
13. T. Minami, H. Nanto, and S. Takata, *Appl.Phys.Lett.* **41**, 958 (1982).
14. J. R. Bellingham, W. A. Phillips, and C. J. Adkins, *J. Mater. Sci. Lett.* **11**, 263 (1992).
15. M. Birkholz, B. Selle, F. Fenske, and W. Fuhs, *Phys. Rev. B* **68**, 205414 (2003).
16. J. Wennerberg, J. Kessler, and L. Stolt, *Solar Energy Materials and Solar Cells* **75**, 47 (2003).
17. I. Sieber, N. Wanderka, I. Urban, I. Dörfel, E. Schierhorn, F. Fenske, and W. Fuhs, *Thin Films* **330**, 108 (1998).

Chapter 18

ZnO/AlGaN ULTRAVIOLET LIGHT EMITTING DIODES

E. V. Kalinina[1], A. E. Cherenkov[1], G. A. Onushkin[1], Ya. I. Alivov[2], D. C. Look[3], B. M. Ataev[4], A. K. Omaev[4], and C. M. Chukichev[5]
[1]A. F. Ioffe Physico-Technical Institute, RAS, 194021 St. Peterburg, Russia, [2]Institute of Microel. Technology, RAS, Chernogolovka, Moscow dist., 142432 Russia, [3]Semiconductor Research Center, Wright State University, Dayton, Ohio 45435, U.S.A., [4]Institute of Physics, Daghestan Scientific Centre of RAS, Makhachkala, 367003 Russia, [5]Department of Physics, Moscow State University, 119899 Moscow, Russia

Abstract: We report on the optical and electrical properties of *n*-ZnO/*p*-AlGaN heterojunctions. Ga doped *n*-type ZnO layers were grown using chemical vapor deposition on Mg doped *p*-type AlGaN epitaxial layers. AlGaN epitaxial layers with 12 at.% Al were grown on 6H-SiC by hydride vapor phase epitaxy. Rectifying diode-like behavior with a threshold voltage of 3.2 V was achieved. Intense ultraviolet electroluminescence peaking at a wavelength of 390 nm was observed at 300 and 500 K as a result of hole-injection from the *n*-ZnO layer into the *p*- AlGaN layer of the heterostructure.

Key words: Electroluminescence, epitaxial layers, heterojunction, hole injection, ultraviolet emission

1. INTRODUCTION

Zinc oxide, with a direct bandgap of ~3.3 eV is a promising semiconductor for the fabrication of ultraviolet light emitting diodes and lasers.[1-3] ZnO has some properties that are perhaps more favorable than those of other wide bandgap semiconductors such as GaN and SiC. These include intense exciton luminescence with a large exciton binding energy of ~60 meV that provides effective exciton luminescence at high temperatures, higher quantum efficiency of the photo- and cathodoluminescence (PL, CL) as well as the relative simplicity of the growth of ZnO epitaxial layers. However, despite much progress in ZnO technology in recent years, high

N.H. Nickel and E. Terukov (eds.),
Zinc Oxide – A Material for Micro- and Optoelectronic Applications, 211–216.
© 2005 *Springer. Printed in the Netherlands.*

quality *p*-type ZnO and therefore, the manufacture of ZnO homojunctions, continues to be problematic. The alternative means for attaining functional device structures with ZnO is the fabrication of ZnO based heterojunctions with other *p*-type semiconductors.[4-7]

The AlGaN alloys are suited to this application since they can be doped *p*-type, have a larger bandgap, and are relatively well lattice-matched to ZnO.[8] In this work, we present the results on optical and electrical properties of *n*-ZnO/*p*-AlGaN heterojunctions.

2. EXPERIMENTAL PROCEDURE

Commercial *n*-type 6H-SiC wafers with a concentration of uncompensated donors $N_d - N_a = 3\times10^{18}$ cm $^{-3}$ were used as substrates. These substrates were covered with a thin epitaxial *n*-GaN buffer layer grown by hybrid vapor phase epitaxy (HVPE). This buffer layer had a thickness of 0.2 μm and a donor concentration of N_d-N_a = $(2\text{-}3)\times10^{17}$cm^{-3}. On top, Mg doped *p*-type AlGaN epitaxial layers with thickness of 0.8 μm and an Al content of 12 at.% were also grown by HVPE with an acceptor concentration of N_a-N_d = $(5\text{-}8)\times10^{17}$ cm^{-3}. Then, Ga doped *n*-ZnO epitaxial layers were deposited using chemical vapor deposition (CVD) with a thickness of 0.8 μm and a donor concentration of $N_d - N_a = 7\times10^{17}$ cm^{-3}. The growth process was stimulated by a discharge plasma, that allowed to reduce the substrate temperature by up to 400 °C and thus improve the structural quality of the ZnO layers.[9]

The heterojunction devices were fabricated by masking the surface, then using a 10 % HNO_3 aqueous solution to etch down through 2×2 mm^2 windows to remove ZnO and leave regions of the AlGaN layer exposed. Ohmic contacts to the *n*-ZnO and *p*-$Al_{0.12}Ga_{0.88}N$ were made by thermal vacuum evaporation of Al and Ni, respectively.[8]

Al compositions in the AlGaN epilayers and the structural quality of epitaxial layers were estimated using x-ray diffraction. The optical properties of the ZnO and AlGaN films were explored with cathodoluminescence (CL) spectroscopy at 80 and 300 K using accelerating voltage of 20 kV and an electron-beam current of 0.1-1 μA. Electroluminescense (EL) measurements were performed under forward DC-biased conditions at 300 and 500 K. The concentration of uncompensated acceptors and donors in epitaxial layers were determined from capacitance-voltage (C-V) characteristics of Cr Schottky barriers and Hall measurements, respectively. Forward and reverse current-voltage characteristics (I-V) were measured under DC conditions.

3. RESULTS AND DISCUSSION

According to x-ray studies, the Al content in the *p*-AlGaN epitaxial layers was estimated to about 12 at.% and the lattice mismatch to the ZnO layer amounted to 2.2 %. At the same time, for both epitaxial layers x-ray measurements revealed a good crystallinity. This is corroborated by CL measurements.[10]

The CL spectrum of the ZnO film consisted of intense, near-band-edge ultraviolet emission with a wavelength maximum at 387 nm and a full width at half maximum of 21 nm. This emission is of excitonic nature and is a result of the radiative annihilation of free and bound excitons. A broad defect-related green band with much lower intensity near 510 nm, typical for ZnO, was also observed (Fig. 1). The CL spectrum of the *p*-$Al_{0.12}Ga_{0.88}N$(Mg) film consisted of a very weak near-band-edge emission with λ_{max} at ~ 356 nm, and of a more intense broad band with a maximum at ~410 nm.

The current-voltage characteristics of the *n*-ZnO/*p*-AlGaN heterostructure were typical for rectified diodes: the direct current amounted to 60 mA at a voltage of 4 V and a current of about 10^{-7} A was observed under reverse voltage of about 30 V (Fig. 2). The cut-off voltage was equal to 3.2 V that is very close to the band-gap energy of ZnO suggesting that ZnO is the active region of the device. The other reason for this supposition we can see from the Anderson model of the energy band-diagram for *n*-ZnO/*p*-AlGaN heterostructures.[8] In this diagram, the electron affinity and

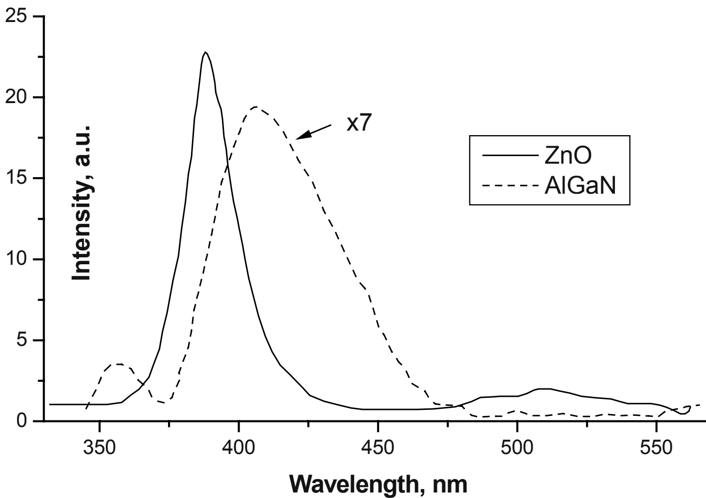

Figure 1. Cathodoluminescence spectra of the ZnO and $Al_{0.12}Ga_{0.88}N$ layers measured at room temperature. I_{max} (ZnO) = 387 nm, FWHM (ZnO) = 21 nm.

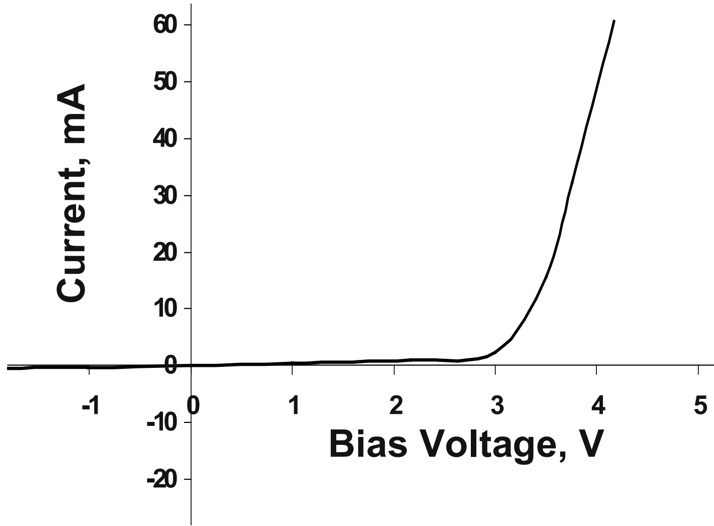

Figure 2. Current - voltage (I - V) characteristics of the n-ZnO / p-Al0.12Ga0.88N structures measured at room temperature: Uc = 4 V, Ic = 60 mA, Urev = 30 V, Irev ≤ 10-7 A.

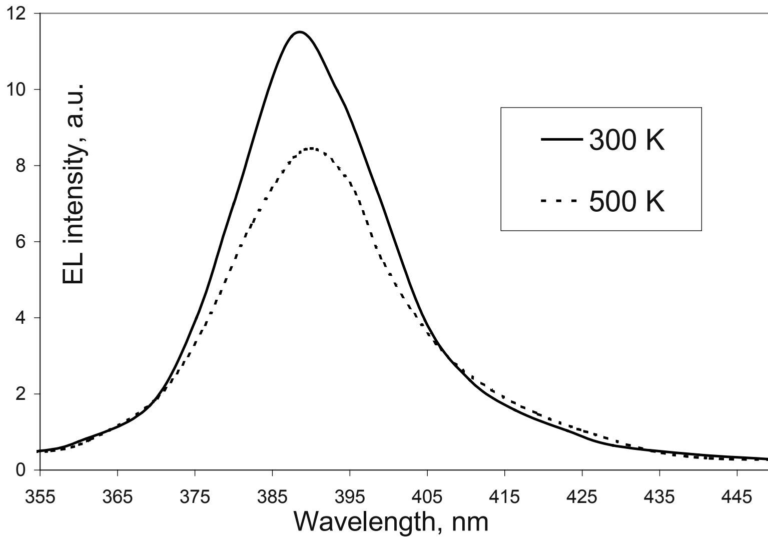

Figure 3. Electroluminescence spectra of the n-ZnO/p-$Al_{0.12}Ga_{0.88}N$ heterostructure of a light-emitting diode at temperatures of 300 and 500 K (I_c = 20 mA).

Under forward bias of 20 mA the device produced intense ultraviolet electroluminescence with a peak emission near 389 nm (3.19 eV) and a full bandgap energy values for ZnO were taken as 4.35 and 3.3 eV, respectively. Taking into account, that the electron affinity and bandgap energy values for AlGaN are assumed to be linearly dependent on the Al content, for our composition with 12 at.% Al these values equal to 3.68 and 3.72 eV, respectively. As a result, the energetic barrier for electrons is 0.67 eV, while the energetic barrier for holes is 0.25 eV. Thus, the energetic barrier for holes is about three times less than the barrier for electrons. Hence, the predominant device current is hole injection from the *p*-AlGaN into the *n*-type ZnO active region. width at half maximum of 26 nm (Fig. 3). Significantly, no other emission bands were observed in the EL spectrum. Also, significant EL emission at temperatures up to 500 K was observed due to a very large exciton binding energy of ZnO of about 60 meV.

4. CONCLUSION

Bright ultraviolet light emitting diodes based on *n*-ZnO/*p*-$Al_{012}Ga_{0.88}N$ heterojunctions were formed for the first time. EL emission was obtained from these heterostructures with a maximum at 389 nm. CL spectra, obtained from the ZnO layer, consisted of an intense emission with a maximum at 387 nm. Hence, we suggest that the dominant EL emission was observed from the ZnO layer. The dominant device current was a hole injection from *p*-$Al_{012}Ga_{0.88}N$ into the *n*-type ZnO active region of the heterojunction. The lattice mismatch between ZnO and *p*-$Al_{012}Ga_{0.88}N$ was estimated to be 2.2 %.

REFERENCES

1. D. C. Look, *Mater. Sci. Eng. B* **80**, 383 (2001).
2. D. M. Bagnall, Y. F. Chen, Z. Zhu, T. Yao, M. Y. Shen, and T. Gata, H, *Appl. Phys. Lett.* **73**, 1038 (1998).
3. V. I. Zinenko and Yu. A. Agafonov, *Solid State Electronics*, **48**, 2343 (2004).
4. A. E. Tsurkan, N. D. Fedotova, L. V. Kicherman, and P. G. Pas'ko, *Semiconductors* **6**, 1183 (1975).
5. I. T. Drapak, *Semiconductors* **2**, 624 (1968).
6. Ya. I. Alivov, J. E. Van Nostrand, D. C. Look, M. V. Chukichev, and B. M. Ataev, *Appl. Phys. Letters* **83**, 1 (2003).
7. B. M. Ataev, Ya. I. Alivov, E. Kalinina, V. V. Mamedov, G. A. Onushkin, S. Sh. Makhmudov, and A. K. Omaev, ICPS2004, July 26-30, 2004, Flagstaff, Arizona, USA.

8. Ya. I. Alivov, E. V. Kalinina, A. E. Cherenkov, D. C. Look, B. M. Ataev, A. K. Omaev, M. V. Chukichev, and D. M. Bagnall, *Appl. Phys. Lett*. **83**, 1 (2003).
9. B. M. Ataev, Ya. I. Alivov, V. V. Mamedov, S. Sh. Makhmudov, and B. A. Magomedov, *Semiconductors* **38**, 699 (2004).
10. D. M. Bagnall, Ya. I. Alivov, E. V. Kalinina, D. C. Look, B. M. Ataev, M. V. Chukichev, A. E. Cherenkov, A. K. Omaev, *Mat. Res. Soc. Symp. Proc. Vol*. **798**, Y3.9.1 (2004).

Chapter 19

ZnO TRANSPARENT THIN-FILM TRANSISTOR DEVICE PHYSICS

J. F. Wager
School of EECS, Oregon State University, Corvallis, Oregon, 97331, U.S.A.

Abstract: ZnO transparent thin-film transistors (TTFTs) are a recent and important development in the emerging field of transparent electronics. The objective of this contribution is to elucidate TTFT device physics issues related to channel mobility and output conductance.

Key words: Transparent thin-film transistor, device physics, effective mobility, field-effect mobility, saturation mobility, average mobility, incremental mobility, output conductance

1. INTRODUCTION

ZnO transparent thin-film transistors (TTFTs) are a very recent development.[1-8] The focus of this article is elucidation of channel mobility and output conductance. Although these device physics issues are important for the development of TTFTs, they are also of relevance for other types of inorganic or organic TFTs.

2. DRAIN CURRENT-DRAIN VOLTAGE MODELING

The simplest approach for specifying the drain current-drain voltage (I_{DS}-V_{DS}) electrical characteristics of a TTFT involves use of the square-law model,[9] as expressed by

$$I_{DS} = \frac{Z}{L} C_i \mu \left[\left(V_{GS} - V_T \right) V_{DS} - \frac{V_{DS}^2}{2} \right] \quad (1)$$

N.H. Nickel and E. Terukov (eds.),
Zinc Oxide – A Material for Micro- and Optoelectronic Applications, 217–224.
© 2005 *Springer. Printed in the Netherlands.*

in the pre-pinch-off regime, defined by $V_{DS} < V_{DSAT}$, and by

$$I_{DS} = \frac{Z}{2L} C_i \mu \left(V_{GS} - V_T\right)^2 \tag{2}$$

in the post-pinch-off regime, defined by $V_{DS} > V_{DSAT}$. In these equations, Z = gate width, L = gate length, C_i = gate capacitance per unit area, μ = channel mobility, and V_T = threshold voltage. Also, V_{DSAT} is the drain voltage at which the channel pinches off, which is specified as $V_{DSAT} = V_{GS} - V_T$, where V_{GS} is the gate voltage referenced to the source. Figure 1 illustrates a typical I_{DS}-V_{DS} curve for a specific V_{GS}.

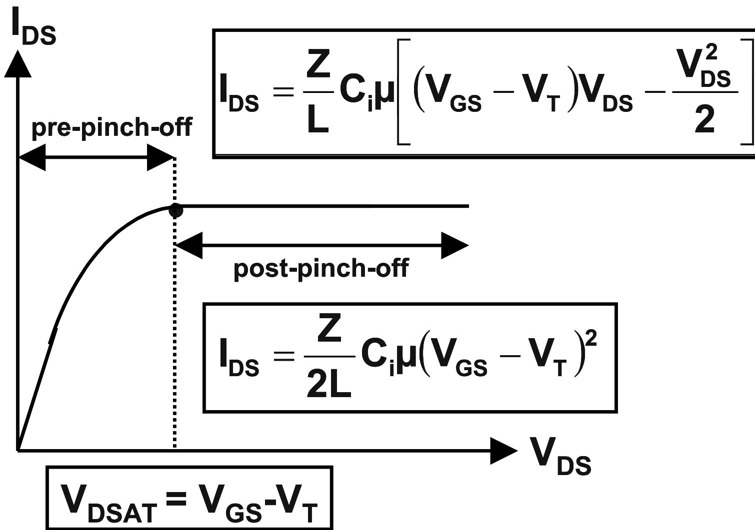

Figure 1. Drain current-drain voltage (I_{DS}-V_{DS}) curve at a given gate voltage (V_{GS}), illustrating the pre-pinch-off and post-pinch-off regimes of operation, which are distinguished by $V_{DSAT} = V_{GS} - V_T$.

It is clear from these square-law equations that mobility is an important physical property of the channel material since its magnitude directly affects the current-drive capability of the device. Additionally, mobility is directly related to the device frequency response, as given by the unity-gain frequency,

$$f_t = \left.\frac{\mu V_{DS}}{2\pi L^2}\right|_{pre-pinch-off} = \left.\frac{\mu (V_{GS} - V_T)}{2\pi L^2}\right|_{post-pinch-off} \tag{3}$$

Given the importance of mobility in establishing the current gain and frequency-response characteristics of a TTFT, it is worth considering channel mobility assessment.

3. CHANNEL MOBLITY ASSESSMENT

There are three common mobility assessment methods,[9] giving rise to (i) effective mobility, μ_{eff}, (ii) field-effect mobility, μ_{FE}, and (iii) saturation mobility, μ_{sat}. Each type of mobility is now individually considered.

3.1 Effective Mobility

Effective mobility, μ_{eff}, is obtained by considering the linear portion of the pre-pinch-off regime, defined by $V_{DS} << V_{GS} - V_T$, in which case,

$$I_{DS} \cong \frac{Z}{L} C_i \mu \left(V_{GS} - V_T\right) V_{DS}, \tag{4}$$

evaluating the output conductance for this situation,

$$g_d = \left.\frac{\partial I_{DS}}{\partial V_{DS}}\right|_{V_{GS}} = \frac{Z}{L} C_i \left(V_{GS} - V_T\right) \left[\mu + \frac{\partial \mu}{\partial V_{DS}} V_{DS} \right], \tag{5}$$

and solving for the mobility arising from this procedure, while neglecting the term involving the change in mobility with respect to drain voltage yields,

$$\mu_{eff} = \left.\frac{g_d}{\frac{Z}{L} C_i \left(V_{GS} - V_T\right)}\right|_{V_{DS} \to 0}. \tag{6}$$

Neglect of the term involving the change in mobility with respect to drain voltage is appropriate for long-channel TTFTs for which velocity saturation is not a relevant consideration.

Of the three common mobilities used for TTFT assessment, the effective mobility is probably the ‘best’ channel mobility figure-of merit since (i) it is evaluated in the linear regime of operation where the channel is most uniform and the concept of mobility as a proportionality constant between the electric field and carrier velocity is most appropriate, and (ii) the term

neglected in deriving μ_{eff} is indeed negligible for the long-channel devices currently of interest in the development of TTFTs. However, there are several disadvantages of the effective mobility, (i) V_T is required, (ii) μ_{eff} is singular when $V_{GS} = V_T$, and (iii) μ_{eff} estimation is sensitive to the magnitude of the source-drain resistance.

3.2 Field-effect Mobility

In a similar manner as to how μ_{eff} is assessed, the field-effect mobility, μ_{FE}, is also evaluated in the linear regime. However, μ_{FE} evaluation involves use of the transconductance rather than the output conductance,

$$g_m = \left.\frac{\partial I_{DS}}{\partial V_{GS}}\right|_{V_{DS}} = \frac{Z}{L} C_i \mu V_{DS} \left[1 + \frac{(V_{GS} - V_T)}{\mu_{eff}} \frac{\partial \mu}{\partial V_{GS}} \right]. \tag{7}$$

If the term involving the change in mobility with respect to a change in the gate voltage is neglected, the defining equation for the field-effect emerges,

$$\mu_{FE} = \left.\frac{g_m}{\frac{Z}{L} C_i V_{DS}}\right|_{V_{DS} \to 0} . \tag{8}$$

The most serious liability of μ_{FE} is the neglect in the derivation of μ_{FE} of the term involving the change in mobility with respect to a change in the gate voltage. This approximation is clearly not accurate at large gate voltages where the accumulation channel thickness decreases and hence electrons drifting in the channel experience more intense scattering at the interface, resulting in a reduction of the channel mobility. Another μ_{FE} demerit is that its estimation is sensitive to the magnitude of the source-drain resistance, as is μ_{eff}. On the other hand, the use of μ_{FE} offers several advantages, (i) it is evaluated in the linear regime of operation where the channel is most uniform and the concept of mobility as a proportionality constant between the electric field and carrier velocity is most appropriate, (ii) V_T is not required, and (iii) μ_{FE} is not singular when $V_{GS} = V_T$. The field-effect mobility is probably the most popular method used for channel mobility estimation.

3.3 Saturation Mobility

Unlike μ_{eff} and μ_{FE}, the saturation mobility, μ_{sat}, is evaluated from an assessment of I_{DS} in the post-pinch-off or saturation regime by taking the square root of the post pinch-off expression for I_{DSAT}, differentiating with respect to V_{GS}, and then solving the resulting equation for mobility to obtain,

$$\mu_{sat} = \left. \frac{\left(\frac{\partial \sqrt{I_{DSAT}}}{\partial V_{GS}} \right)^2}{\frac{Z}{2L} C_i} \right|_{V_{DS} > (V_{GS} - V_T)} , \quad (9)$$

where the condition $V_{DS} > (V_{GS} - V_T)$ ensures that this procedure is accomplished in the post-pinch-off or saturation regime of the I_{DS}-V_{DS} curve. Note that the numerator term is just the square of the slope of the linear portion of a $(I_{DSAT})^{1/2} - V_{GS}$ plot.

Of the three most common channel mobilities, μ_{sat} is probably used the least. The most serious liability of μ_{sat} is that it is evaluated in the post-pinch-off regime of operation where the channel thickness and electric field profile are highly non-uniform, the gradual channel approximation is not valid, and the concept of mobility as a proportionality constant between the electric field and carrier velocity is of questionable viability. However, μ_{sat} offers several advantages, (i) V_T is not required, and (ii) μ_{FE} is not singular when $V_{GS} = V_T$, and (iii) its estimation is relatively insensitive to the magnitude of the source-drain resistance, unlike μ_{eff} and μ_{FE}.

3.4 A New Approach to Mobility Assessment

Recently Hoffman[8] has proposed a new approach for channel mobility assessment that is novel in its interpretation of mobility and yet is closely related to conventional mobility assessment methodologies. This approach involve defining two new mobilities, an average mobility, μ_{avg},

$$\mu_{avg}(V_{GS}) = \left. \frac{g_d(V_{GS})}{\frac{Z}{L} C_i (V_{GS} - V_{ON})} \right|_{V_{DS} \to 0} , \quad (10)$$

and an incremental mobility, μ_{inc},

$$\mu_{inc}(V_{GS}) = \left. \frac{\dfrac{\partial g_d(V_{GS})}{\partial V_{GS}}}{\dfrac{Z}{L} C_i} \right|_{V_{DS} \to 0} \tag{11}$$

Note that both of these mobilities are written as functions of V_{GS}, explicitly indicating that these mobilities are expected to vary with gate voltage. A comparison of the equations defining μ_{eff} and μ_{avg} indicates that these mobilities are identical, except for the use of V_T for μ_{eff}, and V_{ON} for μ_{avg}. V_{ON} is defined as the voltage at which I_{DS} begins to noticeably increase when assessed using a Log(I_{DS})-V_{GS} curve.[8] Use of V_{ON} circumvents problems associated with the $V_{GS} = V_T$ singularity inherent in μ_{eff}. In a similar fashion, a comparison of the equations defining μ_{FE} and μ_{inc} indicates that these mobilities are quite similar, except that the transconductance, which is used in the defining relation for μ_{eff}, is replaced by the derivative of the channel conductance with respect to the gate voltage, i.e., the differential channel conductance, for the case of μ_{inc}.

The compelling aspect of this new approach to channel mobility assessment is the physical picture that emerges. Hoffman argues that μ_{avg} corresponds to the *average* mobility of *all* of the carriers moving in the channel, whereas μ_{inc} corresponds to the mobility of carriers added *incrementally* to the channel with an incremental increase in the gate voltage. Thus, a $\mu_{inc}(V_{GS})$ provides a physical picture of the channel mobility trend in terms of injected carrier trapping and mobility degradation, whereas $\mu_{avg}(V_{GS})$ provides information of relevance to projecting how a device will perform when used in a circuit application. Thus, both of these mobilities are useful, informative, and complementary.

4. OUTPUT RESISTANCE

Figure 2 illustrates a two-port network large-signal equivalent model appropriate for TTFT modeling. The gate-source is the input port and the drain-source is the output port.

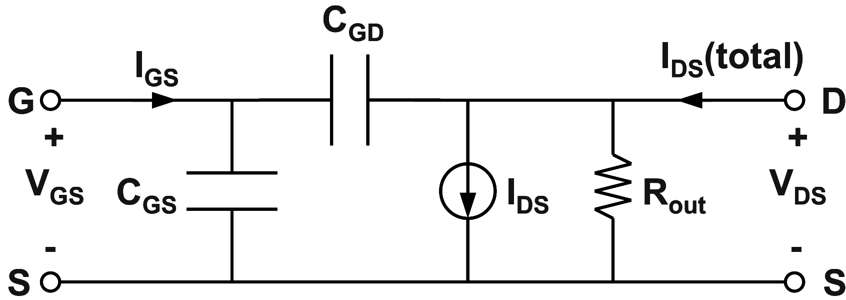

Figure 2. A large-signal TTFT equivalent circuit model.

The important feature of Fig. 1 is that the output current, I_{DS}(total), can arise from either or both of the two output branches shown, and identified by I_{DS} and R_{out}. In the context of the present discussion, I_{DS} represents the square-law theory current-voltage characteristics, which can be written in functional form as $I_{DS}(V_{DS},V_{GS})$, where V_{DS} and V_{GS} act as independent variables. Thus, this I_{DS} branch of the equivalent circuit represents transistor behavior. In contrast, R_{out} is a simple resistor that accounts for the conductivity of the 'bulk' channel layer. If the channel layer is conductive, R_{out} is small, most of the output current flows through R_{out}, and the TTFT operates as a resistor. In contrast, if the channel is highly resistive, R_{out} is large, and most of the output current flows through I_{DS} so that the TTFT functions as a transistor is supposed to function. Intermediate cases in which the output current flows through both branches give rise to voltage-controlled resistor operation. It is our experience that early-stage TTFT development more often results in resistor or voltage-controlled resistor behavior than transistor behavior, at least until the fabrication process is in control.

ACKNOWLEGMENTS

This work was funded by the U.S. National Science Foundation under Grant No. DMR-0071727 and by the Army Research Office under Contract No. MURI E-18-667-G3.

REFERENCES

1. S. Masuda, K. Kitamura, Y. Okumura, S. Miyatake, and T. Kawai, *J. Appl. Phys.* **93**, 1624 (2003).
2. R. L. Hoffman, B. J. Norris, and J. F. Wager, *Appl. Phys. Lett.* **82**, 733 (2003).
3. P. F. Carcia, R. S. McLean, M. H. Reilly, and G. Nunes, *Appl. Phys. Lett.* **82**, 1117 (2003).
4. J. Nishii, F. M. Hossain, S. Takagi, T. Aita, K. Saikusa, Y. Ohmaki, I. Ohkubo, S. Kishimoto, A. Ohtomo, T. Fukumura, F. Matsukura, Y. Ohno, H. Koinuma, H. Ohno, and M. Kawasaki, *Jpn. J. Appl. Phys.* **42**, L347 (2003).
5. J. F. Wager, *Science* **300**, 1245 (2003).
6. B. J. Norris, J. Anderson, J. F. Wager and D. A. Keszler, *J. Phys. D* **36**, L105 (2003).
7. Y. Kwon, Y. Li, Y. W. Heo, M. Jones, P. H. Holloway, D. P. Norton, and S. Li, *Proc. Electrochem. Soc.* **20003**, 68 (2003).
8. R. L. Hoffman, *J. Appl. Phys* **95**, 5813 (2003).
9. D. K. Schroder, *Semiconductor Material and Device Characterization*, 2nd ed., (Wiley, New York, 1998).

Chapter 20

ZINC OXIDE THIN-FILM TRANSISTORS

E. Fortunato, P. Barquinha, A. Pimentel, A. Gonçalves, A. Marques, L. Pereira, and R. Martins
Materials Science Department, Faculty of Sciences and Technology of New University of Lisbon and CEMOP-UNINOVA, Campus da Caparica, 2829-516 Caparica, Portugal

Abstract: ZnO thin film transistors (ZnO-TFT) have been fabricated by rf magnetron sputtering at room temperature with a bottom-gate configuration. The ZnO-TFT operates in the enhancement mode with a threshold voltage of 21 V, a field effect mobility of 20 cm^2/Vs, a gate voltage swing of 1.24 V/decade and an on/off ratio of 2×10^5. The ZnO-TFT present an average optical transmission (including the glass substrate) of 80 % in the visible part of the spectrum. The combination of transparency, high channel mobility and room temperature processing makes the ZnO-TFT a very promising low cost optoelectronic device for the next generation of invisible and flexible electronics. Moreover, the processing technology used to fabricate this device is relatively simple and it is compatible with inexpensive plastic/flexible substrate technology.

Key words: Thin-film transistors, rf magnetron sputtering, transparent electronics, optoelectronic devices

1. THIN FILM TRANSISTORS: (R)EVOLUTION

Even though the field-effect transistor did not come into widespread use until the 1960's, its invention predated both the junction and point-contact transistors by many years. As it is normal with many innovations, its practical realization was delayed until adequate materials and technologies were available for its fabrication. We can even say that the Thin Film Transistor (TFT) was the first solid-state amplifier ever patented. The basic principle of the field-effect transistor (what we call now JFET) was proposed by the first time by Julius Edgar Lilienfeld as early as 1925 and patented in 1930 Ref. (1) (see Fig. 1a) where an adaptation of the cross section of the

N.H. Nickel and E. Terukov (eds.),
Zinc Oxide – A Material for Micro- and Optoelectronic Applications, 225–238.
© 2005 *Springer. Printed in the Netherlands.*

device is shown). The field-effect transistor he describes was probably the first successful solid-state amplifier invented. The advantages of this device over the vacuum tubes, the only alternative high frequency amplifier available at that time, are also described in this patent and in later ones. Lilienfeld's later patent from 1933 (Ref. 2) describe a new field-effect transistor (now well-known as MISFET) were he specifies the thickness of the dielectric layer, which insulates the metal control electrode from the copper sulfide channel, of about 10^{-5} cm (1000 Å). This is, in fact, the typical thickness used in the insulated-gate transistors, which were developed many years later. Claim 1 of this patent reads:

> An electrical device comprising a conducting solid material having one surface an insulating layer of a thickness of the order of magnitude of 10^{-4} mm, and a superposed stratum of solid material integral therewith, of substantially greater conductivity and insulating from the conducting solid material by the said insulating layer.

Nevertheless, the first functional working TFT was demonstrated by Weimer in 1962 (Ref. 2). He used thin films of polycrystalline cadmium sulfide, similar to those ones developed for photodetectors. The simplified structure is shown in Fig. 1(b). Other TFT semiconductor materials like CdSe, Te, InSb and Ge were investigated, but in the mid-1960's the emergence of the metal oxide semiconductor field effect transistor (MOSFET) based on the crystalline silicon technology and the possibility to perform integrated circuits, led to a decline in TFT development activity by the end of the 1960s.

What dramatically changed the prospects for TFTs in the 1970s was the realization that with crystalline silicon, low cost was inseparable from miniaturization, whereas some applications required large arrays of low cost electronics, like for example displays. By this time many researchers and engineers had been engaged in improving the characteristics of liquid crystal displays (LCDs), recently discovered. The first active matrix LCD was successfully demonstrated by Brody[3] in 1973, where a CdSe TFT was used as a switching element for each pixel of a 120×120 matrix.

In spite of the many successful demonstrations of CdSe TFT LCDs, the industry did not enter in this market, until the report on the feasibility of doping amorphous silicon (a-Si:H) by the glow discharge technique.[4,5] After that and in 1979, LeComber, Spear and Ghaith[6] described a TFT using a-Si:H as the active semiconductor material, whose structure is indicated in Fig. 1(c).

After LeComber reported the first a-Si:H TFT, many laboratories started the development of AMLCDs formed on glass substrate. Although this result attracted much attention, the major disadvantage of a-Si:H TFT is its low

electron mobility that limits the ultimate speed of devices. However, an adequate device speed for switching applications in LCD's has been achieved.

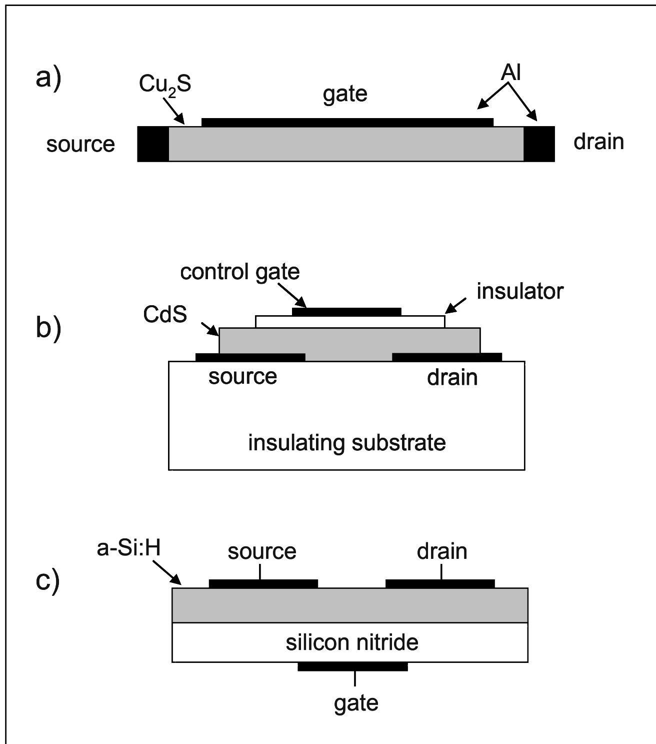

Fig. 1. Schematic cross sectional views of TFTs: a) Adapted from Lilienfeld,[1] b) after Weimer et al.,[2] and c) after LeComber et al.[6]

Since the mid-1980s the silicon-based thin-film transistors become the most important devices for active matrix liquid crystal displays (AMLCDs), and have successful dominated the large area LCD product market.[7]

The year 1990 marked the debut of a new class of TFT, based upon organic semiconductor active layer material,[8] with electron mobilities similar to that of a-Si:H. These new TFTs are very promising candidates for integration onto flexible plastic substrates for a future generation of rugged, lightweight displays than can be rolled up like a map.

More recently a new generation of oxide semiconductors are being studied and applied as the active material to TFT, in special zinc oxide (ZnO). This will be described in the next sections.

2. ZINC OXIDE TFTs: MOTIVATION

Transparent electronics are nowadays an emerging technology for the next generation of optoelectronic devices. Oxide semiconductors are very interesting materials because they combine simultaneously high/low conductivity with high visual transparency and have been widely used in a variety of applications (e.g. antistatic coatings, touch display panels, solar cells, flat panel displays, heaters, defrosters, optical coatings, among others) for more than a half-century. Transparent oxide semiconductor based transistors have recently been proposed using as active channel non-doped ZnO.[9-15] One of the main advantages exhibited by these transistors lies on the magnitude of the electron channel mobility leading to higher drive currents and faster device operating speeds. The mobility reported in the literature is ranging from 0.2 to 7 cm^2/Vs with an on/off current ratio from 10^5 to 10^7 and a threshold voltage (V_{TH}) between -1 and 15 V. To date, ZnO channel layers have been deposited using substrate heating or submitted to post thermal annealing in order to increase, mainly the crystallinity of the ZnO layer and so the film´s mobility. The main advantage of using ZnO deals with the fact that it is possible to growth at/near room temperature high quality polycrystalline zinc oxide, which is a particular advantage for electronic drivers, where the response speed is of major importance. Besides that, since ZnO is a wide band gap material (3.2 eV), it is transparent in the visible region of the spectra and therefore, also less light sensitive.

Table 1. State of the art concerning ZnO TFTs.

Technique	Ion Beam	Sol Gel	Pulsed Laser
Processing temperature	600-800 °C (ref. 11)	700 °C (ref. 15)	450 °C (ref. 10)
Mobility (cm^2/Vs)	0.3-2.5	0.2	0.031-0.97
on/off ratio	10^6	10^7	10^6
V_{TH} (V)	10-20	not mentioned	-1-2.5
TFT operation mode	enhancement	enhancement	enhancement
I_{sat} (μA)	70	14	80

Thin film transistors based on a-Si:H technology present some limitations such as light sensitivity and light degradation accompanied with a low mobility (< 2 cm^2/Vs). On the other hand, the polysilicon TFT in spite exhibiting a high mobility (50 $cm^2/Vs \le \mu \le 500$ cm^2/Vs) their opacity limits the aperture ratio for active matrix arrays, highly important when for instance, organic light emitting diodes (OLED’S) have to be addressed. Apart from that, if flexible substrates based on polymers are intended to be used, the processing temperature is also a quite limiting factor. One possible

way to overcome such problems is the utilization of efficient and reliable oxide based thin film transistors.

Table 1 presents a comparison of fully transparent ZnO-TFTs (data as of March 2004).

3. EXPERIMENTAL DETAILS

3.1 ZnO optimization

The ZnO films (doped and undoped) were deposited onto soda lime glass substrates by rf (13.56 MHz) magnetron sputtering using a ceramic oxide ZnO target from Super Conductor Materials, Inc. with a purity of 99.99% and 2" diameter. The sputtering was carried out at room temperature and the argon deposition pressure was 0.15 Pa. The distance between the substrate and the target was 10 cm and the rf power was varied between 50 and 175 W. The deposition rate was varied between 15 and 30 nm/min. The film thickness was measured using a surface profilometer (Dektak 3 from Sloan Tech.). The electrical resistivity (ρ) was measured as a function of temperature in the range of 300 to 500 K using thermally evaporated aluminum electrodes in a coplanar configuration. X-ray diffraction measurements were performed at RT in air, using the Cu-K_{α} line of a Rigaku DMAX III-C diffractometer. The surface morphologies were analyzed using a Field Effect Scanning Electron Microscope (FE-SEM, S-1400 Hitachi). The optical transmittance measurements were performed with a Shimadzu UV/VIS 3100 PC double beam spectrophotometer in the wavelength from 200 nm to 2500 nm.

3.2 ZnO-TFT fabrication

Fig. 2 shows a schematic illustration of the ZnO-TFT produced, using only oxide materials. In order to evaluate the performances of the TFTs, different channel width and channel lengths were used, varying the W/L ratio from 1 to 65. The devices were electrically characterized in air, at room temperature, and in the dark using a microprobe station connected to a semiconductor parameter analyzer (model HP 4145B). The reproducibility of the device characteristics was confirmed by measuring more than 200 TFTs, each one several times. The gate dielectric of the ZnO-TFT is based on a engineered insulator consisting of a superlattice of Al_2O_3 and TiO_2 (ATO)[16] deposited on a glass coated with an Indium Tin Oxide (ITO). The

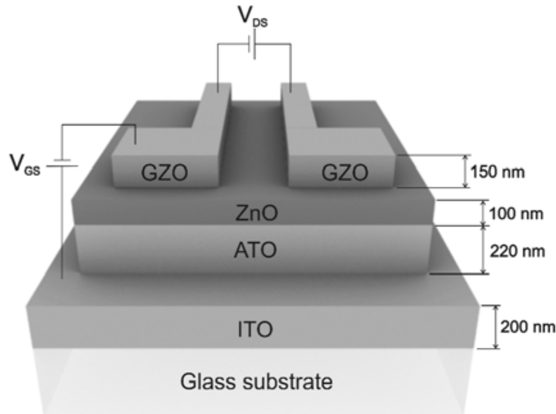

Fig. 2. Schematic illustration of the ZnO based TFT structure. The ZnO channel layer and the ATO gate insulator are 100 nm and 220 nm in thickness, respectively, while the ITO gate and the GZO source and drain are 200 nm and 150 nm in thickness, respectively. The channel length and gate width ratio varied between 1 and 65.

dielectric had a thickness of 200 nm, exhibiting a transparency of 85%, a resistivity of 2.3×10^{-4} Ωcm, a carrier concentration of 7.7×10^{20} cm^{-3}, and a mobility of 36 cm^2/Vs. The average capacitance of the ATO layer measured nearby the TFTs produced was 55 nF/cm^2, having a total thickness of 220 nm. From this measurement the relative dielectric constant, was determined as being around 14.

The channel is based on undoped ZnO, 100 nm thick, whose electrical properties were properly controlled during the deposition pressure aiming to obtain a material where the conduction is dominated by electrons. In this case the background electron concentration must be reduced in order to increase the carrier's mobility. This attempted was achieved by optimizing the deposition conditions for undoped ZnO films produced by rf magnetron sputtering. To do so we choose to vary the rf power instead of the oxygen partial pressure (easier for controlling the stoichiometry), because the use of oxygen during the deposition is not compatible with the lift-off technique used (the photoresist is removed by a plasma that contains oxygen ions) and also to minimize the defects at the channel-insulator interface. Moreover, the processing technology used is relatively simple and it is compatible with inexpensive plastic/flexible substrate technology.

The drain and source are based on highly conductive gallium doped zinc oxide (GZO)[17], 150 nm thick and patterned by the lift-off technique. These depositions were also carried out at room temperature.

4. RESULTS

Fig. 3 shows the dependence of the electrical resistivity and the average optical transmittance at the visible spectra (between 400 and 700 nm), as a function of rf power density (P). The highest resistivity (≈ 10^8 Ωcm) was obtained for P = 5 W/cm^2. For P around 5 W/cm^2 the films became close to stoichiometry with low structural defects and consequently higher resistive. As we decrease or increase the rf power density from 5 W/cm^2, a deviation from stoichiometry is obtained accompanied by a decrease on the electrical resistivity, due to a lower carrier concentration or/and electron mobility.

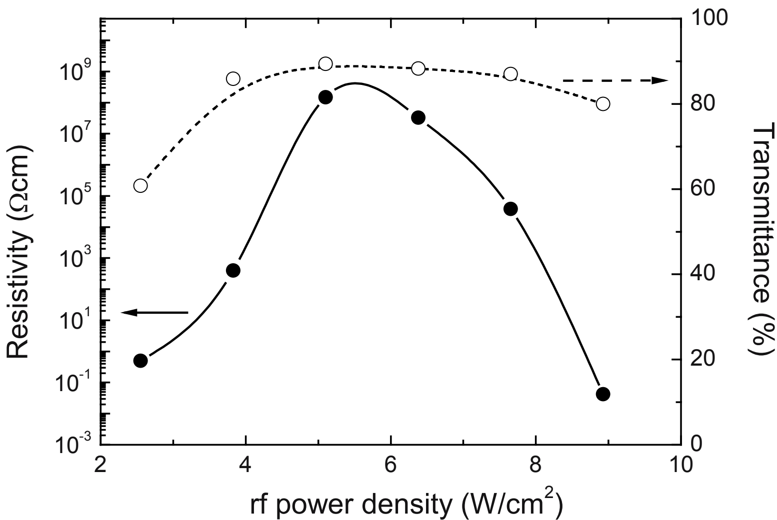

Fig. 3. Electrical resistivity (measurements were performed at room temperature in vacuum using thermally evaporated aluminum contacts on stabilized samples) and average optical transmittance, versus rf power density.

This is also confirmed by a decrease on the optical transmittance, especially for rf power densities lower than 5 W/cm^2. For the films with lower resistivity (< 10^2 Ωcm), we measured Hall mobilities of about 2 cm^2/Vs and a carrier concentration of 3×10^{16} cm^{-3} (n-type). For these undoped films an excess of interstitial Zn ions or/and oxygen vacancies can contribute with free electrons to the electrical conduction. Concerning the ZnO films used for the TFTs, due to the high value of the electrical resistivity (~10^8 Ωcm) it was not possible to measure the Hall.

The X-ray diffraction patterns of these films are shown in Fig. 4(a). As the rf power density increases, the diffraction peak corresponding to the

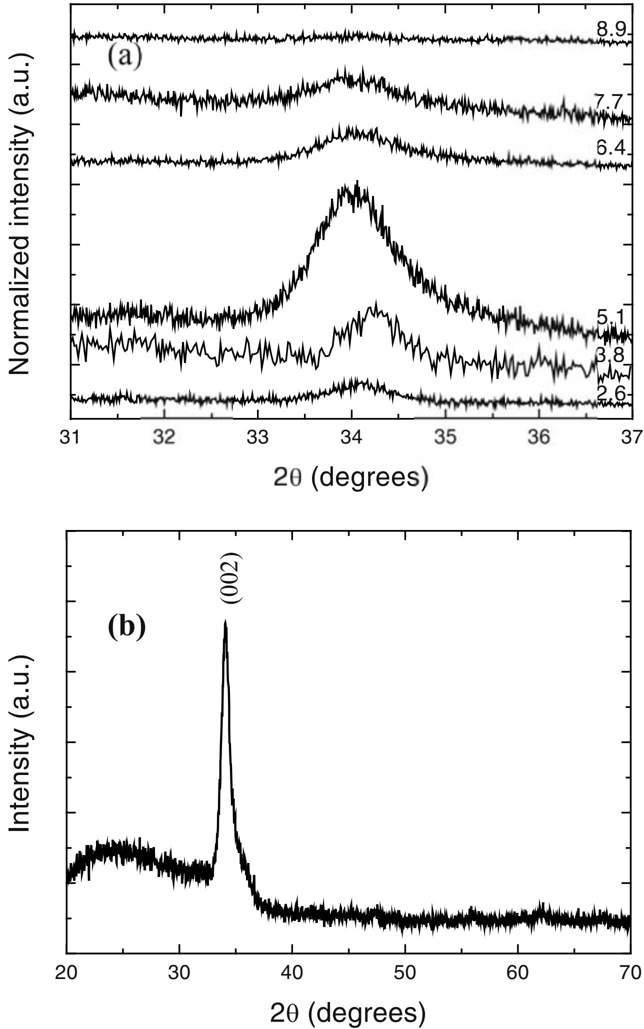

Fig. 4. (a) X-ray diffractograms of ZnO films corrected to the thickness of each sample (ranging from 190 nm to 360 nm), deposited on soda lime substrates, using the Cu-K_α line. The large width of the peaks reveals a limited crystalline domain. For the film produced at 5 W/cm^2, using the full-width at half-maximum of the peak at an angle of 34.1 °, we calculated an average crystallite size of the order of 10 ± 1 nm using the Scherrer equation. The low crystallite size is also associated with the fact that the films were processed at room temperature without any type of post thermal annealing; (b) X-ray diffractogram of a ZnO film produced with an rf power density of 5 W/cm^2 for a wider 2θ range. The film thickness is 130 nm.

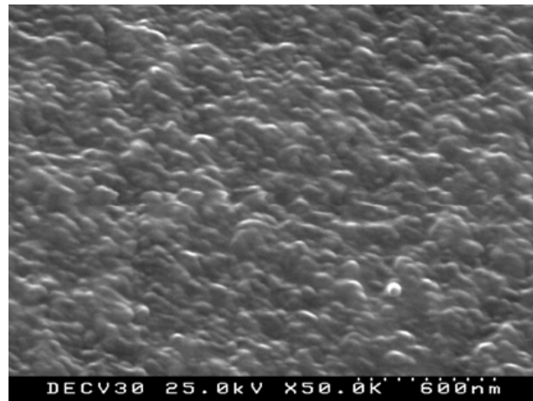

Fig. 5. SEM micrograph with an apparent viewing angle of 40° of the same ZnO film presented in Fig. 4(b).

(002) orientation become predominant up to a rf power density of 5 W/cm^2, where the resistivity is maximum. Besides that the data also show that this film is mainly constituted of dense and small crystallites (nanocrystalline with sizes up to 10 nm). For higher rf power densities the peak disappears, indicating that the crystallinity of the ZnO starts to degrade. This is attributed to a decrease of the oxidation of the films. The amorphous phase starts to become predominant.

Fig. 4(b) shows the X-ray diffraction pattern for the ZnO film produced at P = 5 W/cm^2 for a wider 2θ range. For all the films produced only the ZnO (002) peak at 2θ ≈ 34° is observed, revealing that the films are nanocrystalline with a hexagonal structure and a preferred orientation with the c-axis perpendicular to the substrate. This is also consistent with the results obtained by scanning electron microscopy (see Fig. 5).

Fig. 5(a) shows the source-to-drain (I_{DS}) current as a function of the gate voltage (V_{GS}). It is observed that the ZnO-TFT has an n-channel, since electrons are generated by the positive V_{GS}. A high I_{DS} (230 μA) is obtained for V_{GS} = 40 V and V_{DS} = 20 V. Besides that a hard saturation current at the post pinch-off voltage is observed that is in accordance with the standard theory of field-effect transistors. The saturation mobility (μ_{sat}) and the threshold voltage (V_{TH}) were calculated by fitting a straight line to the plot of the square root of I_{DS} vs V_{GS}, according to the expression (saturation region)

$$I_{DS} = \left(\frac{C_i \mu_{sat} W}{2L}\right)\left(V_{GS} - V_{TH}\right)^2 \quad for \quad V_{DS} > V_{GS} - V_{TH} \tag{1}$$

where C_i is the capacitance per unit area of the gate insulator. The obtained μ_{sat} is around 20 cm^2/Vs and the V_{TH} is 21 V, showing that the ZnO-TFT operates in the enhancement mode. Enhancement mode is preferable to depletion mode since it is not necessary to apply a gate voltage to switch off the transistor, because the circuit design is simpler and the power dissipation is lower. The high value of μ_{sat} agrees with the effective mobility (μ_{eff})[18] determined for $V_{DS} \leq 2$ V (in order to guarantee a uniform distribution of carriers in the channel along the source to drain region) that has a value of about 19 cm^2/Vs. Here we also have to notice that the average field-effect mobility (μ_{FE}) obtained from the transconductance[18] data in the same V_{DS} region and for 30 V $\leq V_{GS} \leq$ 40 V is around 21 cm^2/Vs. These data confirm the high quality of the undoped ZnO films (improved crystallinity fraction of the nanocrystals and low oxygen vacancies and/or Zn interstitials working as donors) as well as the good channel-insulator interface obtained. The magnitude obtained for V_{TH} is directly proportional to the gate insulator thickness. Reducing the gate insulator thickness could easily reduce these values. The off-current is low, on the order of 1.3×10^{-9} A, and the on/off ratio is 2×10^5. That is, the TFT is able to sustain currents as high as 2.3×10^{-4} A. The gate voltage swing, S defined as the voltage required to increase the drain current by a factor of 10 was 1.24 V/decade for the ZnO-TFT under analysis. S is given by the maximum slope in the transfer curve (Fig. 6a).

Fig. 6(b) shows the I_{DS} current curves as a function of the drain current (V_{DS}) for different V_{GS}. The saturation was about 230 μA under a gate bias of 40 V. Besides the high value obtained for the saturation current, the device exhibits "hard" saturation, evidenced by the flatness of slope of each I_{DS} curve, for large V_{DS}, without the need of post heating treatments. This indicates that the entire thickness of the ZnO channel layer is depleted and so the device exhibits a high resistance (defined as the inverse of the slope of the I-V curve for a given gate voltage, in the off saturation regime), which is larger than 20 MΩ, as required for most circuit applications. The on resistance ($R_{ON} = 1/g_d$) defined as

$$R_{ON} = g_d^{-1} = \frac{L}{\mu_{eff} C_i W (V_{GS} - V_{TH})} \tag{2}$$

is of about 45 KΩ (V_{GS} = 30 V). The relation between the R_{OFF} and R_{ON} is within what is expected for fast switching device behavior. Besides that, the device response time, defined as being proportional to $R_{ON}\times Ci$ amounts to values of about 25 ps/μm^2, which is highly promising for device miniaturization.

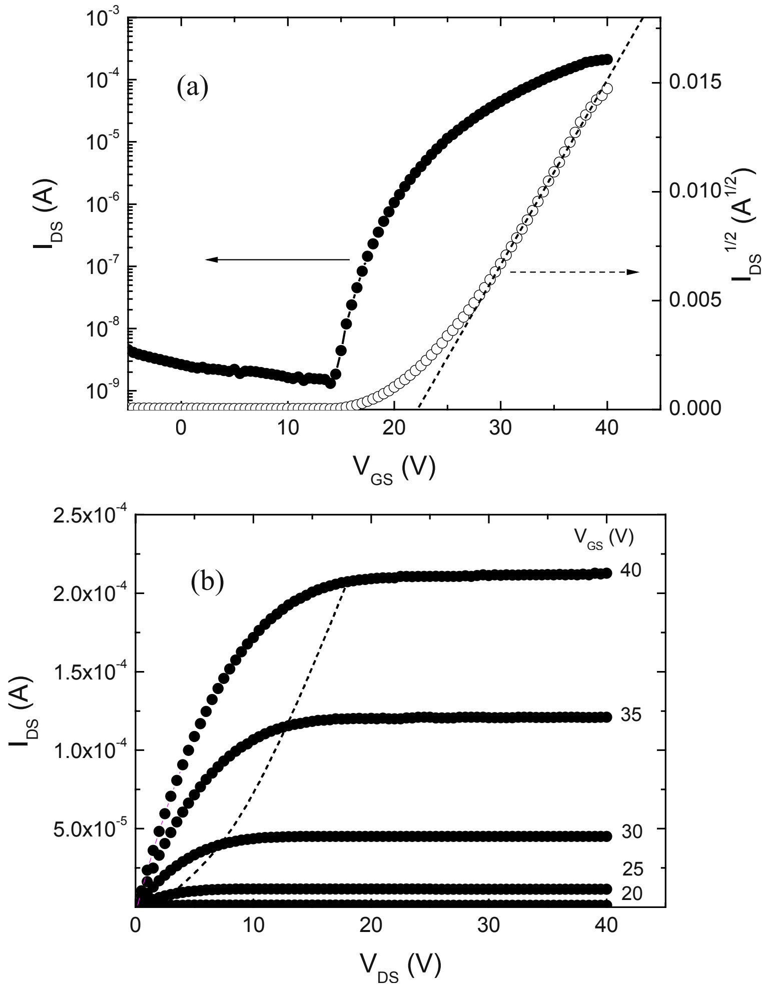

Figure 6. Typical ZnO-TFT characteristics with the channel layer deposited at room temperature by rf magnetron sputtering, for a TFT with a width-to-length ratio of 1.4. (a) Transfer characteristics for V_{DS} = 20 V. The on/off ratio is 2×10^5. The ZnO-TFT operates in the enhancement mode with a threshold voltage of 21 V and a saturation mobility of 20 cm^2/Vs. (b) Output characteristics for a ZnO-TFT. The saturation was about 230 μA under a gate bias of 40 V. The ZnO-TFT exhibits "hard" saturation, evidenced by the flatness of slope of each I_{DS} curve, for large V_{DS}. The dashed line represents the saturation drain current that follows an exponential dependence on the voltage.

The exposure to ambient light of these ZnO-TFTs has no effect on the current-voltage characteristics, which is an advantage in electronic drivers for displays.

Fig. 7 shows the optical transmittance spectrum of the entire ZnO-TFT in the wavelength range between 200 nm and 2500 nm (including the glass substrate with 1.1 mm thickness). The average optical transmission in the visible part of the spectrum is 80% while at 550 nm (maximum sensitivity for the human eye) it is 85%, which indicates that transmission losses due to the ZnO-TFTs in comparison with the uncoated glass substrate are negligible

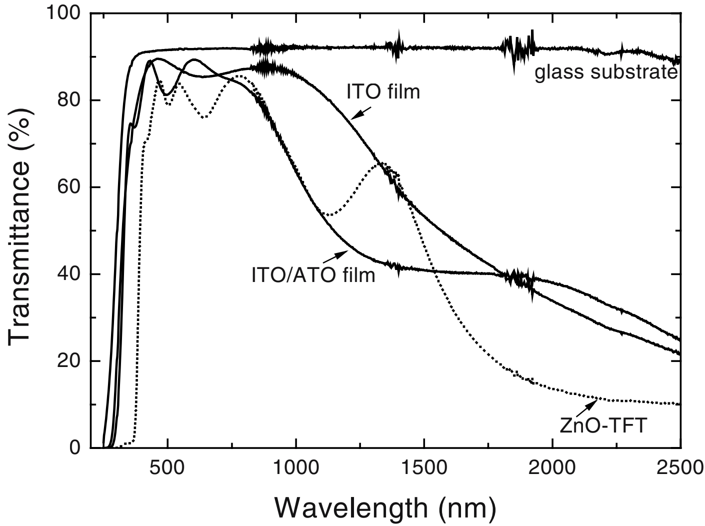

Figure 7. Optical transmission spectra for the entire ZnO-TFT structure including the glass substrate, were it is possible to observe that the ZnO-TFT is fully transparent to visible light. For comparison the optical transmission spectra for the glass substrate (1.1 mm thickness), the ITO, and the ITO/ATO films are also shown. The baseline and reference were measured in air to quantify the total amount of transmitted light. The lower part shows a photograph of a glass substrate (2.5×2.5 cm^2) with ZnO based TFTs.

(7%). The absorbance at the near infrared region is associated with the increase of the carrier concentration of the ITO and GZO films that leads to a lower value associated to the plasma frequency.[19]

5. CONCLUSIONS

In conclusion we have demonstrated the possibility to produce fully transparent high quality ZnO based TFTs at room temperature by rf magnetron sputtering on glass substrates. ZnO is one of a few oxides that can be grown as a polycrystalline or even as a high compact and dense nanocrystalline material at relatively low or even at room temperature, on a variety of substrates, such as amorphous glasses and plastics or metal foils. This particularity together with the possibility to realize efficient and reliable TFTs exhibiting high mobility's, opens new doors for the so called "invisible electronic circuits" that are highly important for the next generation of invisible and flexible electronics.

ACKNOWLEDGEMENTS

We thank A. Pakkala from Planar Systems, Inc., Espoo, Finland, for supplying the ITO/ATO substrates. The authors acknowledge A. Lopes for the SEM analysis.

REFERENCES

1. J. E. Lilienfeld, *U.S. Patent* 1,745,175 (1930).
2. J. E. Lilienfeld, *U.S. Patent* 1,900,018 (1933).
2 P. K. Weimer, *Proceedings of the IRE*, **1462** (1962).
3. T. P. Brody, J. A. Asars, and G. D. Dixon, *IEEE Trans. Electron Devices*, **ED-20**, 995 (1973).
4. W. E. Spear and P. G. LeComber, *Solid State Commun*. **17**, 1193 (1975).
5. W. E. Spear and P. G. LeComber, *Philosophical Magazine* **33**, 935 (1976).
6. P. G. LeComber, W. E. Spear, and A. Gaith, *Elec. Lett.*, **15** 179 (1979).
7. Y. Kuo in *Thin Film Transistors – Materials and Processes* Volume 1: *Amorphous Silicon Thin Film Transistors*, Kluwer Academic Publishers, 2004.
8. F. Garnier, *Adv. Mat.* **2**, 592 (1990).
9. Y. Ohya, T. Niwa, T. Ban, and Y. Takahashi, *Jpn. J. Appl. Phys*., **40**, 297 (2001).
10. S. Masuda, K. Kitamura, Y. Okumura, and S. Miyatake, *J. Appl. Phys*. **93**, 1624 (2003).
11. R. L. Hoffman, B. J. Norris, and J. F. Wager, *Appl. Phys. Lett*. **82**, 733 (2003).
12. P. F. Carcia, R. S. McLean, M. H. Reilly, and G. Nunes, Jr., *Appl. Phys. Lett*. **82**, 1117 (2003).

13. P. F. Carcia, R. S. McLean, M. H. Reilly, I. Malajovich, K. G. Sharp, S. Agrawal, and G. Nunes, Jr., *Mater. Res. Soc. Symp. Proc*. **769**, H7.2.1 (2003).
14. J. Nishii, F. M. Hossain, S. Takagi, T. Aita, K. Saikusa, Y. Ohmaki, I. Ohkubo, S. Kishimoto, A. Ohtomo, T. Fukumura, F. Matsukura, Y. Ohno, H. Koinuma, H. Ohno, and M. Kawasaki, *Jpn. J. Appl. Phys*., **42**, L347 (2003).
15. B. J. Norris, J. Anderson, J. F. Wager, D. A. Keszler, *J. Phys. D: Appl. Phys*. **36**, L105 (2003).
16. ITO/ATO-coated glass substrates from Planar Systems, Inc. Espoo, Finland.
17. V. Assunção, E. Fortunato, A. Marques, A. Gonçalves, I. Ferreira, H. Águas and R. Martins, *Thin Solid Films* **442**, 102. (2003).
18. D. K. Schroder, in *Semiconductor Material and Device Characterization*, 2nd ed. Wiley, New York, 1998.
19. T. J. Coutts and D. L. Li Young. *MRS Bull*. **25**, 58 (2000).

Index

Acceptor 37, 69
Atomic force microscopy

Band structure 171

Cathodoluminescence 83
Cluster 15
Columnar structure 15
Output conductance 217

dc-magnetron sputtering 15
Defects 133
Device physics 217
Dislocations 99
    electrical activity 99
DLTS 47
Donor 37, 69, 115
    hydrogen 115
Doping 197

Electrical properties 3
Electrical transport 197
Electroabsorption spectra 183
Electroluminescence 211
Electron affinity 115
Electron holography 99
Epitaxial layers 211
Electron paramagnetic resonance 69
    photo-EPR 69
Exciton 69, 159, 171, 183

Field effect mobility 225

g-factor 159

Hall effect 37, 47
    single crystal 47
    thin films 47
Heterointerface 197
Heterojunction 211
Heterostructures 25
Hexagonal resonator 83
Hole injection 211
Hydrogen 115, 125

Hydrogen 115, 125, 133
    binding energy 145
    complexes 145
    concentration 145
    density of states 145
    donor 125
    local vibrational modes 145
Hyperfine constant 115

Interband transition 171
IR absorption 133
IR spectroscopy 125

Kinetic analysis 25

Light trapping 197

Magneto-luminescence 159
Magnetron sputtering 59
Metal organic vapor phase epitaxy 99
Microcrystals 83
Mobility 217
  average 217
  effective 217
  field-effect 217
  incremental 217
  saturation 217
Molecular static method 183
MOVPE *See* Metal organic vapor phase epitaxy
Muon spin rotation 115
Muonium 115
Muons 115

Nanocavity 83
Nanostructure 83
n-type 25, 37

O-H complexes 125
Optical spectra 171
Optoelectronic devices 225
Oxygen radicals 25

PEMOCVD
  plasma enhanced MOCVD 59
Permitivity 171
Photoluminescence 59, 69, 83, 159
  thermoluminescence 69
Puldes laser deposition 47
Point defects 69
Polarization 83, 171
Polycrystalline films 197
p-type 25, 37

Raman spectroscopy 145
Recursion method 183
Reflectance 171
rf Magnetron sputtering 225

Schottky contacts 47
Structural properties 3

Thermal evaporation 59
Thermography 47
Thin-film transistors 217, 225
Transmission electron microscopy 99
Transparent electronics 225
Transparent thin-film transistor 217, 225

Ultraviolet emission 211

Valence band symmetry 159
Vapor-liquid-solid mechanism 15
Vibrational density of states 183
Vibrational modes 125

WGM *See* whispering gallery modes
Whisker 15
Whispering gallery modes 83
Window layers 197

Zeeman effect 159
Zn vacancy 133
ZnO synthesis 3
  hydrothermal growth 3
  melt growth 3
  solution growth 3
  vapor growth 3